AWARD NUMBER: W81XWH-18-1-0620

TITLE: Modeling the Effects of Stroma on Clear Cell Renal Cell Carcinoma

PRINCIPAL INVESTIGATOR: Dr. Leif Oxburgh

CONTRACTING ORGANIZATION: The Rogosin Institute, New York, NY

REPORT DATE: December 2022

TYPE OF REPORT: Final

PREPARED FOR: U.S. Army Medical Research and Development Command
Fort Detrick, Maryland 21702-5012

DISTRIBUTION STATEMENT: Approved for Public Release;
Distribution Unlimited

The views, opinions and/or findings contained in this report are those of the author(s) and should not be construed as an official Department of the Army position, policy or decision unless so designated by other documentation.

REPORT DOCUMENTATION PAGE

Form Approved
OMB No. 0704-0188

Public reporting burden for this collection of information is estimated to average 1 hour per response, including the time for reviewing instructions, searching existing data sources, gathering and maintaining the data needed, and completing and reviewing this collection of information. Send comments regarding this burden estimate or any other aspect of this collection of information, including suggestions for reducing this burden to Department of Defense, Washington Headquarters Services, Directorate for Information Operations and Reports (0704-0188), 1215 Jefferson Davis Highway, Suite 1204, Arlington, VA 22202-4302. Respondents should be aware that notwithstanding any other provision of law, no person shall be subject to any penalty for failing to comply with a collection of information if it does not display a currently valid OMB control number. **PLEASE DO NOT RETURN YOUR FORM TO THE ABOVE ADDRESS.**

1. REPORT DATE	2. REPORT TYPE	3. DATES COVERED
December 2022	Final	01Sep2018-31Aug2022

4. TITLE AND SUBTITLE

Modeling the Effects of Stroma on Clear Cell Renal Cell Carcinoma

5a. CONTRACT NUMBER
W81XWH-18-1-0620

5b. GRANT NUMBER
W81XWH-18-1-0620

5c. PROGRAM ELEMENT NUMBER
NA

6. AUTHOR(S)

Leif Oxburgh

E-Mail: leo9022@nyp.org

5d. PROJECT NUMBER
NA

5e. TASK NUMBER
NA

5f. WORK UNIT NUMBER
NA

7. PERFORMING ORGANIZATION NAME(S) AND ADDRESS(ES)

The Rogosin Institute
505 E 70th Street, 2nd Fl
New York
NY 10021-4872

8. PERFORMING ORGANIZATION REPORT NUMBER

9. SPONSORING / MONITORING AGENCY NAME(S) AND ADDRESS(ES)

U.S. Army Medical Research and Development Command
Fort Detrick, Maryland 21702-5012

10. SPONSOR/MONITOR'S ACRONYM(S)

11. SPONSOR/MONITOR'S REPORT NUMBER(S)

12. DISTRIBUTION / AVAILABILITY STATEMENT

Approved for Public Release; Distribution Unlimited

13. SUPPLEMENTARY NOTES

14. ABSTRACT

Clear cell renal cell carcinoma (ccRCC) is the 10th most common cancer. Surgical removal of the tumor is the primary treatment for the majority of patients, and is curative in over 50% of cases. However, therapeutic options are limited for the large number of patients whose cancer recurs. Development of new testing platforms in which patient tumors are established in cell culture provide the possibility to identify new drug targets in a patient-specific manner. In this study we have developed a tumor modeling system with the high fidelity to patient tumors by recreating multiple parameters of the tumor-of-origin such as cellular composition and extracellular matrix (ECM) composition. In proof-of-principle experiments we have used these patient-derived tumor replicas to screen for drug targets that interfere with the transition in the final phase of the cell cycle. We demonstrate that inhibition of FOXM1, PME1 and TMEM167A slow tumor growth using the compounds FDI-6, AMZ-30 and the natural product silibinin.

15. SUBJECT TERMS

Clear cell renal cell carcinoma, ccRCC, tumor stroma, tumor model, precision medicine

16. SECURITY CLASSIFICATION OF:			17. LIMITATION OF ABSTRACT	18. NUMBER OF PAGES	19a. NAME OF RESPONSIBLE PERSON
a. REPORT	b. ABSTRACT	c. THIS PAGE			USAMRDC
Unclassified	Unclassified	Unclassified	Unclassified	104	19b. TELEPHONE NUMBER *(include area code)*

TABLE OF CONTENTS

	Page
1. Introduction	4
2. Keywords	4
3. Accomplishments	4
4. Impact	10
5. Changes/Problems	10
6. Products	11
7. Participants & Other Collaborating Organizations	11
8. Special Reporting Requirements	13
9. Appendices	13

1. Introduction

Clear cell renal cell carcinoma (ccRCC) is the 10th most common cancer. Surgical removal of the tumor is the primary treatment for the majority of patients, and is curative in over 50% of cases. However, therapeutic options are limited for the large number of patients whose cancer recurs. Chemo- and radiotherapies are ineffective, and the current focus is on inhibitors of specific pathways. Broadly, these are targeted to angiogenesis (eg Bevacizumab, Sunitinib) or to metabolism (eg Temsirolimus). It is anticipated that these drugs target pathways in tumor cells, cancer associated fibroblasts, endothelial cells and inflammatory cells. In most cancers, each of these populations plays an important role in determining pathogenesis; in ccRCC the cancer cell – vasculature communication has been the focus of particular attention because of the highly angiogenic nature of the tumor. However, little is known regarding the role of tumor associated fibroblasts. To study this poorly explored but potentially clinically important component of ccRCC we propose to generate an assay system with which we can understand the influence of tumor fibroblasts on tumor aggressiveness using primary patient-derived fibroblasts and tumor cells. We can efficiently generate ccRCC tumor models using porous 3D silk scaffolds with and without fibroblast incorporation, and these synthetic tumors are morphologically similar to patient tumors. Silk scaffolds allow for a controllable 3D structural support for cell growth and cell-cell interactions that is easily modified to mimic the native biophysical and biochemical environment. We have developed conditions for the growth of kidney tissue in the cortex of the kidney, where we see vigorous vascularization by the host. We propose to develop an orthotopic tumor modeling system with the highest possible fidelity by recreating multiple parameters of the tumor-of-origin such as cellular composition, metabolic profile, stiffness of the substrate and extracellular matrix (ECM) composition. Our project will generate high-fidelity patient-specific 3D tumor models in which patient-derived stromal cells and cancer cells are scaffolded on ECM matched to the tumor of origin. This technological platform will provide a high-fidelity assay system in which we can stringently evaluate the influence of cancer associated fibroblasts on tumor aggressiveness, and it will also provide a platform for a precision-medicine approach to determining drug susceptibility for individual patients.

2. Keywords

Clear cell renal cell carcinoma, ccRCC, tumor stroma, tumor model, precision medicine.

3. Accomplishments

Specific Aim 1: Develop synthetic ccRCC tumors using prototype cell lines	Timeline	Site 1	Site 2	Site 3
Subtask 1.A Submit documents for HRPO approvals covering all proposed human specimen experiments in the proposal while project was based at Maine Medical Center (MMC)	Completed in Y1	Dr. Oxburgh		
Subtask 1.B Submit documents for HRPO approvals covering all proposed human specimen experiments in the proposal for grant transfer to The Rogosin Institute (RI)	Completed in Y2	Dr. Oxburgh		
Subtask 2.A Submit documents for ACURO approvals covering all proposed animal experiments in the proposal while project was based at Maine Medical Center (MMC)	Completed in Y1	Dr. Oxburgh		
Subtask 2.B Submit documents for ACURO approvals covering all proposed animal experiments in the proposal for grant transfer to The Rogosin Institute (RI)	Completed in Y2	Dr. Oxburgh		

Subtask 3 (Aim 1A): Retrieve 10 ccRCC tumors for use in the project from University of Pittsburgh Health Sciences Tissue Bank. HAS: 10 human ccRCCs with normal neighboring tissue from University of Pittsburgh Medical Center, de-identified	Completed in Y1	Dr. Oxburgh		Dr. Sims-Lucas
Subtask 4 (Aim 1A): Proteomic analysis of ECM from ccRCCs by SWATH mass spectrometry HAS: human ccRCC from Aim 1A, Subtask 3	Completed in Y1	Dr. Oxburgh	Dr. Coburn	
Subtask 5 (Aim 1A): Construction of ECM-containing scaffolds. Incorporation of patient-defined matrix blends into silk will be tested by mass spectrometry.	Completed in Y2		Dr. Coburn	
Subtask 6 (Aim 1A): Testing tumor cell growth on ECM-containing scaffolds in vitro by measuring proliferation and migration of 786-O and NRK 49F cells. Cell lines used: 786-O [ATCC] & NRK 49F [ATCC]	Completed in Y2	Dr. Oxburgh		
Subtask 7 (Aim 1A): Testing tumor cell growth on ECM-containing scaffolds in vivo by measuring proliferation and invasiveness of 786-O and NRK 49F cells engrafted in scaffolds under the kidney capsule of immunodeficient mice. Cell lines used: 786-O [ATCC] & NRK 49F [ATCC] Animals used: 30 NSG immunodeficient mice	Completed in Y3	Dr. Oxburgh		
Subtask 8 (Aim 1B): Measurement of elastic modulus of ccRCCs using molecular calipers. HAS: human ccRCC from Aim 1A, Subtask 3	Completed in Y1	Dr. Oxburgh	Dr. Coburn	Dr. Sims-Lucas
Subtask 9 (Aim 1B): Formulation of scaffolds mimicking tumor modulus by iterative variations in silk formulation followed by measurements of elastic modulus using molecular calipers.	Completed in Y1		Dr. Coburn	
Subtask 10 (Aim 1B): Testing effects of 786-O fibroblasts on modulus in vitro by evaluating if seeding of 786-O with or without NRK 49F cells into scaffolds alters their elastic modulus as measured using molecular calipers. Cell lines used: 786-O [ATCC] & NRK 49F [ATCC]	Completed in Y2	Dr. Oxburgh	Dr. Coburn	Dr. Sims-Lucas

Subtask 11 (Aim 1B); Testing modified scaffolds in vivo by comparing proliferation and invasiveness of 786-O cells seeded into modified scaffolds with 786-O seeded into unmodified scaffolds. Cell lines used: 786-O [ATCC] & NRK 49F [ATCC] Animals used: 10 NSG immunodeficient mice	Completed in Y3	Dr. Oxburgh		
Milestone Achieved: Obtains HRPO approval at MMC	Completed in Y1			
Milestone Achieved: Obtain ACURO approval at MMC	Completed in Y1			
Milestone Achieved: Generate a library of proteomic profiles of ccRCC ECM	Completed in Y1			
Milestone Achieved: Obtains HRPO approval for transfer to Rogosin Institute	Completed in Y2			
Milestone Achieved: Obtain ACURO approval for transfer to Rogosin Institute	Completed in Y2			
Milestone Achieved: Development of a rapid method to characterize patient-derived tumors and construct replica silk- based synthetic tumors	Completed in Y2			
Milestone Achieved: Submit 1 paper on development of patient-specific tumor models	Completed in Y2			
Specific Aim 2: Determine how ccRCC aggressiveness is influenced by stromal recruitment				
Subtask 1 (Aim 2A): Isolation and culture of cells from ccRCCs using established cell culture methods. Cell lines used: 786-O [ATCC] & NRK 49F [ATCC] HAS: human ccRCC from Aim 1A, Subtask 3	Completed in Y1	Dr. Oxburgh		Dr. Sims-Lucas
Subtask 2 (Aim 2A): Evaluate effects on proliferation and cell viability of recombining patient-derived tumor cells and fibroblasts in vitro by measuring proliferation and migration of tumor cells. Cell lines used: 786-O [ATCC] & NRK 49F [ATCC] HAS: human ccRCC from Aim 1A, Subtask 3	Completed in Y3	Dr. Oxburgh		Dr. Sims-Lucas

Subtask 3 (Aim 2A): Evaluate effects on tumor aggressiveness of recombining patient-derived tumor cells and fibroblasts engrafted under the kidney capsule of immunodeficient mice by measuring proliferation and invasiveness of tumor cells. Cell lines used: 786-O [ATCC] & NRK 49F [ATCC] HAS: human ccRCC from Aim 1A, Subtask 3 Animals used: 11 NSG immunodeficient mice	Incomplete	Dr. Oxburgh		
Subtask 4 (Aim 2A): Transcriptome analysis of patient-derived fibroblasts that modulate tumor cell behavior. Cells will be subjected to RNA-Seq and datasets will be compared using established bioinformatic techniques. HAS: human ccRCC from Aim 1A, Subtask 3	Incomplete	Dr. Oxburgh		
Subtask 5 (Aim 2B): Generate VHL mutant induced pluripotent stem cell line through genome editing of WTC-11 adult induced pluripotent stem cells. Cell line used: WTC-11 [Coriell]	Completed in Y1	Dr. Oxburgh		
Subtask 6 (Aim 2B): Cell biological verification of VHL mutant induced pluripotent stem cells by measuring their capacity to form kidney tissue following directed differentiation through molecular marker analysis. Cell line used: WTC-11 [Coriell]	Completed in Y3/4	Dr. Oxburgh		
Subtask 7 (Aim 2B): Evaluation of tumor progression in kidney tissue derived from VHL mutant induced pluripotent stem cells recombined with patient-derived fibroblasts in vivo by analysis of proliferation and invasiveness and molecular marker analysis. HAS: human ccRCC from Aim 1A, Subtask 3 Cell line used: WTC-11 [Coriell] Animals used: 18 NSG immunodeficient mice	Incomplete	Dr. Oxburgh		Dr. Sims-Lucas

Subtask 8 (Aim 2B): Evaluation of tumor progression in proximal tubule epithelial cells derived from VHL mutant induced pluripotent stem cells recombined with patient-derived fibroblasts in vivo by analysis of proliferation and invasiveness and molecular marker analysis. HAS: human ccRCC from Aim 1A, Subtask 3 Cell line used: WTC-11 [Coriell] Animals used: 18 NSG immunodeficient mice	Incomplete	Dr. Oxburgh		Dr. Sims-Lucas
Milestone Achieved: Development of a VHL-mutant induced pluripotent stem cell line	Completed in Y2			
Milestone Achieved: Understand if patient-derived fibroblasts modify tumor aggressiveness	Incomplete			
Milestone Achieved: Define candidate molecular determinants controlling tumor aggressiveness	Completed in Y3			
Milestone Achieved: Submit 1 paper on effects of fibroblasts on tumor aggressiveness	Completed in Y3			
Milestone Achieved: Understand if patient-derived fibroblasts can promote transformation of VHL-mutant kidney epithelial cells	Incomplete			
Milestone Achieved: Submit 1 paper on effects of fibroblasts on tumor initiation	Incomplete			

Work conducted in this study resulted in publication of 4 primary research papers and one review (appendices 1-5). A brief description of progress made in each publication follows:

1. Bond KH, Chiba T, Wynne KPH, Vary CPH, Sims-Lucas S, Coburn JM, Oxburgh L. The Extracellular Matrix Environment of Clear Cell Renal Cell Carcinoma Determines Cancer Associated Fibroblast Growth. Cancers (Basel). 2021 Nov 23;13(23):5873. PMCID: PMC8657052

Clear cell renal cell carcinoma (ccRCC) is the most common kidney cancer. Cell culture studies have the potential to explain how interactions between cancer cells and their support cells (stroma) determine growth and malignancy of ccRCC. The ability to grow tumor cells together with stroma from patient tumors is critical for studies of these interactions, but conventional culture methods do not provide representation of both cell types. We hypothesized that mimicking the extracellular environment of the tumor would promote growth of both tumor and stromal cells. We characterized the extracellular protein composition of patient ccRCCs and defined a nine-component protein blend to mimic the tumor microenvironment. Adherence of tumor cells, supporting stromal cells, and immune cells was demonstrated. Furthermore, we found that cells from patient tumors grown in our protein blend maintained representation of both tumor cells and cancer-associated fibroblasts (CAFs), a stromal cell type that plays a defining but poorly understood role in establishing the tumor microenvironment. This study demonstrates the dependence of CAFs on the extracellular protein composition and provides a technology to investigate interactions between tumor cells and CAFs isolated from patient ccRCCs.

2. Bond KH, Sims-Lucas S, Oxburgh L. Targets for Renal Carcinoma Growth Control Identified by Screening FOXD1 Cell Proliferation Pathways. Cancers (Basel). 2022 Aug 16;14(16):3958. PMCID: PMC9406217

FOXD1 regulates the proliferation of clear cell renal cell carcinoma (ccRCC) cells, and ccRCC cells in which FOXD1 has been inactivated do not form tumors efficiently in an animal model. Reproducing growth inhibition in tumor cells by inhibiting FOXD1 pathways presents a possible therapeutic approach for ccRCC and other cancers. We have established an analysis strategy to identify FOXD1-regulated target pathways that may be therapeutically tractable, and compounds that modulate these pathways were selected for testing. Targets in three pathways were identified: FOXM1, PME1, and TMEM167A, which were inhibited by compounds FDI-6, AMZ-30, and silibinin, respectively. The effects of these compounds on the growth of tumor cells from patients cultured in a novel 3D tumor-replica culture environment revealed that FDI-6 and silibinin had strong growth inhibitory effects. This investigation informs new therapeutic targets to control ccRCC tumor growth, and provides a strategy to compare the responsiveness of individual patient tumor replicas to growth-inhibitory compounds.

3. Bond KH, Fetting JL, Lary CW, Emery IF, Oxburgh L. FOXD1 regulates cell division in clear cell renal cell carcinoma. BMC Cancer. 2021 Mar 24;21(1):312. PMCID: PMC7988646
Forkhead transcription factors control cell growth in multiple cancer types. Foxd1 is essential for kidney development and mitochondrial metabolism, but its significance in renal cell carcinoma (ccRCC) has not been reported. FOXD1 expression level in ccRCC correlated inversely with patient survival. Knockout of FOXD1 in 786-O cells altered expression of FOXD1 targets, particularly genes involved in metabolism (MICU1) and cell cycle progression. Investigation of metabolic state revealed significant alterations in mitochondrial metabolism and glycolysis, but no net change in energy production. In vitro growth rate assays showed a significant reduction in growth of 786-OFOXD1null. In vivo, xenografted 786-OFOXD1null showed reduced capacity for tumor formation and reduced tumor size. Cell cycle analysis showed that 786-OFOXD1null had an extended G2/M phase. Investigation of mitosis revealed a deficiency in phosphorylation of histone H3 in 786-OFOXD1null, and increased DNA damage. Genes correlate with FOXD1 in the TCGA dataset associate with several aspects of mitosis, including histone H3 phosphorylation. We show that FOXD1 regulates the cell cycle in ccRCC cells by control of histone H3 phosphorylation, and that FOXD1 expression governs tumor formation and tumor growth. Transcriptome analysis supports this role for FOXD1 in ccRCC patient tumors and provides an explanation for the inverse correlation between tumor expression of FOXD1 and patient survival. Our findings reveal an important role for FOXD1 in maintaining chromatin stability and promoting cell cycle progression and provide a new tool with which to study the biology of FOXD1 in ccRCC.

4. Abbott A, Bond K, Chiba T, Sims-Lucas S, Oxburgh L, Coburn JM. Development of a mechanically matched silk scaffolded 3D clear cell renal cell carcinoma model. Mater Sci Eng C Mater Biol Appl. 2021 Jul;126:112141. PMID: 34082952
This study demonstrated the development of lyophilized silk scaffolds that mechanically match the experimentally determined Young's modulus for ex vivo ccRCC samples and normal kidney tissue. Scaffolds fabricated from silk solutions ranging from 3 to 12% (w/v) were evaluated through mechanical testing. Following mechanical characterization of ccRCC samples, it was demonstrated that 6% silk scaffolds mechanically matched ccRCC samples. No impact of pathological grade and stage on the calculated ccRCC modulus was observed and all tumors evaluated mechanically matched the 6% silk scaffold formulation. Stratifying tissue specimens based upon histological observations (e.g. evidence of high levels of collagen deposition) resulted in no significant differences between groups. To investigate the impact of a mechanically matched culturing environment on in vitro ccRCC disease characteristics a model ccRCC cell line, 786-O, was utilized. Scaffolded 786-O cells demonstrated increased lipid droplet accumulation, a hallmark of ccRCC, compared to standard two-dimensional (2D) culture conditions. Additionally, scaffolded 786-O cells demonstrated increased expression of genes associated with ccRCC aggressiveness (ex. VEGFA, TNF, and IL-6) or immune markers under investigation as therapeutic targets (ex. PDL1, CTLA4). Comparison with 786-O cells grown on non-mechanically matched scaffolds demonstrated that these improved ccRCC characteristics were driven by scaffold modulus. Overall, our findings support the use of silk scaffolds in replicating physiologic tumor behavior for clear cell renal cell carcinoma and provide a platform for investigating disease progression.

5. Oxburgh L. The Extracellular Matrix Environment of Clear Cell Renal Cell Carcinoma. Cancers (Basel). 2022 Aug 23;14(17):4072. PMCID: PMC9454539 (Review)
The extracellular matrix (ECM) controls fundamental properties of tumors, including growth, blood vessel investment, and invasion. The ECM defines rigidity of tumor tissue and individual ECM proteins have distinct biological effects on tumor cells. This article reviews the composition and biological functions of the ECM of

clear cell renal cell carcinoma (ccRCC). The most frequent initiating genetic mutation in ccRCC inactivates the *VHL* gene, which plays a direct role in organizing the ECM. This is predicted to result in local ECM modification, which promotes the growth of tumor cells and the invasion of blood vessels. Later in tumor growth, connective tissue cells are recruited, which are predicted to produce large amounts of ECM, affecting the growth and invasive behaviors of tumor cells. Strategies to therapeutically control the ECM are under active investigation and a better understanding of the ccRCC ECM will determine the applicability of ECM-modifying drugs to this type of cancer.

Training & professional development
Research conducted in this project was a component of the PhD thesis work that Alycia Abbott performed to fulfill the research requirements for graduation in 2021.
Research conducted in this project was a component of the PhD thesis work that Kyle Bond performed to fulfill the research requirements for graduation in 2022.

Dissemination to communities of interest
Results were published promptly in scientific journals.

4. Impact

Impact on the development of the principal discipline(s) of the project

- Development of a personalized tumor modeling platform for ccRCC
- Demonstration of utility of personalized tumor models for target discovery in ccRCC
- Identification of specific G2-M cell cycle regulators as potential targets to slow tumor growth
- Characterization of the extracellular matrix profile of ccRCC
- Development of a 3D culture method that can propagate ccRCC-derived fibroblasts
- Characterization of the modulus of ccRCC tissue versus healthy kidney cortex and modifying silk scaffolding material to match tumor modulus

Impact on other disciplines

- FOXD1 is misregulated in many tumors and our studies provide a mechanism of action that is applicable to lung cancer, breast cancer and other cancer types
- Determining the healthy kidney cortex extracellular matrix composition has had an impact on work to model the 3D structure of the kidney cortex in nephrology research
- The approach to developing Matrigel-free 3D models of patient tumors has had impact on efforts to generate patient-specific models of other cancers

Impact on technology transfer
Nothing to report
Impact on society beyond science and technology
Nothing to report

5. Changes/Problems

Disruptions due to the COVID pandemic were particularly severe in the New York City Healthcare system where the Rogosin Institute is located. Although we managed to keep the lab open and running, many facets of operations were shut down. Importantly for these studies, animal facilities were operating with skeleton personnel, and routines are still impacted because so many staff members left during the pandemic years. For this reason, it has been challenging to complete the animal studies proposed in this project. Because the project has been successful and has generated new insights into the regulation of tumor aggressiveness by the local microenvironment, we are still pursuing these questions. A second disruption caused by the pandemic that impacted our work was the lack of availability of reagents for stem cell culture. Although we were able to generate the pluripotent stem cells that we proposed in our application, we were not able to follow through with the coculture studies that were proposed. Again, the project was very successful and we established a novel system for ex vivo tumor growth, so using the stem cell-based system to understand the influence of the local environment on initiating events in renal cell carcinoma remains a priority and we are pursuing these questions. The pandemic disruptions did not change the scope of our study, or our expenditures which increased quite dramatically because of supply shortages. In response, we focused on aspects of the proposed work that were tractable during the pandemic, resulting in the publication of 4 primary research papers and one review (Appendices 1-5).

6. Products

Publications

1. Bond KH, Chiba T, Wynne KPH, Vary CPH, Sims-Lucas S, Coburn JM, Oxburgh L. The Extracellular Matrix Environment of Clear Cell Renal Cell Carcinoma Determines Cancer Associated Fibroblast Growth. Cancers (Basel). 2021 Nov 23;13(23):5873. PMCID: PMC8657052

2. Bond KH, Sims-Lucas S, Oxburgh L. Targets for Renal Carcinoma Growth Control Identified by Screening FOXD1 Cell Proliferation Pathways. Cancers (Basel). 2022 Aug 16;14(16):3958. PMCID: PMC9406217

3. Bond KH, Fetting JL, Lary CW, Emery IF, Oxburgh L. FOXD1 regulates cell division in clear cell renal cell carcinoma. BMC Cancer. 2021 Mar 24;21(1):312. PMCID: PMC7988646

4. Abbott A, Bond K, Chiba T, Sims-Lucas S, Oxburgh L, Coburn JM. Development of a mechanically matched silk scaffolded 3D clear cell renal cell carcinoma model. Mater Sci Eng C Mater Biol Appl. 2021 Jul;126:112141. PMID: 34082952

5. Oxburgh L. The Extracellular Matrix Environment of Clear Cell Renal Cell Carcinoma. Cancers (Basel). 2022 Aug 23;14(17):4072. PMCID: PMC9454539

Websites

https://encyclopedia.pub/entry/26839

Technologies or techniques

- Development of a personalized tumor modeling platform for ccRCC
- Development of a 3D culture method that can propagate ccRCC-derived primary fibroblasts

Inventions, patents

Nothing to report

Other products

Transcriptome analyses were deposited to NCBI GEO for public access: Data Series GSE210145.

The mass spectrometry proteomics data have been deposited for public access to the ProteomeXchange Consortium via the PRIDE partner repository with the dataset identifier PXD030160.

7. Participants & Other Collaborating Organizations

Estimates of annual time spent working on the project rounded to the nearest month is shown in the table below.

Name:	Leif Oxburgh
Project Role:	PI
Research Identifier:	0000-0002-2825-7663
Nearest person month worked:	1
Contribution to Project:	Coordination of the research project, preparation of documents for HRPO and ACURO approval, experiment planning and analysis, reporting.
Funding Support:	N/A
Name:	Kyle Bond
Project Role:	Doctoral Student
Research Identifier:	N/A
Nearest person month worked:	12
Contribution to Project:	Processing patient tumor material, isolation and propagation of primary cells, preparation of samples for mass spectrometry, experiment planning and analysis, preparation of figures.
Funding Support:	N/A
Name:	Jeannine Coburn
Project Role:	Co-Investigator
Research Identifier:	0000-0001-6354-5436
Nearest person month worked:	1
Contribution to Project:	The WPI research team fabricated silk scaffolds for in vitro renal cell culturing and performed mechanical testing on silk scaffolds and renal cell carcinoma biospecimens.
Funding Support:	N/A
Name:	Alycia Abbott
Project Role:	Doctoral Student
Research Identifier:	N/A
Nearest person month worked:	3
Contribution to Project:	Fabrication of silk scaffolds, mechanical testing of materials and biospecimens, 3D cell culture.
Funding Support:	N/A
Name:	Sunder Sims-Lucas
Project Role:	Sub-award Investigator
Research Identifier:	0000-0003-1908-4809
Nearest person month worked:	1
Contribution to Project:	We provide kidney tissue samples and histological support for the project
Funding Support:	N/A
Name:	Takuto Chiba
Project Role:	Postdoctoral Fellow
Research Identifier:	N/A
Nearest person month worked:	1
Contribution to Project:	We provide kidney tissue samples and histological support for the project
Funding Support:	N/A

8. Special Reporting Requirements

Not applicable.

9. Appendices

1. Bond KH, Chiba T, Wynne KPH, Vary CPH, Sims-Lucas S, Coburn JM, Oxburgh L. The Extracellular Matrix Environment of Clear Cell Renal Cell Carcinoma Determines Cancer Associated Fibroblast Growth. Cancers (Basel). 2021 Nov 23;13(23):5873. PMCID: PMC8657052

2. Bond KH, Sims-Lucas S, Oxburgh L. Targets for Renal Carcinoma Growth Control Identified by Screening FOXD1 Cell Proliferation Pathways. Cancers (Basel). 2022 Aug 16;14(16):3958. PMCID: PMC9406217

3. Bond KH, Fetting JL, Lary CW, Emery IF, Oxburgh L. FOXD1 regulates cell division in clear cell renal cell carcinoma. BMC Cancer. 2021 Mar 24;21(1):312. PMCID: PMC7988646

4. Abbott A, Bond K, Chiba T, Sims-Lucas S, Oxburgh L, Coburn JM. Development of a mechanically matched silk scaffolded 3D clear cell renal cell carcinoma model. Mater Sci Eng C Mater Biol Appl. 2021 Jul;126:112141. PMID: 34082952

5. Oxburgh L. The Extracellular Matrix Environment of Clear Cell Renal Cell Carcinoma. Cancers (Basel). 2022 Aug 23;14(17):4072. PMCID: PMC9454539

cancers

MDPI

Article

The Extracellular Matrix Environment of Clear Cell Renal Cell Carcinoma Determines Cancer Associated Fibroblast Growth

Kyle H. Bond [1,2], Takuto Chiba [3], Kieran P. H. Wynne [4,5], Calvin P. H. Vary [4], Sunder Sims-Lucas [3], Jeannine M. Coburn [6] and Leif Oxburgh [1,*]

1 Rogosin Institute, 310 East 67th St., Room 2-43, New York, NY 10065, USA; kyb9010@nyp.org
2 Graduate School of Biomedical Science and Engineering, University of Maine, 5775 Stodder Hall, Room 44S, Orono, ME 04469, USA
3 Children's Hospital of Pittsburgh, 4401 Penn Ave., Rangos Research Building, Pittsburgh, PA 15224, USA; chibat@pitt.edu (T.C.); Sunder.Sims-Lucas@chp.edu (S.S.-L.)
4 Maine Medical Center Research Institute, 81 Research Drive, Scarborough, ME 04074, USA; kieran.wynne1@ucd.ie (K.P.H.W.); VaryC@mmc.org (C.P.H.V.)
5 Systems Biology Ireland, University College Dublin, Belfield, Dublin 4, Ireland
6 BME Department, Worcester Polytechnic Institute, 60 Prescott St., Worcester, MA 01605, USA; jmcoburn@wpi.edu
* Correspondence: leo9022@nyp.org

Simple Summary: Clear cell renal cell carcinoma (ccRCC) is the most common kidney cancer. Cell culture studies have the potential to explain how interactions between cancer cells and their support cells (stroma) determine growth and malignancy of ccRCC. The ability to grow tumor cells together with stroma from patient tumors is critical for studies of these interactions, but conventional culture methods do not provide representation of both cell types. We hypothesized that mimicking the extracellular environment of the tumor would promote growth of both tumor and stromal cells. We characterized the extracellular protein composition of patient ccRCCs and defined a nine-component protein blend to mimic the tumor microenvironment. Adherence of tumor cells, supporting stromal cells, and immune cells was demonstrated. Furthermore, we found that cells from patient tumors grown in our protein blend maintained representation of both tumor cells and cancer-associated fibroblasts (CAFs), a stromal cell type that plays a defining but poorly understood role in establishing the tumor microenvironment. This study demonstrates the dependence of CAFs on the extracellular protein composition and provides a technology to investigate interactions between tumor cells and CAFs isolated from patient ccRCCs.

Abstract: Clear cell renal cell carcinoma (ccRCC) is the most common kidney cancer and is often caused by mutations in the oxygen-sensing machinery of kidney epithelial cells. Due to its pseudo-hypoxic state, ccRCC recruits extensive vasculature and other stromal components. Conventional cell culture methods provide poor representation of stromal cell types in primary cultures of ccRCC, and we hypothesized that mimicking the extracellular environment of the tumor would promote growth of both tumor and stromal cells. We employed proteomics to identify the components of ccRCC extracellular matrix (ECM) and found that in contrast to healthy kidney cortex, laminin, collagen IV, and entactin/nidogen are minor contributors. Instead, the ccRCC ECM is composed largely of collagen VI, fibronectin, and tenascin C. Analysis of single cell expression data indicates that cancer-associated fibroblasts are a major source of tumor ECM production. Tumor cells as well as stromal cells bind efficiently to a nine-component ECM blend characteristic of ccRCC. Primary patient-derived tumor cells bind the nine-component blend efficiently, allowing to us to establish mixed primary cultures of tumor cells and stromal cells. These miniature patient-specific replicas are conducive to microscopy and can be used to analyze interactions between cells in a model tumor microenvironment.

check for updates

Citation: Bond, K.H.; Chiba, T.; Wynne, K.P.H.; Vary, C.P.H.; Sims-Lucas, S.; Coburn, J.M.; Oxburgh, L. The Extracellular Matrix Environment of Clear Cell Renal Cell Carcinoma Determines Cancer Associated Fibroblast Growth. *Cancers* **2021**, *13*, 5873. https://doi.org/10.3390/cancers13235873

Academic Editors: Paul J. Higgins and Ralf-Peter Czekay

Received: 3 October 2021
Accepted: 19 November 2021
Published: 23 November 2021

Publisher's Note: MDPI stays neutral with regard to jurisdictional claims in published maps and institutional affiliations.

Copyright: © 2021 by the authors. Licensee MDPI, Basel, Switzerland. This article is an open access article distributed under the terms and conditions of the Creative Commons Attribution (CC BY) license (https://creativecommons.org/licenses/by/4.0/).

Keywords: collagen VI; collagen XII; periostin; fibronectin; tenascin C; HSPG2; TGFBI; lumican; laminin

1. Introduction

Renal cell carcinoma (RCC) is among the ten most common cancers [1], and the most common histological subtype is clear cell renal cell carcinoma (ccRCC) [2]. Loss of the tumor suppressor *VHL* through genetic or epigenetic mechanisms is seen in over 90% of ccRCCs [3]. VHL is an essential component of the cellular oxygen sensor [4], and its loss induces a persistent pseudo-hypoxic state that results in a strong angiogenic profile of tumors [5]. Epithelial cells within the kidney cortex are thought to be the cells of origin for ccRCC, most likely proximal tubule epithelial cells [6]. Within the tumor, transformed epithelial cells are interspersed with a network of blood vessels, and the ccRCC stroma also contains interstitial fibroblasts and inflammatory and immune cells [7]. Cellular components of the tumor are embedded in the extracellular matrix (ECM).

The ECM environment controls many fundamental properties of tumors, including their proliferation [8,9], vascularization [10,11], and invasion [12], and is therefore a key determinant of their malignancy. The interplay between ECM and tumor cells is complex and multifactorial. In addition to providing the substrate for cancer cell attachment, ECM determines rigidity, which profoundly influences tumor malignancy [13]. Additionally, it directly controls signal transduction in cancer cells, which governs their behaviors [14]. The ECM is a complex mix of components [15], each with distinct physicochemical and signaling properties. Thus, the particular ECM composition characteristic of a tumor type is predicted to play an important role in determining the tumor's behavior. Distinct tumors are predicted to differ in their ECM profiles, and this is likely a characteristic of the organ from which they arise as well as the tumor's cellular composition, with cancer-associated fibroblasts (CAFs) acting as a major source of new tumor ECM [16]. CAFs are major contributors to the tumor ECM, but difficulties in isolating and maintaining these cells has limited their study. One important factor to the difficulties in culturing CAFs may be their dependence on the complex ECM environment that they generate [17]. Very little has been reported on CAFs in ccRCC, a tumor type with an extensive angiogenic and immunomodulatory stromal component. CAFs are lost over the course of a few weeks in cultures of dissociated ccRCC tumors encapsulated in collagen I [18], and mimicking the ECM from which these cells are isolated may be key to their longer-term maintenance.

Cell culture provides an essential tool for the study of human tumor biology, and cultured cells can be used as avatars of individual patient tumors for drug-response prediction [19]. Considering the strong influence of ECM on tumor cell biology, it is important that cultures replicate this component of tumors in addition to the cellular components. The matrix produced by the Engelbreth–Holm–Swarm (EHS) mouse sarcoma [20] known as Matrigel, Geltrex, or EHS matrix extract, is widely used to replicate the ECM environment for cultured tumor cells. The matrix isolated from this tumor is composed of three major components: laminin, collagen IV, and entactin/nidogen. It is used as the substrate to form organoids from both healthy and transformed intestinal tissue [21] and has been widely applied to the study of transformed tissues from other organs [22]. However, the composition of EHS matrix is similar to the ECM composition of healthy kidney cortex, leading us to question its utility in modeling ccRCC in vitro. We employed mass spectrometry to identify the major components of ccRCC ECM and found that in contrast to healthy kidney cortex, laminin, collagen IV, and entactin/nidogen are minor contributors. Instead, the tumor ECM is composed largely of collagen VI, fibronectin, and tenascin C. Analysis of single cell expression data indicates that CAFs may be a major source of tumor ECM production. Tumor cells as well as stromal cells bind efficiently to a nine-component ECM blend characteristic of ccRCC, whereas little binding is seen to Matrigel. Primary patient-derived tumor cells bind the nine-component blend efficiently, allowing us to estab-

lish mixed primary cultures with representation of tumor cells and stromal cells. These miniature patient-specific replicas are conducive to microscopy and can be used to analyze interactions between cells in a model tumor microenvironment.

2. Materials and Methods

2.1. Sample Collection

Kidney tumor tissue was obtained from surgical nephrectomies performed at the University of Pittsburgh Medical Center. Cancer diagnosis was performed by certified pathologists. Tissue adjacent to the surgical biopsy was collected at the discretion of the surgeon. All tissue was maintained in PBS at 4 °C and tested within 24 h of collection. All tissue specimens received were de-identified using an honest broker system. Demographical and pathological information provided for the nephrectomy specimens and whole kidneys may be found in Table 1.

Table 1. Tissue samples used in this study. Stage and grade determined by pathologist using the TNM and Fuhrman systems, respectively. p = primary T = Tumor N = lymph nodes (x = not determine, 0 = none detected, 1 = spread) M = metastasis (x = not determined, 0 = none detected, 1 = spread).

ID	Diagnosis	Stage	Grade	Sex	Race	Age	Applications
Tp17-S560	ccRCC	pT3 Nx Mx	3	M	White	72	Mass Spec
Tp18-S435	ccRCC	pT3a NX	4	M	White	50–59	Mass Spec
R19-6098	ccRCC	pT3 pN0	2	N/A	White	29	Mass Spec
Tp19-S80	ccRCC	pT3a N0 Mx	4	M	White	69	Mass Spec
Tp19-S79	ccRCC	pT3a Nx	4	F	White	68	Mass Spec
Tp18-S109	ccRCC	pT3a	2	M	White	60–69	Mas Spec, Primary Culture
Tp18-S114	ccRCC	pT3a	3	M	White	80–89	Mass Spec, Primary Culture
Tp18-S108	ccRCC	pT1a Nx Mx	2	F	White	60–69	Primary Culture
R18-6256	ccRCC	pT1a pNC	1	N/A	N/A	61	Flow Cytometry
R19-6200	ccRCC	pT1b Nx	2	M	White	61	Flow Cytometry
Tp18-S601	ccRCC	pT1b Nx	2	M	White	61	Flow Cytometry
R18-1453	ccRCC	pT2a pNx	3	F	White	83	Flow Cytometry
Tp21-S145	ccRCC	pT3a Nx Mx	2	F	White	76	3D Culture
Tp20-S199	ccRCC	pT3a Nx	2	M	N/A	74	3D Culture
Tp21-S27	ccRCC (Syndromic VHL)	pT1a Nx Mx	4	M	White	68	3D Culture
Tp20-S215	ccRCC	pT4 Nx M1	4	M	White	52	3D Culture
Tp20-S238	ccRCC	PT3 + Nx M1	4	M	White	71	3D Culture

2.2. Sample Processing

Samples were processed following the protocol from Pauli et al. [23]. Fresh tumor and adjacent normal tissue samples were diced and weighed. One hundred milligrams of tissue was flash frozen for Mass Spectrometry analysis, while remaining tissue was digested in 20× volume DMEM containing 250 U/mL Collagenase IV (ThermoFisher, Waltham, MA, USA) + 0.02% Trypsin-EDTA at 37 °C in a shaking incubator set to 200 RPM for up to 2 h or until media became cloudy. Digestion was stopped by adding an equal volume of ice-cold DMEM containing 10% FBS. Any undigested material was filtered with 100 µM filter and placed in a vessel containing 5× volume TrypLE Express (ThermoFisher) and returned to the 37 °C shaking incubator set to 220 RPM for an additional 15 min. Samples were pooled if necessary and centrifuged at 500× *g* for 7 min 30 s at 4 °C. Cells were washed

with ice-cold DMEM and counted, and their viability was determined using Trypan Blue exclusion and utilized for downstream assays or frozen in Nutrifreeze (Sartorius, Göttingen, Germany) freezing media.

2.3. Proteomic Analysis

Peptide quantitative SWATH mass spectrometry was conducted as described elsewhere [24,25]. Proteins were prepared to provide approximately 100 µg total protein lysates. Proteins were reduced (DTT, 60 min at 30 °C) and then thiols were capped (iodoacetamide, 30 min at 30 °C) in 8 M urea. Urea was diluted to 1 M with Tris-HCl 8.0, and 1 µg sequencing grade trypsin was added per 30–40 µg protein and incubated overnight at 37 °C. Peptides were isolated on preparative C18 reverse-phase spin columns. LC for mass spec: 30 cm × 75 µm (inner diameter) high resolution C18 reverse phase chromatography. For proteomics informatics, an isotope-free unbiased scanning workflow, SWATH (Sequential Windowed Acquisition of All Theoretical Mass Spectra) [26,27] was used to allow isotope-free quantitation of proteins via LC/MS-based measurement of the levels of constituent tryptic peptides. A Triple-TOF 5600 (Sciex, Framingham, MA, USA) was programmed to acquire MS/MS data from as many as 100 variable retention time-widths, as determined by the LC trace of the proteome being analyzed. From these data, lists of proteins and their relative levels, with appropriate statistics (e.g., p-values < 0.05, false discovery rate, FDR < 1%) were provided using a software workflow that is comprised of Sciex proprietary programs; ProteinPilot (data-dependent peptide ion libraries), PeakView (SWATH app to link SWATH data and ion library data, quantify peaks, provide FDR and quality control analytics), and MarkerView (principle component visualization [28] and statistical analysis of group comparisons). Additional detail may be found in Supplemental Methods. SWATH and ion library raw data will be located at the PeptideAtlas repository and accessible via the web. PeptideAtlas is a part of the ProteomeXchange Consortium.

2.4. Pathway Analysis

Processed SWATH data were functionally annotated using DAVID, Gene Set Enrichment Analysis (GSEA), and Gene Ontology Analysis (GO) using only proteins showing significant differential expression (p-value < 0.05). Exported data can be found in Tables S2–S4. Additional detail may be found in Supplemental Methods.

2.5. Kidney Tumor ECM Analysis

Processed Mass Spectrometry data were further annotated and sorted using definitions from matrisomeDB [29,30] and can be found in Table S1. Samples were grouped and analyzed based on origin, either tumor or adjacent normal kidney. ECM components containing the gene ontology term GO:0050817 (coagulation) were labeled and excluded from this analysis. SWATH and DIA datasets were combined and annotated for differential expression (p-value < 0.05) and relative total protein abundance (%LFQ). Highly abundant core matricellular proteins (>0.1% LFQ), were renormalized to total percent core matrisome and statistically characterized. The most abundant targets (% ≧ Quartile 3) were used in the construction of "ccRCC ECM" blend.

2.6. Flow Cytometry

Digested tumor or adjacent normal cells were centrifuged and resuspended at 5×10^5–2×10^6 cells/100 µL FACs buffer (Miltenyi, Bergisch Gladbach, Germany). Cells were divided into no antibody control, viability analysis panel (Propidium iodide, Hoeschst33342, DRAQ7), IgG control (REA-VioBlue, REA-FITC, REA-PE, REA-APC, REA-PE-Vio770), staining panel 1 (1:50 CD31-VioBlue (Miltenyi 130-117-227), 1:11 CA9-PE (Miltenyi 130-110-057), 1:10 PDGFRβ-APC (Miltenyi 130-105-322), 1:10 PDGFRα-APC (Miltenyi 130-115-239), 1:50 CD326-PE-Vio770 (Miltenyi 130-111-002), 1:50 CD45-FITC (Miltenyi 130-110-631), Propidium Iodide), or staining panel 2 (1:50 CD10-VioBlue (Miltenyi 130-114-509), 1:11 CA9-PE, 1:50 CD105-PE-Vio770 (Miltenyi 130-112-167), CD184-APC (Miltenyi 130-098-357), 1:50

CD326-PE-Vio770, Propidium Iodide), and incubated in the dark at 4 °C for 15 min. Cells were washed two times with flow buffer and analyzed using Miltenyi AutoMACs flow cytometer. Side and forward scatter gating were determined using viability analysis panel to identify cells vs. debris. Doublets were excluded using SSR-H versus SSR-L. Positive gating for each marker was determined using IgG control. Compensation was performed using the MACS Comp Bead kit, anti-REA (Miltenyi 130-104-693).

2.7. Primary Cell Culture

Adapted from Williams et.al [31]. Digested tumor cells were washed and resuspended in 1×10^6 cells/5 mL High Glucose DMEM containing 10% FBS, 1% GlutaMax (ThermoFisher), 1% Penicillin-Streptomycin, 1% Non-Essential Amino Acids (ThermoFisher), and 1% Sodium Pyruvate and plated onto 5 cm tissue culture treated plates. Plates were incubated at 37 °C for 24 h before media change and imaging. Cells were monitored with media change every 72 h. After reaching 70–80% confluency, cells were expanded into a 10 cm tissue culture treated dish. Upon reaching 70–80% confluency, passaged cells were either frozen in FBS/DMSO freeze media or further expanded for downstream applications.

2.8. Cell Line Culture

All cells were obtained from ATCC, Manassas, VA, USA. 786-O (ATCC CRL-1932), NRK-49F (ATCC CRL-1570), MS1 (ATCC CRL-2279), and RAW264.7 (ATCC TIB-71) cells were maintained or adapted to RPMI-1640 containing 10% FBS, 1% GlutaMax (ThermoFisher), and 1% Penicillin-Streptomycin and grown to 70–80% confluency on tissue culture treated plates before experiments. Cells were detached from plates using TrypLE Express (ThermoFisher) with the exception of RAW264.7 cells, which required use of a cell lifter.

2.9. Immunocytochemistry Validation of Primary Cell Lines

Upon freeze or expansion of primary cell cultures, 5000 cells in 500 µL of culture media were transferred into a Cytofunnel and centrifuged for 5 min at 1000 RPM in a Shandon CytoSpin centrifuge (ThermoFisher cat#A78300003). Slides were dried and frozen at −70 °C. Slides were brought to room temperature submerged in 4% PFA for 15 min. Slides were washed before permeabilization with 0.02% TritonX-100 in PBS for 10 min. Blocking was done using 5% Donkey Serum in PBST for 1 h at room temperature. Primary antibody staining was done at 4 °C overnight with the following antibodies and dilutions: Vimentin 1:400 (MilliporeSigma, Burlington, MA, USA V6630), Cytokeratin 18 (R&D, Minneapolis, MN, USA AF7619), and PDGFRα/β 1:100 (abcam, Cambridge, UK ab32570). Secondary staining was done alongside DAPI using the following antibodies: Donkey anti-Mouse AlexaFluor 647 (ThermoFisher A31571), Donkey anti-Rabbit AlexaFluor 568 (ThermoFisher A10042), and Donkey anti-Sheep AlexaFluor 488 (ThermoFisher A11015). Slides were mounted in Vectashield (Vector, Burlingame, CA, USA) and imaged on a Leica DMI 6000B. Tumor cells were identified as $VIM^+CK18^+PDGFR\alpha/\beta^-$, while fibroblasts were defined as $VIM^+CK18^-PDGFR\alpha/\beta^+$. Analysis was repeated for three primary tumor lines at passages 1, 2, and 4.

2.10. Cell Line Attachment Assays

One day in advance, sterile non-tissue culture treated 96-well plates were coated with ECM substrates at a concentration of 2 µg/mL in sodium carbonate/bicarbonate binding buffer for 2 h at 37 °C. Matrigel coating was created by dilution to 8 µg/mL in cell culture media. Plates were then transferred to 4 °C to incubate overnight. Uncoated wells were incubated with just binding buffer. ECM coating solution was aspirated before preparing cells and left to air dry in the back of the tissue culture hood. The following proteins were used for this and all other experiments: Collagen VI (Corning, Corning, NY, USA 8064002), HSPG2 (R&D 2364-ER), Laminin (MilliporeSigma L6264), Tenascin-C (R&D 3358-TC-050)

Fibronectin (MilliporeSigma FC010), Fibrillin-1 (R&D 10224-F1-050), Lumican (R&D 2846-LV), Collagen 12 (Novus, Uppsala, Sweden NBP1-88062PEP), Periostin (R&D 3548-F2-050), and TGFBI (R&D, 3409-BG-050). Single cell suspensions were diluted to 20 cells/µL in assay media (RPMI-1640 without FBS), and 100 µL were added to each well of coated or uncoated 96-well plates. Plates were incubated at 37 °C in a cell culture incubator. After 2 h, wells were aspirated and briefly rinsed with DPBS. Wells were imaged using EVOS microscope (ThermoFisher). Cell attachment was determined by morphological characteristics such as cell spreading, elongation, and presence of projections.

2.11. Primary Cell ECM Attachment and Growth

Eight-well Permanox chamber slides (Nunc, Rochester, NY, USA) were coated with ccRCC ECM blend or DPBS only and incubated for 2 h at 37 °C. Plates were then transferred to 4 °C to incubate overnight. Prior to cell seeding, chambers were aspirated and dried in back of tissue culture hood. Primary cell digests were diluted in DMEM without FBS and cultured up to 4 h at 37 °C. Chambers were then either rinsed and fixed in 4% PFA for 15 min or replaced with DMEM + 10% FBS culture media for an additional culture period of 72 h before fixation. Fixed chambers were rinsed with PBS before permeabilization with 0.02% TritonX-100 in PBS for 10 min. Blocking was done using 5% Donkey Serum in PBST for 1 h at room temperature. Primary antibody staining was performed overnight at 4 °C against the following targets; PDGFRα/β 1:100 (abcam ab32570), CD45 1:100 (Novus NBP2-80652), CD34 (BioRad, Hercules, CA, USA, MCA547G), PAX2/8 1:200 (ThermoFisher 71-6000, ProteinTech, Rosemont, IL, USA 10336-1-AP), Vimentin 1:1000 (MilliporeSigma AB5733), CK18 (R&D AF7619), and CXCR4 1:100 (abcam ab124824). After washing, secondary antibody staining alongside DAPI was performed for 1 h at room temperature with the following antibodies: Donkey anti-Rabbit AlexaFluor 568 (ThermoFisher A10042), Donkey anti-Chicken AlexaFluor 488 (abcam ab150169), Donkey anti-Mouse AlexaFluor 647 (ThermoFisher A-31571), Donkey anti-Rat AlexaFluor 647 (ThermoFisher A-21247), and Donkey anti-Sheep AlexaFluor 488 (ThermoFisher A11015). Mounting in EverBrite (Biotium, Fremont, CA, USA cat#23018). Imaging was performed using Leica Thunder Imager. Images were deconvolved using the Leica Thunder small volume processing algorithm and analyzed using LASX software. Fibroblasts were defined as PDGFRα/β^{+}CD45^{-}Vim^{+} and negative for all carcinoma markers. Endothelial cells were defined as CD34^{+}CD45^{-} and negative for all carcinoma markers. Immune cells were defined as CD45^{+}CXCR4$^{+/-}$ and negative for remaining carcinoma markers. Tumor cells were defined as PDGFRα/β^{-}CD45^{-}CD34^{-} and positive for any two of the following carcinoma markers: CK18, VIM, PAX2/8, and CXCR4. All other cells were categorized as "Other". Distribution of cell types was clustered using ClustVis webtool (https://biit.cs.ut.ee/clustvis/ (accessed on 6 January 2021)) using Pareto row scaling. For EdU incorporation analysis, EdU was added to culture media at final concentration of 5 µM and added to wells of 4 h after attachment. Cells were cultured for up to three weeks, at which chambers were fixed in 4% PFA and immunostained as previously summarized. EdU was detected using the Click-iT EdU Cell Proliferation Kit (ThermoFisher) standard protocol. Imaging was conducted as stated above.

2.12. D Cultures

Fibrin domes were created following modifications to protocol by Liu et al. [32]. In summary, fibrin domes were generated by combining fibrinogen (MilliporeSigma cat#F8630) at a 1:1 ratio with cells suspended in culture media with or without addition of ECM proteins. Cell concentration was cell-line-dependent following testing; 786-O = 50 cells/µL, S108 = 150 cells/µL, S109 = 150 cells/µL, S114 = 100 cells/µL, Primary Tissue Digests = 200 cells/µL. Thrombin (MilliporeSigma cat#10602370001) at a concentration of 0.01 U/µL was added at a volume equal to 10% of total to cell–fibrinogen mix, then immediately spotted onto glass coverslips at 5 µL per replicate. Domes were immediately placed into a 37 °C cell culture incubator for 10 min to facilitate gelation. Pre-warmed

cell culture media (786-O: RPMI-1640 containing 10% FBS, 1% GlutaMax (ThermoFisher), and 1% Penicillin-Streptomycin; primary cultures and tissue digests: DMEM containing 10% FBS, 1% GlutaMax, 1% NEAA (ThermoFisher), and 1% Penicillin-Streptomycin, or CHM obtained from Weill Cornell Englander Institute for Precision Medicine [23]) were carefully added to wells and allowed to culture in cell culture incubator. Media were changed every 2–3 days. Matrigel domes were created following modification of protocol by Sato et al. [21]. In summary, Matrigel domes were generated by combining Matrigel GFR (Corning cat#354230) at a 1:1 ratio with cell suspended in culture media at before mentioned concentrations, then immediately spotted onto glass coverslips at 5 µL per replicate. Domes were immediately placed into a 37 °C cell culture incubator for 30 min to facilitate gelation. Pre-warmed cell culture media were carefully added to wells and allowed to culture in cell culture incubator. Media were changed every 2–3 days.

2.13. Live/Dead and Structure Analysis

At designated end-points (786-O = 6 days, Primary ccRCC Tumor Lines = 30 days, Primary Tumor Digests = 19 days), media were replaced with Live/Dead staining solution containing 2 µM Calcein-AM and 4 µM Ethidium homodimer-2 (Ethd2) in culture media (ThermoFisher cat#L3224) and incubated for 30 min in culture incubator. In the last remaining 8 min, Hoechst 33,342 (ThermoFisher cat# H3570) at a final concentration of 5 µg/mL was added to each sample. Three-dimensional domes were washed 3 × with DPBS and mounted for fluorescent imaging in phenol-free media. Collected images were deconvolved using Leica LasX Thunder deconvolution algorithm. Deconvolved images were analyzed for Hoechst 33,342 positivity to identify number of cellular structures. Each structure was designated as either live ($Calcein^+$) or dead ($Ethd2^+$). Comparisons between culture conditions were done via Students' *t*-test.

2.14. D Dome Immunostaining

3D cultures were fixed in 4% PFA for 15 min at room temperature and washed 3x with PBS. Cell permeabilization was performed using 0.2% TritonX-100 in PBS for 15 min. Blocking was performed using 5% Donkey Serum (Jackson Immunoresearch, West Grove, PA, USA, cat# 017-000-121) in PBST for 1 h. Primary antibody incubation against listed targets was done by incubating overnight at 4 °C at associated dilutions in PBST: PDGFRα/β 1:100 (abcam ab32570), CD31 1:200 (ThermoFisher MA3100), Vimentin 1:1000 (MilliporeSigma AB5733), Renin 1:100 (abcam ab212197), CD45 1:100 (Novus NBP2-80652), ACTA2 1:50 (MilliporeSigma A5228), and CXCR4 1:100 (abcam ab124824). Rigorous washing was performed the next day for 6 h before secondary incubation with DAPI and following antibodies at 1:250 dilution in PBST at 4 °C overnight: Donkey anti-Rabbit AlexaFluor 568 (ThermoFisher A10042), Donkey anti-Chicken AlexaFluor 488 (abcam ab150169), Donkey anti-Mouse AlexaFluor 647 (ThermoFisher A-31571), and Donkey anti-Rat AlexaFluor 647 (ThermoFisher A-21247). Rigorous washing was performed the next day for 6 h, followed by an additional overnight wash at 4 °C overnight. Sample clearing was performed in series moving from 25%, 50%, and 80% glycerol every 30 min before mounting in EverBrite (Biotium cat#23018). Imaging was performed using Leica Thunder Imager. Selected images for publication were deconvolved using Leica LasX Thunder deconvolution algorithm.

2.15. EdU Incorporation and Detection

EdU was added to culture media at final concentration of 5 µM and maintained for 48 h. Domes were then fixed and immunostained following above procedure above. EdU was detected using the Click-iT EdU Cell Proliferation Kit (ThermoFisher) standard protocol. Imaging was conducted as stated above.

2.16. scRNA-seq Analysis

Publicly available scRNA-seq data from Young et al. 2018 (European Genome-Phenome Archive study IDs EGAS00001002171, EGAS00001002486, EGAS00001002325 and EGAS00001002553) was downloaded from BBrowser and used for analysis [33]. Plots were generated using t-SNE, and clusters were generated by unsupervised k-means. Identification of clusters was determined through the normalized expression of chosen cell identity markers (Fibroblasts: PDGFRβ, PDGFRα; Epithelia: AQP1, AQP2, EPCAM; Endothelia: PLVAP, CD31, CD34; Immune: CD45; Cancer; CXCR4, VIM, KRT18, PAX8, PAX2, CA9, CD10), in which a cluster presented higher than average expression levels of one or multiple cell fate markers and exclusion of other fate determining markers. After manual categorization of clusters, expression of identified ECM markers was scored across all clusters based of normalized expression (above average = +, 2 × above average = ++, >2 × above average = +++). Comparisons between clusters was done via differential expression analysis of transcript counts and weighted by log fold change. Data can be found in Tables S5 and S6.

2.17. ProteinAtlas Analysis

Identified ECM proteins were investigated for expression pattern from immunostained tissue on ProteinAtlas [34]. If multiple antibodies were available for reference, we chose the one with the highest level of validation ("Enhanced"). We included or eliminated ECM markers from further analysis if they met the following criteria: A. If present, had only an interstitial staining pattern in tumors; B. If present, had only an interstitial staining pattern in normal kidney; and C. If present, did not have staining in the glomeruli of normal kidney. This is summarized in Figure S15.

2.18. Immunohistochemistry

Immunostaining of serial sections was conducted as previously described [35] on paraffin-embedded ccRCC tumor sections. Primary antibody PDGFRα/β 1:100 (abcam ab32570) or ACTA2 1:50 (MilliporeSigma A5228) and biotinylated goat anti-rabbit 1:500 (Vector BA-1000) were used for immunohistochemistry using Vectastain ABC Elite kit (Vector PK-7100), and the color reaction was performed using DAB. Imaging was performed on a Zeiss Axioskop 2.

3. Results

3.1. Isolation and Culture of Cells from ccRCC Tumors Using Standard Methods

To understand the representation of cell types in cultures of ccRCCs, we dissociated four ccRCC tumor samples using previously published methods [23] and analyzed cells by flow cytometry (Figure 1A and Figure S1). Using a panel of markers for tumor cells (CA9 and CD10), immune cells (CD45), endothelial cells (CD31), epithelia (CD326), and fibroblasts (PGFRα/β$^+$), we found significant representation of viable cells, determined via propidium iodide exclusion, corresponding to all of these different cell types (Figures 1A,B and S1). In particular we were interested to see that approximately 7% of cells isolated from tumors were PGFRα/β$^+$ putative fibroblasts (Figure 1B,C). Using a standard protocol for monolayer tumor cell growth on tissue-culture-treated plastic in serum-containing medium [31], primary cell cultures were established and stained for tumor (CK18, vimentin) and fibroblast (PDGFRα/β) cell markers. PDGFRα/β $^+$ cells were poorly represented in these monolayer cultures; initially, the proportion of PDGFRα/β$^+$ cells plated was 15.04 ± 3.76%, but after outgrowth the percentage was only 3.22 ± 0.39% (Figures 1D and S2). The discrepancy between the flow analysis (7% of cells PGFRα/β $^+$) and first passage of culture (15% of cells PGFRα/β $^+$) indicates that other cell types may also be disadvantaged in this culture system. One explanation for the paucity of fibroblasts seen after outgrowth of primary cells may be a lack of attachment; in establishment of monolayer cultures from primary tumor isolates, a substantial proportion of cells remained unattached 48 h after plating. However, the small number of fibroblasts that did grow out

displayed a rounded morphology rather than the characteristic elongated morphology of fibroblasts, and they were outcompeted after serial passaging (the proportion at passage 5 was 0.55 ± 0.15%) (Figure S2). This was unanticipated since the culture conditions included 10% fetal bovine serum, which is reported to provide a potent growth advantage to fibroblasts in primary cell culture [36,37]. To ask if we could use a three-dimensional (3D) culture system to improve the representation of tumor fibroblasts, we seeded cells into Matrigel domes using standard tumor organoid procedures [21]. While viable cells were detected in the Matrigel (Figure 1E), no PDGFRα/β $^{+}$ fibroblasts could be found after 19 days of culture (Figure 1F), demonstrating that these conditions further disadvantaged fibroblast growth. Based on these findings, we concluded that primary ccRCC-derived fibroblasts are unexpectedly fastidious in their culture requirements and may require growth conditions that more accurately reflect the tumor microenvironment. The ECM is a key component of the microenvironment that strongly influences cell behavior, which led us to investigate the composition of ccRCC ECM.

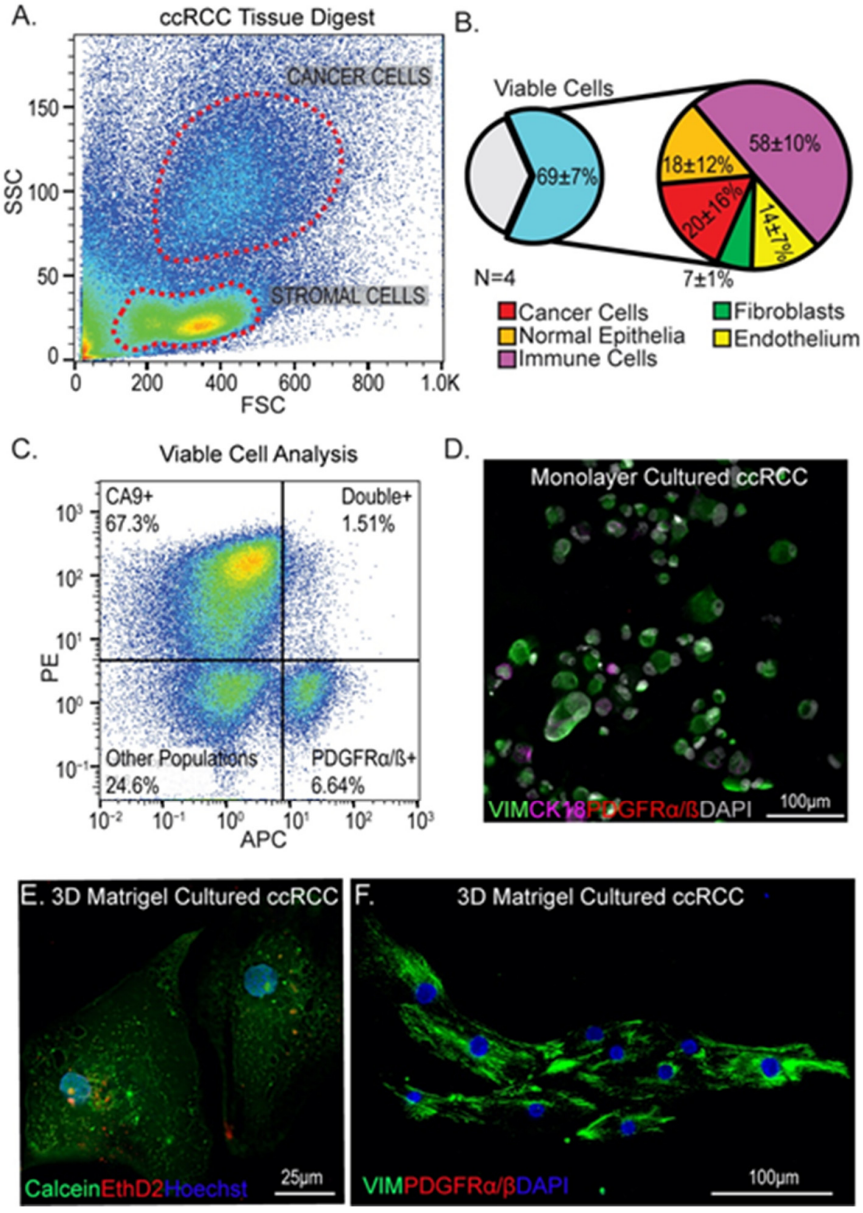

Figure 1. Identification and culture of fibroblasts from ccRCC tumors. (**A**) Representative flow cytometry

cell marker analysis of ccRCC tumors can allow distinction of stromal populations (low-side scatter) from cancer cells (high side scatter). (**B**) Summary of marker analysis of different cell types from four different patient tumors. Viability determined by propidium iodide exclusion. (**C**) Identification of fibroblasts using PDGFRα/β, showing distinction from CA9+ tumor cells. (**D**) Standard monolayer culture of isolated tumor cells showing lack of PDGFRα/β+ stromal cells. Green = vimentin, magenta = CK18, red = PDGFRα/β, gray = DAPI. (**E**,**F**) Subsets of cells from primary tumor digests are viable when cultured in Matrigel domes (**E**) but no evidence of PDGFRα/β + stromal cells could be found (**F**). Green = vimentin, red = PDGFRα/β, blue = DAPI.

3.2. Differences in ECM Composition between ccRCC and Neighboring Healthy Cortex

Considering its major constituents, Matrigel quite accurately represents epithelial basement membrane, and we hypothesized that cells isolated from tumors may require a tumor-matched ECM in order to grow out in proportions representative of the tumor of origin. To compare ECM composition between ccRCC tumor and healthy neighboring cortex, we performed mass spectrometry analysis of patient tumor samples. Kidney tumor samples were obtained from surgical nephrectomies, stored on ice at the time of surgery, dissected, and flash frozen within 24 h of collection. Tumors with healthy margins used in this analysis were all stage 3, as determined by a pathologist, and are listed in Table 1. Exploratory SWATH mass spectrometry, conducted using a kidney-sample-derived ion library [38], as previously described [24,25], was used for this analysis since previous studies have demonstrated its utility in quantitative profiling of the matrisome in unenriched tissues [39]. Unsupervised clustering of normalized proteomic data, presented as a principal component analysis (PCA) [28], shows separation between the tumor and adjacent normal cortex tissue primarily on the first principal component (Figure 2A).

SWATH analysis provided relative protein differences between grouped stage 3 ccRCC tumors and adjacent healthy kidney cortex using Sciex MarkerView (Table S1). To determine which biological pathways differ between ccRCC and neighboring healthy cortex, we performed Gene Ontology (GO) analysis (Figure 2B, Table S2). Mitochondrial metabolism, including oxireductases, metabolite interconversion enzymes, and dehydrogenases, were the most downregulated pathways. This provides a degree of confirmation of our approach since these pathways are predicted to be downregulated in ccRCC due to the heavily glycolytic profile of the tumor [40]. Interestingly, the most significant upregulated class was PC00102: Extracellular Matrix. Confirmatory analyses using GSEA and DAVID were performed, showing similar results such as clustering of pathways related to ECM signaling (Figure S3A, Table S3) and significant enrichment of ECM (Figure S3B, Table S4), respectively.

To define the specific differences in ECM composition between ccRCC and neighboring healthy cortex, we used the matrisome database MatrisomeDB [29] to identify ECM proteins from each proteomic profile. Since we were interested in structural changes between ccRCC and the healthy cortex, we narrowed our analysis to components of the "kidney cortex matrisome", i.e., glycoproteins, collagens, and proteoglycans [41]. Substantial differences between tumor and neighboring healthy cortex were found in both interstitial matrix proteins, such as collagen 6 (COL6A1, COL6A2, COL6A3), and basement membrane components such as collagen 4 (COL4A1, COL4A2) and laminins (LAMA5, LAMA4, LAMB1, LAMB2, LAMC1) (Figure 2C). While it revealed significant relative changes in protein abundance, SWATH analysis did not have the sensitivity to accurately measure the abundance of each protein. Using the same samples, we performed data-dependent acquisition (DDA) mass spectrometry, selecting for the 50 most intense ions. Due to its superior sensitivity, a DDA approach allowed for accurate quantitation of ECM proteins using Maxquant [42]. The most abundant proteins, based on a normal distribution, were selected and segregated for further analysis (Figure 2D). Using both the SWATH and DDA data, a combined dataset was produced that compares both the differential expression and quantity of proteins between stage 3 ccRCC tumors and adjacent health cortex (Figure 2E, Table S1).

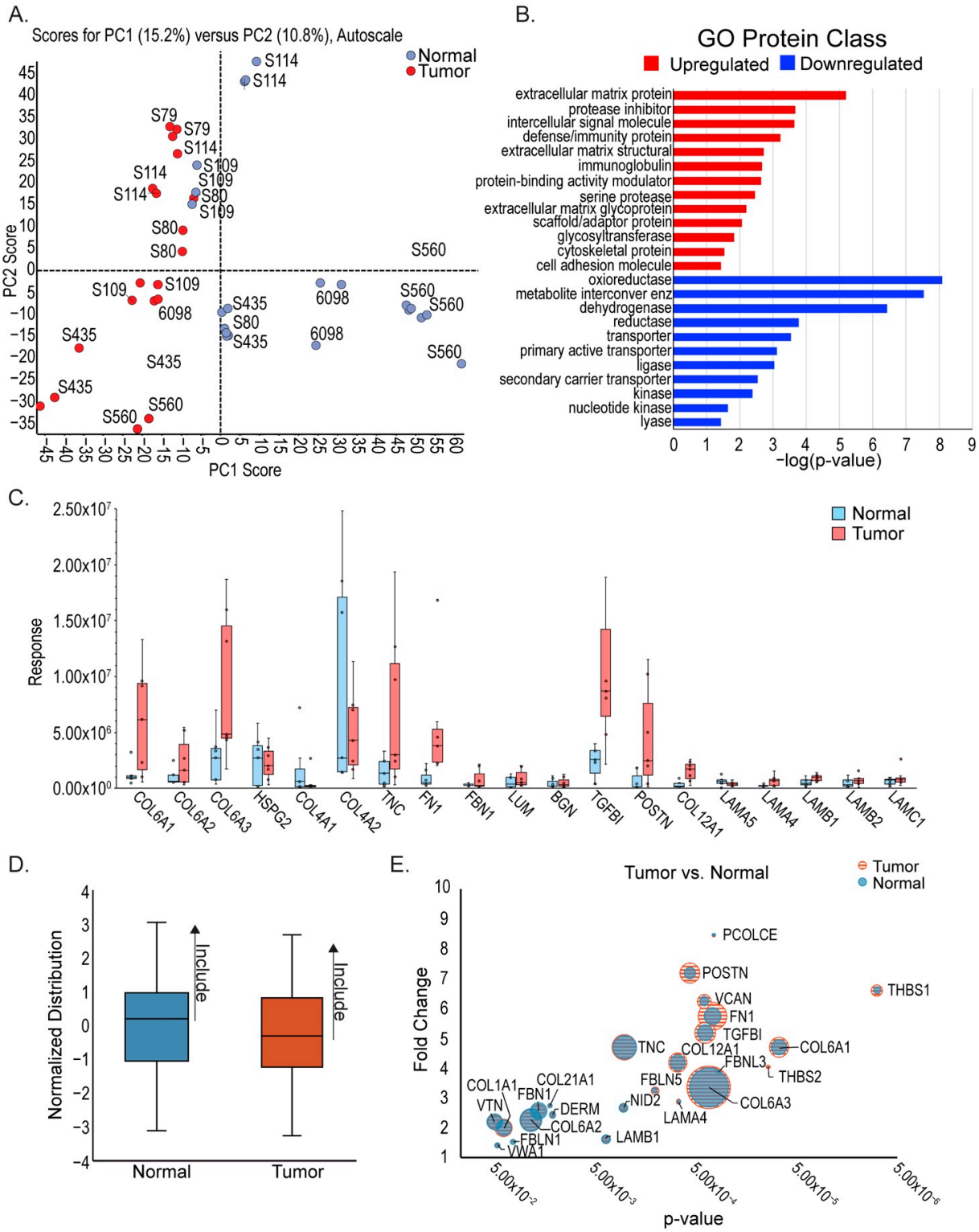

Figure 2. ECM protein upregulation in ccRCC. (**A**) Principal component analysis of mass spectrometry data from stage 3 ccRCC tumors and matched adjacent healthy cortex shows separation between tumor and normal. (**B**) Gene Ontology (GO) analysis of identified proteins shows highest upregulation of the protein class PC00102: extracellular matrix protein. (**C**) Analysis of highest upregulated and downregulated ECM proteins identified by mass spectrometry data and cross-referenced with the Matrisome database (MatrisomedDB). (**D**) Summary of DDA mass spectrometry analysis, indicating inclusion of only the most abundant ECM proteins. (**E**) Combined SWATH and DDA analyses to visually represent most significant ECM protein changes between tumor and adjacent normal kidney.

3.3. Transcriptional Analysis Indicates That Tumor Fibroblasts Are Major Contributors to ccRCC ECM

Stromal populations are commonly associated with tumor ECM remodeling and contribute significantly to tumor growth [43–45]. To determine if these cells could be the source of ECM in ccRCCs, we analyzed scRNA-seq data from Young et al. [33] for transcripts related to the top ECM targets we identified. First, we categorized clustered data into tumor and stromal populations using a panel of markers for each (epithelial: AQP1, AQP2, EPCAM; endothelial: PLVAP, CD31, CD34; fibroblast: PDGFRα, PDGFRβ; immune: CD45; tumor cell: CXCR4, VIM, KRT18, PAX8, PAX2, CA9, CD10) (Figure 3A, Table S4). Then, we stratified the expression of each ECM component for mean expression and scored clusters for high and low expression (Figure 3B). Two clusters of cells were identified as fibroblasts, and interestingly, these showed the highest expression of a number of genes encoding ECM proteins that are abundant in ccRCC such as collagen VI isoforms, fibronectin, lumican, and collagen XII. Fibroblast cluster 23 was the most predominant ECM-expressing subset of all cells in the analysis. We hypothesized that this subpopulation of PDGFRα/β$^+$ fibroblasts may be a cancer-associated fibroblast (CAF) population, and we analyzed it further to determine if it expressed a characteristic transcriptome profile. ACTA2, IGFBP7, TAGLN, MYL9, and MYLK are significantly overexpressed in cluster 23 compared with other PDGFRα/β$^+$ cells, suggesting that this subpopulation may indeed be a ccRCC CAF population (Figure 3C, Table S6) [46–48].

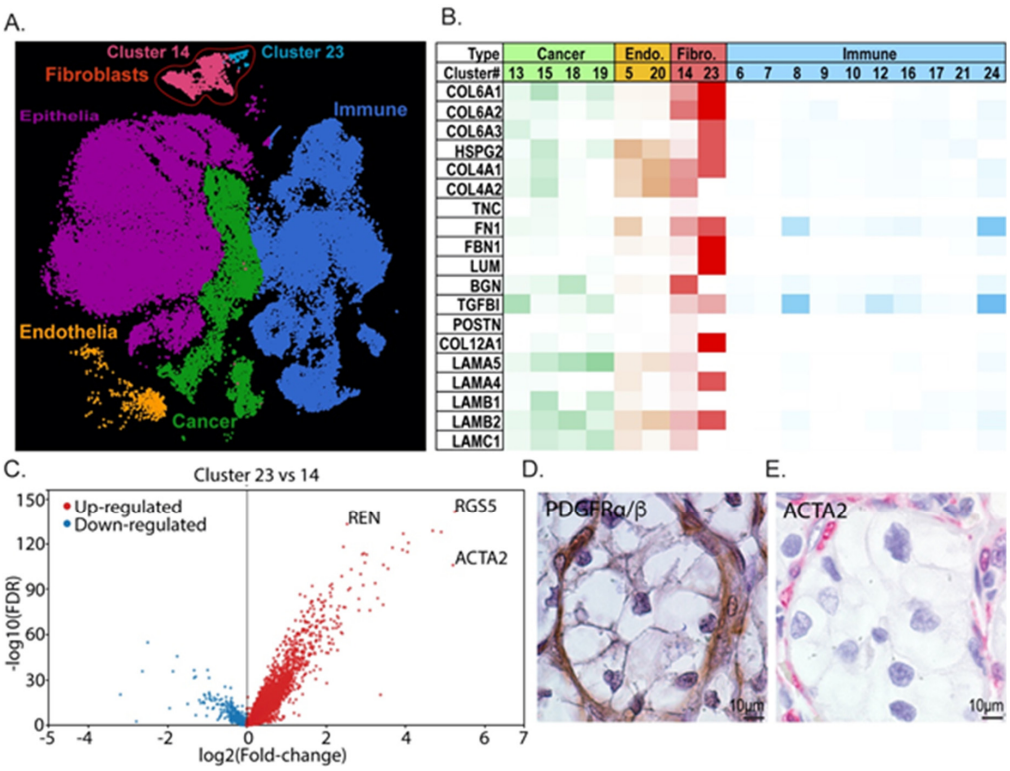

Figure 3. Prediction of cellular sources of matrix molecules based on scRNA-seq. (**A**) scRNA-seq analysis of ccRCC tumors from Young et al. [33]. Unbiased clustering was performed, and clusters were identified using cell-type-representative transcripts. Distinct fibroblast subclusters are indicated and outlined in red. (**B**) Differential ECM gene expression analysis of clusters identified as discrete cell populations. Endo. = endothelial cells, Fibro. = fibroblast cells. (**C**) Comparative transcript analysis between fibroblast sub-clusters 23 and 14 shows differential expression of cancer associated fibroblast markers. (**D**,**E**) Representative IHC from patient ccRCCs for PDGFRα/β$^+$ (**D**).

To spatially identify putative CAFs within tumor tissue, we immunostained patient tumors with PDGFRα/β to label fibroblasts and pericytes, and ACTA2 to label activated tumor fibroblasts (Figure 3D,E). Reflecting the single cell data, there is an ex-

tensive PDGFRα/β population within the stroma of the tumor tissue (Figure 3D). The ACTA2-expressing population is a small subset of these cells that is disseminated within the stroma (Figure 3E). The scRNA-seq analysis also revealed that the ACTA2-high putative CAF population shows high expression of REN (Figure 3C, Table S6), suggesting that it overlaps with the renin-producing cell population identified within the ccRCC stroma by other investigators [49].

3.4. Binding of Tumor and Stromal Cells to ccRCC ECM Components

In healthy tissue of the cortex, ECM is organized into basal lamina on which epithelial cells sit, and interstitial ECM, which provides structural integrity and conduits for vasculature and nerves. A representative section from adjacent healthy cortex stained for the basal lamina component laminin and the interstitial component collagen VI is shown in Figure 4A. Healthy proximal tubule epithelia are characterized by basal localization of laminin, which separates them from interstitial ECM components. In contrast, ccRCC tissue shows a breakdown of this stereotypical arrangement with mixing of basal lamina and interstitial ECM components (Figure 4B). Based on this analysis, we conclude that cells within tumors are exposed to a mixture of basal lamina and interstitial ECM components, in contrast to healthy proximal tubule epithelial cells, which are only exposed to the basal lamina. Using the relative abundances of ECM proteins characterized in our proteomic analysis, we generated an ECM blend characteristic for ccRCC (Figure 4C). This blend is based on the nine most abundant components identified in our analysis and includes approximately 80% of all components identified in tumor ECM (Table S1). To define the binding profiles of tumor and stromal cells to individual proteins that are most abundant in tumor ECM, we measured the binding capacity of cell lines representative for each cell type to ECM components using a monolayer attachment assay. Tumor cells (786-O), fibroblasts (NRK-49F), endothelial cells (MS1), and macrophages (RAW 264.7, abbreviated to RAW) were used to represent the common cell populations found in tumors. Single cell suspensions were given 2 h to attach to ECM-coated or uncoated wells before quantification of bound cells (Figure S4). This time-point was chosen as it precedes non-specific attachment of cells to uncoated polystyrene (data not shown). As a comparator we included Matrigel, which is commonly used to model tumor ECM and enhance attachment of tumor cells. Attachment to Matrigel was seen with endothelial cells and fibroblasts, while tumor cells and macrophages attached poorly. In contrast, all cell types attached efficiently to the two most abundant ECM molecules that we identified in tumors by mass spectrometry: collagen VI and fibronectin. We found that the cell lines analyzed shared common preferences to our chosen ECM components (Figure 4D). Fibronectin (FN1), collagen VI (COL6), collagen XII (COL12), and heparan sulfate proteoglycan 2/perlecan (HSPG2) showed the strongest binding across all cell types. Some components repelled certain cell types, for example, TGFBI, which decreased cell attachment of fibroblasts, and lumican and tenascin C, which reduced attachment of tumor cells.

To validate if these findings could be applied more broadly to ccRCC tumor cells, we isolated primary tumor cell cultures from three patient tumors as described in [23]. Cell lines S108, S109, and S114 express characteristic markers of ccRCC tumor cells but show distinct morphologies (Figure S5). The cell binding study was repeated using these primary tumor cell lines and showed a binding profile very similar to 786-O, with strong binding to fibronectin, collagen VI, and collagen XII and inefficient binding to or repulsion by periostin, lumican, and tenascin C (Figure 4D). Results from these experiments suggest that a core group of ECM molecules promotes attachment of diverse ccRCC tumor cells.

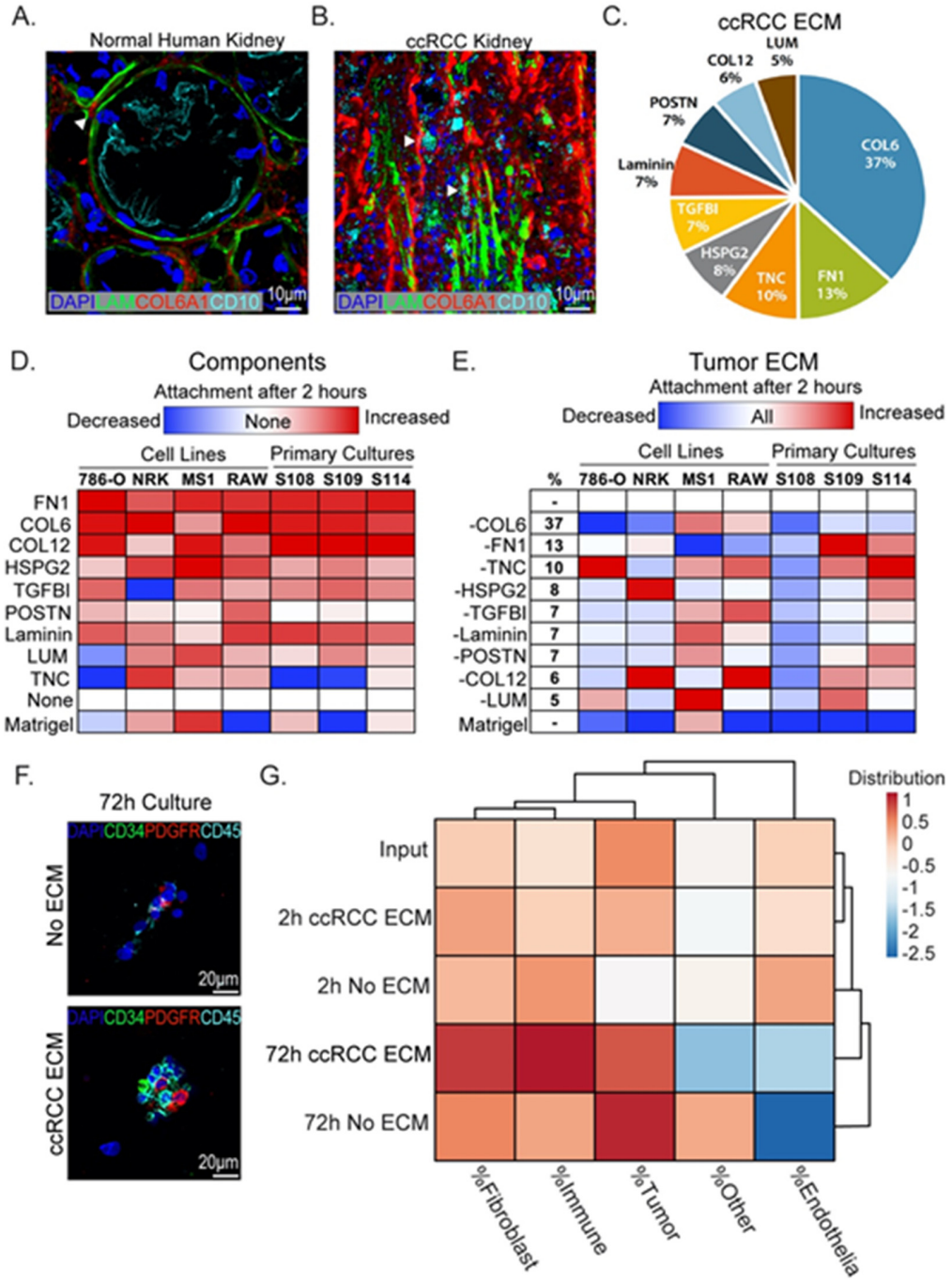

Figure 4. ECM effects on tumor and stromal cell attachment. (**A**) Immunofluorescence staining of healthy human kidney showing structured tubule basement membrane separating CD10+ proximal tubule epithelium from interstitial collagens (white arrowheads). Blue = DAPI, green = laminin, Red = collagen 6 alpha 1, cyan = CD10. (**B**) Immunofluorescence staining of ccRCC tumor for ECM components showing loss of the tubule basement membrane and mixing of laminin and interstitial collagens (white arrowheads). Blue = DAPI, green = laminin, red = collagen 6 alpha 1, cyan = CD10. (**C**) Pie chart summarizing major components of ccRCC ECM from mass spectrometry analysis. (**D**) Analysis of attachment of cell cultures to ECM components identified by mass spectrometry. Cell attachment to 2 μg/mL of indicated ECM-coated wells was determined after 2 h. Heatmap indicates increased cell attachment (red) and decreased attachment (blue) relative to no coating condition ("None"). (**E**) Cell attachment to coated dishes in the presence of all proteins or lacking one component, indicated by "-" sign. Analysis was done relative to complete blend condition "All".

Total percentage each individual component takes up in the total blend (2 µg/mL total protein) is indicated in the "%" column. (**F**) Freshly digested tumor tissue 72 h after plating on ccRCC ECM or noncoated plates. Scale bar = 20 µm. Blue = DAPI, green = CD34, red = PDGFRα/β, cyan = CD45. (**G**) Cluster analysis comparing cultures grown on coated or uncoated chamber slides to initial cell input.

We were interested to understand if there could be synergistic activities between ECM molecules identified in our study, and we next asked how the effects of the single components would compare to a combination of all molecules in our ECM blend. We found that all cell types adhered more efficiently to our ccRCC ECM blend compared to Matrigel with the exception of endothelial cells (Figure 4E). To understand the contribution of each component of the blend, we subtracted them individually and compared the binding efficiency of cells to the complete blend (Figure 4E). Although removal of certain components could increase the binding efficiency of individual populations, removal of no one individual component promoted attachment of all.

3.5. ccRCC ECM Blend Binds Diverse Cell Types Isolated from Patient Tumors

Based on the results of our cell binding experiments with immortalized and primary cell lines, we predicted that the ccRCC ECM blend could capture discrete cell populations directly from patient tumors. Utilizing previously published techniques [23], we dispersed ccRCC patient tumor samples into single cell suspensions, which we gave 2 to 72 h to attach to ECM-coated or uncoated chamber slides. Due to the poor attachment of cells to Matrigel, we did not include this coating as a comparator. The following markers were used to identify stromal cell populations: fibroblasts (PDGFRα/β), endothelia (CD34), and immune cells (CD45) (Figure 4F). At each time point analyzed, the percentage of each cell type was compared to the percentage of original input cells determined from a smear of the cell suspension isolated from each tumor. Cluster analysis based on cell composition was performed to identify the culture condition that best matched the repertoire of original input cells derived from the tumor (Figure 4G). While showing an increased preference for fibroblasts and tumor cells, the ccRCC ECM blend after 2 h was the closest match to the input. Following 72 h, while no longer accurately reflecting the initial input, the ccRCC ECM blend better maintained the distribution between fibroblast and immune cells when compared to no ECM. Additionally, endothelial cells were also better maintained, although at reduced abundance compared to earlier time points. To understand if the change in cell distribution after 72 h was due to differences in cell growth, primary cell mixes were cultured on ccRCC ECM-coated chamber slides in the presence of the thymidine analog EdU, which is incorporated into DNA of cycling cells. EdU was supplemented for the first week of culture ("pulse") and subsequently removed for one week ("chase") to label dividing cells. Two out of three samples analyzed had viable cells by the end of this time course. Although the distribution of fibroblasts was better maintained on ccRCC ECM compared to no ECM, little EdU labeling was found on these cells, indicating that ccRCC ECM promoted survival but not proliferation (Figure S6).

In conclusion, the use of ccRCC ECM can improve the capture of unique cell populations from a tumor sample and can better maintain different cell identities from 2 to 72 h when compared to conventional monolayer tissue culture conditions. However, the monolayer culture system was unable to promote outgrowth of fibroblast populations, regardless of ECM coating.

3.6. Design of a 3D Model of ccRCC with Native ECM Environment

Although the inclusion of ccRCC ECM in monolayer culture showed improved cell representation from tumors over Matrigel- and non-coated conditions, poor viability after extended culture was problematic. The use of 3D organoid culture systems for in vitro tumor modeling has gained traction over the past decade due in part to the ability to maintain characteristics of the tumor of origin [50–53]. However, attempts to establish 3D

organoid cultures from ccRCC tissue have shown a low rate of success [23]. The basis for many 3D organoid model systems is generally Matrigel, which poorly matches the ECM environment of ccRCC (Figure 2B–E). We postulated that utilization of ccRCC ECM in a 3D culture system would improve both viability of tumor cells and representation of stromal populations from ccRCC tumors. Fibrinogen is an attractive hydrogel substrate due to its tunability, and fibrin gels have been used in wound healing, drug delivery, cell differentiation, and cancer modeling [54]. Fibrinogen is abundantly represented in tumors and can therefore be considered a component of the tumor microenvironment, making it a particularly attractive candidate matrix for in vitro modeling. Differential analysis of tumor versus normal mass spectrometry data from this study showed increases in fibrinogen components FIBA, FIBB, and FIBG in tumors relative to healthy cortex (Table S1), making up a significant percentage of total protein identified in ccRCC tumor samples (FIBA = 4.00%, FIBB = 4.83%, FIBG = 6.79%). Additionally, analysis of the Renal Cancer subset of The Cancer Genome Atlas (TCGA) database identifies fibrinogen genes as highly upregulated in kidney cancer tissue (fibrinogen-High > 60% of samples), indicating that it is locally expressed and not simply deposited by the circulation (Figure S7). From these observations we conclude that fibrinogen is a native ccRCC tumor component that can be used as a versatile matrix to mimic the tumor ECM environment by mixing with ECM components identified in this study.

Fibrin 3D cultures were established by mixing single cell suspensions with fibrinogen and thrombin and spotting onto glass coverslips. The surface tension of the glass maintains a dome of cell-fibrinogen mixture that gelates at 37 °C. Dome volumes up to 20 µL gelated within 10 min and were subsequently submerged in medium for the duration of the culture period. Growth of tumor cells in domes was monitored by microscopy throughout the culture period. Fibrinogen concentration determines viscosity of the hydrogel, which determines growth properties of tumor cells. Spheroidal and branching tumor cell aggregates have been identified in previous studies of 3D tumor cell growth. While the spheroidal conformation has been associated with growth of colonies from tumor stem cells [55,56], branching growth patterns have been associated with invasive behaviors of tumors [57,58]. To define a concentration for use in our studies, we analyzed 3D growth patterns of 786-O ccRCC cells in fibrin domes at three concentrations of fibrinogen: 2 mg/mL, 4 mg/mL, and 10 mg/mL. Cells were grown in Matrigel domes as a comparator. One hundred 786-O cells were seeded per 5 µL dome and subsequently cultured for 2 weeks to ensure that the fibrin remained polymerized over an extended culture period (Figure 5A–C). Fibrin dome integrity and tumor cell growth were observed in all conditions, but variations in fibrinogen concentration drastically changed 3D growth patterns. At 2 mg/mL, cells grew predominantly in branching structures (Figure 5A), while a mix of spheroid and branching structures was seen at 4 mg/mL (Figure 5B). At 10 mg/mL, cells grew in spheroids (Figure 5C). Both branched and spheroidal structures contained viable cells (Figure 5D–F). Necrotic centers were observed in spheres larger than 40 microns in diameter (Figure 5F). We reasoned that an intermediate concentration would be best for maintaining heterogeneity in patient-derived samples since it promoted both growth patterns. To verify this, we studied growth patterns of three primary tumor cell lines in fibrin dome cultures at 4 mg/mL fibrinogen concentration and confirmed that we can generate viable multicellular structures with a variety of morphologies (Figure S8). We next asked if we could incorporate ccRCC ECM components into the 3D culture system and if this would enable analysis of 3D cell growth. 786-O cells were grown in Matrigel or 4 mg/mL fibrin domes containing 4 µg/mL ECM proteins (Figures 5G,H and S9). Nine days after seeding, cultures were analyzed for the presence of multicellular spheroid structures (Figure 5I). While larger spheroids were formed in Matrigel, the total number of structures was small, and many cells spread in a monolayer on the glass instead of growing in the 3D gel (Figure 5H). In comparison, cells grown in fibrin generated more multicellular structures (Figures 5I and S9). The incorporation of ECM components into fibrin significantly increased the size of structures (Figure 5G). Interestingly, the inclusion

of laminin, a primary component of Matrigel, to fibrin increased spheroid size when compared to fibrin alone while also maintaining a greater number of clusters when compared to Matrigel (Figure 5G). This suggests that other components of Matrigel limit abundance of multicellular structures. In conclusion, we show that fibrin is an appropriate carrier for ccRCC ECM components, can be used to culture both immortalized and primary cell lines, and can be a useful tool for studying the effects that the ECM has on ccRCC growth.

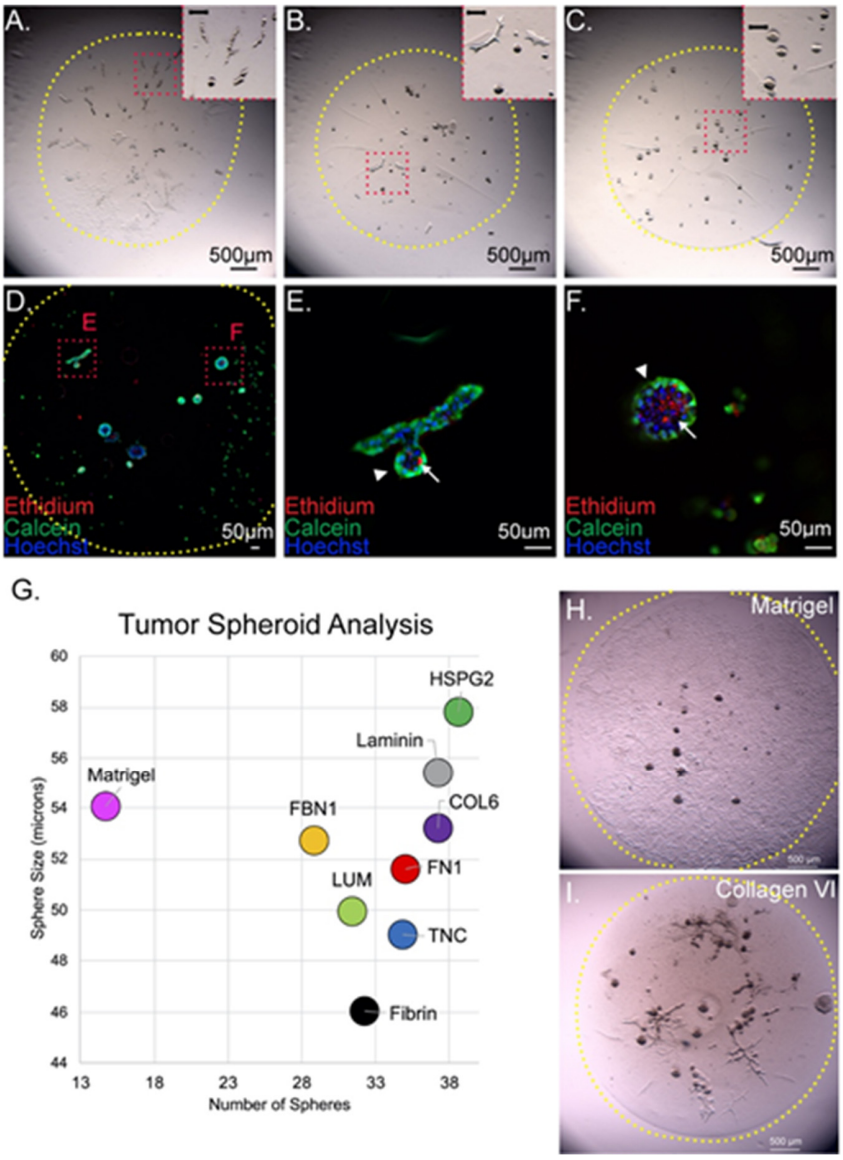

Figure 5. Three-dimensional culture of 786-O utilizing tumor-specific ECM. (**A**–**C**) Modification of fibrinogen concentrations, 2 µg/mL, 4 µg/mL, and 10 µg/mL changes morphology of cell structures formed by 786-O cells. Yellow dotted line outlines region containing 3D dome. Red dotted line indicates region of magnified inset. (**D**–**F**) Live–dead analysis of cell structures found in fibrin domes with 4 mg/mL fibrinogen shows viable elongated structures (**E**) as well as ones with necrotic cores (**F**). Arrowhead indicates viable cells. Arrow indicates dead cells. Blue = Hoechst33342, green = calcein-AM, red = ethidium homodimer 2. (**G**) Analysis of spheroids in Matrigel or fibrin with or without added ccRCC ECM proteins showing changes in number of spheroids and size. (**H**,**I**) Example of 786-O growth in Matrigel versus fibrin mixed with collagen VI (additional single ECM component blends with fibrin are shown in Figure S6). Yellow dotted line outlines region containing 3D dome.

3.7. D ccRCC ECM Model Maintains ccRCC Fibroblast Representation

Having established both that ccRCC ECM supports attachment of diverse cell types isolated from primary tumors, and that these factors can be mixed into a fibrin hydrogel matrix that supports 3D tumor cell growth, we wanted to know how this tumor-mimicking 3D environment affects growth of primary tumor isolates compared to the current standard Matrigel. We digested five different patient tumor samples into single cells using previously described methods [23]. We then seeded 750–1000 viable cells into replicate 3D domes of either Matrigel or fibrin/ccRCC ECM. Three-dimensional cultures were maintained for 19 days, at which point we analyzed the number of multicellular structures and cell viability using Calcein-AM and Ethidium Homodimer-2 (Figure S10). As expected, significant variation was observed between patient samples. For all samples, multicellular structures were seen in both fibrin/ccRCC ECM and Matrigel domes. However, for samples S215 and S145, significantly more 3D structures were seen in ccRCC ECM compared with Matrigel (Figure 6A). Approximately half of the structures seen in all samples were composed of viable cells in both fibrin/ccRCC ECM and Matrigel, and S145 displayed significantly more viable cells in Matrigel (Figure 6B,C). Interestingly, the lowest viability was seen in the samples with most abundant 3D structures. To understand if viability could be improved by culture in medium tailored to tumor organoids, we compared viability of cells from sample S215 in our growth medium versus CHM growth medium developed specifically for tumor organoid culture [23]. Tumor organoid medium significantly reduced cell viability in Matrigel, fibrin alone, and in fibrin/ccRCC ECM domes (Figure S11), and further studies were conducted using standard growth medium. From these studies we conclude that fibrin/ccRCC ECM can be used to propagate 3D structures from primary tumor isolates with a similar efficiency to Matrigel.

To understand which cell types are represented in 3D cultures from primary tumor isolates grown using ccRCC ECM versus Matrigel, we immunostained them for molecular markers on day 19 of culture. Vimentin and CXCR4 are widely used to identify cell types within tumor cultures; co-staining differentiates vimentin-positive CXCR4-negative ($VIM^+/CXCR4^-$) presumptive fibroblasts from vimentin and CXCR4 co-expressing ($VIM^+/CXCR4^+$) presumptive cancer stem cells that have previously been reported to grow out in 3D Matrigel cultures [59,60]. As expected, clusters of VIM^+ tumor cells were prevalent throughout cultures established in both Matrigel domes (Figures 6D and S12) and fibrin/ccRCC ECM cultures (Figures 6E and S12). Quantification revealed that 66% of cells in Matrigel were VIM^+ whereas over 90% of cells in fibrin/ccRCC ECM were $VIM^{+\cdot}$ (Figure 6F). Comparison of CXCR4 expression within the VIM^+ cell populations showed that CXCR4 was expressed in over 80% of cells in Matrigel domes, as expected (Figure 6F). However, only in 41% of VIM^+ cells were $CXCR4^+$ in fibrin/ccRCC ECM (Figure 6F). From this we conclude that approximately 55% of cells in 3D Matrigel cultures are $VIM^+/CXCR4^+$ presumptive tumor cells, and approximately 10% are $VIM^+/CXCR4^-$ presumptive fibroblasts. In fibrin/ccRCC ECM cultures approximately 37% of cells are $VIM^+/CXCR4^+$ presumptive tumor cells, and 53% are $VIM^+/CXCR4^-$ presumptive fibroblasts. Our previous studies and published reports have shown that fibroblasts fail to thrive in Matrigel, and we were therefore interested in understanding the identities and growth properties of the $VIM^+/CXCR4^-$ presumptive primary fibroblasts in Matrigel versus fibrin/ccRCC ECM cultures.

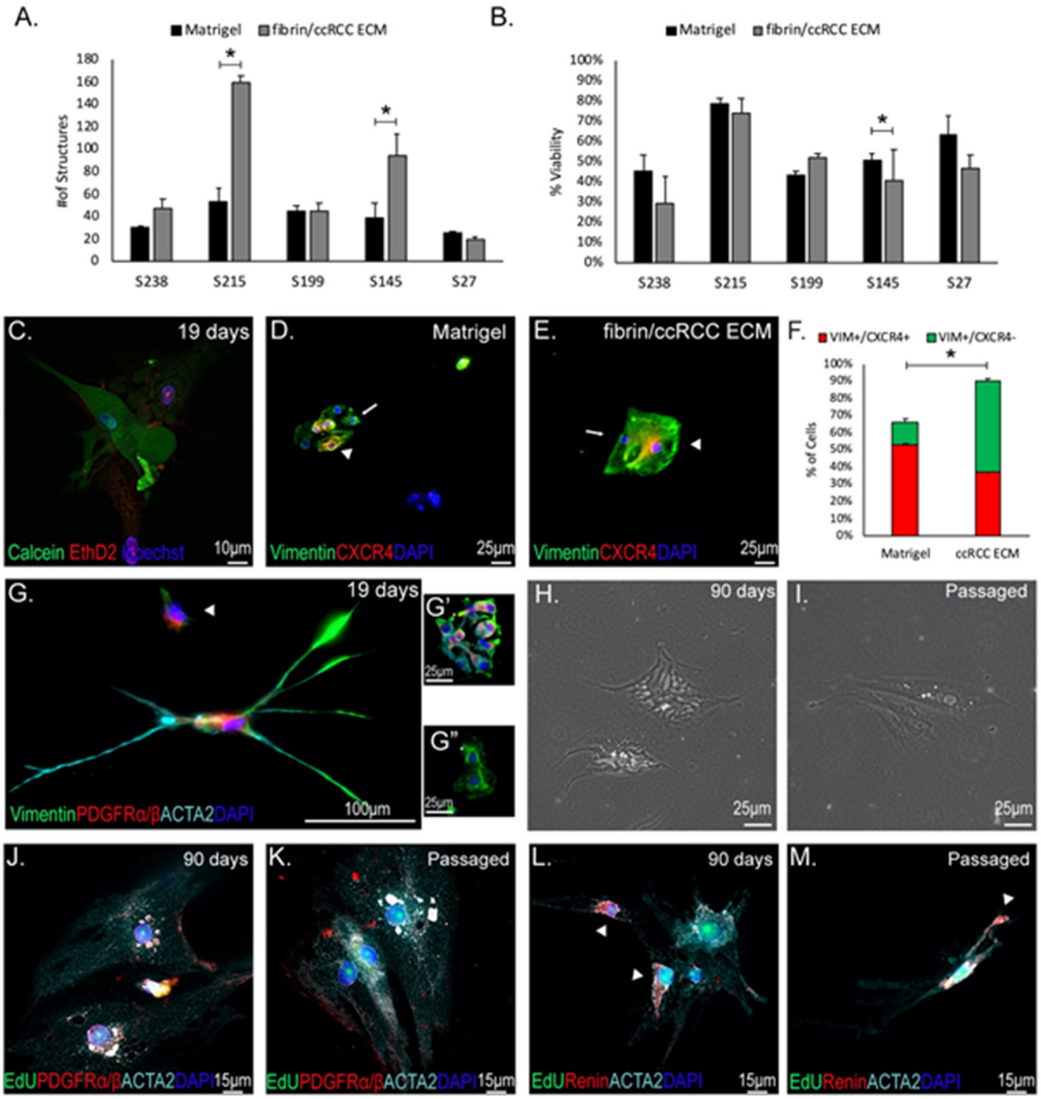

Figure 6. Fibrin/ccRCC ECM 3D culture maintains viable ccRCC fibroblasts. (**A**) Three-dimensional cultures of primary tumor digests culture either in Matrigel or fibrin/ccRCC ECM domes. * $p \leq 0.05$. (**B**) Viability analysis of structures based on calcein-AM/ethidium homodimer 2 staining. * $p \leq 0.05$. (**C**) Representative example of viable multicellular structures from patient-derived ccRCC tumor digests cultured in fibrin/ccRCC ECM domes. Green = calcein-AM, red = ethidium homodimer 2, blue = Hoechst33342 (**D**,**E**) Presence of VIM+/CXCR4+ in both Matrigel and ccRCC ECM cultured ccRCC primary digests. Arrowhead indicates CXCR4+ cells and arrow indicates CXCR4- cells. Green = vimentin, red = CXCR4, blue = DAPI. (**F**) Quantification of VIM+ cells in Matrigel versus fibrin/ccRCC ECM shows significantly more positive cells in cultures from fibrin/ccRCC ECM compared to Matrigel. However, significantly more VIM+/CXCR4+ are found in Matrigel compared to fibrin/ccRCC ECM * $p \leq 0.05$ (**G**,**G'**) Multicellular structures show expression of fibroblast markers PDGFRα/β (red) and vimentin (green), as well as presumed ccRCC CAF marker ACTA2 (cyan). Blue = DAPI. Arrowhead indicates presence of PDGFRα/β+/ACTA2- cells. (**G"**) Some VIM+ structures do not express PDGFRα/β. Green = vimentin, red = PDGFRα/β, blue = DAPI. (**H**–**K**) Fibrin/ccRCC ECM cultures were maintained for 90 days (**H**) or passaged 1:4 into fibrin/ccRCC ECM (**I**), at which point EdU was incorporated for 48 h. Cultures were immunostained (**J**,**K**) for EdU (green), PDGFRα/β (red), and ACTA2 (cyan). Blue = DAPI. (**L**,**M**) Cultures were immunostained additionally for renin (red). Arrowheads indicate renin+ cells. Green = EdU, cyan = ACTA2, blue = DAPI. White staining is overlap between red and cyan. Arrowheads indicate renin+ cells.

To compare fibroblast representation, cultures were stained for the fibroblast marker PDGFRα/β and, as previously observed in this study, few PDGFRα/β$^+$ fibroblasts were found in Matrigel cultures (less than 3% of cells in the culture) (Figures 1F and S13). However, abundant clusters of fibroblasts were observed in the fibrin/ccRCC ECM cultures

(more than 33% of cells in the culture) (Figures 6G,G' and S13). Interestingly, we also found expression of ACTA2 in many PDGFRα/β$^+$ clusters in fibrin/ccRCC ECM cultures (Figure 6G, arrowhead; 16.5% ACTA2$^+$ in the culture). In contrast to Matrigel, the fibrin/ccRCC ECM 3D culture method maintains robust representation of ccRCC fibroblast populations from primary tumor isolates.

To understand if ccRCC fibroblasts can be maintained in fibrin/ccRCC ECM 3D culture, we took two separate approaches. First, we extended the culture period to 90 days to understand if fibroblasts remained viable over longer periods in this culture system (Figure 6H). Second, we subcultured ccRCC ECM domes into fibrin/ccRCC ECM domes to determine if it was possible to propagate fibroblasts (Figure 6I). EdU was incorporated into the culture medium to assay for proliferation in both experiments (Figure 6J–M). Following long-term culture, 28.5% of cells were PDGFRα/β$^+$/ACTA2$^+$ and showed EdU incorporation (Figures 6J and S14), revealing very little decline in fibroblast number from the 33% proportion quantified at 19 days and suggesting that they continue to proliferate to maintain their proportion of the total culture. Following subculture, 63.6% of cells in the second passage were PDGFRα/β$^+$/ACTA2$^+$ fibroblasts with EdU incorporation (Figure 6K), showing that these cells can be propagated in these conditions without losing marker expression. The proportion of fibroblasts isolated directly from tumors is approximately 7% (Figure 1C), indicating that these cells are advantaged in our culture conditions. Furthermore, their proportion of the total culture can be expanded by passaging.

Although the renin expressing subset of fibroblasts is small in patient ccRCCs, transcriptome analysis indicates that it may be a significant contributor of ECM proteins (Figure 3B). To understand if this cell type is maintained following extended culture or subculture, we co-stained samples for ACTA2 and renin. Following 90 days of culture, analysis of ACTA2$^+$ cells show that 29.2% are renin$^+$, and following subculture, 27.7% are renin$^+$ (Figures 6L,M and S14). In both cases, ACTA2$^+$/renin$^+$ were labeled with EdU indicating that they are proliferative (90-day culture = 21.42% EdU$^+$; subculture = 31.8% EdU$^+$). Thus, the unique and poorly understood ccRCC CAF population is maintained and propagated in fibrin/ccRCC ECM with maintenance of the distinct tumor fibroblast repertoire.

4. Discussion

Neoplastic transformation of an epithelial cell initiates tumor formation, but the interaction of the transformed cell with non-transformed cells in its environment controls tumor formation. Numerous studies have shown that the reciprocal interactions between transformed cells and their untransformed environments are highly complex and should be considered an aberrant form of organogenesis [61]. Genetic evidence supports inactivation of the oxygen sensor VHL as the initiating event in ccRCC, with the resulting pseudohypoxia promoting a persistent state of angiogenic recruitment in the transformed cell [62]. The axis of communication between tumor cells and endothelium has been a major research focus that has yielded effective therapies [63]. How tumor cells interact with surrounding cells to control the immunological environment and escape lymphocyte attack has also become a major research question given the success of immunotherapies [64]. Studies in tumor biology and developmental biology support an essential role for fibroblasts in regulating both angiogenesis and the local immune environment [65–67]. Our study reveals the complex requirements required for growth of these cells and provides a strategy to culture them that may be used to answer basic questions regarding their influence on tumor cell growth and immunomodulation.

ECM governs cell behaviors through complex mechanisms including acting as a sink for growth factors and controlling tissue stiffness and elasticity. For this series of experiments, the cell attachment properties of ECM are of particular interest. Cells associate with ECM molecules such as collagens, laminin, and fibronectin through receptors at the cell surface that include integrins, the laminin receptor, syndecans, and dystroglycan. These have different affinities for distinct ECM components and are generally redundantly expressed, forming a cell-specific ECM-binding signature. Interactions between these

surface proteins and ECM components are the basis of physical association of cells with the tissue scaffold. For this reason, it is important to accurately reproduce the ECM protein repertoire in culture so that the combination of ECM molecules required for the attachment of diverse cell types liberated from dissociated tumors are represented. Our analysis defined specific differences in ECM-binding affinities between the predominant cell types found in tumors. However, we showed that by generating a blend of the most abundant tumor ECM components with proportions reflecting those in the ccRCC tumors we could promote binding of all cell types. Capturing the cells within the culture system is an essential first step towards establishing long-term cultures of patient tumors, and further investigations of metabolite composition and oxygenation of medium will guide efforts to grow cells in 3D matrix to a density similar to that seen in tumors.

In addition to their role in cellular adhesion, ECM-binding cell surface receptors control cytoskeletal contacts with the surroundings. Our study identified an interesting contrast between the ECM of healthy neighboring kidney cortex and tumors. In the healthy kidney, epithelial cells sit on basement membranes and stromal cells are embedded within the adjacent interstitial ECM which functions as a scaffold for the organ. The compositions of basement membranes and interstitial ECM are highly distinct, but ccRCC appears to consist of a mixture of components, with interstitial ECM components most highly represented. Thus, tumor cells and stromal cells are embedded in a single ccRCC ECM and this unique structural arrangement is anticipated to have profound effects on cell behaviors. Culture systems based on outgrowth of cells from tumor fragments including native tumor ECM have been successfully used to grow mixed cultures of tumor and stromal cells [68]. We speculate that the mismatch in ECM profile between Matrigel, which mimics basement membrane, and fibrin/ccRCC ECM, which largely contains interstitial ECM components, may be the reason that the few fibroblasts that do adhere to Matrigel are rapidly lost in culture. A previous report comparing the growth of patient-derived ccRCC tumor cells in Matrigel versus a polysaccharide scaffold found little growth of fibroblasts in Matrigel and suggested that polysaccharide biomaterials would be preferable for outgrowth of non-tumor cells [69]. The rounded structure of fibroblasts in Matrigel suggests aberrant cytoskeletal arrangement consistent with a lack of ECM interaction. Fibroblasts in ccRCC ECM display characteristic morphology and are maintained in culture.

A defining feature of the ccRCC ECM composition characterized in this work is its qualitative similarity to healthy kidney cortex ECM. Within the detection limits of our analysis, neoplastic transformation does not lead to de novo expression of matrix molecules but rather alters the relative abundances of components. In contrast to healthy cortex, ccRCC ECM is highly enriched in collagen VI, fibronectin, tenascin C, TGFBI, and periostin. The role of each of these components has been studied in tumor cell biology. Collagen VI is abundantly expressed in tumors from several organs including breast [70], colon, and lung [71]. It promotes survival of tumor cells [72] and fibroblasts [73] and has been shown to stimulate tumor angiogenesis [74]. Expression of collagen VI in xenografted ccRCC cells results in increased tumor size [75]. Fibronectin promotes tumor growth through activation of PI3K/AKT signaling in tumor cells [76,77]. Tenascin C closely resembles fibronectin and shares receptor-binding properties, promoting proliferation [78] and migration [79] of tumor cells. Similarly, TGFBI promotes proliferation and migration of cancer cells [80]. Periostin promotes tumor cell growth through increased survival [81] and expression in xenografted ccRCC cells promotes tumor size [82]. All of these ECM proteins may activate multiple signal transduction pathways through their cell surface receptor interactions, including PI3K, TGFβ, ERK, and STAT.

In many tumors, the alteration in ECM content results in a more rigid matrix that promotes malignancy [83], but in ccRCC we have found that this is not the case: modulus testing of tumors versus adjacent healthy cortex revealed a lower modulus in tumors [84]. This suggests that the ECM profile of ccRCCs defined in our analysis reduces tissue rigidity in comparison with the healthy surrounding tissue, perhaps contributing to the indolent

progression of ccRCC tumors, which genetic analysis has revealed generally develop over decades [85].

Our reanalysis of published single cell data from ccRCCs indicates that tumor fibroblasts serve as a major source of ECM. This is certainly in line with observations from tumors that develop in other organ systems [86], where myofibroblast-derived ECM has been identified as a major determinant of the tumor microenvironment. Interestingly, we found that PDGFRα/β-expressing fibroblasts identified in the Young et al. single-cell dataset [33] segregated into two distinct clusters; the less abundant subset of these had high expression of ACTA2 (smooth muscle actin), identifying them as the putative myofibroblast population. In agreement with published reports on myofibroblast production of ECM, this subset of cells displayed strong expression of ECM components identified by mass spectrometry; collagen VI, HSPG2/perlecan, fibronectin, lumican, laminin, and collagen 12. Thus, we propose that these cells play a major role in forming the ECM environment of ccRCC. Immunostaining reveals that ACTA2-expressing cells surround clusters of clear cells in ccRCC tissue, indicating that they deposit their matrix within the network of stroma that contains vessels and immune cells. Our study indicates that these ccRCC myofibroblasts express renin, an angiotensinogen protease that promotes vasoconstriction through the renin-angiotensin (RAS) cascade. The presence of a renin expressing cell in ccRCC stroma has previously been reported [49], and subsequent work has identified it as a cancer stem cell [87]. However, based on our findings we propose that it is a myofibroblast subpopulation of CAFs in ccRCC. In the healthy kidney, renin is expressed in a specialized subpopulation of cells within vessel walls [88] that is essential for maintaining blood pressure by secreting renin in response to neural and chemical cues [89]. Clinical observations support a role for the RAS system in ccRCC progression, with patients treated with angiotensin inhibitors displaying improved survival in metastatic ccRCC [90]. A recent study showed that RAS inhibition prevents ccRCC tumor colony formation, indicating direct effects of this pathway on tumor tissue [91]. Contribution of the ccRCC myofibroblast to activation of the RAS system in ccRCC is therefore an intriguing possibility. Our demonstration that the renin-expressing myofibroblast can be propagated in culture provides a novel and unique tool to investigate specific roles of the ccRCC CAF in tumor biology.

5. Conclusions

Proteomic analysis identified drastic changes in the ECM environment of ccRCC compared with healthy neighboring kidney cortex tissue, including structural changes such as loss of tubule basal lamina and alterations in the composition of ECM. scRNA-seq analysis identified a subset of CAFs with a strong transcriptomic profile for ECM expression, identifying them as the source of increased matrix deposition. We were unable to culture these ACTA2 and renin expressing CAFs using conventional cell culture techniques, including monolayer and Matrigel domes. To isolate and propagate these cells we devised a ccRCC specific ECM combination (ccRCC ECM) based on the proteomic profiles of patient ccRCCs. Cell types representative of the tumor showed efficient attachment to this substrate and incorporation of this ccRCC-characteristic ECM mix into fibrin gels enabled creation of a tunable 3D ccRCC environment (fibrin/ccRCC ECM). Patient tumor-derive primary ccRCC cell isolates grew out in this 3D tumor culture, and molecular marker analysis revealed representation of both tumor cells and fibroblasts. The fibroblast repertoire found in tumors was preserved with subsets of cells showing high expression of ACTA2 and renin. In conclusion, we found that the use of ccRCC specific ECM components in a fibrin-based 3D culture system allows for robust culture of ccRCC fibroblasts for use in studying tumor-CAF-ECM interactions, as well as further exploration of different fibroblast subtypes within ccRCC tumors.

Supplementary Materials: The following are available online at https://www.mdpi.com/article/10.3390/cancers13235873/s1, Supplemental Methods; Figure S1: Flow-cytometry-based cell type marker analysis; Figure S2: Loss of PDGFRα/β after passaging primary ccRCC cultures; Figure S3:

Pathway analyses of ccRCC mass spectrometry dataset; Figure S4: Cell attachment on ECM; Figure S5: ccRCC cell marker analysis of primary cell lines; Figure S6: EdU analysis of primary tumor isolates; Figure S7: Analysis of fibrinogen transcripts from TCGA; Figure S8: Primary RCC cultures in fibrin domes; Figure S9: Incorporation of ECM into fibrin domes; Figure S10: ccRCC tumor isolate culture in Matrigel vs. fibrin/ccRCC ECM; Figure S11: Media formulation influences cell viability of 3D cultures; Figure S12: Further characterization of 3D cultures; Figure S13: Immunostaining analysis of fibrin/ccRCC ECM cultures for fibroblast markers; Figure S14: Additional analysis of fibroblast markers after 90 days of culture; Figure S15: Protein localization validation; Table S1: Mass Spectrometry Matrisome Analysis; Table S2: Gene Ontology (GO) Analysis; Table S3: Gene Set Enrichment Analysis (GSEA); Table S4: Database for Annotation, Visualization and Integrated Discovery (DAVID) Analysis; Table S5: RCC scRNA-seq Analysis; Table S6: Fibroblast clusters analysis.

Author Contributions: Conceptualization, K.H.B., L.O.; methodology, K.H.B., K.P.H.W., C.P.H.V., J.M.C., S.S.-L.; software, K.H.B., K.P.H.W.; validation, K.H.B., K.P.H.W., J.M.C.; formal analysis, K.H.B.; investigation, K.H.B., L.O.; resources, C.P.H.V., S.S.-L., L.O.; data curation, K.H.B., T.C., K.P.H.W.; writing—original draft preparation, K.H.B., L.O.; writing—review and editing, K.H.B., C.P.H.V., L.O.; visualization, K.H.B.; supervision, C.P.H.V., S.S.-L., L.O.; project administration, L.O.; funding acquisition, L.O. All authors have read and agreed to the published version of the manuscript.

Funding: This work was supported by The Assistant Secretary of Defense for Health Affairs endorsed by the Department of Defense, through the Kidney Cancer Research Program under Award No. KC170016 (L.O.). Opinions, interpretations, conclusions, and recommendations are those of the author and are not necessarily endorsed by the Department of Defense. Mass Spectrometry reported in this publication was supported by an Institutional Development Award (IDeA) from the National Institute of General Medical Sciences of the National Institutes of Health under award number P20GM121301 (C.P.H.V.).

Institutional Review Board Statement: The study was conducted according to the guidelines of the Declaration of Helsinki and approved by the Institutional Review Board of the New York Blood Center, where the Rogosin Institute laboratory space is located (protocol 1493860-1, approved 09.11.2019l).

Informed Consent Statement: Informed consent was obtained from all subjects involved in the study.

Data Availability Statement: SWATH and ion library raw data will be located at the PeptideAtlas repository, and accessible via the web. PeptideAtlas is a part of the ProteomeXchange Consortium. scRNA-seq data from Young et al. [33] and can be downloaded from the European Genome-phenome Archive (EGA) under study IDs EGAS00001002171, EGAS00001002486, EGAS00001002325 and EGAS00001002553. ProteinAtlas staining data are publicly available at https://www.proteinatlas.org (accessed on 6 January 21). Data from The Cancer Genome Atlas are publicly available from the TCGA repository, https://portal.gdc.cancer.gov/projects/TCGA (accessed on 6 January 21).

Acknowledgments: We would like to acknowledge the New York Blood Center Flow Cytometry and Confocal Microscopy Core Facility for their assistance in confocal imaging. Additional acknowledgment to Tingshien Chuang and Jennifer Fetting for contributions to fibrin assay development and immunohistochemistry, respectively.

Conflicts of Interest: The authors declare no conflict of interest.

References

1. Siegel, R.L.; Miller, K.D.; Jemal, A. Cancer Statistics, 2020. *CA Cancer J. Clin.* **2020**, *70*, 7–30. [CrossRef]
2. Haake, S.M.; Rathmell, W.K. Renal Cancer Subtypes: Should We be Lumping or Splitting for Therapeutic Decision Making? *Cancer* **2017**, *123*, 200–209. [CrossRef]
3. Nickerson, M.L.; Jaeger, E.; Shi, Y.; Durocher, J.A.; Mahurkar, S.; Zaridze, D.; Matveev, V.; Janout, V.; Kollarova, H.; Bencko, V.; et al. Improved Identification of Von Hippel-Lindau Gene Alterations in Clear Cell Renal Tumors. *Clin. Cancer Res.* **2008**, *14*, 4726–4734. [CrossRef]
4. Iliopoulos, O.; Levy, A.P.; Jiang, C.; Kaelin, W.G., Jr.; Goldberg, M.A. Negative Regulation of Hypoxia-Inducible Genes by the Von Hippel-Lindau Protein. *Proc. Natl. Acad. Sci. USA* **1996**, *93*, 10595–10599. [CrossRef] [PubMed]
5. Choueiri, T.K.; Kaelin, W.G., Jr. Targeting the HIF2-VEGF Axis in Renal Cell Carcinoma. *Nat. Med.* **2020**, *26*, 1519–1530. [CrossRef]
6. Lindgren, D.; Sjölund, J.; Axelson, H. Tracing Renal Cell Carcinomas back to the Nephron. *Trends Cancer* **2018**, *4*, 472–484. [CrossRef] [PubMed]

7. Delahunt, B.; Srigley, J.R. The Evolving Classification of Renal Cell Neoplasia. *Semin. Diagn. Pathol.* **2015**, *32*, 90–102. [CrossRef]
8. Weaver, V.M.; Petersen, O.W.; Wang, F.; Larabell, C.A.; Briand, P.; Damsky, C.; Bissell, M.J. Reversion of the Malignant Phenotype of Human Breast Cells in Three-Dimensional Culture and in Vivo by Integrin Blocking Antibodies. *J. Cell Biol.* **1997**, *137*, 231–245. [CrossRef] [PubMed]
9. Mettouchi, A.; Klein, S.; Guo, W.; Lopez-Lago, M.; Lemichez, E.; Westwick, J.K.; Giancotti, F.G. Integrin-Specific Activation of Rac Controls Progression through the G(1) Phase of the Cell Cycle. *Mol. Cell* **2001**, *8*, 115–127. [CrossRef]
10. Brooks, P.C.; Clark, R.A.; Cheresh, D.A. Requirement of Vascular Integrin Alpha V Beta 3 for Angiogenesis. *Science* **1994**, *264*, 569–571. [CrossRef]
11. Brooks, P.C.; Montgomery, A.M.; Rosenfeld, M.; Reisfeld, R.A.; Hu, T.; Klier, G.; Cheresh, D.A. Integrin Alpha V Beta 3 Antagonists Promote Tumor Regression by Inducing Apoptosis of Angiogenic Blood Vessels. *Cell* **1994**, *79*, 1157–1164. [CrossRef]
12. Wang, Y.; McNiven, M.A. Invasive Matrix Degradation at Focal Adhesions Occurs via Protease Recruitment by a FAK-p130Cas Complex. *J. Cell Biol.* **2012**, *196*, 375–385. [CrossRef] [PubMed]
13. Paszek, M.J.; Zahir, N.; Johnson, K.R.; Lakins, J.N.; Rozenberg, G.I.; Gefen, A.; Reinhart-King, C.A.; Margulies, S.S.; Dembo, M.; Boettiger, D.; et al. Tensional Homeostasis and the Malignant Phenotype. *Cancer Cell* **2005**, *8*, 241–254. [CrossRef]
14. Guo, W.; Pylayeva, Y.; Pepe, A.; Yoshioka, T.; Muller, W.J.; Inghirami, G.; Giancotti, F.G. Beta 4 Integrin Amplifies ErbB2 Signaling to Promote Mammary Tumorigenesis. *Cell* **2006**, *126*, 489–502. [CrossRef] [PubMed]
15. Naba, A.; Clauser, K.R.; Ding, H.; Whittaker, C.A.; Carr, S.A.; Hynes, R.O. The Extracellular Matrix: Tools and Insights for the "Omics" Era. *Matrix Biol.* **2016**, *49*, 10–24. [CrossRef]
16. Tian, C.; Clauser, K.R.; Öhlund, D.; Rickelt, S.; Huang, Y.; Gupta, M.; Mani, D.R.; Carr, S.A.; Tuveson, D.A.; Hynes, R.O. Proteomic Analyses of ECM during Pancreatic Ductal Adenocarcinoma Progression Reveal Different Contributions by Tumor and Stromal Cells. *Proc. Natl. Acad. Sci. USA* **2019**, *116*, 19609–19618. [CrossRef] [PubMed]
17. Avery, D.; Govindaraju, P.; Jacob, M.; Todd, L.; Monslow, J.; Puré, E. Extracellular Matrix Directs Phenotypic Heterogeneity of Activated Fibroblasts. *Matrix Biol.* **2018**, *67*, 90–106. [CrossRef]
18. Neal, J.T.; Li, X.; Zhu, J.; Giangarra, V.; Grzeskowiak, C.L.; Ju, J.; Liu, I.H.; Chiou, S.H.; Salahudeen, A.A.; Smith, A.R.; et al. Organoid Modeling of the Tumor Immune Microenvironment. *Cell* **2018**, *175*, 1972–1988.e16. [CrossRef]
19. Driehuis, E.; Kretzschmar, K.; Clevers, H. Establishment of Patient-Derived Cancer Organoids for Drug-Screening Applications. *Nat. Protoc.* **2020**, *15*, 3380–3409. [CrossRef]
20. Orkin, R.W.; Gehron, P.; McGoodwin, E.B.; Martin, G.R.; Valentine, T.; Swarm, R. A Murine Tumor Producing a Matrix of Basement Membrane. *J. Exp. Med.* **1977**, *145*, 204–220. [CrossRef]
21. Sato, T.; Stange, D.E.; Ferrante, M.; Vries, R.G.; Van Es, J.H.; Van den Brink, S.; Van Houdt, W.J.; Pronk, A.; Van Gorp, J.; Siersema, P.D.; et al. Long-Term Expansion of Epithelial Organoids from Human Colon, Adenoma, Adenocarcinoma, and Barrett's Epithelium. *Gastroenterology* **2011**, *141*, 1762–1772. [CrossRef]
22. Xia, X.; Li, F.; He, J.; Aji, R.; Gao, D. Organoid Technology in Cancer Precision Medicine. *Cancer Lett.* **2019**, *457*, 20–27. [CrossRef]
23. Pauli, C.; Hopkins, B.D.; Prandi, D.; Shaw, R.; Fedrizzi, T.; Sboner, A.; Sailer, V.; Augello, M.; Puca, L.; Rosati, R.; et al. Personalized In Vitro and In Vivo Cancer Models to Guide Precision Medicine. *Cancer Discov.* **2017**, *7*, 462–477. [CrossRef] [PubMed]
24. Rostama, B.; Beauchemin, M.; Bouchard, C.; Bernier, E.; Vary, C.P.H.; May, M.; Houseknecht, K.L. Understanding Mechanisms Underlying Non-Alcoholic Fatty Liver Disease (NAFLD) in Mental Illness: Risperidone and Olanzapine Alter the Hepatic Proteomic Signature in Mice. *Int. J. Mol. Sci.* **2020**, *21*, 9362. [CrossRef] [PubMed]
25. Peterson, S.M.; Turner, J.E.; Harrington, A.; Davis-Knowlton, J.; Lindner, V.; Gridley, T.; Vary, C.P.H.; Liaw, L. Notch2 and Proteomic Signatures in Mouse Neointimal Lesion Formation. *Arter. Thromb. Vasc. Biol.* **2018**, *38*, 1576–1593. [CrossRef]
26. Kang, Y.; Burton, L.; Lau, A.; Tate, S. SWATH-ID: An Instrument Method Which Combines Identification and Quantification in a Single Analysis. *Proteomics* **2017**, *10*, e150052. [CrossRef] [PubMed]
27. Beauchemin, M.; Geguchadze, R.; Guntur, A.R.; Nevola, K.; Le, P.T.; Barlow, D.; Rue, M.; Vary, C.P.H.; Lary, C.W.; Motyl, K.J.; et al. Exploring Mechanisms of Increased Cardiovascular Disease Risk with Antipsychotic Medications: Risperidone Alters the Cardiac Proteomic Signature in Mice. *Pharmacol. Res.* **2020**, *152*, 104589. [CrossRef]
28. Ivosev, G.; Burton, L.; Bonner, R. Dimensionality Reduction and Visualization in Principal Component Analysis. *Anal. Chem.* **2008**, *80*, 4933–4944. [CrossRef]
29. Shao, X.; Taha, I.N.; Clauser, K.R.; Gao, Y.T.; Naba, A. MatrisomeDB: The ECM-Protein Knowledge Database. *Nucleic Acids Res.* **2020**, *48*, D1136–D1144. [CrossRef]
30. Hynes, R.O.; Naba, A. Overview of the Matrisome—an Inventory of Extracellular Matrix Constituents and Functions. *Cold Spring Harb. Perspect. Biol.* **2012**, *4*, a004903. [CrossRef]
31. Williams, R.D.; Elliott, A.Y.; Stein, N.; Fraley, E.E. In Vitro Cultivation of Human Renal Cell Cancer. II. Characterization of cell lines. *In Vitro* **1978**, *14*, 779–786. [CrossRef] [PubMed]
32. Liu, J.; Tan, Y.; Zhang, H.; Zhang, Y.; Xu, P.; Chen, J.; Poh, Y.C.; Tang, K.; Wang, N.; Huang, B. Soft Fibrin Gels Promote Selection and Growth of Tumorigenic Cells. *Nat. Mater.* **2012**, *11*, 734–741. [CrossRef]
33. Young, M.D.; Mitchell, T.J.; Vieira Braga, F.A.; Tran, M.G.B.; Stewart, B.J.; Ferdinand, J.R.; Collord, G.; Botting, R.A.; Popescu, D.M.; Loudon, K.W.; et al. Single-Cell Transcriptomes from Human Kidneys Reveal the Cellular Identity of Renal Tumors. *Science* **2018**, *361*, 594–599. [CrossRef] [PubMed]

34. Uhlén, M.; Fagerberg, L.; Hallström, B.M.; Lindskog, C.; Oksvold, P.; Mardinoglu, A.; Sivertsson, Å.; Kampf, C.; Sjöstedt, E.; Asplund, A.; et al. Proteomics. Tissue-based map of the human proteome. *Science* **2015**, *347*, 1260419. [CrossRef] [PubMed]
35. Fetting, J.L.; Guay, J.A.; Karolak, M.J.; Iozzo, R.V.; Adams, D.C.; Maridas, D.E.; Brown, A.C.; Oxburgh, L. FOXD1 Promotes Nephron Progenitor Differentiation by Repressing Decorin in the Embryonic Kidney. *Development* **2014**, *141*, 17–27. [CrossRef] [PubMed]
36. McKeehan, W.L.; Ham, R.G. Methods for Reducing the Serum Requirement for Growth in Vitro of Nontransformed Diploid Fibroblasts. *Dev. Biol. Stand.* **1976**, *37*, 97–98.
37. Whateley, J.G.; Knox, P. Isolation of a Serum Component that Stimulates the Spreading of Cells in Culture. *Biochem. J.* **1980**, *185*, 349–354. [CrossRef]
38. Wu, J.X.; Song, X.; Pascovici, D.; Zaw, T.; Care, N.; Krisp, C.; Molloy, M.P. SWATH Mass Spectrometry Performance Using Extended Peptide MS/MS Assay Libraries. *Mol. Cell Proteom.* **2016**, *15*, 2501–2514. [CrossRef]
39. Krasny, L.; Bland, P.; Kogata, N.; Wai, P.; Howard, B.A.; Natrajan, R.C.; Huang, P.H. SWATH Mass Spectrometry as a Tool for Quantitative Profiling of the Matrisome. *J. Proteom.* **2018**, *189*, 11–22. [CrossRef]
40. Courtney, K.D.; Bezwada, D.; Mashimo, T.; Pichumani, K.; Vemireddy, V.; Funk, A.M.; Wimberly, J.; McNeil, S.S.; Kapur, P.; Lotan, Y.; et al. Isotope Tracing of Human Clear Cell Renal Cell Carcinomas Demonstrates Suppressed Glucose Oxidation In Vivo. *Cell Metab.* **2018**, *28*, 793–800.e2. [CrossRef]
41. Naba, A.; Clauser, K.R.; Hoersch, S.; Liu, H.; Carr, S.A.; Hynes, R.O. The Matrisome: In Silico Definition and in Vivo Characterization by Proteomics of Normal and Tumor Extracellular Matrices. *Mol. Cell Proteom.* **2012**, *11*, M111.014647. [CrossRef] [PubMed]
42. Gillet, L.C.; Navarro, P.; Tate, S.; Röst, H.; Selevsek, N.; Reiter, L.; Bonner, R.; Aebersold, R. Targeted Data Extraction of the MS/MS Spectra Generated by Data-Independent Acquisition: A New Concept for Consistent and Accurate Proteome Analysis. *Mol. Cell. Proteom.* **2012**, *11*, O111.016717. [CrossRef]
43. Sahai, E.; Astsaturov, I.; Cukierman, E.; DeNardo, D.G.; Egeblad, M.; Evans, R.M.; Fearon, D.; Greten, F.R.; Hingorani, S.R.; Hunter, T.; et al. A Framework for Advancing our Understanding of Cancer-Associated Fibroblasts. *Nat. Rev. Cancer* **2020**, *20*, 174–186. [CrossRef]
44. Lin, Y.; Xu, J.; Lan, H. Tumor-Associated Macrophages in Tumor Metastasis: Biological Roles and Clinical Therapeutic Applications. *J. Hematol. Oncol.* **2019**, *12*, 76. [CrossRef] [PubMed]
45. Cornil, I.; Theodorescu, D.; Man, S.; Herlyn, M.; Jambrosic, J.; Kerbel, R.S. Fibroblast Cell Interactions with Human Melanoma Cells Affect Tumor Cell Growth as a Function of Tumor Progression. *Proc. Natl. Acad. Sci. USA* **1991**, *88*, 6028–6032. [CrossRef] [PubMed]
46. Costa, A.; Kieffer, Y.; Scholer-Dahirel, A.; Pelon, F.; Bourachot, B.; Cardon, M.; Sirven, P.; Magagna, I.; Fuhrmann, L.; Bernard, C.; et al. Fibroblast Heterogeneity and Immunosuppressive Environment in Human Breast Cancer. *Cancer Cell* **2018**, *33*, 463–479.e10. [CrossRef] [PubMed]
47. Torres, S.; Garcia-Palmero, I.; Herrera, M.; Bartolomé, R.A.; Peña, C.; Fernandez-Aceñero, M.J.; Padilla, G.; Peláez-García, A.; Lopez-Lucendo, M.; Rodriguez-Merlo, R.; et al. LOXL2 Is Highly Expressed in Cancer-Associated Fibroblasts and Associates to Poor Colon Cancer Survival. *Clin. Cancer Res.* **2015**, *21*, 4892–4902. [CrossRef]
48. Rupp, C.; Scherzer, M.; Rudisch, A.; Unger, C.; Haslinger, C.; Schweifer, N.; Artaker, M.; Nivarthi, H.; Moriggl, R.; Hengstschläger, M.; et al. IGFBP7, A Novel Tumor Stroma Marker, with Growth-Promoting Effects in Colon Cancer Through a Paracrine Tumor-Stroma Interaction. *Oncogene* **2015**, *34*, 815–825. [CrossRef]
49. Lindop, G.B.; Fleming, S. Renin in Renal Cell Carcinoma—An Immunocytochemical Study Using an Antibody to Pure Human renin. *J. Clin. Pathol.* **1984**, *37*, 27–31. [CrossRef]
50. Bregenzer, M.E.; Horst, E.N.; Mehta, P.; Novak, C.M.; Raghavan, S.; Snyder, C.S.; Mehta, G. Integrated Cancer Tissue Engineering Models for Precision Medicine. *PLoS ONE* **2019**, *14*, e0216564.
51. Puca, L.; Bareja, R.; Prandi, D.; Shaw, R.; Benelli, M.; Karthaus, W.R.; Hess, J.; Sigouros, M.; Donoghue, A.; Kossai, M.; et al. Patient Derived Organoids to Model Rare Prostate Cancer Phenotypes. *Nat. Commun.* **2018**, *9*, 2404. [CrossRef] [PubMed]
52. Kim, M.; Mun, H.; Sung, C.O.; Cho, E.J.; Jeon, H.J.; Chun, S.M.; Jung, D.J.; Shin, T.H.; Jeong, G.S.; Kim, D.K.; et al. Patient-Derived Lung Cancer Organoids as in Vitro Cancer Models for Therapeutic Screening. *Nat. Commun.* **2019**, *10*, 3991. [CrossRef]
53. Yuki, K.; Cheng, N.; Nakano, M.; Kuo, C.J. Organoid Models of Tumor Immunology. *Trends Immunol.* **2020**, *41*, 652–664. [CrossRef]
54. Janmey, P.A.; Winer, J.P.; Weisel, J.W. Fibrin Gels and Their Clinical and Bioengineering Applications. *J. R. Soc. Interface* **2009**, *6*, 1–10. [CrossRef] [PubMed]
55. Singh, S.K.; Clarke, I.D.; Terasaki, M.; Bonn, V.E.; Hawkins, C.; Squire, J.; Dirks, P.B. Identification of a Cancer Stem Cell in Human Brain Tumors. *Cancer Res.* **2003**, *63*, 5821–5828. [PubMed]
56. Gimona, M.; Buccione, R.; Courtneidge, S.A.; Linder, S. Assembly and Biological Role of Podosomes and Invadopodia. *Curr. Opin. Cell Biol.* **2008**, *20*, 235–241. [CrossRef]
57. Friedl, P.; Alexander, S. Cancer Invasion and the Microenvironment: Plasticity and Reciprocity. *Cell* **2011**, *147*, 992–1009. [CrossRef]
58. Anderson, A.R.; Weaver, A.M.; Cummings, P.T.; Quaranta, V. Tumor Morphology and Phenotypic Evolution Driven by Selective Pressure from the Microenvironment. *Cell* **2006**, *127*, 905–915. [CrossRef]
59. Miki, J.; Furusato, B.; Li, H.; Gu, Y.; Takahashi, H.; Egawa, S.; Sesterhenn, I.A.; McLeod, D.G.; Srivastava, S.; Rhim, J.S. Identification of Putative Stem Cell Markers, CD133 and CXCR4, in hTERT-Immortalized Primary Nonmalignant and Malignant

Tumor-Derived Human Prostate Epithelial Cell Lines and in Prostate Cancer Specimens. *Cancer Res.* **2007**, *67*, 3153–3161. [CrossRef]
60. Fendler, A.; Bauer, D.; Busch, J.; Jung, K.; Wulf-Goldenberg, A.; Kunz, S.; Song, K.; Myszczyszyn, A.; Elezkurtaj, S.; Erguen, B.; et al. Inhibiting WNT and NOTCH in Renal Cancer Stem Cells and the Implications for Human Patients. *Nat. Commun.* **2020**, *11*, 929. [CrossRef]
61. Egeblad, M.; Nakasone, E.S.; Werb, Z. Tumors as organs: Complex Tissues that Interface with the Entire Organism. *Dev. Cell* **2010**, *18*, 884–901. [CrossRef] [PubMed]
62. Shen, C.; Kaelin, W.G., Jr. The VHL/HIF Axis in Clear Cell Renal Carcinoma. *Semin. Cancer Biol.* **2013**, *23*, 18–25. [CrossRef] [PubMed]
63. Wang, Z.; Dabrosin, C.; Yin, X.; Fuster, M.M.; Arreola, A.; Rathmell, W.K.; Generali, D.; Nagaraju, G.P.; El-Rayes, B.; Ribatti, D.; et al. Broad Targeting of Angiogenesis for Cancer Prevention and Therapy. *Semin. Cancer Biol.* **2015**, *35*, S224–S243. [CrossRef] [PubMed]
64. Rini, B.I.; Battle, D.; Figlin, R.A.; George, D.J.; Hammers, H.; Hutson, T.; Jonasch, E.; Joseph, R.W.; McDermott, D.F.; Motzer, R.J.; et al. The Society for Immunotherapy of Cancer Consensus Statement on Immunotherapy for the Treatment of Advanced Renal Cell Carcinoma (RCC). *J. Immunother. Cancer* **2019**, *7*, 354. [CrossRef] [PubMed]
65. De Palma, M.; Biziato, D.; Petrova, T.V. Microenvironmental Regulation of Tumour Angiogenesis. *Nat. Rev. Cancer* **2017**, *17*, 457–474. [CrossRef] [PubMed]
66. Flavell, R.A.; Sanjabi, S.; Wrzesinski, S.H.; Licona-Limón, P. The Polarization of Immune Cells in the Tumour Environment by TGFbeta. *Nat. Rev. Immunol.* **2010**, *10*, 554–567. [CrossRef]
67. Yang, X.; Lin, Y.; Shi, Y.; Li, B.; Liu, W.; Yin, W.; Dang, Y.; Chu, Y.; Fan, J.; He, R. FAP Promotes Immunosuppression by Cancer-Associated Fibroblasts in the Tumor Microenvironment via STAT3-CCL2 Signaling. *Cancer Res.* **2016**, *76*, 4124–4135. [CrossRef]
68. Esser, L.K.; Branchi, V.; Leonardelli, S.; Pelusi, N.; Simon, A.G.; Klümper, N.; Ellinger, J.; Hauser, S.; Gonzalez-Carmona, M.A.; Ritter, M.; et al. Cultivation of Clear Cell Renal Cell Carcinoma Patient-Derived Organoids in an Air-Liquid Interface System as a Tool for Studying Individualized Therapy. *Front. Oncol.* **2020**, *10*, 1775. [CrossRef]
69. Batchelder, C.A.; Martinez, M.L.; Duru, N.; Meyers, F.J.; Tarantal, A.F. Three Dimensional Culture of Human Renal Cell Carcinoma Organoids. *PLoS ONE* **2015**, *10*, e0136758. [CrossRef]
70. Motrescu, E.R.; Blaise, S.; Etique, N.; Messaddeq, N.; Chenard, M.P.; Stoll, I.; Tomasetto, C.; Rio, M.C. Matrix Metalloproteinase-11/Stromelysin-3 Exhibits Collagenolytic Function against Collagen VI under Normal and Malignant Conditions. *Oncogene* **2008**, *27*, 6347–6355. [CrossRef] [PubMed]
71. Nanda, A.; Carson-Walter, E.B.; Seaman, S.; Barber, T.D.; Stampfl, J.; Singh, S.; Vogelstein, B.; Kinzler, K.W.; St Croix, B. TEM8 Interacts with the Cleaved C5 Domain of Collagen Alpha 3(VI). *Cancer Res.* **2004**, *64*, 817–820. [CrossRef]
72. Iyengar, P.; Espina, V.; Williams, T.W.; Lin, Y.; Berry, D.; Jelicks, L.A.; Lee, H.; Temple, K.; Graves, R.; Pollard, J.; et al. Adipocyte-Derived Collagen VI Affects Early Mammary Tumor Progression in Vivo, Demonstrating a Critical Interaction in the Tumor/Stroma Microenvironment. *J. Clin. Investig.* **2005**, *115*, 1163–1176. [CrossRef]
73. Rühl, M.; Sahin, E.; Johannsen, M.; Somasundaram, R.; Manski, D.; Riecken, E.O.; Schuppan, D. Soluble Collagen VI Drives Serum-Starved Fibroblasts through S Phase and Prevents Apoptosis via Down-Regulation of Bax. *J. Biol. Chem.* **1999**, *274*, 34361–34368. [CrossRef] [PubMed]
74. You, W.K.; Bonaldo, P.; Stallcup, W.B. Collagen VI Ablation Retards Brain Tumor Progression due to Deficits in Assembly of the Vascular Basal Lamina. *Am. J. Pathol.* **2012**, *180*, 1145–1158. [CrossRef] [PubMed]
75. Wan, F.; Wang, H.; Shen, Y.; Zhang, H.; Shi, G.; Zhu, Y.; Dai, B.; Ye, D. Upregulation of COL6A1 Is Predictive of Poor Prognosis in Clear Cell Renal Cell Carcinoma Patients. *Oncotarget* **2015**, *6*, 27378–27387. [CrossRef]
76. Han, S.W.; Roman, J. Fibronectin Induces Cell Proliferation and Inhibits Apoptosis in Human Bronchial Epithelial Cells: Pro-oncogenic Effects Mediated by PI3-Kinase and NF-Kappa B. *Oncogene* **2006**, *25*, 4341–4349. [CrossRef] [PubMed]
77. Han, S.; Khuri, F.R.; Roman, J. Fibronectin Stimulates Non-Small Cell Lung Carcinoma Cell Growth through Activation of Akt/Mammalian Target of Rapamycin/S6 Kinase and Inactivation of LKB1/AMP-Activated Protein Kinase Signal Pathways. *Cancer Res.* **2006**, *66*, 315–323. [CrossRef]
78. Huang, W.; Chiquet-Ehrismann, R.; Moyano, J.V.; Garcia-Pardo, A.; Orend, G. Interference of Tenascin-C with Syndecan-4 Binding to Fibronectin Blocks Cell Adhesion and Stimulates Tumor Cell Proliferation. *Cancer Res.* **2001**, *61*, 8586–8594.
79. Yoshida, T.; Yoshimura, E.; Numata, H.; Sakakura, Y.; Sakakura, T. Involvement of Tenascin-C in Proliferation and Migration of Laryngeal Carcinoma Cells. *Virchows Arch.* **1999**, *435*, 496–500. [CrossRef]
80. Guo, S.K.; Shen, M.F.; Yao, H.W.; Liu, Y.S. Enhanced Expression of TGFBI Promotes the Proliferation and Migration of Glioma Cells. *Cell Physiol. Biochem.* **2018**, *49*, 1097–1109. [CrossRef]
81. Bao, S.; Ouyang, G.; Bai, X.; Huang, Z.; Ma, C.; Liu, M.; Shao, R.; Anderson, R.M.; Rich, J.N.; Wang, X.F. Periostin Potently Promotes Metastatic Growth of Colon Cancer by Augmenting Cell Survival via the Akt/PKB Pathway. *Cancer Cell* **2004**, *5*, 329–339. [CrossRef]
82. Jia, Y.Y.; Yu, Y.; Li, H.J. POSTN Promotes Proliferation and Epithelial-Mesenchymal Transition in Renal Cell Carcinoma through ILK/AKT/mTOR Pathway. *J. Cancer* **2021**, *12*, 4183–4195. [CrossRef] [PubMed]

83. Levental, K.R.; Yu, H.; Kass, L.; Lakins, J.N.; Egeblad, M.; Erler, J.T.; Fong, S.F.; Csiszar, K.; Giaccia, A.; Weninger, W.; et al. Matrix Crosslinking Forces Tumor Progression by Enhancing Integrin Signaling. *Cell* **2009**, *139*, 891–906. [CrossRef] [PubMed]
84. Abbott, A.; Bond, K.; Chiba, T.; Sims-Lucas, S.; Oxburgh, L.; Coburn, J.M. Development of a Mechanically Matched Silk Scaffolded 3D Clear Cell Renal Cell Carcinoma Model. *Mater. Sci. Eng. C Mater. Biol. Appl.* **2021**, *126*, 112141. [CrossRef]
85. Mitchell, T.J.; Turajlic, S.; Rowan, A.; Nicol, D.; Farmery, J.H.R.; O'Brien, T.; Martincorena, I.; Tarpey, P.; Angelopoulos, N.; Yates, L.R.; et al. Timing the Landmark Events in the Evolution of Clear Cell Renal Cell Cancer: TRACERx Renal. *Cell* **2018**, *173*, 611–623.e17. [CrossRef] [PubMed]
86. De Wever, O.; Demetter, P.; Mareel, M.; Bracke, M. Stromal Myofibroblasts Are Drivers of Invasive Cancer Growth. *Int. J. Cancer* **2008**, *123*, 2229–2238. [CrossRef]
87. Siljee, S.; Milne, B.; Brasch, H.D.; Bockett, N.; Patel, J.; Davis, P.F.; Kennedy-Smith, A.; Itinteang, T.; Tan, S.T. Expression of Components of the Renin-Angiotensin System by Cancer Stem Cells in Renal Clear Cell Carcinoma. *Biomolecules* **2021**, *11*, 537. [CrossRef]
88. Everett, A.D.; Carey, R.M.; Chevalier, R.L.; Peach, M.J.; Gomez, R.A. Renin Release and Gene Expression in Intact Rat Kidney Microvessels and Single Cells. *J. Clin. Investig.* **1990**, *86*, 169–175. [CrossRef]
89. Sequeira López, M.L.; Pentz, E.S.; Nomasa, T.; Smithies, O.; Gomez, R.A. Renin Cells Are Precursors for Multiple Cell Types That Switch to the Renin Phenotype When Homeostasis Is Threatened. *Dev. Cell* **2004**, *6*, 719–728. [CrossRef]
90. McKay, R.R.; Rodriguez, G.E.; Lin, X.; Kaymakcalan, M.D.; Hamnvik, O.P.; Sabbisetti, V.S.; Bhatt, R.S.; Simantov, R.; Choueiri, T.K. Angiotensin System Inhibitors and Survival Outcomes in Patients with Metastatic Renal Cell Carcinoma. *Clin. Cancer Res.* **2015**, *21*, 2471–2479. [CrossRef]
91. Khanna, P.; Soh, H.J.; Chen, C.H.; Saxena, R.; Amin, S.; Naughton, M.; Joslin, P.N.; Moore, A.; Bakouny, Z.; O'Callaghan, C.; et al. ACE2 Abrogates Tumor Resistance to VEGFR Inhibitors Suggesting Angiotensin-(1–7) as a Therapy for Clear Cell Renal Cell Carcinoma. *Sci. Transl. Med.* **2021**, *13*, eabc0170. [CrossRef] [PubMed]

cancers

MDPI

Article

Targets for Renal Carcinoma Growth Control Identified by Screening FOXD1 Cell Proliferation Pathways

Kyle H. Bond [1], Sunder Sims-Lucas [2] and Leif Oxburgh [1,*]

[1] Rogosin Institute, Room 2-43, 310 East 67th St., New York, NY 10065, USA
[2] Children's Hospital of Pittsburgh, Rangos Research Building, 4401 Penn Ave, Pittsburgh, PA 15224, USA
* Correspondence: leo9022@nyp.org

Simple Summary: FOXD1 regulates the proliferation of clear cell renal cell carcinoma (ccRCC) cells, and ccRCC cells in which *FOXD1* has been inactivated do not form tumors efficiently in an animal model. Reproducing growth inhibition in tumor cells by inhibiting FOXD1 pathways presents a possible therapeutic approach for ccRCC and other cancers. We have established an analysis strategy to identify *FOXD1*-regulated target pathways that may be therapeutically tractable, and compounds that modulate these pathways were selected for testing. Targets in three pathways were identified: FOXM1, PME1, and TMEM167A, which were inhibited by compounds FDI-6, AMZ-30, and silibinin, respectively. The effects of these compounds on the growth of tumor cells from patients cultured in a novel 3D tumor-replica culture environment revealed that FDI-6 and silibinin had strong growth inhibitory effects. This investigation informs new therapeutic targets to control ccRCC tumor growth, and provides a strategy to compare the responsiveness of individual patient tumor replicas to growth-inhibitory compounds.

Abstract: Clinical association studies suggest that FOXD1 is a determinant of patient outcome in clear cell renal cell carcinoma (ccRCC), and laboratory investigations have defined a role for this transcription factor in controlling the growth of tumors through regulation of the G2/M cell cycle transition. We hypothesized that the identification of pathways downstream of FOXD1 may define candidates for pharmacological modulation to suppress the G2/M transition in ccRCC. We developed an analysis pipeline that utilizes RNA sequencing, transcription factor binding site analysis, and phenotype validation to identify candidate effectors downstream from FOXD1. Compounds that modulate candidate pathways were tested for their ability to cause growth delay at G2/M. Three targets were identified: FOXM1, PME1, and TMEM167A, which were targeted by compounds FDI-6, AMZ-30, and silibinin, respectively. A 3D ccRCC tumor replica model was used to investigate the effects of these compounds on the growth of primary cells from five patients. While silibinin reduced 3D growth in a subset of tumor replicas, FDI-6 reduced growth in all. This study identifies tractable pathways to target G2/M transition and inhibit ccRCC growth, demonstrates the applicability of these strategies across patient tumor replicas, and provides a platform for individualized patient testing of compounds that inhibit tumor growth.

Keywords: kidney cancer; FOXD1; FOXM1; PME1; TMEM167A; FDI-6; AMZ30; silibinin; cell cycle; bioengineering

check for updates

Citation: Bond, K.H.; Sims-Lucas, S.; Oxburgh, L. Targets for Renal Carcinoma Growth Control Identified by Screening FOXD1 Cell Proliferation Pathways. *Cancers* **2022**, *14*, 3958. https://doi.org/10.3390/cancers14163958

Academic Editors: Scott S. Tykodi and Evan T. Hall

Received: 16 June 2022
Accepted: 14 August 2022
Published: 16 August 2022

Publisher's Note: MDPI stays neutral with regard to jurisdictional claims in published maps and institutional affiliations.

Copyright: © 2022 by the authors. Licensee MDPI, Basel, Switzerland. This article is an open access article distributed under the terms and conditions of the Creative Commons Attribution (CC BY) license (https://creativecommons.org/licenses/by/4.0/).

1. Introduction

Clinical association studies and laboratory investigations have identified the FOXD1 transcription factor as a driver of tumor development. Understanding how this may be targeted has implications for a variety of cancers [1–4]. Due to the central role *Foxd1* plays in regulating the embryonic development of the kidney [5,6], we are interested in understanding its role in clear cell renal cell carcinoma (ccRCC), which is the most common form of kidney cancer. Renal cell carcinoma represents 3% of all tumors, with 75% of those

being ccRCC. Primary care for non-metastatic disease includes resection, while metastatic disease involves combinatorial adjuvant therapy using tyrosine kinase inhibitors (TKIs) and immune checkpoint inhibitors [7].

In previous work, we showed that *FOXD1* expression correlates with poor patient outcomes in ccRCC, that its inactivation in ccRCC cells delays progression through the G2/M phase of the cell cycle, and that *FOXD1* loss prevents tumor growth in a xenograft model [8]. Phosphorylation of CDC2 and histone H3 is perturbed by the loss of *FOXD1*, suggesting that FOXD1 expression is an adaptation in tumor cells that promotes their proliferation by enabling their progression through the G2/M checkpoint. *FOXD1* null tumor cells display aberrant cytokinesis and limited proliferation; replicating this phenotype in cancer cells presents an interesting therapeutic approach for ccRCC, and possibly other cancers. However, few strategies have been reported to directly target transcription factors in tumor cells. In the case of FOXD1, very little is known regarding its molecular functions, such as regulation by upstream kinases or interactions with other transcription factors, making it a particularly difficult target. A more tractable strategy is to modulate pathways regulated by FOXD1, and in this study we used a transcriptomic analysis to identify specific pathways downstream from FOXD1 that can be pharmacologically modulated to suppress the G2/M transition in ccRCC tumor cells.

An analysis pipeline was developed that utilizes RNA sequencing, transcription factor binding site analysis, and phenotype validation to identify candidate effectors downstream from FOXD1. We identified candidates with known functions related to the *FOXD1* null phenotype, and compounds that modulate their function were evaluated for their potential to replicate the cell cycle phenotype caused by the loss of *FOXD1*. A panel of patient-derived 3D tumor replicas was developed using a method recently described by our group to validate the effects of candidate compounds in clinically relevant models [9]. Our study uncovers FOXM1, PME1, and TMEM167A as potential targets for pharmaceutical intervention to slow ccRCC tumor cell growth and provides a strategy for patient-specific compound testing.

2. Materials and Methods

2.1. Cell Lines

The 786-O cell line was obtained from ATCC (ATCC CRL-1932). The 786-O^{FOXD1null} line was generated in our laboratory, as previously reported [8]. Cells were maintained in RPMI-1640 containing 10% FBS, 1% GlutaMax (Thermo Fisher, Waltham, MA, USA), and 1% Penicillin-Streptomycin, and were grown to 70–80% confluency on tissue culture-treated plates before experiments. Cells were detached from the plates using TrypLE Express (Thermo Fisher).

2.2. RNA Sequencing and Data Acquisition

RNA from 70% confluent plates of 786-O and 786-O^{FOXD1null} cells was extracted using a Qiagen RNeasy Microkit (Qiagen GmbH, Hilden, Germany). RNA purity was determined by measuring the 260/280 ratio in a Thermo Fisher Nanodrop. RNA quality was determined by running an RNA gel and analyzing the ratio between 28 S and 18 S. Samples with a 28 S/18 S ratio greater than 2.0 were submitted for RNA sequencing by Genewiz (Chelmsford, MA, USA). Pre-made total RNA libraries were prepared and sequenced using a HiSeq 2000 in 2 $\times$ 150 bp sequencing mode. Quality was assessed per base sequence, and mean quality was calculated. Quality scores greater than 30 were deemed acceptable for further downstream analysis. Primer and adaptor sequences were trimmed using Trimmomatic v.0.36, and only high-quality reads with $\geq$30 bp over a 4 bp sliding window based on the phred algorithm were accepted. Reads were aligned to the human genome build hg38, using STAR aligner v.2.5.2b with default settings for mammalian genomes. Unique gene hit counts were calculated using the featureCounts function from the Subread RNA-seq package v.1.5.2. This did not include intron or intergenic regions and used Gene ID as the identifier.

2.3. Gene Set Enrichment Analysis

Differentially expressed genes from RNA sequencing were ranked for fold change and analyzed using a gene set enrichment analysis (GSEA) [10]. Pathway interactions were mapped using the Reactome database [11]. Pathways and interactors were mapped using Cytoscape [12].

2.4. RNA-Seq Data Analysis

Uniquely mapped reads were analyzed for differential gene expression using DESeq2, comparing 786-O and 786-O^{FOXD1null}. Fold change and *p*-values were calculated using the Wald test. Only adjusted *p*-values less than or equal to 0.05 were considered "differentially expressed". Genes without *p*-values were deemed "uninterpretable" and discarded from further analysis. All other genes were labeled "equally expressed". Differentially expressed genes were divided into upregulated (foldchange >1) or downregulated (foldchange <1), and the top 100 most up- or downregulated genes were set aside for scoring. In parallel, the entire list of differentially expressed genes was analyzed for transcription factor binding sites using CiiiDER [13]. Briefly, transcription factor matrices from the JASPAR2020 database were mapped to the input gene list with the gene look-up manager (GLM) from the human genome atlas build hg38, using a deficit cutoff of 0.15 (15%). Genes with FOXD1 motifs were further analyzed for "clustered FOXD1" or FOXD1 binding motifs within 100 bp from each other. These "clustered FOXD1" targets were separated for further analysis as candidate FOXD1-regulated genes.

2.5. Conditioned Media Growth Rate Analysis

The 786-O and 786-O^{FOXD1null} cells were seeded into 15 cm dishes and allowed to grow to confluency. At confluency, the culture media was replaced and cultured for an additional 48 h. Conditioned media was collected and centrifuged at 14,000× *g* for 20 min at 4 °C to pellet any cell debris. Supernatant was collected and stored at 4 °C. For the growth assay, 5000 cells per well of 786-O or 786-O^{FOXD1null} cells were seeded into 24-well tissue culture plates in either conditioned media from 786-O or 786-O^{FOXD1null}. Every day after seeding, cells were collected from triplicate wells and counted. Media in remaining wells was changed daily. This was undertaken until day 7 and cell numbers were graphed using Excel.

2.6. Native ECM Growth Rate Analysis

Plates covered in native ECM from 786-O and 786-O^{FOXD1null} were derived following the protocol from Harris et al. [14]. In brief, 786-O or 786-O^{FOXD1null} were seeded at confluency into 24-well plates, then cultured for 5 days. Plates were washed twice with DPBS, and 3 times with wash buffer 1 (100 mM Na_2PO_4, 2 mM $MgCl_2$, 2 mM EGTA, pH 9.6). Cells were lysed twice with a lysis buffer (8 mM Na_2PO4, 1% NP-40, pH 9.6) for a total of 1 h and 30 min at 37 °C. Plates were then washed 3 times with wash buffer 2 (10 mM Na_2PO_4, 300 mM KCl, pH 7.5) and finally washed 4 times with sterile DI water. Plates were stored filled with DPBS at 4 °C until the assay. At the start of the assay, 70% confluent plates of 786-O and 786-O^{FOXD1null} were detached using TrypLE express, counted, and seeded into plates containing native ECM from 786-O or 786-O^{FOXD1null} at 5×10^4 cells per well. Every 24 h after seeding, triplicate wells were imaged, detached, and counted. Media was changed daily in all other wells. This was undertaken until day 7 and cell numbers were graphed using Excel.

2.7. Target Gene Selection

Genes selected from the RNA-seq analysis (top 100 up- and downregulated genes, genes with unclustered FOXD1 motifs from 15% cutoff analysis) were cross-referenced with the following databases: Mitotic G2-G2/M phases (Reactome R-HAS-453274) [15], Human kinome (Kinbase) [16], Matrisome [17], and Cell Adhesion (GO: 0007155) [18]. Scores were weighted as follows: Mitotic G2-G2/M phases = +2, Human kinome = +1,

Matrisome = +0.5, Cell Adhesion = +0.5. Genes that scored greater than or equal to a final score of 2 were assessed further for targetability. All candidates were divided into requiring either inhibition (log fold change >0) or activation (log fold change <0). Targets requiring inhibition were first searched online as follows: "Protein Name" + ("Inhibitor" OR "Antagonist"). If a specific inhibitor exists, the search ended, and the compound was added to the panel. For targets requiring activation, the Uniprot protein description was reviewed to identify if the protein was secreted or not. If yes, and a recombinant exists, it was added to the candidate panel. If not, an online search was conducted as follows: "Protein Name" + ("Activator" OR "Agonist"). If a specific activator or agonist exists, then it was added to the candidate panel. The final panel was further refined to remove secreted growth factors, extracellular matrix (ECM) components, and targets with known or contradictory effects based on the literature. All other targets from this analysis were not explored further in this study.

2.8. Compound Toxicity Screening

786-O cells were seeded into 96-well plates at 2×10^4 cells per well and cultured for 2 h at 37 °C. The 5- to 6-point dose-responses were determined based on the following: 1. IC50 (1×, 2×, 3×, 4×, 5×, and 50–100×), 2. ED50 (1×, 2×, 3×, 4×, 5×, and 50–100×), or 3. from reported working concentrations. Exact titrations are summarized in Table S2. Selected target compounds were prepared according to manufacturer specifications, diluted to selected dose ranges in the culture media, and added to wells in triplicate. Vehicle-treated controls were included in each plate. After 3 days, wells were stained with Hoechst 33342 and Ethidium Homodimer-1 for 30 min at room temperature. Wells were imaged using a Thermo Fisher EVOS microscope. Images were quantified for number of cells per well (# Hoechst 33342 stained nuclei) and number of dead cells (# Ethidium Homodimer-1-stained nuclei). Percent growth inhibition was calculated based on the average number of cells per well compared to untreated wells. Percent viability was calculated based on the average number of Ethidium Homodimer-1 negative cells to the average total number of cells. Pairwise comparisons between treatments and untreated wells were conducted using a Student's *t*-test, with *p*-values less than 0.05 designated as significant. The optimal dose per compound was chosen based on the greatest amount of inhibition without toxicity.

2.9. Synchronized Cell Cycle Analysis

The 786-O and 786-O^{FOXD1null} cells were seeded into culture treated dishes at 10.5×10^3 cells per cm^2 and cultured overnight at 37 °C. Cells were then treated with 2.5 mM thymidine in culture media for 16 h, followed by a media change and retreatment with 2.5 mM thymidine for an additional 9–12 h. One plate was left untreated as a control. Plates were then washed with DPBS 2 times before adding the culture media. One synchronized plate was collected and fixed at this point as a control. For treatments, media containing the different compounds selected from our dose-response analysis was added instead. Cells were cultured for 11 h at 37 °C and then lifted off the plates with TrypLE, centrifuged, and resuspended in 100 µL of the culture media. Following this, 900 µL of freezing 100% methanol was added drop-wise and cells were transferred to a −20 °C freezer and fixed for at least 2 h. Afterwards, cells were washed with MACS flow buffer (Miltenyi Biotec, Bergisch Gladbach, Germany) 3 times, then resuspended in 1 mL MACS flow buffer containing 50 µg/mL DAPI and incubated at 4 °C on a nutator overnight. Cells were washed 3 times with MACS flow buffer, resuspended in 400 µL of MACS flow buffer, and analyzed using Miltenyi MACSquant VYB flow cytometer. The G1 phase was determined by analyzing synchronized controls, in which all cells are in G1. The G2 phase was determined by doubling the value of suspected G1, while the S phase was all values in between.

2.10. 3D Cultures

Three-dimensional fibrin cultures of 786-O, 786-O^{FOXD1null}, and primary RCC cell lines were created following our previously reported protocol [9]. In summary, 3D cultures

were generated by combining fibrinogen (MilliporeSigma, Burlington, MA, USA cat#F8630) at a 1:1 ratio with cells suspended in a culture media, with or without the addition of ECM proteins. Thrombin (MilliporeSigma cat#10602370001) was added at a concentration of 0.002 U/μL at a volume equal to 10% of the total cell-fibrinogen mix, then immediately spotted onto glass coverslips at 5 μL per replicate. Three-dimensional cultures were immediately placed into a 37 °C cell culture incubator for 30 min to facilitate gelation. Pre-warmed cell culture media, with or without treatments, was then carefully added to wells.

2.11. Live/Dead Analysis

After 3 days of culture, the media was replaced with a live/dead staining solution containing 2 μM Calcein-AM and 4 μM Ethidium homodimer-1 (Etd1) in the culture media (Thermo Fisher cat#L3224) and incubated for 30 min in a culture incubator. In the final 8 min, Hoechst 33342 (Thermo Fisher cat# H3570) was added at a concentration of 5 μg/mL to each sample. Images were collected on an EVOS imaging system. Images were analyzed for Calcein-AM positivity to identify the number of cellular structures. Each structure was designated as either live (Calcein+) or dead (Ethd2+). Higher magnifications were taken to analyze the nuclear structure stained with Hoechst 33342. Comparisons between culture conditions were done via z-test.

2.12. 3D Culture Structure Analysis

Structures from images were analyzed using FIJI [19]. First, all channels were binarized using the threshold tool. Calcein images, which include the whole body of the cells, were used as regions of interest (ROIs). Descriptive statistics, including number of structures and area of each structure, were calculated using the measure tool. Comparisons between conditions were analyzed using a Student's *t*-test and z-test.

2.13. Nuclear Size Analysis

Nuclei from images were analyzed using FIJI. In brief, Hoechst 33342 stained nuclei were binarized using the threshold tool, the background was subtracted with the despeckle tool, and they were separated using the watershed tool. The pixel area of each nucleus was measured using the measure tool. Descriptive statistics were performed and comparisons between conditions was performed using a Student's *t*-test. Over 500 nuclei were analyzed per condition.

2.14. Tissue Processing

Kidney tumor tissue was obtained from surgical nephrectomies performed at the University of Pittsburgh Medical Center. Cancer diagnosis was performed by certified pathologists. Voluntary informed consent was obtained from patients for use of their tumors and diagnostic results in this research. All tissue specimens and associated medical information received were de-identified using an honest broker system. Samples were processed as previously described [9]. Fresh tumor tissue samples were diced and weighed. A total of 100 mg of tissue was digested in 20× volume DMEM containing 250 U/mL Collagenase IV (Thermo Fisher) + 0.02% Trypsin-EDTA at 37 °C in a shaking incubator set to 200 RPM for up to 2 h or until media became cloudy. The digest was stopped by adding an equal volume of ice cold DMEM containing 10% FBS. Any undigested material was filtered with 100 μM filter and placed in a vessel containing 5× volume TrypLE Express (Thermo Fisher) and returned to the 37 °C shaking incubator set to 220 RPM for an additional 15 min. Samples were pooled if necessary and centrifuged at 500× *g* for 7 min 30 s at 4 °C. Cells were washed with ice cold DMEM, counted, and their viability was determined using Trypan Blue exclusion. This was utilized for downstream assays or frozen in Nutrifreeze (Sartorius, Göttingen, Germany) freezing media. Patient samples used in this study are summarized in Table 1.

Table 1. Tissue samples used in this study. NA = not applicable.

	Diagnosis	Stage	Grade	Race	Gender/Age
Tp17-s322	Unclassified renal neoplasm	NA	NA	White	F/70–79
Tp17-s438	Unclassified renal neoplasm	2	3	White	F/30–39
Tp18-S453	Clear cell renal cell carcinoma	1	3	White	M/80–86
Tp18-s109	Clear cell renal cell carcinoma	3	2	White	M/60–60
Tp18-s114	Clear cell renal cell carcinoma	3	3	White	M/80–89
Tp20-s199	Clear cell renal cell carcinoma	3	2	NA	M/74
Tp20-s277	Leiomyosarcoma	3	NA	White	M/69

2.15. Primary Cell Culture

De-identified kidney tumors obtained through voluntary informed consent (as described in 2.14) were processed following our previously reported protocol [9]. Digested tumor cells were washed and resuspended at 1×10^6 cells/5 mL High Glucose DMEM containing 10% FBS, 1% GlutaMax (Thermo Fisher), 1% Penicillin-Streptomycin, 1% Non-Essential Amino Acids (Thermo Fisher), and 1% Sodium Pyruvate, and plated onto 5 cm tissue culture treated plates. Plates were incubated at 37 °C for 24 h before media change and imaging. Cells were monitored with media change every 72 h. After reaching 70–80% confluency, cells were expanded into a 10 cm tissue culture treated dish. Upon reaching 70–80% confluency, passaged cells were either frozen in freeze media or expanded for downstream applications. Three-dimensional cultures were established as previously reported [9].

2.16. Western Blot Analysis

Protein was collected from cell lines using a 1× Laemmli Buffer. Western Blotting was performed following manufacturer guidelines using the BioRad Western Blotting system (BioRad, Hercules, CA, USA). Blots were stained for beta-tubulin (Thermo Fisher MA5-16308), VHL (Cell Signaling Technologies, Danvers, MA, USA #68547), and HIF1α (R&D Systems, Minneapolis, MN, USA, AF1936). Molecular weight and densitometry analyses were performed using BioRad Imagelab software and normalized to beta-tubulin density.

3. Results

3.1. RNA-Seq Analysis Identifies Novel Targets Downstream of FOXD1

We have previously demonstrated that loss of FOXD1 in 786-O ccRCC cells causes impairment of the cell cycle, severely limiting their proliferation [8]. Knockout of *FOXD1* perturbs phosphorylation of the key cell cycle proteins CDC2 and histone H3 and dysregulates the G2/M transition. Comparison of 786-O and 786-O^{FOXD1null} transcriptomes has the potential to reveal transcriptional networks essential for G2/M control that may yield therapeutic targets; these could be either direct transcriptional targets of FOXD1, or genes in pathways downstream from direct targets that are mis-regulated by the loss of FOXD1.

Comparison of 786-O with 786-O^{FOXD1null} by RNA-seq revealed 5828 differentially expressed genes using a false discovery rate (FDR) and an adjusted p-value cutoff of 0.05. To prioritize a subset of these genes for downstream analysis, we used the selection pipeline shown in Figure 1. For our most stringently selected subset of potential direct FOXD1 targets, we identified genes with a FOXD1 binding motif (15% tolerance for mismatch of bases outside the core consensus sequence of the extended TFBS matrix) located within 1.5 kilobases upstream or 0.5 kilobases downstream of the locus [20]. Predicted FOXD1 binding motifs in differentially expressed genes were mapped using the CiiiDER tool for predicting

and analyzing transcription factor binding sites, resulting in a list of 4298 genes [13]. Clustering of transcription factor motifs associates with transcriptional control [21], and we identified a subset of 23 genes with two or more predicted FOXD1 motifs within 100 bases. This high stringency subset of differentially expressed genes were selected for downstream analysis (Table S1).

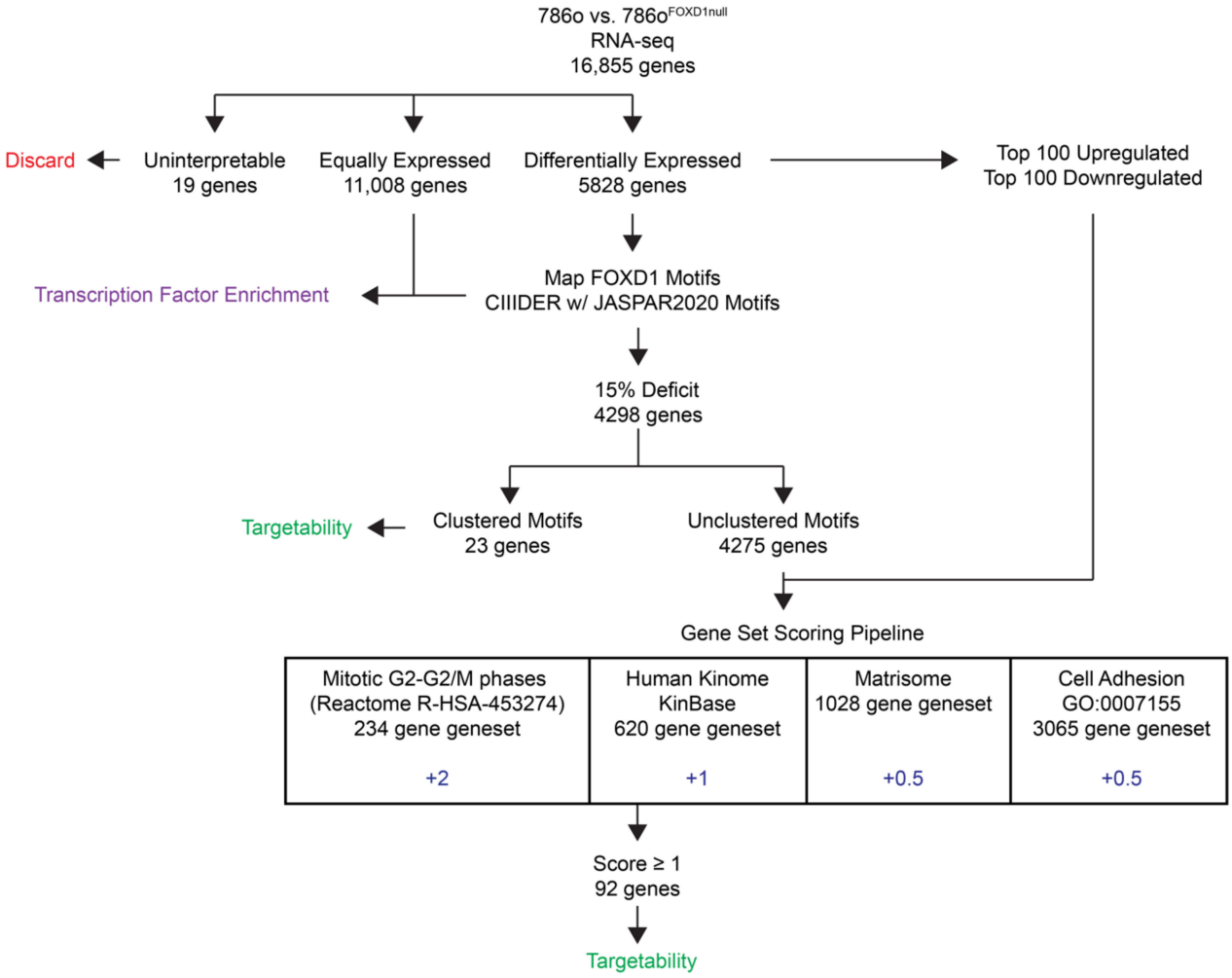

Figure 1. RNA-sequencing analysis and candidate selection.

In a second selection strategy, differentially expressed genes were manually cross-referenced to four databases representing cellular phenotypes that are perturbed following *FOXD1* inactivation, with the rationale that mis-regulation of any of these pathways may impair the G2/M transition. Databases included Mitotic G2-G2/M phases (Reactome R-HAS-453274) [15], Human kinome (Kinbase) [16], Matrisome [17], and Cell Adhesion (GO: 0007155) [18]. The top 100 upregulated and top 100 downregulated genes, based on log fold change and the remaining 4275 differentially expressed genes with predicted FOXD1 binding motifs, were screened in this manner. To weight our gene selection in favor of G2/M, we used the scoring system shown in Figure 1 to rank candidates. The 92 top-ranked genes were selected, and together with the 23 candidates with clustered FOXD1 binding sites, this generated a list of 110 candidates for downstream analysis (Table S1).

3.2. Exclusion of Secreted Factors

Candidates included genes in secreted signaling pathways, suggesting that autocrine signaling may be modified in *FOXD1* null cells. To test this hypothesis, we collected and purified conditioned media from both 786-O and 786-O^{FOXD1null} and performed a growth

rate analysis of cells grown in their own conditioned medium or in the medium of the other line (Figure 2A). Conditioned medium from either line did not reduce growth, indicating that changes in secreted factor signaling are not the cause of growth inhibition caused by the loss of FOXD1, and secreted factors were excluded from further analysis.

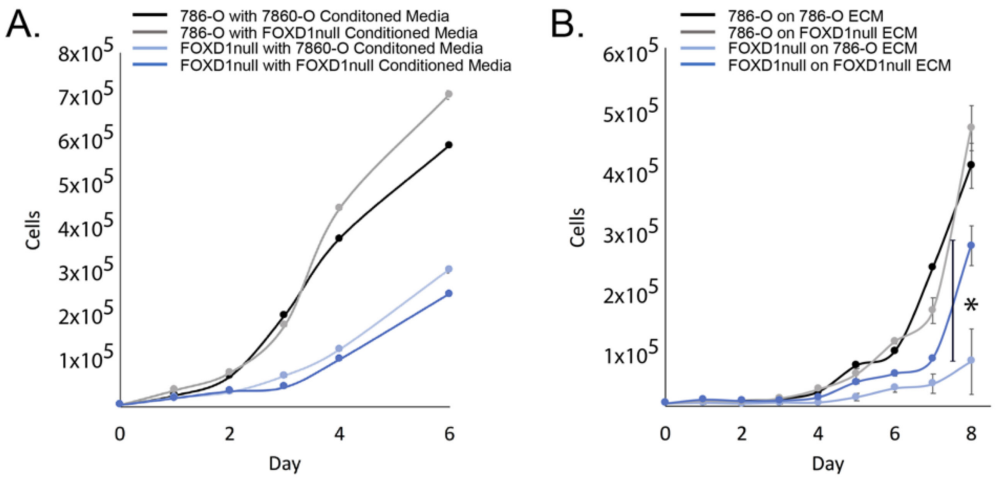

Figure 2. Exclusion of secreted factors and ECM from target discovery. (**A**) growth rate analysis of 786-O and 786-O^{FOXD1null} grown in conditioned media from 786-O or 786-O^{FOXD1null}; (**B**) growth rate analysis of 786-O and 786-O^{FOXD1null} grown on native decellularized ECM from 786-O or 786-O^{FOXD1null}. * = p-value < 0.05 by Student's t-test at end-point.

3.3. Exclusion of ECM

Candidates also included genes involved in formation and deposition of ECM. Appropriate attachment substrates can strongly influence cell division [22], and to test if aberrant ECM deposited by *FOXD1* null cells affects cell growth, we coated plates with native ECM from 786-O or 786-O^{FOXD1null} by decellularizing confluent plates of 786-O ECM or 786-O^{FOXD1null} as previously described [14]. We found that 786-O cells were unaffected by growth on 786-O^{FOXD1null} ECM, suggesting that changes in ECM composition in the 786-O^{FOXD1null} do not cause growth impairment. Interestingly, 786-O^{FOXD1null} were growth inhibited when cultured on 786-O ECM (Figure 2B). This series of experiments shows that the ECM deposited by 786-O^{FOXD1null} cells is itself not growth inhibitory, and based on this observation, we excluded ECM from further analysis.

3.4. Selection of Activators and Inhibitors

For the remaining 73 candidate genes, we manually searched for compounds that could be used to modulate their function in vitro. Since directionality of gene expression change was not used as a criterion for candidate gene selection, it was necessary to search both for inhibitors and activators, including recombinant proteins. Twelve candidate compounds that inhibit the products of genes downregulated in 786-O^{FOXD1null} and six candidate compounds that activate products of genes upregulated in 786-O^{FOXD1null} were selected for analysis for their potential to phenocopy the G2/M delay seen with the loss of FOXD1 (Table 2).

Table 2. Candidate compounds identified from transcriptome analysis.

#	Compound	Target	Action	Reference
1	WAY 170523	MMP13	INHIBIT	[23–25]
2	EED226	SUZ12	INHIBIT	[26,27]
3	APE1 Inhibitor III	APEX1	INHIBIT	[28]
4	Silibinin	TMEM167A	INHIBIT	[29]
5	Recombinant Netrin	UNC5B	ACTIVATE	[30]
6	CINPA 1	CXADR	INHIBIT	[31]
7	BITC	AGPS	INHIBIT	[32,33]
8	AMZ-30	PME1	INHIBIT	[34]
9	FDI-6	FOXM1	INHIBIT	[35,36]
10	CPI-637	EP300	INHIBIT	[37]
11	Anti-Galectin-9 Antibody	LGALS9	INHIBIT	[38,39]
12	Recombinant Sonic Hedgehog/Shh	HHIP	INHIBIT	[40,41]
13	C5OH	S100P	INHIBIT	[25,42,43]
14	Recombinant C1qTNF1	C1QTNF1	ACTIVATE	[44]
15	Recombinant Angiopoietin-like 4	ANGPTL4	ACTIVATE	[45]
16	Recombinant CXCL5/ENA-7	CXCL5	ACTIVATE	[46]
17	Recombinant Semaphorin 3C	SEMA3C	ACTIVATE	[47]
18	Recombinant LTBP1	LTBP1	ACTIVATE	[48]

3.5. Inhibition of Cell Growth with Minimal Toxicity by Compounds Targeting Candidate Genes

To assess if any of these targets can mimic the phenotype seen in 786-O^{FOXD1null}, we screened all candidate compounds in a dose-response study. Doses were chosen based on IC50, EC50, or literature-reported concentrations summarized in Table S2. Cells were treated for three days to assess growth inhibition and toxicity, which we defined as a significant increase in cell death compared with the vehicle-treated control. At the end-point, wells were stained for the nuclear marker Hoechst 33342 and dead cell marker Ethidium homodimer-1. Cell number per well was counted and percent cell death was calculated. As our goal was to replicate the *FOXD1* null G2/M phenotype, our target for each compound was the concentration at which cell number was reduced without overt cell death, indicating an effect on proliferation rather than cytotoxicity. To control for the possibility that the viable cell count may be lowered by cell death prior to harvest, we quantified death in all cells in the culture including those floating in the medium. Of the tested compounds, 10 showed significant reduction in cell growth compared to untreated controls, without significant toxicity (93 $\pm$ 5% viable) (Figure 3).

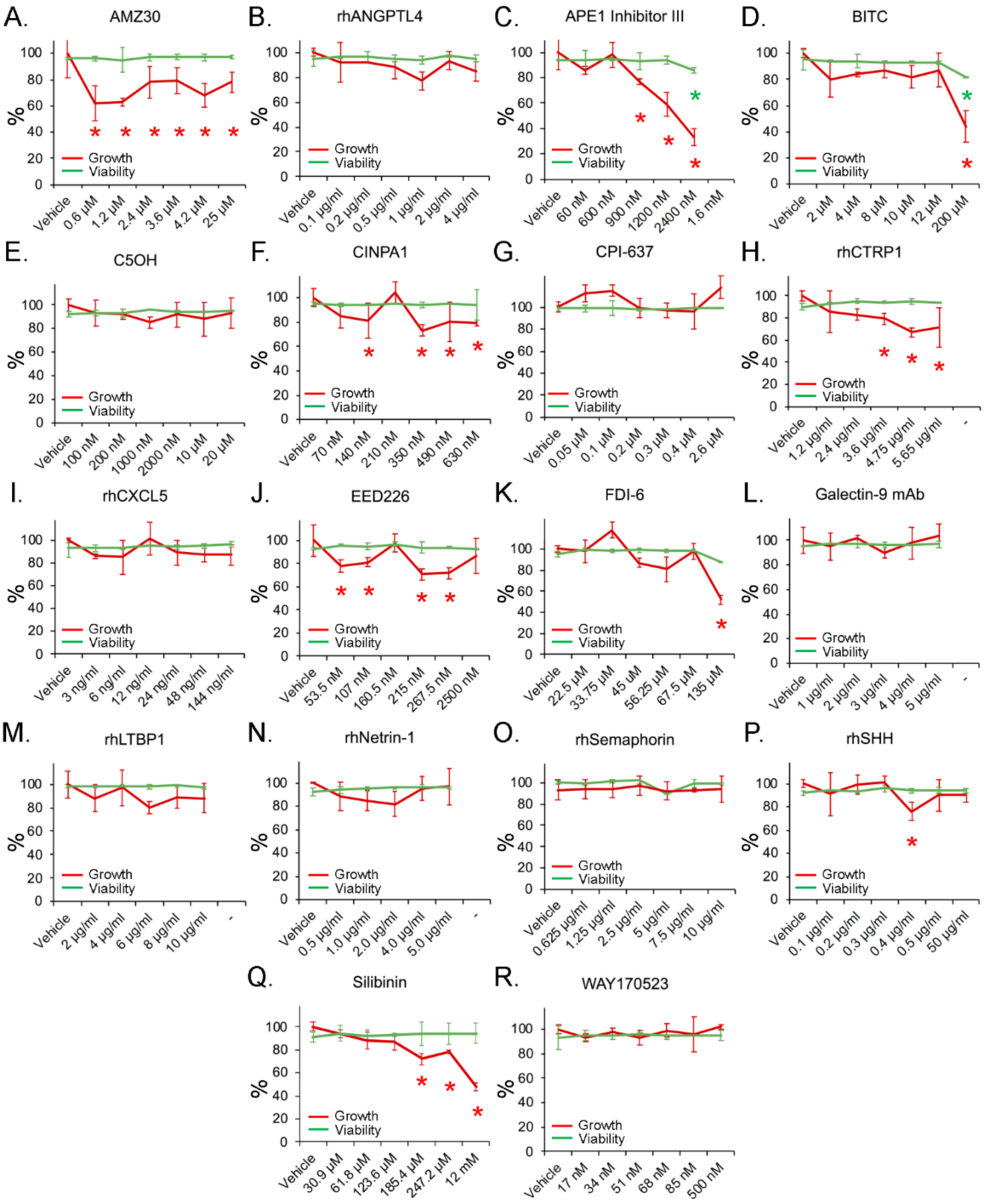

Figure 3. Cell growth and viability screen of compound-treated 786-O cells cultured for three days. (**A**–**R**) cells treated with compounds at doses specified on *x*-axis. Percentage growth (red line) was calculated based on the average number of Hoechst 33342$^+$ cells in each condition. Percentage viability (green line) was calculated based on the average proportion of Ethidium Homodimer-1 positive nuclei to negative nuclei. Color matched asterisks indicate significance compared to vehicle control, as determined by a Student's *t*-test.

3.6. Selection of Candidate Compounds That Induce Cell Cycle Arrest Resembling the Effect of FOXD1 Inactivation

To determine if growth reduction is due to growth arrest at G2/M, we synchronized cells using the double thymidine block method. We previously showed that after synchro-

nization, it took 786-O cells 12 h to complete the cell cycle, while 786-O^{FOXD1null} required 14 h [8]. After synchronizing cells, we allowed them to proceed through the cell cycle and treated them with the maximal tolerated dose of each compound that was shown to inhibit growth without significant effect on viability. Cells were cultured for 10 h, at which point we measured the ratio between cells at G1 and G2/M to assess if any compound recapitulates 786-O^{FOXD1null} growth delay (Figure 4). The 786-O^{FOXD1null} cells were included in the analysis for direct comparison. Three compounds showed an increase in distribution of cells at G2/M when compared to 786-O 11h after lifting the thymidine block: 3 µM AMZ30, 135 µM FDI-6, and 247.2 µM silibinin. Others showed effects on the S-phase transition (0.8 µg/mL recombinant ANGPTL4, 24 µM APE inhibitor III, 2 µM BITC, 0.2 µg/mL recombinant SHH), but were excluded from further analysis as our focus was on reproducing the effect of *FOXD1* loss on G2/M.

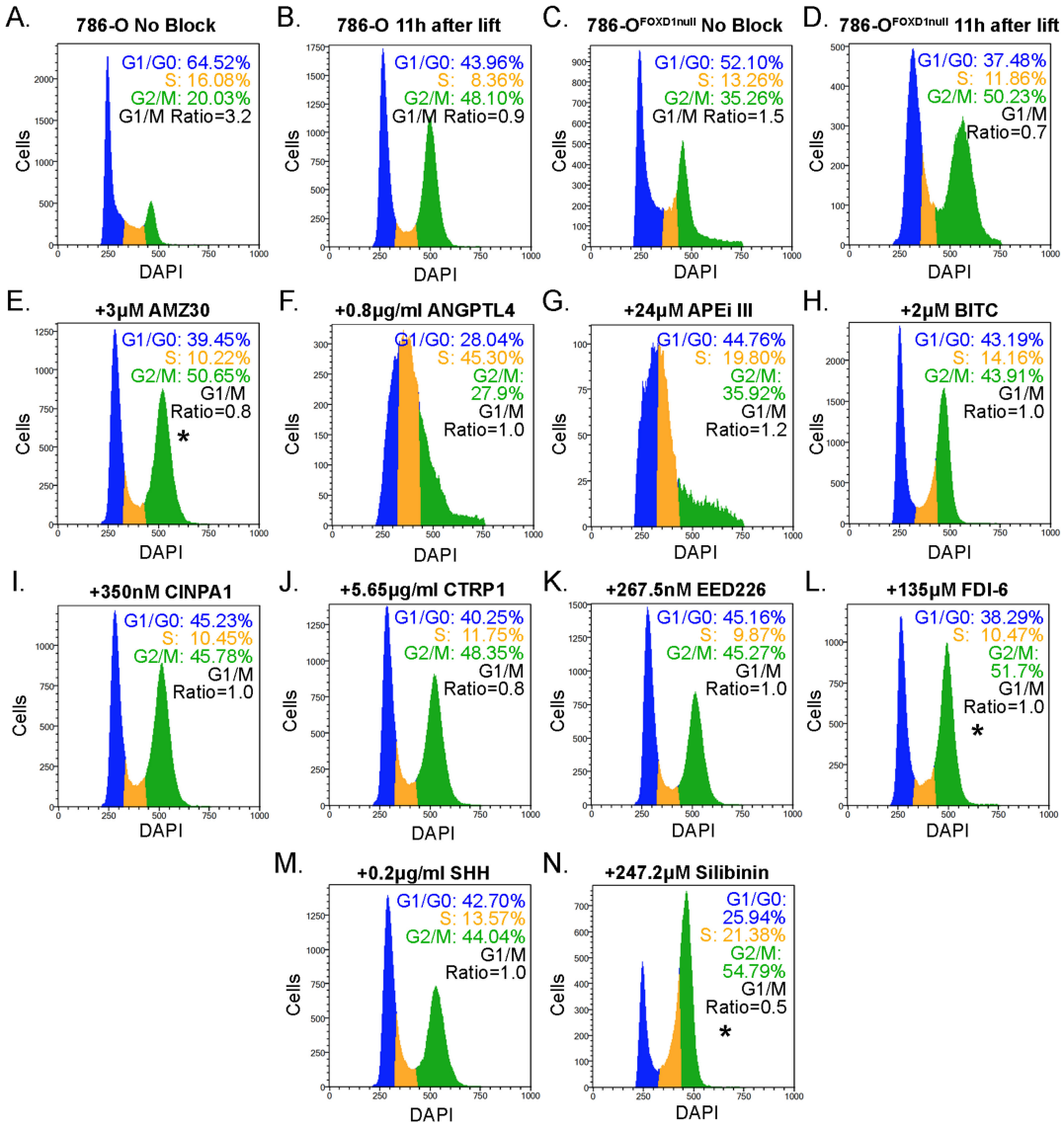

Figure 4. Synchronized cell cycle analysis identifies targets that inhibit G2/M progression. (**A**–**D**) untreated controls were compared to non-synchronized cells to confirm that the blocking and lifting strategy worked as predicted. (**E**–**N**) synchronized cells were treated with indicated treatment upon removal from the block and allowed to grow for 11 h. Fixed cells were analyzed for cell cycle distribution using DAPI, and the distribution of cells at G2/M was compared to untreated. * indicates $p < 0.05$ by a Student's *t*-test.

3.7. FOXD1 Inactivation Affects Three-Dimensional Growth

Three-dimensional (3D) culture provides a cellular environment with higher physiological fidelity than monolayer growth, particularly with regard to growth and proliferation characteristics. To extend our analysis of the growth-limiting effects of compounds selected in our screen, we established 3D growth models using a cell culture system developed in our laboratory to mimic the specific ECM environment of ccRCC in 3D [9]. In brief, cells are scaffolded in a fibrin hydrogel containing a combination of nine ECM components characteristic of ccRCC including fibronectin, collagen 6, and tenascin C, where their invasive versus colony-forming growth can be followed by light microscopy. The 786-O cells displayed an invasive phenotype in the 3D culture system, whereas the 786-O^{FOXD1null} cells grew in round, expansive clusters, and did not display an invasive phenotype (Figure 5). We have previously shown that this 3D culture system can be used to generate replicas of ccRCC tumors from patients [2], providing an opportunity to test the potential of candidate compounds to inhibit growth of patient tumor replicas in addition to testing effects on characteristic 786-O 3D growth.

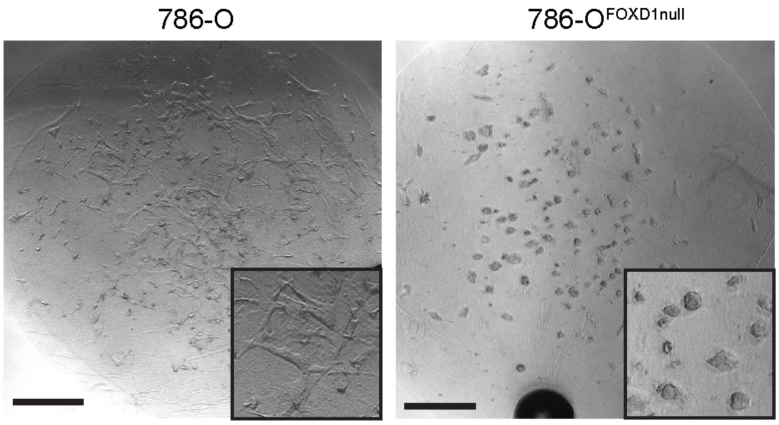

Figure 5. 786-O 3D growth. 786-O (**left**) or 786-O^{FOXD1null} (**right**) 3D cultures grown in fibrin/Tumor ECM. Inset images show higher magnification to detail structural differences in cell colony growth. Scalebar = 500 microns.

3.8. Treatment-Induced Growth Delay Affects 3D Growth and Nuclear Structure of 786-O Cells

Morphological differences between 3D-cultured 786-O and 786-O^{FOXD1null} included both changes in cell colony shape and changes in the shapes of individual nuclei within colonies. We used these two independent parameters to measure the effects of our candidate compounds on the 3D growth of 786-O cells. Three-dimensional cultures of 786-O cells were treated with 3 µM AMZ30, 135 µM FDI-6, and 247.2 µM silibinin, and were compared to 786-O^{FOXD1null}. After three days of culture, cells were stained with the nuclear dye Hoechst 33342, the live-cell dye Calcein-AM, and the dead-cell marker Ethidium homodimer-1. Compared with control 786-O, compound-treated 786-O showed growth perturbations (Figure 6A–E). Cultures treated with AMZ30 and silibinin showed larger cell colony sizes (similar to 786-O^{FOXD1null}), while FDI-6 had the opposite effect, promoting the growth of smaller and rounder cell colonies compared to the untreated cultures (Figure 6F). By quantifying the number of colonies in each 3D culture, we can see a significant increase in number following treatment with FDI-6 and silibinin, similar to 786-O^{FOXD1null} (Figure 6G).

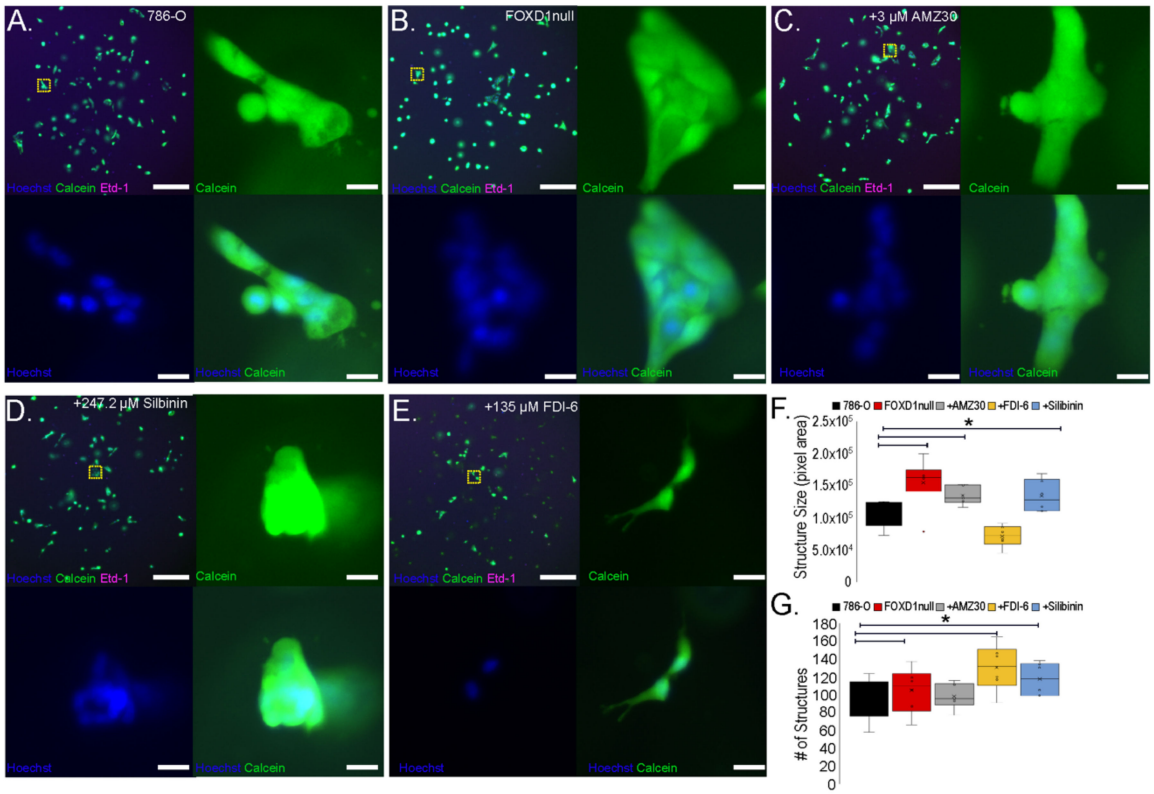

Figure 6. Effects of candidate compounds on 3D growth of 786-O tumor cells. (**A**–**E**) the 786-O 3D cultures were treated with specified compounds and allowed to grow for three days. Three-dimensional cultures were then stained for nuclei (Hoechst 33342 (blue)), viability (Calcein-AM (green)), and death (Ethidium homodimer-1 (magenta)). Upper left panels are widefield images (scalebar = 500 microns). Upper right, bottom left, and bottom right panels show split channels of representative cell colonies outlined in the widefield image (yellow box). The scalebar for higher magnification images is 20 microns. (**F**) the size distribution of Calcein-AM$^+$ cell colonies was quantified. * = p-value < 0.05 calculated by Z-test. (**G**) The total number of Calcein-AM$^+$ cell colonies in each culture was quantified. * = p-value < 0.05 calculated by Z-test. X = median, line through box = average.

Loss of *FOXD1* leads to an increase in cells at G2 with large nuclei, as well as an increase in cells with mitotic defects and nuclear fragmentation [9]. Considering that our compounds were selected to mimic the 786-O^{FOXD1null} phenotype, we hypothesized that the analysis of nuclear morphology of treated cultures would be informative (Figure 7A–F). Compared with 786-O, 786-O^{FOXD1null} cultures contain cells with larger nuclei (2.6-fold increase), with some evidence of nuclear defects (Figure 7A,B,F). Similarly, increased nuclear size was found following treatment with silibinin (1.36-fold increase) (Figure 7E). In contrast, treatment with AMZ30 and FDI-6 caused a reduction in nuclear size in the 786-O cells (1.4-fold and 2-fold decrease) (Figure 7C,D,F). In both treatments, nuclear mitotic defects were apparent in subsets of cells (115/186 nuclei: 62% fragmented) and with FDI-6, a large proportion of cells were anuclear, with darkened, protruding cell bodies (191/377 cells: 51%) (Figure 7D).

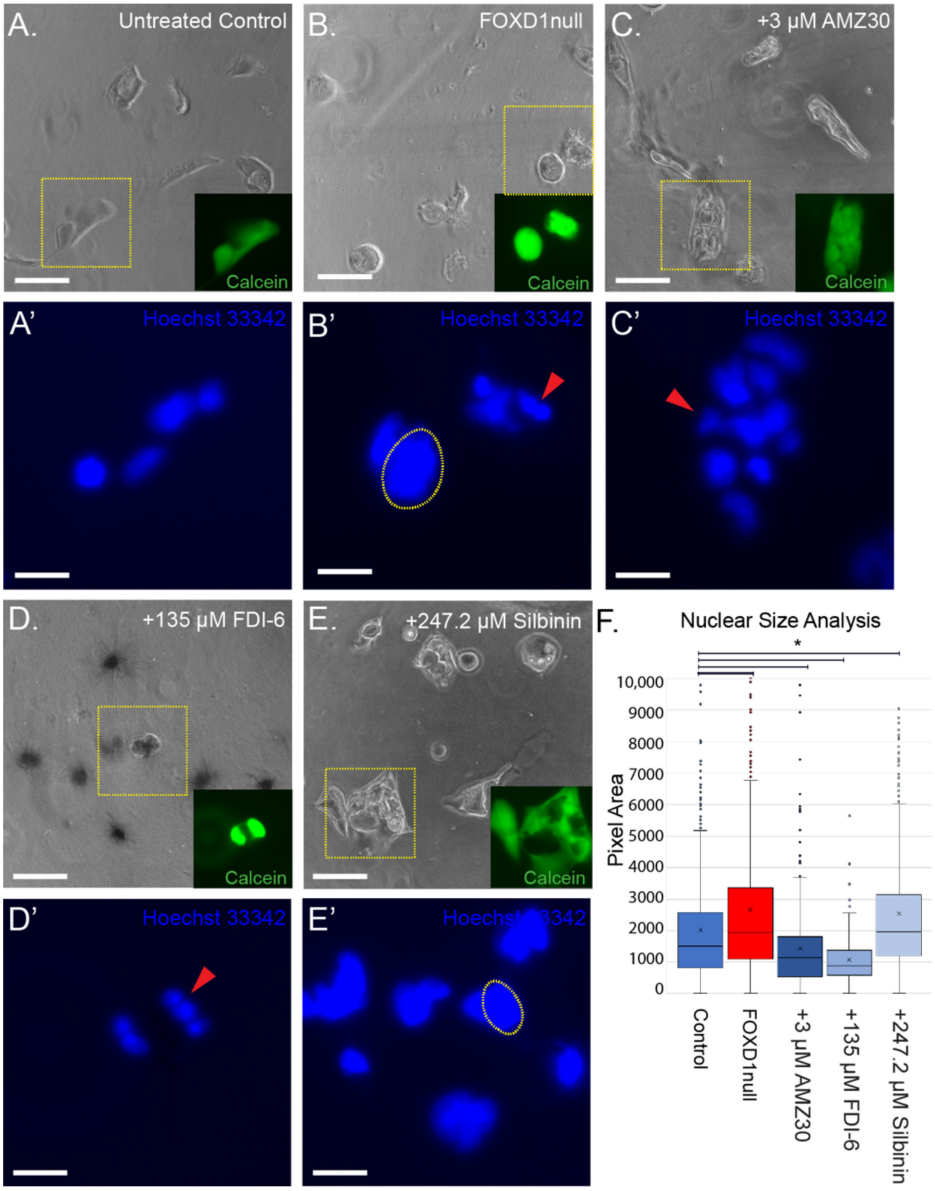

Figure 7. Effects of candidate compounds on nuclear structure in 786-O tumor cells grown in 3D culture. (**A**–**E**) images of 3D cultures treated with each candidate compound. Yellow box shows representative cell colony and inlay shows Calcein-AM (green) staining of that colony. Scalebar = 100 microns. (**A′**–**E′**) Hoechst 33,342 nuclear staining of cell colonies in yellow boxes in (**A**–**E**). Yellow-dotted outlines highlight enlarged nuclei. Red arrows indicate nuclear defects causing reduced nucleus size. Scalebar = 20 microns. (**F**) quantification of nuclear size in each treatment. * = $p < 0.05$ by Z-test. X = median, line through box = average. Circles outside the box are outliers.

In summary, 3D growth and nuclear morphology of 786-O were strongly affected by inhibiting PME-1 (AMZ30), FOXM1 (FDI-6), and TMEM16A (silibinin), replicating aspects of the *FOXD1* loss of function phenotype in these cells. A summary of the findings is presented in Table 3. No one candidate entirely phenocopied 786-O^{FOXD1null}; silibinin replicated most aspects of the phenotype, while FDI-6 had a distinct but severe effect on nuclear morphology. Our transcriptome analysis suggests that loss of *FOXD1* perturbs numerous pathways (Table S1), and the finding that candidate compounds targeting individual pathways downstream from FOXD1 replicate discrete aspects of the phenotype is anticipated.

Table 3. Key FOXD1 related effects analyzed in 786-O cells. Summary of results from analysis of 3D growth of 786-O treated with chosen compounds compared to 786-O^{FOXD1,} with descriptions. + = less, ++ = more, +++ = most.

	786-O	FOXD1 null	+AMZ30	+Silibinin	+FDI6
# of Structures	+	++	+	+++	++
Colony Size	++	+++	+++	++	+
Colony Morphology	**Invasive**	**Round**	**Round**	**Round and Vacuolated**	**Irregular and protruding**
Nuclear Defects	+ **Normal**	++ **Large, mitotic defects prevalent**	++ **Small and irregular**	++ **Large and swollen**	+++ **Very small, fragmented**

3.9. Effects of Blocking FOXD1 G2/M Targets on 3D Patient Tumor Replica Growth

To understand if the compounds inhibit the growth of primary tumor replicas from patients, we isolated seven cell lines from patient tumors following a published protocol [9]. Previous reports indicate that many cell lines grown out from *VHL*-mutant patient tumor samples do not harbor *VHL* mutations [49], which is contradictory to genetic studies showing that *VHL* is a truncal mutation in the majority of ccRCCs [50], and suggests that outgrowth of bystander untransformed cells may be a common phenomenon. Cell lines were grown to at least passage three, and protein was collected to assess VHL expression status. The 786-O cell has a mutated VHL and was used as a comparator. Of seven isolated lines, three lacked VHL (S109, S114, S438) and showed expression of HIF1α, indicating a pseudo-hypoxic state (Figure 8A). Conversely, two cell lines displayed strong VHL expression and no detectable HIF1α (S322, S453). Two cell lines showed intermediate VHL and HIF1α expression (S199, S277). From this analysis, five of seven cell lines display some degree of pseudohypoxia, and were categorized as tumor cells.

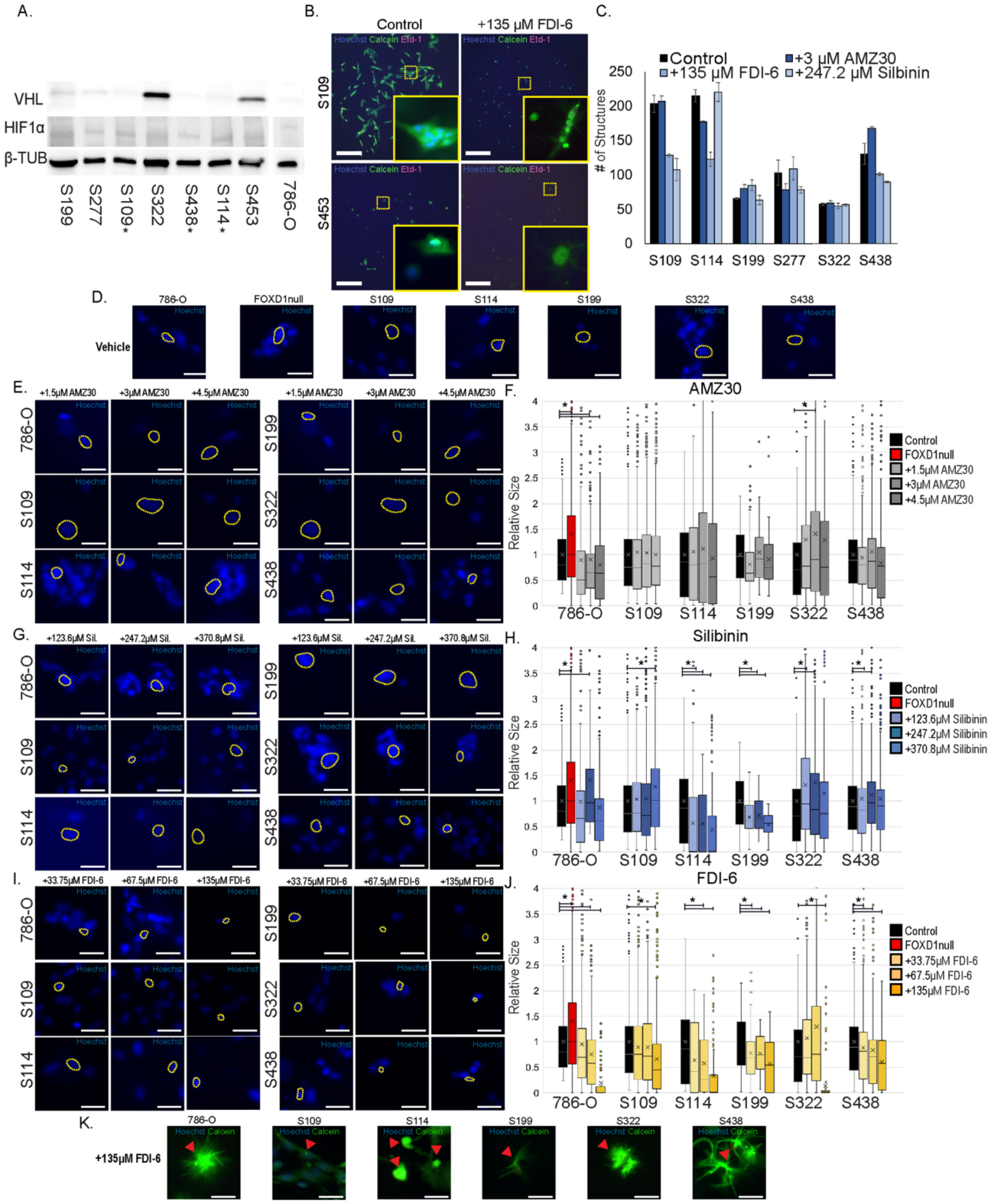

Figure 8. Test of candidate compounds on primary patient tumor replicas. (**A**) pseudo-hypoxia analysis of isolated primary cell lines and 786-O cells through Western Blotting (Figure S4 uncropped Western Blot Figures). * indicates potential true VHL null. (**B**) representative images of 3D cultures after three days treatment with FDI-6. All images can be found in Figure S1. Three-dimensional

cultures were stained with Hoechst 33342 (blue), Calcein-AM (green), and Ethidium homodimer-1 (magenta). Yellow-dotted box indicates region of inlay image. Scalebar = 500 microns (**C**) structure quantification of treated 3D cultures. (**D**) nuclei from colonies stained with Hoechst.33342 from each line tested. Yellow-dotted outlined nuclei are representative of each line (**E**,**F**). Nuclear morphology analysis of cells treated with indicated doses of AMZ30. Yellow-dotted outlined nuclei are representative of each treatment. Quantifications of nuclei sizes were normalized to average size from vehicle-treated control. * indicates significant difference in nuclear morphology compared to vehicle-control nuclei. (**G**,**H**) nuclear morphology analysis of cells treated with indicated doses of silibinin. Yellow-dotted outlined cells are representative of each treatment. Quantifications of nuclei sizes were normalized to average size from vehicle-treated control nuclei. * indicates significant difference in nuclear morphology compared to vehicle controls. (**I**,**J**) nuclear morphology analysis of cells treated with indicated doses of FDI-6. Yellow-dotted outlined cells are representative from each treatment. Quantifications of nuclei sizes were normalized to average size from vehicle-treated control nuclei. * indicates significant difference in nuclear morphology compared to vehicle controls. (**K**) representative cells from lines treated with a high dose of FDI-6. Red arrows indicate cells without Hoechst3342 staining.

To determine whether these patient-derived cell lines could provide a testing platform for our candidate compounds, we cultured them in 3D and treated them with candidate compounds at the effective and non-toxic concentrations determined using 786-O cells (Figure 3). After three days of treatment, cultures were stained with Hoechst 33342, Calcein-AM, and Ethidium homodimer-1, and the number of viable cell colonies was compared between treatment conditions (Figure 8B,C and Figure S1). Three lines showed changes in the number of colonies when treated with AMZ30 (S114 1.2-fold decrease = 1.2; S199 1.2-fold decrease; S438 1.3-fold increase); interestingly only S114 showed a reduction in the number of overall colonies, while S199 and S438 both showed an increase. Four lines showed a strong response to FDI-6 (S109 1.6-fold decrease; S114 1.8-fold decrease; S199 1.3-fold increase; S438 1.3-fold decrease), all showing a reduction in the number of colonies, with the exception of S199. Morphological changes could be observed following FDI-6 treatment, with thinning of cells and pronounced cellular projections (Figure 8B and Figure S1). Additionally, we observed a loss of Hoechst 33342 staining in cells showing such morphological characteristics. Silibinin treatment reduced colony numbers in two lines (S109 1.9-fold decrease; S438 1.4-fold decrease). In summary, the concentrations of all three compounds derived by titration on 786-O cells did have significant effects on 3D cell growth in subsets of patient tumor cells.

Although effects on colony growth were seen with compound concentrations determined using 786-O cells, each patient line is unique and may have differing dose requirements. To assess if this was the case, we repeated the 3D-treatment assay with patient lines using a three-point range for each compound. Only FDI-6 showed a strong dose-dependent response with a number of cell colonies. However, this increase is also associated with an increase in nuclear defects (Figure S2).

Nuclear morphology changes were observed in 786-O cells treated with compounds, so we analyzed the nuclear morphologies of primary lines. Lines showed distinct nuclear size distributions (examples shown in Figure 8D), and thus analyses were controlled by comparison with vehicle-treated samples for each individual line. The 786-O^{FOXD1null} cell was controlled by comparison with the 786-O cell. Treatment with AMZ30 showed a modestly increased nuclear size in the S322 line (1.4-fold) at the dose predicted for 786-O, but not at any higher dose (Figure 8E,F). All lines tested showed dose-dependent changes in nuclear size in response to silibinin treatment, albeit with different sensitivities and different effects. S109 showed increased nuclear size (1.28-fold) at the highest dose (4.5 μM), while S114 and S199 showed a decrease in nuclear size (-1.6-fold and -1.9-fold respectively) at the same dose. Both S322 and S438, interestingly, showed significant changes in size only at lower doses (1.36-fold and 1.2-fold), suggesting a potential biphasic response which was unanticipated based on the dose-response curve for 786-O (Figure 3Q). Lastly, FDI-6 showed the most consistent response between lines tested, all showing a dose-dependent

decrease in nuclear size (Figure 8I,J). Some lines were more sensitive to treatment than others; however, the dose predicted from 786-O induced a significant, non-toxic effect in all lines (less than 5% stained with Ethidium Homodimer). Interestingly, as observed with 786-O, the high-dose treatment with FDI-6 induced morphological changes in many cells, including loss of Hoechst 33342 staining (Figure 8K). These colonies with degenerated nuclei are excluded from the nuclear morphology analysis because it is based only on Hoechst 33342 stained cells, and our quantification methods may therefore underrepresent the inhibitory effect of FDI-6 treatment on tumor colony formation. Our analyses show that silibinin and FDI-6 target pathways that profoundly modify cell behavior and tumor colony growth in patient tumor replicas, identifying them and their related compounds as interesting candidates for further investigation in ccRCC models. Furthermore, dose titration using 786-O provided relevant starting doses for treatment of patient-specific tumors in 3D cultures.

4. Discussion

The screen developed in our study identified three candidate compounds that replicate aspects of the cell cycle phenotype caused by inactivation of *FOXD1* in 786-O cells. Using patient-derived tumor replicas, we demonstrate that the selected compounds perturb growth in multiple primary tumor lines. The 3D culture method that we developed to mimic the ECM environment of ccRCC provides a sensitive platform to study treatment responses and may provide important information on patient-specific tumor sensitivity to panels of compounds. At the doses tested, we found that subsets of patient replicas were sensitive to silibinin, while sensitivity to FDI-6 appears more general across patient tumor replicas. In addition to identifying these factors as compounds of interest for further studies in tumor models, our analysis provides a foundation for a screening method that could be used to select candidate treatments specific to a patient's tumor. Further development of this concept will include the addition of tumor stroma elements, which our previous studies have shown are maintained in this culture system [9].

We have previously shown that loss of FOXD1 dysregulated phosphorylation of CDC2 (which is essential for progression through the G2/M checkpoint) and histone H3. Two of the three candidates identified in our study are known to have effects on CDC2 and Histone H3. FOXM1 has been shown to directly regulate CDC2, with its loss impairing CDC2 activity [51]. CDC2 is also regulated by the phosphatase PP2A [52], which is inhibited by PME-1. Additionally, PP2A also regulates phosphorylation of Histone H3, giving more credence to the role of PME-1 in the G2/M growth delay phenotype.

FOXM1 is a master regulator of the cell cycle and regulates the passage of cells through S and G2/M [53]. It has been implicated in several cancer subtypes, including RCC, and is highly prognostic [36]. Loss of FOXM1 has been shown to lead to mitotic decline, senescence, and necrosis in both aging and in cancer treatment with FDI-6 [54,55]. FDI-6 has been shown to cause nuclear fragmentation and subsequent dissolution in cancer cells [55]. We report this effect occurring in an immortal cell line, as well as in primary tumor cells lines. Revisiting the initial RNA-seq, GSEA analysis identified a cluster of pathways related to cell senescence, necrosis, and apoptosis that are upregulated with loss of *FOXD1* (Figure S3). Induction of senescence in tumors is an attractive therapeutic strategy, and the possibility that FDI-6 induces senescence in ccRCC cells will be explored in future studies.

PME-1 is a methylesterase that binds to the active site of protein phosphatase 2A (PP2A), resulting in demethylation and inactivation. It has been shown to influence formation and elongation of the mitotic spindle, with inhibition by AMZ-30 resulting in mitotic crises and cell death [56]. In this analysis, we see that inhibition of PME-1 did not completely inhibit the ability of cells to create colonies but did result in increased mitotic defects similar to the loss of *FOXD1* in 786-O cells. Long-term inhibition of PME-1 would likely result in gradual growth inhibition with the accumulation of mitotic defects. However, in primary lines tested in this study, AMZ-30 was observed to have little effect on tumor

colony growth or nuclear morphology. Re-titration of AMZ-30 in each patient line and investigation of the effects of other inhibitory compounds will address if PME-1 is a useful target to modify ccRCC tumor growth.

Little is known about TMEM167A, but it has prognostic significance in lung cancer and glioma [57,58]. TMEM167A regulates vesicular trafficking, TNF and EGF signaling, and p53 transcription [29]. The compound silibinin has been shown to inhibit the TMEM family of receptors [57,58]. While being the least specific, it has known antitumor effects [59]. Further investigation of the targets of silibinin in ccRCC cells will be required to understand if its growth inhibitory effect is due specifically to the inhibition of TMEM167A.

Empirical determination of the specificities of compounds selected from our screen was beyond the scope of this study, in which the main aim was to find compounds that recapitulate the phenotypic effect of *FOXD1* inactivation. Further investigation of candidate compounds will be required to identify their precise mechanisms of action. If we confirm that they target independent pathways, it is possible that combined treatment of cells will result in synergistic effects that may more closely replicate the *FOXD1* loss of function phenotype with higher fidelity than single compounds.

Our analysis of FOXD1 targets revealed three therapeutically interesting candidates and demonstrated profound effects of their growth inhibition on both 786-O and primary patient tumor cells. Although our study did identify other candidates with effects on the cell cycle, we chose to focus on FOXM1, PME-1, and TMEM167A because they recapitulated the G2/M delay that we previously characterized in *FOXD1* loss of function cells. The profound change in growth characteristics of tumor cells caused by loss of *FOXD1* makes it an attractive therapeutic target, and since there is no reported strategy to inactivate FOXD1 itself, our work focused on the downstream pathways that are targetable. Considering the success of our approach in identifying potent targets, it could be expanded using large compound libraries in conjunction with our tumor replica modeling to develop a high throughput screen of candidate treatments for ccRCC. A challenge with the current study is the dependence on microscopy to observe changes in nuclear morphology, which limits the ability to test a large range for dose-response or to analyze many replicates. Utilization of an automated imaging system may overcome these limitations.

Given the tractability of outgrowth of primary patient material in our tumor replica cultures, an intriguing possibility for further development would be to compare compound responsiveness of primary versus metastatic ccRCC tumors from the same patient. While this is a technically challenging study due to the limited availability of patient material, it would provide clinically important insights into differences in tumor cell treatment sensitivity that arise following seeding to a non-renal location.

5. Conclusions

In this work we have developed an analysis strategy to discover pathways downstream of FOXD1 that control the G2/M phase of the cell cycle in ccRCC using a 786-O^{FOXD1null} ccRCC cell line. This strategy generated a list of actionable candidates that could be experimentally modulated. Eighteen candidate compounds were tested, of which three were able to copy aspects of the *FOXD1* loss of function phenotype: FDI-6 (against FOXM1), AMZ-30 (against PME-1), and silibinin (against TMEM167A).

A novel 3D culture system that replicates the ccRCC environment was used to test the capacity of selected compounds to inhibit tumor cell growth, and strong growth inhibitory effects were observed for silibinin and FDI-6. The 3D culture system enabled testing of patient-derived tumor cells, which showed varying susceptibility to the candidate compounds. In addition to the identification of target pathways for further investigation as ccRCC tumor growth inhibitors, the study identified significant variability in responsiveness to inhibitory compounds between patient-derived tumor models, suggesting that personalized tumor replicas may be an important addition to a discovery pipeline at an early stage.

Supplementary Materials: The following supporting information can be downloaded at: https://www.mdpi.com/article/10.3390/cancers14163958/s1, Figure S1: compound treatment of patient tumor avatars; Figure S2: compound treatment of primary 3D cultures structure analysis; Figure S3: pathway analysis identifies actionable pathways; Figure S4: uncropped Western Blot Figures; Table S1: RNA-seq analysis uncovers downstream targets of FOXD1; Table S2: compound titrations used in study.

Author Contributions: Conceptualization, K.H.B. and L.O.; methodology, K.H.B.; software, K.H.B.; validation, K.H.B.; formal analysis, K.H.B.; investigation, K.H.B. and L.O.; resources, S.S.-L. and L.O.; data curation, K.H.B.; writing—original draft preparation, K.H.B. and L.O.; writing—review and editing, K.H.B. and L.O.; visualization, K.H.B.; supervision, L.O.; project administration, L.O.; funding acquisition, L.O. All authors have read and agreed to the published version of the manuscript.

Funding: This work was supported by the Assistant Secretary of Defense for Health Affairs endorsed by the Department of Defense, through the Kidney Cancer Research Program under award no. KC170016 (LO). Opinions, interpretations, conclusions, and recommendations are those of the author and are not necessarily endorsed by the Department of Defense.

Institutional Review Board Statement: The study was conducted according to the guidelines of the Declaration of Helsinki and approved by the Institutional Review Board of the New York Blood Center, where the Rogosin Institute laboratory space is located (protocol 1493860-1, approved 09.11.2019).

Informed Consent Statement: Informed consent was obtained from all subjects involved in the study.

Data Availability Statement: RNA sequencing used in this study is available on GEO repository and accessible via the web (GSE210145).

Acknowledgments: Thanks to the Rogosin Institute for supporting for this work and for their efforts to tackle all issues kidney related.

Conflicts of Interest: The authors declare no conflict of interest.

References

1. Fu, L.; Hu, Y.; Song, M.; Liu, Z.; Zhang, W.; Yu, F.X.; Wu, J.; Wang, S.; Izpisua Belmonte, J.C.; Chan, P.; et al. Up-regulation of FOXD1 by YAP alleviates senescence and osteoarthritis. *PLoS Biol.* **2019**, *17*, e3000201. [CrossRef] [PubMed]
2. Wu, H.; Larribère, L.; Sun, Q.; Novak, D.; Sachindra, S.; Granados, K.; Umansky, V.; Utikal, J. Loss of neural crest-associated gene FOXD1 impairs melanoma invasion and migration via RAC1B downregulation. *Int. J. Cancer* **2018**, *143*, 2962–2972. [CrossRef] [PubMed]
3. Zhao, Y.F.; Zhao, J.Y.; Yue, H.; Hu, K.S.; Shen, H.; Guo, Z.G.; Su, X.J. FOXD1 promotes breast cancer proliferation and chemotherapeutic drug resistance by targeting p27. *Biochem. Biophys. Res. Commun.* **2015**, *456*, 232–237. [CrossRef] [PubMed]
4. Gao, Y.F.; Zhu, T.; Mao, X.Y.; Mao, C.X.; Li, L.; Yin, J.Y.; Zhou, H.H.; Liu, Z.Q. Silencing of Forkhead box D1 inhibits proliferation and migration in glioma cells. *Oncol. Rep.* **2017**, *37*, 1196–1202. [CrossRef] [PubMed]
5. Hatini, V.; Huh, S.O.; Herzlinger, D.; Soares, V.C.; Lai, E. Essential role of stromal mesenchyme in kidney morphogenesis revealed by targeted disruption of Winged Helix transcription factor BF-2. *Genes Dev.* **1996**, *10*, 1467–1478. [CrossRef] [PubMed]
6. Fetting, J.L.; Guay, J.A.; Karolak, M.J.; Iozzo, R.V.; Adams, D.C.; Maridas, D.E.; Brown, A.C.; Oxburgh, L. FOXD1 promotes nephron progenitor differentiation by repressing decorin in the embryonic kidney. *Development* **2014**, *141*, 17–27. [CrossRef] [PubMed]
7. Gkolfinopoulos, S.; Psyrri, A.; Bamias, A. Clear-cell renal cell carcinoma—A comprehensive review of agents used in the contemporary management of advanced/metastatic disease. *Oncol. Rev.* **2021**, *15*, 530. [CrossRef]
8. Bond, K.H.; Fetting, J.L.; Lary, C.W.; Emery, I.F.; Oxburgh, L. FOXD1 regulates cell division in clear cell renal cell carcinoma. *BMC Cancer* **2021**, *21*, 312. [CrossRef]
9. Bond, K.H.; Chiba, T.; Wynne, K.P.H.; Vary, C.P.H.; Sims-Lucas, S.; Coburn, J.M.; Oxburgh, L. The Extracellular Matrix Environment of Clear Cell Renal Cell Carcinoma Determines Cancer Associated Fibroblast Growth. *Cancers* **2021**, *13*, 5873. [CrossRef]
10. Subramanian, A.; Tamayo, P.; Mootha, V.K.; Mukherjee, S.; Ebert, B.L.; Gillette, M.A.; Paulovich, A.; Pomeroy, S.L.; Golub, T.R.; Lander, E.S.; et al. Gene set enrichment analysis: A knowledge-based approach for interpreting genome-wide expression profiles. *Proc. Natl. Acad. Sci. USA* **2005**, *102*, 15545–15550. [CrossRef]
11. Jassal, B.; Matthews, L.; Viteri, G.; Gong, C.; Lorente, P.; Fabregat, A.; Sidiropoulos, K.; Cook, J.; Gillespie, M.; Haw, R.; et al. The reactome pathway knowledgebase. *Nucleic Acids Res.* **2020**, *48*, D649–D655. [CrossRef] [PubMed]
12. Shannon, P.; Markiel, A.; Ozier, O.; Baliga, N.S.; Wang, J.T.; Ramage, D.; Amin, N.; Schwikowski, B.; Ideker, T. Cytoscape: A software environment for integrated models of biomolecular interaction networks. *Genome. Res.* **2003**, *13*, 2498–2504. [CrossRef] [PubMed]
13. Gearing, L.J.; Cumming, H.E.; Chapman, R.; Finkel, A.M.; Woodhouse, I.B.; Luu, K.; Gould, J.A.; Forster, S.C.; Hertzog, P.J. CiiiDER: A tool for predicting and analysing transcription factor binding sites. *PLoS ONE* **2019**, *14*, e0215495. [CrossRef] [PubMed]
14. Harris, G.M.; Raitman, I.; Schwarzbauer, J.E. Cell-derived decellularized extracellular matrices. *Methods Cell Biol.* **2018**, *143*, 97–114.

15. Lorca, T.; Manfredi, J.J.; Orlic-Milacic, M. Mitotic G2-G2/M phases. *Reactome Reactome* **2018**.
16. Eid, S.; Turk, S.; Volkamer, A.; Rippmann, F.; Fulle, S. KinMap: A web-based tool for interactive navigation through human kinome data. *BMC Bioinform.* **2017**, *18*, 16. [CrossRef]
17. Shao, X.; Taha, I.N.; Clauser, K.R.; Gao, Y.T.; Naba, A. MatrisomeDB: The ECM-protein knowledge database. *Nucleic Acids Res.* **2020**, *48*, D1136–D1144. [CrossRef]
18. Gaudet, P.; Livstone, M.S.; Lewis, S.E.; Thomas, P.D. Phylogenetic-based propagation of functional annotations within the Gene Ontology consortium. *Brief. Bioinform.* **2011**, *12*, 449–462. [CrossRef]
19. Schindelin, J.; Arganda-Carreras, I.; Frise, E.; Kaynig, V.; Longair, M.; Pietzsch, T.; Preibisch, S.; Rueden, C.; Saalfeld, S.; Schmid, B.; et al. Fiji: An open-source platform for biological-image analysis. *Nat. Methods* **2012**, *9*, 676–682. [CrossRef]
20. Kel, A.E.; Goößling, E.; Reuter, I.; Cheremushkin, E.; Kel-Margoulis, O.V.; Wingender, E. MATCHTM: A tool for searching transcription factor binding sites in DNA sequences. *Nucleic Acids Res.* **2003**, *31*, 3576–3579. [CrossRef]
21. Arnone, M.I.; Davidson, E.H. The hardwiring of development: Organization and function of genomic regulatory systems. *Development* **1997**, *124*, 1851–1864. [CrossRef]
22. Taneja, N.; Fenix, A.M.; Rathbun, L.; Millis, B.A.; Tyska, M.J.; Hehnly, H.; Burnette, D.T. Focal adhesions control cleavage furrow shape and spindle tilt during mitosis. *Sci. Rep.* **2016**, *6*, 29846. [CrossRef]
23. Meierjohann, S.; Hufnagel, A.; Wende, E.; Kleinschmidt, M.A.; Wolf, K.; Friedl, P.; Gaubatz, S.; Schartl, M. MMP13 mediates cell cycle progression in melanocytes and melanoma cells: In vitro studies of migration and proliferation. *Mol. Cancer* **2010**, *9*, 201. [CrossRef]
24. Kominsky, S.L.; Doucet, M.; Thorpe, M.; Weber, K.L. MMP-13 is over-expressed in renal cell carcinoma bone metastasis and is induced by TGF-beta1. *Clin. Exp. Metastasis* **2008**, *25*, 865–870. [CrossRef]
25. Jaffré, F.; Friedman, A.E.; Hu, Z.; Mackman, N.; Blaxall, B.C. β-adrenergic receptor stimulation transactivates protease-activated receptor 1 via matrix metalloproteinase 13 in cardiac cells. *Circulation* **2012**, *125*, 2993–3003. [CrossRef]
26. Cui, Y.; Chen, J.; He, Z.; Xiao, Y. SUZ12 depletion suppresses the proliferation of gastric cancer cells. *Cell Physiol. Biochem.* **2013**, *31*, 778–784. [CrossRef]
27. Pasini, D.; Bracken, A.P.; Jensen, M.R.; Lazzerini Denchi, E.; Helin, K. Suz12 is essential for mouse development and for EZH2 histone methyltransferase activity. *EMBO J.* **2004**, *23*, 4061–4071. [CrossRef]
28. Ströbel, T.; Madlener, S.; Tuna, S.; Vose, S.; Lagerweij, T.; Wurdinger, T.; Vierlinger, K.; Wöhrer, A.; Price, B.D.; Demple, B.; et al. Ape1 guides DNA repair pathway choice that is associated with drug tolerance in glioblastoma. *Sci. Rep.* **2017**, *7*, 9674. [CrossRef]
29. Segura-Collar, B.; Gargini, R.; Tovar-Ambel, E.; Hernández-SanMiguel, E.; Epifano, C.; Pérez de Castro, I.; Hernández-Laín, A.; Casas-Tintó, S.; Sánchez-Gómez, P. The EGFR-TMEM167A-p53 Axis Defines the Aggressiveness of Gliomas. *Cancers* **2020**, *12*, 208. [CrossRef]
30. Huang, Y.; Zhu, Y.; Zhang, Z.; Li, Z.; Kong, C. UNC5B mediates G2/M phase arrest of bladder cancer cells by binding to CDC14A and P53. *Cancer Gene Ther.* **2020**, *27*, 934–947. [CrossRef]
31. Wu, G.; Cheng Zhang, C. Membrane protein CAR promotes hematopoietic regeneration upon stress. *Haematologica* **2021**, *106*, 2180–2190. [CrossRef]
32. Zhu, Y.; Zhu, L.; Lu, L.; Zhang, L.; Zhang, G.; Wang, Q.; Yang, P. Role and mechanism of the alkylglycerone phosphate synthase in suppressing the invasion potential of human glioma and hepatic carcinoma cells in vitro. *Oncol. Rep.* **2014**, *32*, 431–436. [CrossRef]
33. Stazi, G.; Battistelli, C.; Piano, V.; Mazzone, R.; Marrocco, B.; Marchese, S.; Louie, S.M.; Zwergel, C.; Antonini, L.; Patsilinakos, A.; et al. Development of alkyl glycerone phosphate synthase inhibitors: Structure-activity relationship and effects on ether lipids and epithelial-mesenchymal transition in cancer cells. *Eur. J. Med. Chem.* **2019**, *163*, 722–735. [CrossRef]
34. Morita, K.; He, S.; Nowak, R.P.; Wang, J.; Zimmerman, M.W.; Fu, C.; Durbin, A.D.; Martel, M.W.; Prutsch, N.; Gray, N.S.; et al. Allosteric Activators of Protein Phosphatase 2A Display Broad Antitumor Activity Mediated by Dephosphorylation of MYBL2. *Cell* **2020**, *181*, 702–715. [CrossRef]
35. Chen, X.; Müller, G.A.; Quaas, M.; Fischer, M.; Han, N.; Stutchbury, B.; Sharrocks, A.D.; Engeland, K. The forkhead transcription factor FOXM1 controls cell cycle-dependent gene expression through an atypical chromatin binding mechanism. *Mol. Cell. Biol.* **2013**, *33*, 227–236. [CrossRef]
36. Xue, Y.J.; Xiao, R.H.; Long, D.Z.; Zou, X.F.; Wang, X.N.; Zhang, G.X.; Yuan, Y.H.; Wu, G.Q.; Yang, J.; Wu, Y.T.; et al. Overexpression of FoxM1 is associated with tumor progression in patients with clear cell renal cell carcinoma. *J. Transl. Med.* **2012**, *10*, 200. [CrossRef]
37. Goodman, R.H.; Smolik, S. CBP/p300 in cell growth, transformation, and development. *Genes Dev.* **2000**, *14*, 1553–1577. [CrossRef]
38. Akashi, E.; Fujihara, S.; Morishita, A.; Tadokoro, T.; Chiyo, T.; Fujikawa, K.; Kobara, H.; Mori, H.; Iwama, H.; Okano, K.; et al. Effects of galectin-9 on apoptosis, cell cycle and autophagy in human esophageal adenocarcinoma cells. *Oncol. Rep.* **2017**, *38*, 506–514. [CrossRef]
39. Jikuya, R.; Kishida, T.; Sakaguchi, M.; Yokose, T.; Yasui, M.; Hashizume, A.; Tatenuma, T.; Mizuno, N.; Muraoka, K.; Umemoto, S.; et al. Galectin-9 expression as a poor prognostic factor in patients with renal cell carcinoma. *Cancer Immunol. Immunother. CII* **2020**, *69*, 2041–2051. [CrossRef]
40. Taniguchi, H.; Yamamoto, H.; Akutsu, N.; Nosho, K.; Adachi, Y.; Imai, K.; Shinomura, Y. Transcriptional silencing of hedgehog-interacting protein by CpG hypermethylation and chromatic structure in human gastrointestinal cancer. *J. Pathol.* **2007**, *213*, 131–139. [CrossRef]
41. Kotulak-Chrzaszcz, A.; Klacz, J.; Matuszewski, M.; Kmiec, Z.; Wierzbicki, P.M. Expression of the Sonic Hedgehog pathway components in clear cell renal cell carcinoma. *Oncol. Lett.* **2019**, *18*, 5801–5810. [CrossRef] [PubMed]

42. Du, M.; Wang, G.; Barsukov, I.L.; Gross, S.R.; Smith, R.; Rudland, P.S. Direct interaction of metastasis-inducing S100P protein with tubulin causes enhanced cell migration without changes in cell adhesion. *Biochem. J.* **2020**, *477*, 1159–1178. [CrossRef] [PubMed]
43. Arumugam, T.; Ramachandran, V.; Sun, D.; Peng, Z.; Pal, A.; Maxwell, D.S.; Bornmann, W.G.; Logsdon, C.D. Designing and Developing S100P Inhibitor 5-Methyl Cromolyn for Pancreatic Cancer Therapy. *Mol. Cancer Ther.* **2013**, *12*, 654–662. [CrossRef] [PubMed]
44. Stojic, L.; Lun, A.T.L.; Mascalchi, P.; Ernst, C.; Redmond, A.M.; Mangei, J.; Barr, A.R.; Bousgouni, V.; Bakal, C.; Marioni, J.C.; et al. A high-content RNAi screen reveals multiple roles for long noncoding RNAs in cell division. *Nat. Commun.* **2020**, *11*, 1851. [CrossRef]
45. Yang, L.; Wang, Y.; Sun, R.; Zhang, Y.; Fu, Y.; Zheng, Z.; Ji, Z.; Zhao, D. ANGPTL4 Promotes the Proliferation of Papillary Thyroid Cancer via AKT Pathway. *OncoTargets Ther.* **2020**, *13*, 2299–2309. [CrossRef]
46. Cui, D.; Zhao, Y.; Xu, J. Activation of CXCL5-CXCR2 axis promotes proliferation and accelerates G1 to S phase transition of papillary thyroid carcinoma cells and activates JNK and p38 pathways. *Cancer Biol. Ther.* **2019**, *20*, 608–616. [CrossRef]
47. Tominaga, K.; Minato, H.; Murayama, T.; Sasahara, A.; Nishimura, T.; Kiyokawa, E.; Kanauchi, H.; Shimizu, S.; Sato, A.; Nishioka, K.; et al. Semaphorin signaling via MICAL3 induces symmetric cell division to expand breast cancer stem-like cells. *Proc. Natl. Acad. Sci.* **2019**, *116*, 625–630. [CrossRef]
48. Isogai, Z.; Ono, R.N.; Ushiro, S.; Keene, D.R.; Chen, Y.; Mazzieri, R.; Charbonneau, N.L.; Reinhardt, D.P.; Rifkin, D.B.; Sakai, L.Y. Latent transforming growth factor beta-binding protein 1 interacts with fibrillin and is a microfibril-associated protein. *J. Biol. Chem.* **2003**, *278*, 2750–2757. [CrossRef]
49. Sinha, R.; Winer, A.G.; Chevinsky, M.; Jakubowski, C.; Chen, Y.B.; Dong, Y.; Tickoo, S.K.; Reuter, V.E.; Russo, P.; Coleman, J.A.; et al. Analysis of renal cancer cell lines from two major resources enables genomics-guided cell line selection. *Nat. Commun.* **2017**, *8*, 15165. [CrossRef]
50. Gossage, L.; Eisen, T.; Maher, E.R. VHL, the story of a tumour suppressor gene. *Nat. Rev. Cancer* **2015**, *15*, 55–64. [CrossRef]
51. Pal-Ghosh, R.; Xue, D.; Warburton, R.; Hill, N.; Polgar, P.; Wilson, J.L. CDC2 Is an Important Driver of Vascular Smooth Muscle Cell Proliferation via FOXM1 and PLK1 in Pulmonary Arterial Hypertension. *Int. J. Mol. Sci.* **2021**, *22*, 6943. [CrossRef]
52. Jeong, A.L.; Yang, Y. PP2A function toward mitotic kinases and substrates during the cell cycle. *BMB Rep.* **2013**, *46*, 289–294. [CrossRef]
53. Liao, G.B.; Li, X.Z.; Zeng, S.; Liu, C.; Yang, S.M.; Yang, L.; Hu, C.J.; Bai, J.Y. Regulation of the master regulator FOXM1 in cancer. *Cell Commun. Signal. CCS* **2018**, *16*, 57. [CrossRef]
54. Macedo, J.C.; Vaz, S.; Bakker, B.; Ribeiro, R.; Bakker, P.L.; Escandell, J.M.; Ferreira, M.G.; Medema, R.; Foijer, F.; Logarinho, E. FoxM1 repression during human aging leads to mitotic decline and aneuploidy-driven full senescence. *Nat. Commun.* **2018**, *9*, 2834. [CrossRef]
55. Wang, S.P.; Wu, S.Q.; Huang, S.H.; Tang, Y.X.; Meng, L.Q.; Liu, F.; Zhu, Q.H.; Xu, Y.G. FDI-6 inhibits the expression and function of FOXM1 to sensitize BRCA-proficient triple-negative breast cancer cells to Olaparib by regulating cell cycle progression and DNA damage repair. *Cell Death Dis.* **2021**, *12*, 1138. [CrossRef]
56. Xia, X.; Gholkar, A.; Senese, S.; Torres, J.Z. A LCMT1-PME-1 methylation equilibrium controls mitotic spindle size. *Cell Cycle* **2015**, *14*, 1938–1947. [CrossRef]
57. Guo, S.; Bai, X.; Liu, Y.; Shi, S.; Wang, X.; Zhan, Y.; Kang, X.; Chen, Y.; An, H. Inhibition of TMEM16A by Natural Product Silibinin: Potential Lead Compounds for Treatment of Lung Adenocarcinoma. *Front. Pharmacol.* **2021**, *12*, 643489. [CrossRef]
58. Portela, M.; Segura-Collar, B.; Argudo, I.; Sáiz, A.; Gargini, R.; Sánchez-Gómez, P.; Casas-Tintó, S. Oncogenic dependence of glioma cells on kish/TMEM167A regulation of vesicular trafficking. *Glia* **2019**, *67*, 404–417. [CrossRef]
59. Comelli, M.C.; Mengs, U.; Schneider, C.; Prosdocimi, M. Toward the definition of the mechanism of action of silymarin: Activities related to cellular protection from toxic damage induced by chemotherapy. *Integr. Cancer Ther.* **2007**, *6*, 120–129. [CrossRef]

Bond et al. BMC Cancer (2021) 21:312
https://doi.org/10.1186/s12885-021-07957-8

BMC Cancer

RESEARCH ARTICLE Open Access

FOXD1 regulates cell division in clear cell renal cell carcinoma

Kyle H. Bond[1,2], Jennifer L. Fetting[3,4], Christine W. Lary[3], Ivette F. Emery[3] and Leif Oxburgh[1*]

Abstract

Background: Forkhead transcription factors control cell growth in multiple cancer types. *Foxd1* is essential for kidney development and mitochondrial metabolism, but its significance in renal cell carcinoma (ccRCC) has not been reported.

Methods: Transcriptome data from the TCGA database was used to correlate *FOXD1* expression with patient survival. *FOXD1* was knocked out in the 786-O cell line and known targets were analyzed. Reduced cell growth was observed and investigated in vitro using growth rate and Seahorse XF metabolic assays and in vivo using a xenograft model. Cell cycle characteristics were determined by flow cytometry and immunoblotting. Immunostaining for TUNEL and γH2AX was used to measure DNA damage. Association of the *FOXD1* pathway with cell cycle progression was investigated through correlation analysis using the TCGA database.

Results: *FOXD1* expression level in ccRCC correlated inversely with patient survival. Knockout of *FOXD1* in 786-O cells altered expression of FOXD1 targets, particularly genes involved in metabolism (*MICU1*) and cell cycle progression. Investigation of metabolic state revealed significant alterations in mitochondrial metabolism and glycolysis, but no net change in energy production. In vitro growth rate assays showed a significant reduction in growth of 786-O^{FOXD1null}. In vivo, xenografted 786-O^{FOXD1null} showed reduced capacity for tumor formation and reduced tumor size. Cell cycle analysis showed that 786-O^{FOXD1null} had an extended G2/M phase. Investigation of mitosis revealed a deficiency in phosphorylation of histone H3 in 786-O^{FOXD1null}, and increased DNA damage. Genes correlate with *FOXD1* in the TCGA dataset associate with several aspects of mitosis, including histone H3 phosphorylation.

Conclusions: We show that FOXD1 regulates the cell cycle in ccRCC cells by control of histone H3 phosphorylation, and that FOXD1 expression governs tumor formation and tumor growth. Transcriptome analysis supports this role for FOXD1 in ccRCC patient tumors and provides an explanation for the inverse correlation between tumor expression of *FOXD1* and patient survival. Our findings reveal an important role for FOXD1 in maintaining chromatin stability and promoting cell cycle progression and provide a new tool with which to study the biology of FOXD1 in ccRCC.

Keywords: Cell cycle, DNA damage, Forkhead, Kidney cancer

* Correspondence: leo9022@nyp.org
[1]The Rogosin Institute, 310 East 67th Street, New York, NY 10065, USA
Full list of author information is available at the end of the article

© The Author(s). 2021 **Open Access** This article is licensed under a Creative Commons Attribution 4.0 International License, which permits use, sharing, adaptation, distribution and reproduction in any medium or format, as long as you give appropriate credit to the original author(s) and the source, provide a link to the Creative Commons licence, and indicate if changes were made. The images or other third party material in this article are included in the article's Creative Commons licence, unless indicated otherwise in a credit line to the material. If material is not included in the article's Creative Commons licence and your intended use is not permitted by statutory regulation or exceeds the permitted use, you will need to obtain permission directly from the copyright holder. To view a copy of this licence, visit http://creativecommons.org/licenses/by/4.0/. The Creative Commons Public Domain Dedication waiver (http://creativecommons.org/publicdomain/zero/1.0/) applies to the data made available in this article, unless otherwise stated in a credit line to the data.

Background

Forkhead transcription factors play diverse roles in cancer cells [1]. Members of the FOXA, C, M, O, and P subfamilies are involved in cancer initiation, progression and drug resistance. Expression of several forkhead family members has been described in clear cell renal cell carcinoma (ccRCC), a highly angiogenic tumor originating from nephron epithelium in the cortex of the kidney [2, 3].

The forkhead transcription factor FOXD1 plays an essential role in kidney development [4], and because developmental programs are frequently misregulated in cancer, we were interested to know what role it plays in cancer of the adult kidney, specifically ccRCC which is the most common form. Studies in other types of cancer suggest that it may be an important determinant of tumor biology. FOXD1 is highly expressed in Hodgkin's lymphoma and in breast cancer, where it suppresses p27 expression, thereby promoting cell proliferation [5]. In non-small cell lung cancer, *FOXD1* expression correlates with poor survival and increases proliferation [6]. In glioma, FOXD1 expression correlates with tumor grade and influences proliferation and migration of cells [7]. FOXD1 expression is also downregulated in chemoresistant ovarian cancers [8].

In this study, we defined an inverse correlation between probability of survival in ccRCC patients and expression of *FOXD1* in their tumors. A knockout was generated to investigate the biological function of *FOXD1* in ccRCC cells. Expression of the known transcriptional target *MICU1*, a regulator of mitochondrial bioenergetics, was increased. While a shift in balance between mitochondrial respiration and glycolysis was seen, overall energy production in null cells was unaltered. Inactivation of *FOXD1* caused a significant reduction in cellular proliferation both in vitro and in tumor xenograft assays, and studies of cells with synchronized cycling times revealed that the G2/M phase of the cell cycle was extended in mutant cells. Transcriptional pathway analysis in patient tumors supported this finding, and investigation of phosphorylation state of histone H3 revealed that it is almost completely abrogated in *FOXD1* null cells. We propose that *FOXD1* is required for histone H3 phosphorylation, which is an essential step in the transition through G2/M.

Methods

Experimental model and subject details

Cell lines

786-O (ATCC® CRL-1932™) cells and 786-O ^{FOXD1null} were maintained in RPMI 1640 with 1x GlutaMax, 25mM HEPES, 10% FBS, and 1x penicillin-streptomycin in 37 °C cell culture incubators at 5% CO_2. Cells were passaged for expansion using TrypLE express. For immunostaining, cells were grown on gelatin-coated sterile coverslips. Mycoplasma testing was performed prior to all experimental testing.

In vivo animal studies

Animal care was in accordance with the National Research Council Guide for the Care and Use of Laboratory Animals, and all experiments were approved by the Institutional Animal Care and Use Committee of New York Blood Center, where the Rogosin Institute laboratory is located. All animal experiments followed the housing protocols of the New York Blood Center: Complete health surveillance testing is performed for each murine room quarterly. Interim testing is performed as necessary. Serology is performed by Charles River Laboratories. Parasitology is performed in-house. The mice are housed in ventilated microisolator cages with 1 cup of 1/8 in. Bed-o'cobs. Mice are on 5P76 rodent feed and acidified water. Full PPE including head and shoe covers, isolation gown, mask and gloves, are required before room entry. All procedures are done inside a hood. Once animals leave the room, they do not return. Cages and water bottles are changed weekly and other cage materials are changed every 2 weeks. 6 week old female NCr nude mice (CrTac:NCr-*Foxn1nu*) were purchased from Taconic and housed at the New York Blood Center animal facility. Animals were housed in groups of 3–4 per cage. To establish xenografts, 786-O cells and 786-O^{FOXD1null} were expanded, resuspended at 10 million cells per 200 μl PBS and injected subcutaneously in the right flanks of 6-week old NCr mice, 6 animals per cell type. 48 h post-injection, tumor volume was measured using electronic calipers ($V = LxW^2$). Tumor establishment was determined 7 days from first measurement, as determined from pilot studies (Fig. S3). Tumor growth was monitored every 2–3 days for 60 days. At the end-point, animals were euthanized with isoflurane followed by cervical dislocation.

Methods detail

TCGA data analysis

Level 3 RNA sequencing data from the Illumina HiSeq platform was downloaded from the TCGA data portal (www.cancergenome.nih.gov) for 20,532 genes and 528 unique samples. We used the RPKM (reads per kilobase mapped) as gene expression values and linked this data to the clinical patient data using the patient barcode. Kaplan-Meier analyses were performed by stratifying gene expression data for each gene at the median and tested using the log-rank statistic. The survdiff and survtest R functions were using for Kaplan-Meier analyses, and the coxph function was used for fitting a Cox Proportional Hazards model to each gene to obtain the hazard ratio.

Patient samples

One hundred and forty two de-identified formalin-fixed, paraffin-embedded ccRCC samples from resected tumors were obtained from the Maine Medical Center BioBank, which obtains surgical samples with the written informed consent of patients. This study was approved by the Maine Medical Center Institutional Review Board (IRB #4202X and IRB #4392).

Immunohistochemistry

Section immunostaining was conducted as previously described [9]. Primary antibody FOXD1 (1:100, LSBio LS-B6453) and biotinylated rabbit anti-goat (1:500, Vectorlabs BA-5000) were used for immunohistochemistry using Vectastain ABC Elite kit (Vectorlabs PK-7100), and the color reaction performed using DAB. FOXD1 immunofluorescence in embryonic sections was amplified using the TSA amplification kit per manufacturer's instructions (Perkin Elmer NEL756001KT).

FIJI analysis and quantification of expression

To quantify molecular marker expression, immunostained tumor sections were imaged at five separate regions, and the percentage of stained cells in each image was calculated using FIJI and used to calculate FOXD1 staining confidence ratio. To assign FOXD1+ scores to individual tumors, the mean percentage of FOXD1+ cells from all five images was calculated.

Generation of the 786-O^{FOXD1null} line

786-O cells (ATCC: CL-188; 70,003,535) were the parental cells used to generate a pool of *FOXD1*-null cells. CRISPR/Cas9-mediated knockout cells were generated by the Synthego Corporation (Cambridge, MA, USA). In brief, guide RNAs were designed to create premature stop codons through frameshift mutations in the coding region via insertions and/or deletions (Indels) directly upstream of the start codon of *FOXD1*. The following sgRNA sequence was used: *5′ AUCGGACAUCUCAG UGCUCA-3′ [GGG]-PAM*. To generate these cells, ribonucleoproteins (RNPs) containing the Cas9 protein and synthetic sgRNA were electroporated into the cells. Editing efficiency was assessed upon recovery, 48 h post-electroporation. Genomic DNA was extracted, PCR-amplified, sequenced using Sanger sequencing, and analyzed for editing efficiency using Synthego Inference of CRISPR Edits (ICE) software (ice.synthego.com). Limiting dilution was performed to generate 84 clonal populations and screened for indels using ICE software as described above. Top scoring lines were analyzed for FOXD1 protein expression using immunocytochemistry described below.

qPCR analysis of predicted FOXD1 targets

RNA was extracted from 786-O and 786-O^{FOXD1null} cells at 70% confluency using Qiagen RNeasy Minikit (Qiagen Cat#74134) with DNase step included. cDNA was generated using BioRad iScript Synthesis kit (BioRad Cat#1708891). A screen of 31 reference genes was performed using BioRad SsoAdvanced Universal SYBR Green Supermix using the manufacturer's protocol, and selection of appropriate reference genes was performed using BioRad CFX Maestro software Reference Gene Selector Tool. *RPLP PO*, *HBB*, and *B2M* were chosen for this application. qPCR primers of predicted FOXD1 target genes were assayed and fold changes were calculated using BioRad CFX Maestro software using parental 786-O as reference. All assays were performed on CFX384 or CFX96 Touch Real-Time PCR Detection Systems, in triplicates.

Immunocytochemistry analysis

Immunostaining for FOXD1 in cells is described in brief; cells were fixed in 4% PFA for 12 min at room temperature, permeabilized with 0.2% Triton X-100 for 10 min at room temperature and blocked with 10% chicken serum in PBS for 1 h at room temperature. Binding of FOXD1 primary antibody (1:100, LSBio Cat#LS-B6453), biotinylated chicken anti-goat (1:250, ImmunoReagents Cat#CkxGt-003-EBio), and Cy5-conjugated streptavidin (1:250, Jackson Immunoresearch Cat#016–170-084) were performed sequentially at room temperature, 1 h each step and counterstained with DAPI. Coverslips were mounted using ProLong Diamond (Invitrogen Cat#P36961) mounting medium. The staining protocol was modified for phosphoproteins γH2AX (1:400, EMD Millipore Cat#05–636) and pH3 (1:100, EMD Millipore Cat#06–579) as follows; cells were fixed in ice cold 100% methanol and blocked overnight with 10% goat serum and 0.1% BSA in TBS. Primary antibody incubation was performed overnight, followed by secondary antibody incubation in goat anti-mouse IgG1 Alexa Fluor 568 (Life Technologies Cat#A21124) and goat anti-rabbit Alexa Fluor 647 (Life Technologies Cat#A21245). Coverslips were counterstained with DAPI, phalloidin Oregon-green (Invitrogen Cat#07466), or EdU (Invitrogen Cat#C10337) as pertaining to experiment. Staining for mitochondria using TOMM20 (1:100, abcam Cat# ab186735) was performed using standard immunocytochemistry techniques. Coverslips were mounted in EverBrite Mounting Media (Biotium Cat#23001). All staining was repeated to confirm staining patterns.

In vitro growth rate analysis

Five thousand cells of 786-O parent or 786-O^{FOXD1null} were plated into each well of a 6-well plate. Every 24 h for 4 days, cells were trypsinized and counted in

triplicates. After 4 days, cells were collected and counted every 48 h. This experiment was repeated 3 times.

DNA damage analysis (TUNEL)

786-O or 786-O^{FOXD1null} cells were plated in 8-well chamber slides and cultured for 24 h. Cells were then fixed in 4% paraformaldehyde, permeabilized with 2:1 ethanol:acetic acid, and DNA damage was detected using the ApopTag® Red In Situ Apoptosis Detection Kit (Millipore Cat#S7165). In brief, damaged DNA was tagged with digoxigenin-dNTP, then detected using a fluorescently conjugated anti-digoxigenin antibody. Cells were counterstained with DAPI. Extent of DNA damage was analyzed by counting the number of TUNEL positive foci per nucleus in approximately 300 cells in each group.

Metabolic analyses

Two thousand cells of 786-O and 786-O^{FOXD1null} were plated into Seahorse XF96 Cell Culture Microplates and assayed using XF Glycolytic Rate Assay ($N = 2$) (Agilent Cat#103592–100), XF Cell Mito Stress Test ($N = 3$) (Agilent Cat#103015–100), or XF ATP Real-Time rate assay ($N = 2$) (Agilent Cat#103020–100) following manufacturer procedures. Six technical replicates were analyzed for each biological replicate.

EdU pulse-chase analysis

786-O parent and 786-O^{FOXD1null} were treated ("pulse") with 5 μM EdU for 6, 8, or 10 h. After treatment, cells were washed and media was replaced with standard cell culture media. Cells were cultured ("chased") for an additional 0, 2, 4, or 6 h. At each time point, cells were fixed in 100% ice cold methanol and stored in TBS at 4 °C until all time points were collected. Following all collections, cells were stained using the ICC protocol above, and counterstained with DAPI. EdU was detected following the manufacturer's protocol. Cells were imaged using a Leica Thunder Imager. Cells were analyzed for co-expression of EdU, γH2AX, and pH3 using the Leica LasX multi-channel analysis package.

Cell cycle analysis

786-O parent and 786-O^{FOXD1null} were synchronized using double thymidine block. In brief, cells were treated for 16 h with thymidine, washed, and cultured for 9 h. A second round of thymidine was added for an additional 16 h to synchronize cells into G1. Cells were washed and fresh media was added. Cells were collected at various time points and either fixed in 100% ice cold methanol or protein extracted using Laemmli Buffer. Following fixation, cells were stained overnight with DAPI at 4 °C before flow cytometry. Flow cytometry was conducted at New York Blood Center Flow Cytometry Core Facility. Cell cycle distribution was performed on FlowJo software. Entry into mitosis was determined by Western blot analysis staining for H3 (CST Cat#9706 L), pH3(Ser10) (CST Cat#9715), CDC2 (CST Cat# 28439S), pCDC2(Tyr15) (CST Cat#9111S), pCDC2 (Thr161) (CST Cat#9114S), and CyclinB1 (CST Cat#12231). Molecular weight and densitometry analysis were performed using BioRad Imagelab software and normalized to total protein loaded.

In silico FOXD1 molecular signaling pathway prediction analysis

Gene correlation values were ranked for correlation strength and analyzed using Gene Set Enrichment Analysis (GSEA), mapping pathway interactions using the Reactome database and further analyzed using Gene Ontology (GO) analysis [10]. Pathways and interactors were mapped using Cytoscape [11]. Genes involved in pathways grouped under "Cell Cycle" were summarized and marked for further investigation.

Quantification and statistical analysis

For in vivo experiments, 3–4 animals were used per group. Due to the low tumor retention rate after 2 weeks of 786-O^{FOXD1null} (12.5%), statistical comparisons between end-point tumor size at 60 days were not possible, and instead comparisons at 15 and 30 days were performed, using Student's two tailed t-test. All in vitro experiments utilized the Student's t-test for comparisons between 786-O and 786-O^{FOXD1null}. Correlation analyses were conducted using either the Pearson or Spearman rank correlation as implemented with the R function cor.test, and chi-squared tests were conducted to test the association between dichotomized variables.

Results

FOXD1 expression in ccRCC correlates with poor patient survival

To understand if there could be a role for *FOXD1* in ccRCC, we correlated tumor expression with patient outcomes using data from The Cancer Genome Atlas (TCGA). Five hundred and twenty-eight ccRCC cases were grouped into high or low *FOXD1* expression relative to the median. Patients with *FOXD1*-low tumors showed significantly higher probability of survival at all time-points analyzed (Fig. 1a), supporting a role for tumor expression of *FOXD1* in disease progression. Comparison of FOXD1 expression in tumors of different grades showed higher *FOXD1* levels in higher grades (G1 vs. G3 $p = 1.2 \times 10^{-2}$; G1 vs. G4 $p = 5.0 \times 10^{-4}$; G2 vs. G3 $p = 3.8 \times 10^{-2}$; G2 vs. G4 $p = 1.4 \times 10^{-3}$) (Fig. S1A). Comparison of FOXD1 expression at different tumor stages revealed a significant difference only between stage 1

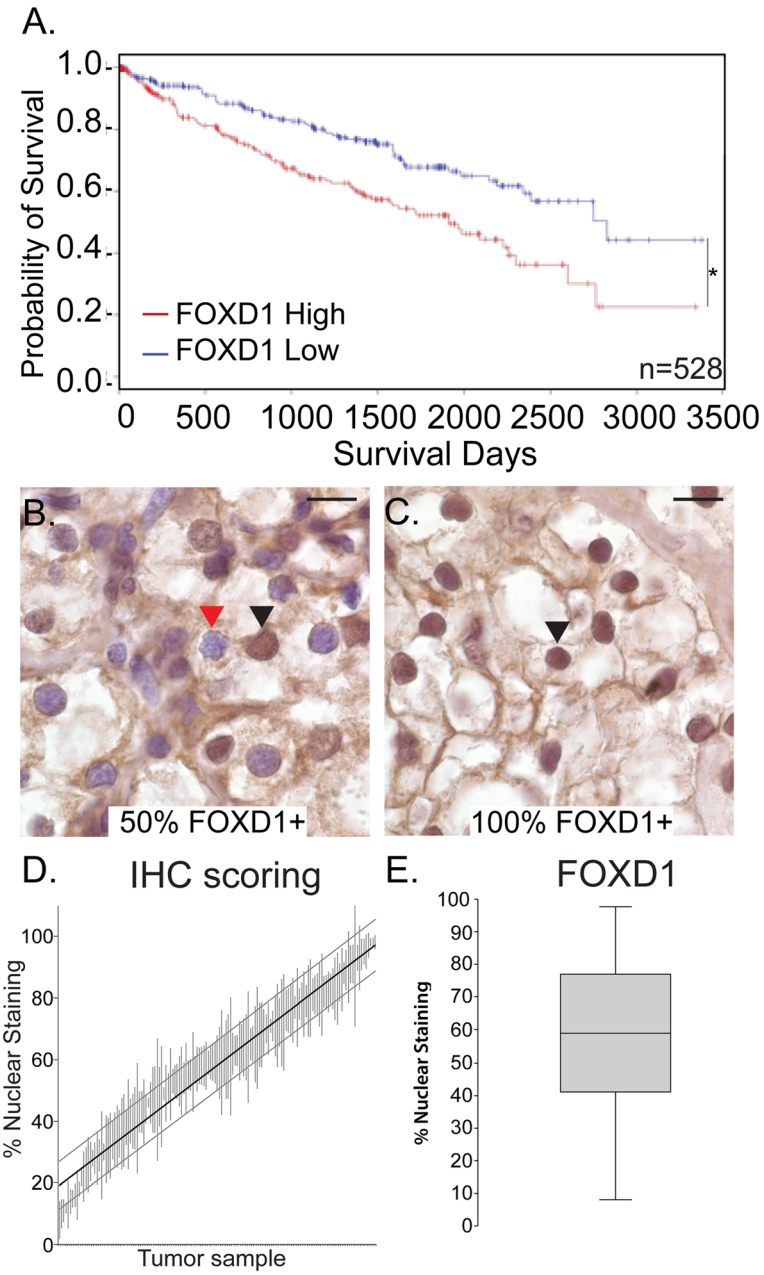

Fig. 1 FOXD1 expression in ccRCC. **a** Kaplan-Meier survival analysis for ccRCC patients with high versus low tumor expression of *FOXD1* based on transcriptome data from The Cancer Genome Atlas (TCGA). High and low expression were plotted relative to median expression of FOXD1. *p = 6.85E-05. **b**-**e** FOXD1 expression in ccRCC tumors. Representative examples of tumors with mosaic nuclear staining **b** and ubiquitous nuclear staining **c**. Black arrows indicate positive and red arrow indicates negative nuclei. **d** Scoring of percentage nuclear staining in 142 resected ccRCC tumors. For each tumor, five high power fields were scored for percentage of positive nuclei. **e** The median percentage of FOXD1-positive nuclei in tumors is 58.15% (95% CI 50.6 to 65.7)

and stage 4 (S1 vs. S4 $p = 1.9 \times 10^{-2}$) (Fig. S1B). We further investigated if increased *FOXD1* expression could have poor outcomes related to any particular stage and found that high *FOXD1* expression significantly correlated with worse outcomes for patients at stages 2 and 3 (stage 2 $p = 4.5 \times 10^{-2}$; stage 3 $p = 3.3 \times 10^{-3}$) (Fig. S1C-F).

To define the expression pattern of the FOXD1 transcription factor in ccRCC, we immunostained 142 patient tumors with a histopathological diagnosis of ccRCC (Table S1). Considering the high degree of relatedness between forkhead proteins, cross-reactivity of antisera presents a problem. To identify a FOXD1-specific antibody for these studies, we used *Foxd1* null

mice to screen for specificity. *Foxd1* is strongly and specifically expressed in cortical interstitial cells of the developing kidney [4]. Comparison of immunohistochemical staining using several commercial FOXD1 antibodies revealed that the LS Bio FOXD1 antibody (LS-B6453) showed specificity for nuclear FOXD1 in cortical interstitial cells of the developing kidney and did not stain *Foxd1* null tissue (Fig. S2A,B). In immunohistochemistry, diffuse staining is seen in epithelial tubules of adult human kidney tissue (Fig. S2C), and immunohistochemical analysis of *Foxd1* null mouse tissue reveals a similar pattern (Fig. S2D), indicating that this is antibody trapping. For this reason, we limited our analysis to nuclear staining. Nuclear FOXD1 was observed in all tumors (Fig. 1b ,c), with extensive inter-tumor variability in proportion of positive nuclei (Fig. 1d). Taking into account the variability of scores between and within samples, we generated a 95% confidence interval for proportion of FOXD1-positive nuclei in tumors as 58.15 +/− 7.55% (Fig. 1e). We note a potential bias in that a fraction of patients (8/142) received neoadjuvant treatment prior to sample collection. As expected, approximately 50% of Stage IV tumors were from treated patients, and any effect of treatment on FOXD1 expression would primarily be seen in this group. However, the proportion of tumors from treated patients overall is approximately 5% and would only constitute a minor effect on the aggregated data if FOXD1 expression is affected by neoadjuvant treatment.

Effect of *FOXD1* knockout on expression of known transcriptional targets

To understand the function of FOXD1, we generated a loss of function renal cell carcinoma cell line using CRISPR/Cas9. The 786-O cell line, which has a mutation in the *VHL* gene, is diploid for chromosome 5 on which *FOXD1* is located [12] and is therefore a good candidate cell line in which to generate a loss of function. A guide sequence was identified that would cleave the gene 4 codons downstream of the ATG and enable selection of edited clones with insertions or deletions causing truncating mutations (Fig. 2a). Inference of CRISPR Edits (ICE), a regression algorithm for predicting editing outcomes from Sanger sequencing data, was used to predict knockout of *FOXD1* in clones of edited cells (Fig. 2b). Clone 2, with a single thymine insertion at the same position in both copies of *FOXD1*, was predicted to encode a protein that is truncated 4 amino acids downstream of the methionine (Fig. 2c). Sequencing of the top potential off-target genes revealed no unwanted modifications (Table S2). Immunostaining showed an absence of FOXD1 in the nucleus and cell body of Clone 2 (Fig. 2d). We conclude that Clone 2 carries a null mutation in *FOXD1* originating from a homozygous single nucleotide insertion, and we refer to it hereafter as 786-O^{FOXD1null}.

To understand transcriptional effects of inactivating *FOXD1*, we compiled a list of candidate targets from previous reports [9, 13–15]. To ensure accurate measurement of expression by RT-QPCR, we selected reference genes with stable expression between 786-O and 786-O^{FOXD1null}. Commonly used reference genes such as *GAPDH*, *HPRT*, *TUBB*, and *TBP* showed very poor stability between these cell lines (Fig. S3A). We selected *RPLPPO*, *B2M*, and *HBB* (Fig. S2B-D), and used the geometric mean of these three assays as the reference value. Target genes associated with the cell cycle were misregulated, with the exception of PRC1, suggesting a cell cycle perturbation (Fig. 2e). *DCN*, *PGF*, *PUM1*, and *MICU1* were also misregulated in 786-O^{FOXD1null}.

FOXD1 influences cellular energetics, but does not affect overall ATP production

Considering that ccRCC is a disease of cellular metabolism, misregulation of *MICU1* is particularly interesting because it affects calcium signaling between cytoplasm and mitochondria [14]. In agreement with previous studies, our data shows that FOXD1 represses *MICU1* transcription [14]. Immunoblot revealed a significant increase in MICU1 protein in the 786-O^{FOXD1null} compared to the parent 786-O (Fig. 3a). To understand if this reflects an increased abundance of mitochondria in the 786-O^{FOXD1null}, we immunostained both lines for the mitochondrial marker TOMM20, and found increased signal intensity in 786-O^{FOXD1null}, suggesting increased mitochondrial abundance (Fig. 3b, c). To test if this altered utilization of oxidative metabolism, we compared 786-O versus 786-O^{FOXD1null} using Seahorse XF. Surprisingly, we found a significant reduction in basal mitochondrial respiration in 786-O^{FOXD1null} (Fig. 3d), and an increase in basal glycolysis (Fig. 3e). However, total ATP production between the lines was equivalent (Fig. 3f), indicating that energy derived from increased glycolysis compensates for the decrease in mitochondrial respiration. Thus, despite elevated MICU1 expression and evidence of increased mitochondrial abundance, mitochondrial respiration is depressed in the 786-O^{FOXD1null}. The 786-O cell line has a *VHL* inactivating mutation and is constitutively hypoxic with elevated baseline expression of HIF2. Persistent expression of HIF transcription factors represses respiratory chain subunits [16], and we therefore analyzed expression of genes in the mitochondrial respiration pathway (Fig. 3g). Modest changes were found for electron transport chain components, with *UQRC2* and *COXIV* showing elevated expression in 786-O^{FOXD1null}. The ATP transporters *ANT1* and *ANT2* both showed significant changes,

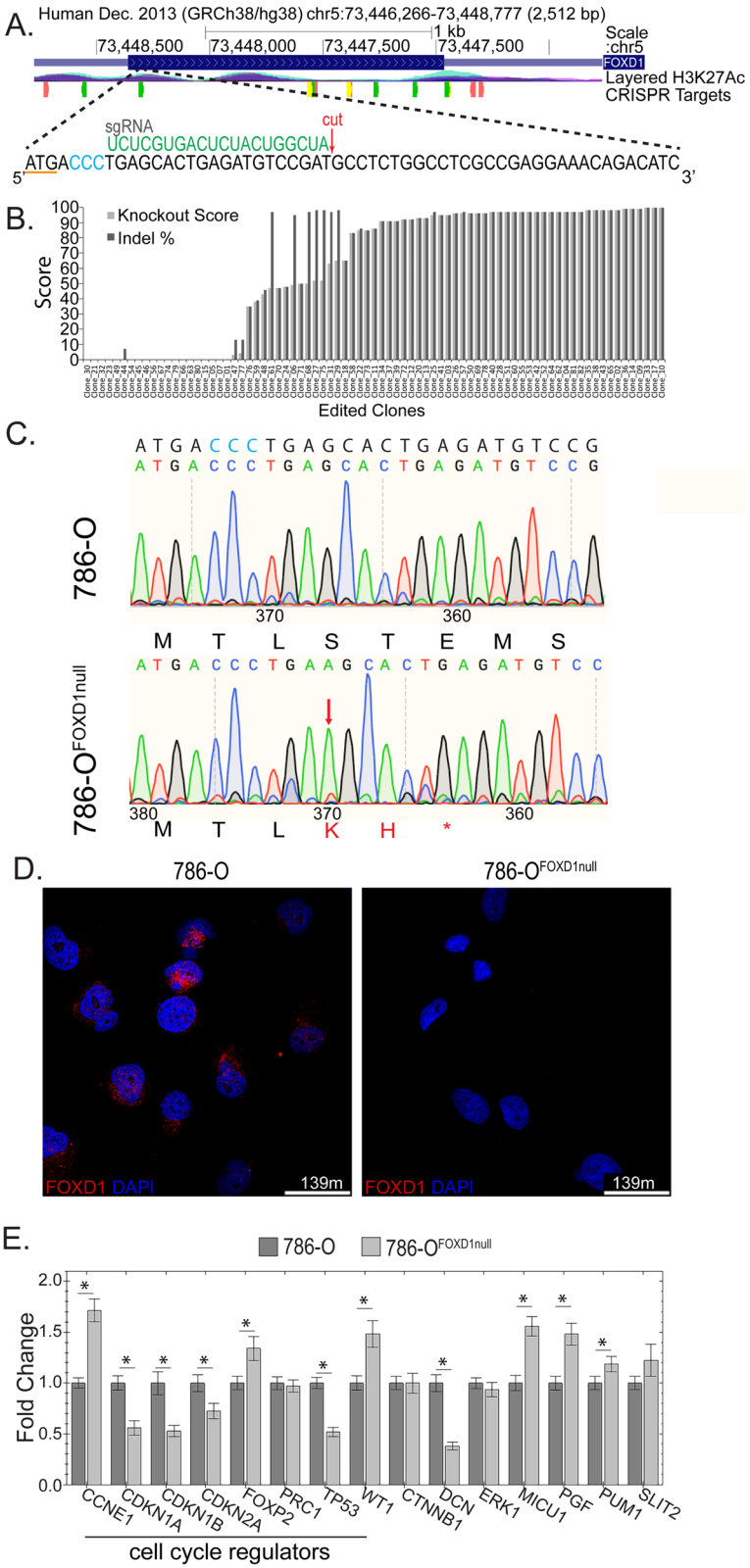

Fig. 2 (See legend on next page.)

(See figure on previous page.)
Fig. 2 *FOXD1* knockout affects expression of cell cycle regulators and alters cellular energetics. **a** CRISPR/Cas9 knockout targeting strategy for *FOXD1*. The *FOXD1* locus on chromosome 5 shows the single *FOXD1* exon with the CDS in dark blue and UTRs in light blue. The placement of the guide RNA (green) relative to the ATG (underlined) is shown below. **b** Knockout prediction score and percentage of alleles with insertions or deletions (indels) for 82 clones isolated from the CRISPR-edited pool. Chromosome 5 is diploid in 786-O and clones with 50% indel frequency are predicted to be heterozygous, while those with 100% indel frequency are predicted to be homozygous. **c** Sequencing trace of 786-O versus 786-O^{FOXD1null}. Red arrow indicates nucleotide insertion. Bottom: Predicted protein sequence showing insertion event resulting in modified amino acid sequence (red text) and premature stop (*). **d** FOXD1 (red) immunofluorescence staining in 786-O versus 786-O^{FOXD1null}, counterstained with DAPI (blue). **e** Expression of predicted FOXD1 target genes in edited versus parent cells. *$p < 0.05$

but in opposite directions making the net effect unclear. Expression of genes encoding pyruvate dehydrogenase kinase 1 (*PDK1*) and pyruvate dehydrogenase phosphatase catalytic subunit 1 (*PDP1*) was significantly elevated. PDK1 and PDP1 act in opposition on the enzyme pyruvate dehydrogenase, which is essential for energy production from the TCA cycle. Their simultaneous upregulation in the 786-O^{FOXD1null} suggests that elevated PDK1 may inhibit the TCA cycle, reducing mitochondrial respiration [17], with concomitant upregulation of the PDP1 phosphatase as a feedback response. This would be predicted to result in aerobic glycolysis being favored over mitochondrial metabolism in the 786-O^{FOXD1null} cell. In summary, although mitochondria may be more abundant in 786-O^{FOXD1null}, our data supports reduced mitochondrial energy production, and our gene expression analysis suggests inhibition of the TCA cycle.

FOXD1 is essential for tumor growth in vivo

Although total ATP production is unaffected by inactivation of *FOXD1*, proliferation is attenuated in 786-O^{FOXD1null} (Fig. 4a), suggesting that effects on the cell cycle (Fig. 2e) may be primary rather than a consequence of energy deficit. To understand if the effect of FOXD1 on cellular proliferation is reflected in a tumor model, we xenografted cohorts of 6 nude mice with either 786-O or 786-O^{FOXD1null} (Fig. 4b) as previously

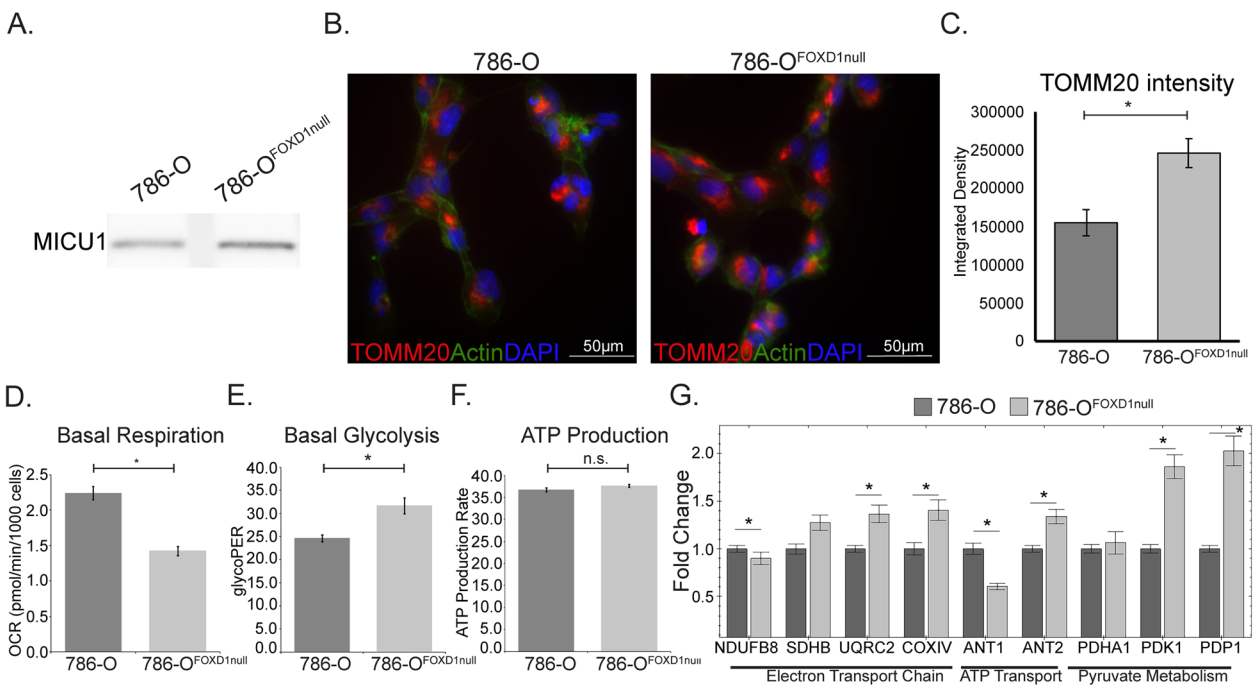

Fig. 3 FOXD1 influences mitochondria levels, but does not promote glycolysis. **a** Western Blot analysis of MICU1 in 786-O versus 786-O^{FOXD1null}. Loading was normalized by total protein in each lane and the full length blot is available in Supplemental Fig. S7. **b** Immunofluorescence analysis of mitochondria marker TOMM20 (red). Actin filaments (green) used to outline cell body and DAPI (blue) used to outline nucleus ($N = 2$ biological replicates). **c** Quantification of TOMM20 fluorescence intensity between 786-O and 786-O^{FOXD1null} using integrated density. * $p < 0.05$. **d** Basal mitochondrial respiration measured by Seahorse XF mitochondrial stress test (3 biological replicates). **e** Representative basal glycolytic rate comparison via Seahorse XF glycolytic rate assay (2 biological replicates). Y axis values are in pmol/min/1000cells. **f** Representative total ATP production rate comparison via Seahorse XF real-time ATP rate assay (2 biological replicates). Y axis values are in pmol/min/1000cells. For all Seahorse measurements, each biological replicate was measured in 5 technical replicates. *$p < 0.05$ **g** Expression of genes involved in mitochondrial respiration in edited versus parent cells. *$p < 0.05$

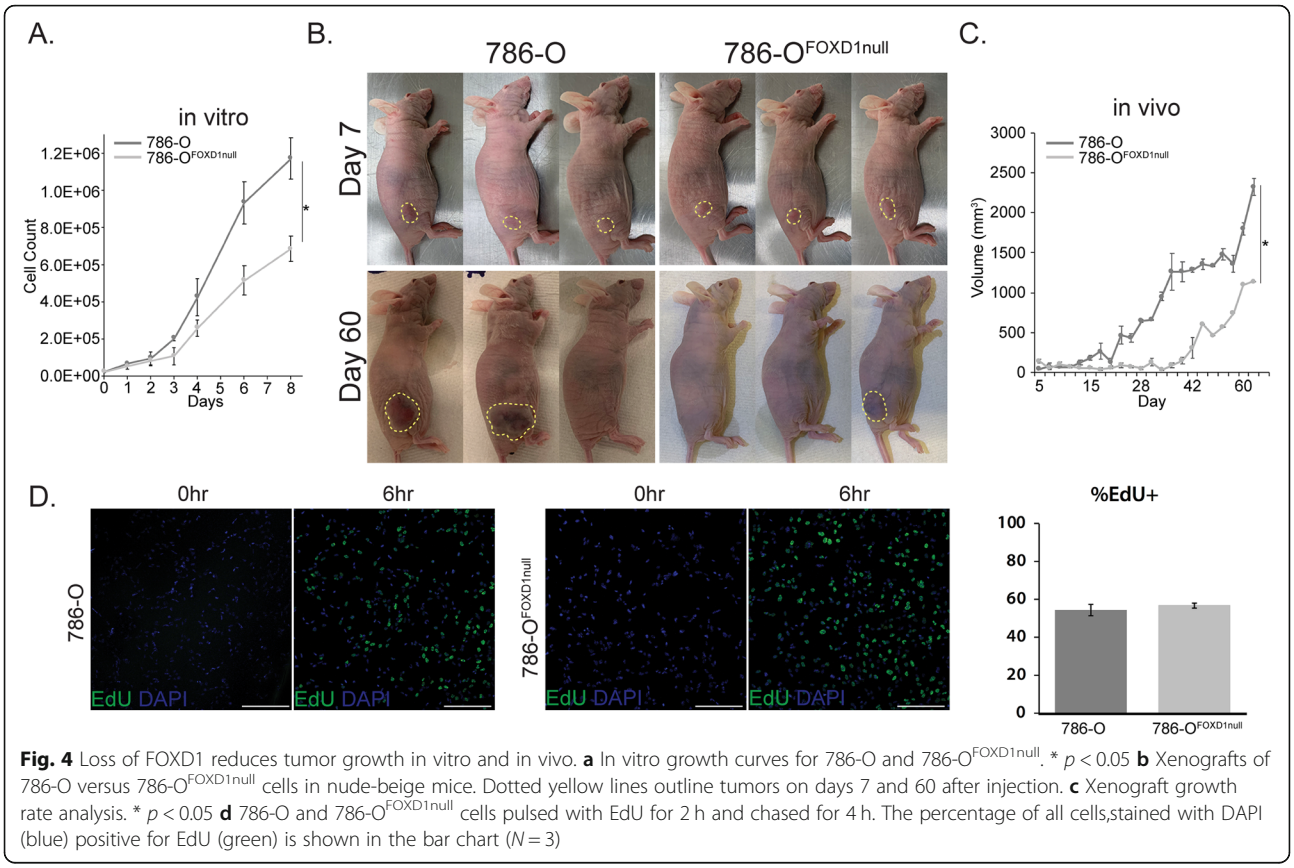

Fig. 4 Loss of FOXD1 reduces tumor growth in vitro and in vivo. **a** In vitro growth curves for 786-O and 786-O^{FOXD1null}. * $p < 0.05$ **b** Xenografts of 786-O versus 786-O^{FOXD1null} cells in nude-beige mice. Dotted yellow lines outline tumors on days 7 and 60 after injection. **c** Xenograft growth rate analysis. * $p < 0.05$ **d** 786-O and 786-O^{FOXD1null} cells pulsed with EdU for 2 h and chased for 4 h. The percentage of all cells,stained with DAPI (blue) positive for EdU (green) is shown in the bar chart ($N = 3$)

described [18, 19]. After tumor establishment, 70% of 786-O^{FOXD1null} tumors regressed, compared to only 30% for 786-O (Fig. S4A,B). 786-O^{FOXD1null} tumors that were established showed significantly reduced growth rate compared to 786-O (Fig. 4c). FOXD1 promotes expression of CDKN1A/p21 [20], and our expression analysis of 786-O^{FOXD1null} showed reduced *CDKN1A/p21* expression (Fig. 2e). CDKN1A/p21 delays the G1 to S transition, and reducing its expression is predicted to accelerate cycling time, which is contradictory to our observations in vitro and in vivo. To investigate if *FOXD1* inactivation influences the G1-S transition, we performed an EdU pulse-chase experiment to analyze the percentage of cells able to enter S phase. A 2 h EdU pulse followed by a 4 h chase did not show any difference in S phase entry between 786-O and 786-O^{FOXD1null} (Fig. 4d), and it is unlikely that the reduced proliferation in *FOXD1* null cells is due to delayed G1-S transition.

Loss of FOXD1 causes cell cycle delay at G2/M and inability to phosphorylate histone H3

To determine if the reduced proliferation caused by loss of *FOXD1* may be due to stalling at the G2/M checkpoint, we synchronized cells with a double thymidine block and timed phases of the cell cycle by analyzing DAPI incorporation (Fig. 5a). Corroborating the EdU analysis, both lines proceed at the same rate from G1 to S phase and by 8 h both have entered G2/M. While 786-O cells have largely transitioned out of M by 10 h, the transition of 786-O^{FOXD1null} out of M is delayed by 2–4 h. G2/M delay provides an explanation for the reduced growth of 786-O^{FOXD1null} in tumor xenografts and in vitro.

To further understand when cells pass the G2/M checkpoint, we investigated a panel of markers selected as follows. CDC2 and CyclinB1: The activated CDC2-CyclinB1 complex is necessary for progression through the G2/M checkpoint into mitosis [21]. CyclinB1 steadily rises through the early stages of the cell cycle until peaking at late G2, after which its level rapidly declines. CDC2, when phosphorylated on T161, activates the CDC2-CyclinB1 complex and initiates progression through the G2/M checkpoint. However, phosphorylation at Y15 inactivates the complex and prevents progression through the checkpoint. In order for cells to proceed into mitosis, CDC2 would need phosphorylation at T161 and dephosphorylation at Y15. In 786-O cells, phosphorylation of CDC2 occurs at both T161 and Y15 until 10 h, at which time phosphorylation of Y15 significantly decreases while T161 levels are still

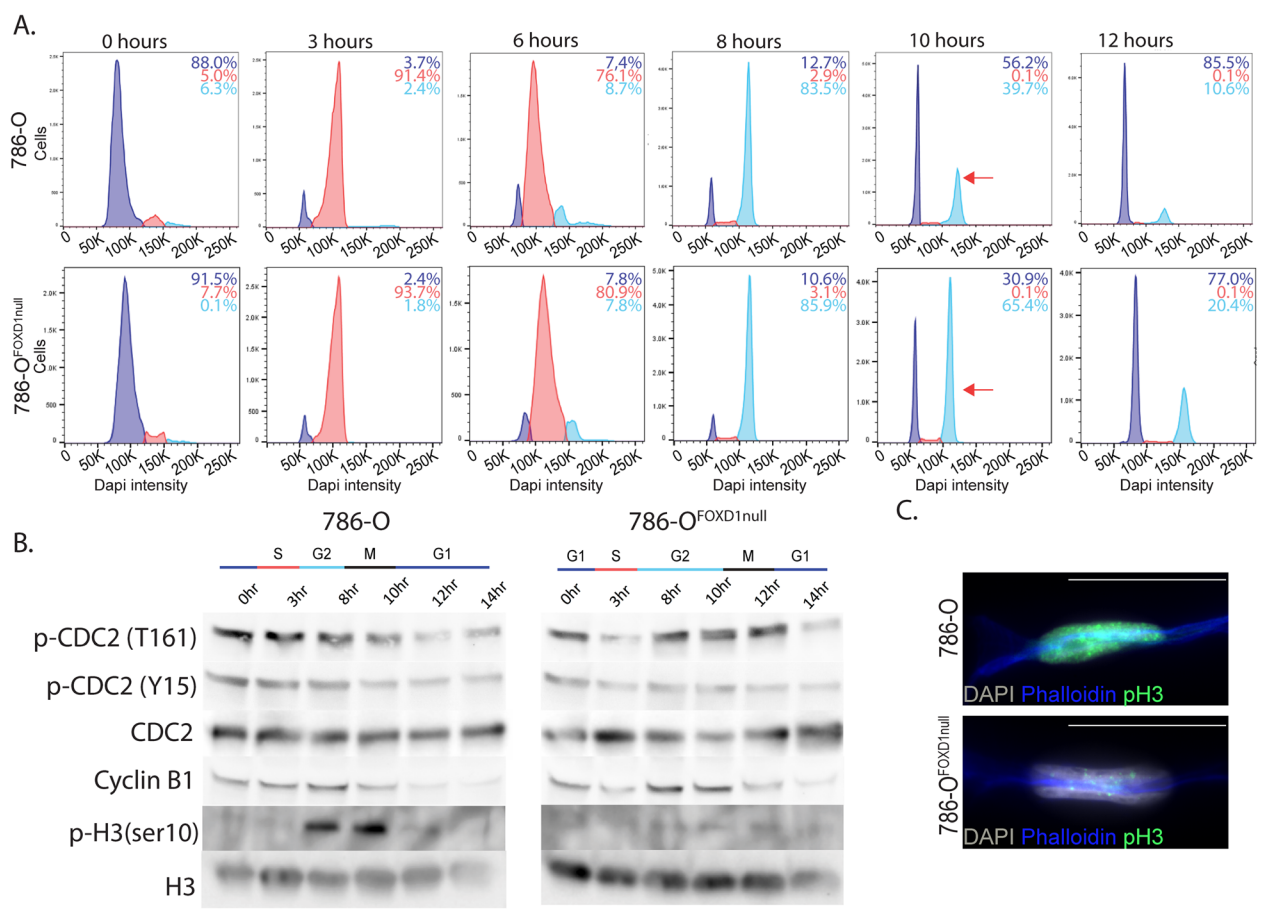

Fig. 5 G2 progression and histone H3 phosphorylation at ser10 are impaired in FOXD1 null cells. **a** Cell cycle analysis of synchronized cells at intervals after release from double thymidine block. Red arrows indicate a significant difference ($p < 0.05$) in phase distribution between lines after 10 h post-block ($N = 2$). **b** Western blot analysis of proteins necessary for progression through G2/M at intervals after release from synchronized block, comparing 786-O and 786-O^{FOXD1null}. Predicted cell cycle phases at each time point are graphically represented above the blots. Full-length blots are presented in Supplementary Figs. S5, S6, and S7. **c** Representative pH3 (green) immunocytochemistry of 786-O parent and 786-O^{FOXD1null} of cells in metaphase, counterstained with phalloidin (blue) and DAPI (gray)

elevated. By 12 h, phosphorylation at T161 significantly drops, indicating completion of mitosis. Additionally, CyclinB1 levels steadily increase until 8 h before rapidly dropping at 10 h. This supports our previous prediction that cells enter G2/M by 8 h post-synchronization, and complete mitosis by 12 h post-synchronization. In comparison, the 786-O^{FOXD1null} cells maintain elevated p-CDC2(T161) levels through the same time course, only reducing levels at 14 h. p-CDC2(Y15) levels in parallel showed constitutively high levels until 12 h post-synchronization. CyclinB1 peaks at 8 h, like the parental line, but this level is maintained until 12 h post-synchronization. Serine 10 phosphorylation of histone H3 at promoter regions of select genes such as *FOS* and *JUN* [22] regulates abundance of the AP1 transcription factor that is required for expression of mitotic regulators including Aurora kinase B [23]. Because of the abundance of this phosphorylation, it is commonly used as a marker of mitosis. We thus chose to look additionally at pH 3 and found that 786-O^{FOXD1null} showed significantly reduced levels of pH3 compared to 786-O at the G2/M-G1 interface (Fig. 5b, Fig. S5). Despite abundant expression of histone H3 in 786-O^{FOXD1null}, phosphorylation is very modest compared with 786-O.

Cells were immunostained to understand if the phosphorylation of H3 is reduced in all cells, or if there are fewer cells with H3 phosphorylation in 786-O^{FOXD1null} compared with 786-O. All nuclei in 786-O^{FOXD1null} showed depressed phosphorylation of H3. Phosphorylation of H3 peaks at metaphase, a stage that is defined histologically by colocalization of actin fibers with chromosomes. Comparing nuclei of 786-O with 786-O^{FOXD1null} at this stage revealed little pH3 in the 786-O^{FOXD1null} (Fig. 5c, Table S4). These findings support a

requirement for FOXD1 in pan-chromosome phosphorylation of H3 serine 10. Overall, loss of FOXD1 results in prolonged time spent at the G2/M checkpoint and an inability to phosphorylate histone H3.

FOXD1 expression is necessary for genomic integrity through mitosis

A second essential function of histone H3 phosphorylation is the condensation of chromosomes, which depends on serine 10 phosphorylation of H3 throughout each chromosome [24]. Improper chromosome condensation promotes DNA damage [25], and we therefore compared strand breaks in 786-O with 786-O^{FOXD1null} by staining for TUNEL and found that 786-O^{FOXD1null} cells show a significantly increased numbers of TUNEL-positive foci per nucleus than 786-O (Fig. 6a). Each TUNEL puncta represents DNA strand breakage, and the analysis suggests that only approximately 50% of 786-O^{FOXD1null} cells have intact genomes compared with 80% of 786-O. In response to DNA damage, cells typically phosphorylate H2AX (γH2AX) at locations of double strand breaks to indicate regions needing DNA repair. We further investigated if γH2AX levels were also elevated in 786-O^{FOXD1null} cells, and found a similar pattern to TUNEL, although the proportions of nuclei staining with γH2AX was greater, suggesting that this assay is more sensitive (Fig. 6b). DNA damage is normally repaired during G2/M and cells that have undergone mitosis should display strongly reduced γH2AX staining. To understand if DNA damage is repaired during G2, we performed an EdU pulse-chase experiment. Although synchronizing cells as shown in Fig. 5a would facilitate this experiment, the synchronization procedure introduces DNA damage, and would confound the analysis. Based on an S phase length of approximately 6 h (Fig. 5a), we performed an 8 h pulse to label cells entering G2 (Fig. S6). Expression of pH3 in 786-O showed a peak at 2 h following EdU wash-out and defined a subpopulation that had synchronously transitioned to mitosis (Fig. 6c). By 4 h after wash-out, the number of pH3+ cells had returned to baseline, indicating exit of this subpopulation from mitosis. Immunostaining for γH2AX in this subpopulation revealed that staining peaked concomitantly with pH3 and declined to 0% 4 h after wash-out (Fig. 6d), showing a complete reset of the chromosomal markers for DNA damage and suggesting comprehensive DNA damage repair in 786-O. As anticipated, 786-O^{FOXD1null} did not show a pH3 peak (Fig. 6c), but γH2AX immunostaining of the pH3+ subpopulation did show a peak at 2 h after wash-out (Fig. 6d). However, γH2AX declined only modestly following the peak, showing that chromosomal damage markers were not reset, and suggesting remaining DNA damage following mitosis in 786-O^{FOXD1null}. These findings were replicated with 3 different EdU-pulse labeling time periods (Fig. S6). To determine if DNA damage was reduced in all 786-O^{FOXD1null} cells, or if the 786-O culture may be a mosaic of cells in which DNA damage is repaired and cells in which it is not, we compared nuclei of 786-O and 786-O^{FOXD1null} cells immunostained with γH2AX, phalloidin, and DAPI to define mitotic cells with colocalized chromatin and actin (Fig. 6e). Interestingly, while γH2AX was not detected in cells going through anaphase in either 786-O or 786-O^{FOXD1null}, we found a significant number of cells with γH2AX in at least one daughter cell during cytokinesis, indicating that the sustained DNA damage found in 786-O^{FOXD1null} is likely due to strand breaks that arise during mitosis (Table S4).

Taken together, our data shows that *FOXD1* is required for 786-O tumor cells to undergo mitosis with DNA damage repair of both daughter cells. To understand if this mechanism could underlie the reduced patient survival seen in ccRCC cases with high *FOXD1* tumor expression (Fig. 1a), we performed a correlation analysis between *FOXD1* expression in ccRCC tumors and biological pathways. First, *FOXD1* expression was correlated with expression of all other genes in ccRCC transcriptomes from the TCGA database (Fig. 6f). Strongly correlated genes were then analyzed using Gene Set Enrichment Analysis to identify biological pathways (Fig. 6g). *FOXD1* expression was associated with cell cycle checkpoint pathways and pathways controlling chromosomal architecture in mitosis, suggesting that FOXD1 may indeed participate in these processes in patient tumors. The top common pathway components include members of the nuclear pore complex (*SEC13, NUP37)*, centromere subunits (CENPM, CENPN, CENP Q), and enzymes (PPP2R5A, PPP2R5B, CDC20, BUB1). Candidate genes within the top scoring pathways include kinases and phosphatases involved in phosphorylation of Histone H3 (Fig. S7).

Discussion

Our analysis indicates that FOXD1 is required for the appropriate phosphorylation of histone H3, which maintains DNA integrity during mitosis. The capacity for DNA damage repair differs widely between different types of tumors, and ccRCC displays moderate genomic damage [26]. ccRCC is generally resistant to both cisplatinum and radiation-induced DNA damage, suggesting active DNA damage repair in these tumors. Our data suggests that FOXD1 expression is necessary for proper cell division and may serve a protective role during mitosis in tumor cells predisposed to severe genetic damage.

Based on previous work demonstrating a role for FOXD1 in controlling expression of MICU1, which

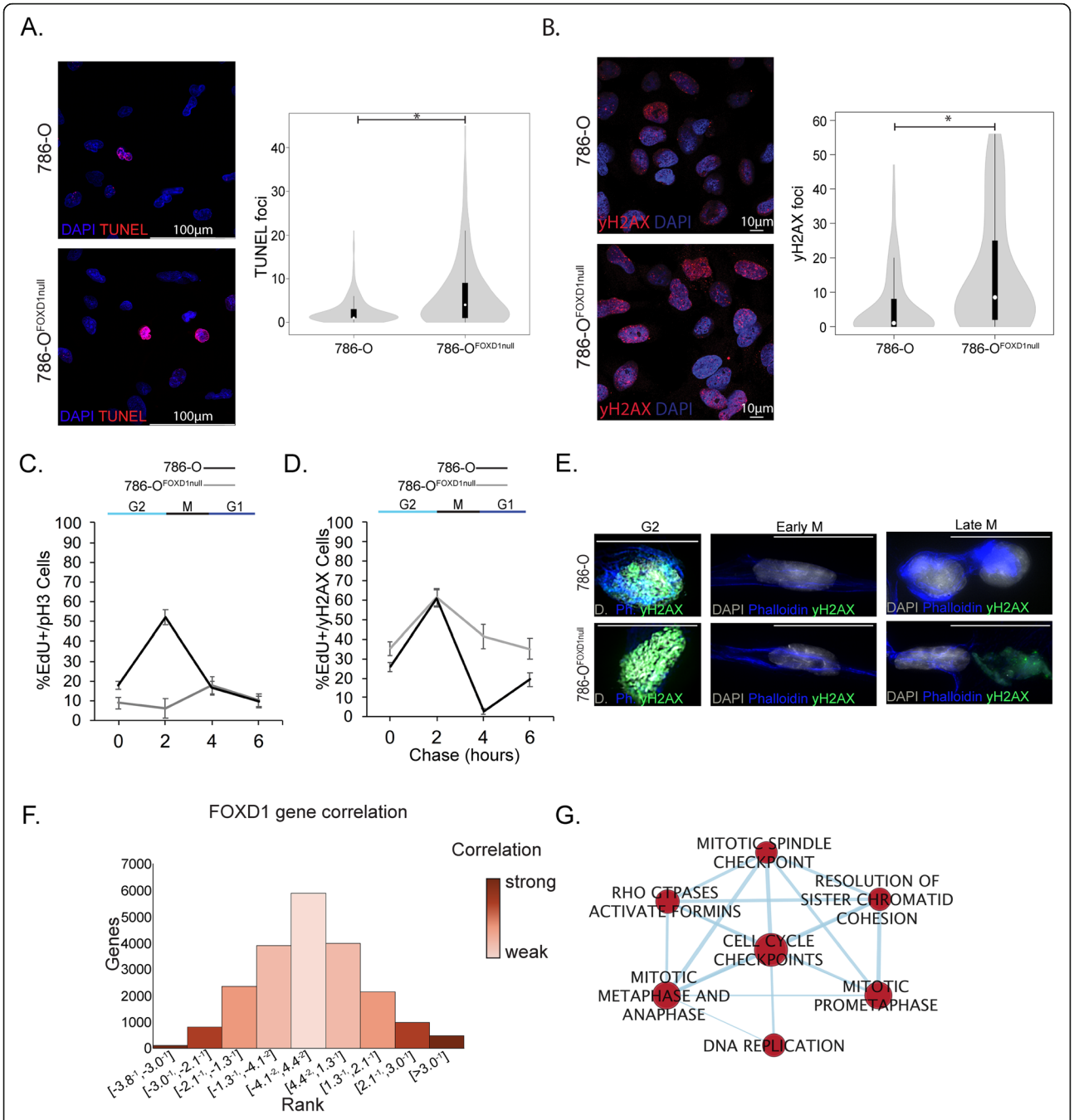

Fig. 6 FOXD1 is necessary for maintaining DNA integrity following mitosis. **a** Representative TUNEL (red) staining of 786-O versus 786-O^{FOXD1null}, counterstained with DAPI (blue) . Nuclear TUNEL foci were counted and compared using Student's t-test ($N = 3$). *$p < 0.05$ **b** Representative γH2AX (red) immunocytochemistry of 786-O versus 786-O^{FOXD1null} cells, counterstained with DAPI (blue). Nuclear γH2AX foci were counted and compared using Student's t-test ($N = 3$). *$p < 0.05$ **c** EdU pulse-chase cell cycle progression analysis. Cells in G2 were labeled with EdU following 8 h incubation with EdU. Labeled cells were analyzed for pH3 expression every 3 h post-labeling using immunocytochemistry. One hundred EdU+ cells were analyzed ($N = 3$). **d** Analysis of EdU labeled cells in G2 for γH2AX expression every 2 h post- labeling by immunocytochemistry. One hundred EdU+ cells were analyzed ($N = 3$). **e** Immunocytochemistry analysis of γH2AX (green) at different phases of the cell cycle, costained with DAPI (gray) and phalloidin (blue). Early M represented by cells in metaphase and late M representing cells undergoing cytokinesis and entering post-mitosis G1. **f** Correlation of mean FOXD1 expression against all genes found in the KIRC TCGA database. Ranked values scored using the Pearson correlation coefficient. **g** Gene set enrichment analysis of ranked FOXD1-correlated genes shows enrichment of REACTOME pathways related to mitotic entry and progression

regulates calcium flux in the mitochondrion, we hypothesized that reduced proliferative capacity of *FOXD1* null tumor cells may be due to reduced energy production capacity [14]. Metabolic analyses revealed a bioenergetic shift away from mitochondrial respiration but also demonstrated compensation by increased glycolysis resulting in unaltered ATP production. In light of this finding, reduced energy production does not explain the reduced proliferative capacity. Despite maintained energy production, a shift towards glycolysis may have consequences for basic cell behaviors through the production of a range of metabolites for biosynthetic pathways, and in other tumor cell contexts this is characteristic of increased proliferation [27]. Thus, it is counterintuitive that the bioenergetic shift seen in *FOXD1* null cells would explain reduced proliferation, and the cause is more likely to be a direct effect on the cell cycle.

The loss of histone H3 phosphorylation seen upon *FOXD1* inactivation does not prevent entry into mitosis, and compensatory mechanisms, such as CENPA nucleosome formation, may allow mutant cells to complete the cell cycle [28]. We found centromere subunits associated with this complex were highly correlated with FOXD1 expression, further supporting this possibility (Fig. 6g). However, the CENPA nucleosome complex is known to be unstable in vivo and this compensatory mechanism may be limited to cell culture [29, 30], providing an explanation for the difficulty in generating tumors from 786-$O^{FOXD1null}$ xenografts.

FOXD1 expression is tightly controlled in the adult, and our analyses of healthy human kidney tissue showed no expression in tubule epithelium, which is the cell population of origin for ccRCC [31]. *Foxd1* was initially characterized as a regulator of kidney development through studies in knockout mice [4], and it is specifically expressed in the progenitor population of the kidney interstitium [32]. Interestingly, recent gene expression analysis has shown a slightly broader expression pattern for *FOXD1* in the human fetal kidney, including a subset of progenitor cells of the tubule epithelium [33]. Thus, the expression of FOXD1 in dedifferentiated tubule epithelial cells in ccRCC may represent partial regression to a developmental progenitor for the tubule epithelium. The nephron progenitor cell population of the developing kidney is highly proliferative, and studies in mouse suggest that it relies heavily on glycolysis, similarly to the ccRCC cell [34]. *FOXD1* is located on chromosome 5 approximately 60 megabases from *VHL*, which is the most common primary mutation in ccRCC. Thus, an alternate possibility is that *FOXD1* expression becomes deregulated by the genetic hit at the *VHL* locus that initiates transformation, rather than being activated as a component of a dedifferentiation program.

The finding that FOXD1 expression is mosaic in the majority of tumors indicates that it may be activated or inactivated in subpopulations of tumor cells. Given its role in promoting cell cycle progression and DNA damage repair, *FOXD1* would be expected to confer a growth advantage, and for this reason it seems most likely that it is activated in subsets of cells as the tumor ages. Mechanisms governing cellular localization of FOXD1 are not known, and an alternate explanation for the mosaicism that we see in patient tumors may be that nuclear FOXD1 accumulation is dynamic and regulated by environmental factors that differ in distinct regions of tumors. Structure-function studies of the FOXD1 protein and a better understanding of tumor architecture will be required to evaluate these possibilities.

This study uncovers a novel and important role for FOXD1 in controlling division and DNA repair of ccRCC tumor cells. Further studies aimed at defining how the activity of FOXD1 is regulated will determine if this is a tractable therapeutic pathway.

Conclusions

This work supports a role for FOXD1 as a potent driver of tumor growth in ccRCC. *FOXD1* expression inversely correlated with patient outcome and was also shown to be grade and stage dependent. Inactivation of *FOXD1* significantly decreased the expression of components of mitochondrial metabolism in ccRCC cells and promoted glycolysis, but did not influence overall energy production. The cell cycle was altered by loss of *FOXD1*, with a delay in progression through the G2/M checkpoint, which associated with increased DNA damage. Phosphorylation of histone H3 was lost in *FOXD1* null cells, providing an explanation for the increase in mitotic defects. Based on our investigation, we propose that FOXD1 is required for histone H3 phosphorylation in rapidly cycling ccRCC cells, ensuring that they can proceed through the cell cycle without catastrophic DNA damage. Transcriptomic evidence from human ccRCC tumors correlating *FOXD1* expression with expression of kinases and phosphatases that modulate histone H3 phosphorylation supports this interpretation. Understanding how FOXD1 controls mechanisms governing histone H3 phosphorylation in ccRCC has potential therapeutic applications that will be explored in future work.

Abbreviations

TCGA: The Cancer Genome Atlas; ccRCC: Clear cell renal cell carcinoma; ICE: Inference of CRISPR Edits; H3: Histone H3; pH 3: Phosphorylated histone H3

Supplementary Information

The online version contains supplementary material available at https://doi.org/10.1186/s12885-021-07957-8.

Additional file 1 Table S1: Summary of patient clinical data used for FOXD1 immunohistochemistry analysis. **Table S2:** Primers used for FOXD1 genotyping and off-target analysis. * Blue indicates primers used for sequencing mismatch region. ** Red bases indicate mismatches from FOXD1. **Table S3**: Primers for reference genes, FOXD1 targets, and mitochondrial metabolism components. **Table S4**: Nuclear morphology analysis of 786-O and 786-O^{FOXD1null}. *Immunocytochemistry analysis of cells in different phases of the cell cycle after low density plating, based on nuclear and actin morphologies and localization. Percentage values are based on analysis of 100 cells per group across several fields. **Defects panel indicates collection of possible mitotic defects including lack of chromosome condensation (prophase), loss of spindle polarity (metaphase/anaphase), incomplete sister chromosome separation (cytokinesis), and death of daughter cell (post-mitosis G1). **Figure S1**: FOXD1 grade and stage analyses. (A) *FOXD1* expression level comparisons at different ccRCC tumor grades based on transcriptome data from The Cancer Genome Atlas (B) *FOXD1* expression level comparisons at different ccRCC tumor stages based on transcriptome data from The Cancer Genome Atlas. (C-D) Kaplan-Meier survival analyses for ccRCC patients with high versus low tumor expression of *FOXD1*, analyzed based of tumor stage. *$p < 0.05$. **Figure S2**: FOXD1 antibody validation. (A-B) TSA amplification staining for FOXD1 (green) on E12.5 mouse kidneys on normal and FOXD1-null backgrounds. Nuclei counterstained with DAPI (blue), (C-D) Immunohistochemistry staining of adult human kidney tissue (C) and FOXD1-null E12.5 mouse kidney (D). **Figure S3**: FOXD1 qPCR reference gene selection. (A) Stability scores generated by comparing candidate reference gene assays (Table S3) on equivalent mRNA quantities of 786-O versus 786-O^{FOXD1null} analyzed using the BioRad Reference Gene Selector Tool. Colors of bars denote genes that are over (green) or under the acceptable stability threshold between samples. (B-D) Standard curves for reference genes selected for this study. **Figure S4**: FOXD1-null cells difficulty in tumor establishment. (A) Xenograft of 786-O and 786-O^{FOXD1null} into flanks of 6-week old NCG mice. Red dotted line outlines tumors. Resected tumors from shown mice are shown in right-hand corner of image (B) Xenograft growth rate analysis. **Figure S5**: Histone H3 phosphorylation analysis. (A-B) Full membranes used for Western Blot analysis, with proteins visualized using the Bio-Rad Stain-Free gel system. Protein loading was quantified in each lane for normalization. (C-F) Full protein blots for histone H3 and phosphorylated histone H3 (Ser10) of synchronized 786-O and 786-O^{FOXD1null} cells at designated time points after release from thymidine block. Blue boxes indicate areas used for quantification. (G) Densitometry analysis (Ser10), normalized to total protein in well. **Figure S6**: CDC2 Phosphorylation analysis. Full membranes and quantification used for western blot analysis of CDC2 (A-B) and phosphorylated forms at T161 (C-D) and Y15 (E-F). All protein levels were normalized to total protein loaded. **Figure S7**: CyclinB1 and MICU1 protein analysis. Full membranes and quantification used for western blot analysis of CyclinB1 (A-B) and MICU1 (C-D). All protein levels were normalized to total protein loaded. **Figure S8**: EdU pulse-chase analysis. (A) Labeling schematic of pulse-chase experiment. Cells in S phase incorporate EdU and are labeled (yellow circles). After 8 h EdU treatment, cells in G2 are labeled with EdU. After 2 h (2 h chase), labeled cells in G2 progress into mitosis (M). After an additional 2 h (4 h chase), labeled cells in M divide and enter G1. (B) Representative images showing staining of pH 3 and γH2AX at 2 h intervals following EdU pulse of both 786-O and 786-O^{FOXD1null}. (C) EdU pulse-chase cell cycle progression analysis. Cells in G2 were labeled with EdU following 6 h or 10 h incubation with EdU. Labeled cells were analyzed for pH3 expression every 2 h post-labeling using immunocytochemistry. One hundred EdU+ cells were analyzed ($N = 3$). (D) Analysis of EdU labeled cells, for 6 h or 10 h inncubations, for γH2AX expression every 2 h post- labeling by immunocytochemistry. One hundred EdU+ cells were analyzed ($N = 3$). **Figure S9**: FOXD1 correlated genes involved in cell cycle regulation. Leading edge analysis of FOXD1 correlated genes from TCGA and top scoring candidates. *indicates kinases linked to phosphorylation of histone H3.

Acknowledgments

Seahorse assays were performed and analyzed on a Seahorse XF96 extracellular flux analyzer at Maine Medical Center Physiology Core facility (supported by NIH/NIGMS 3P20GM121301-03). Flow cytometry / cell sorting was performed at the Flow Cytometry Core Facility, LFKRI, New York Blood Center, New York, NY. We extend our sincere thanks to the staff of the New York Blood Center mouse facility for their dedication to maintaining the highest standards of animal care through the COVID-19 pandemic shutdown.

Authors' contributions

KHB performed all molecular and cellular biology experiments, and was aware of all group allocations throughout animal studies. JLF performed immunohistochemistry analysis of FOXD1 in patient samples. CWL performed all database analyses. IFE collected patient samples and provided insight necessary to compete this project. LO conceptualized and coordinated the project. All authors read and approved the final manuscript.

Funding

This work was supported by The Assistant Secretary of Defense for Health Affairs endorsed by the Department of Defense, through the Kidney Cancer Research Program under Award No. KC170016 (LO). Opinions, interpretations, conclusions and recommendations are those of the authors and are not necessarily endorsed by the Department of Defense. Funding was also provided by the Maine Cancer Foundation (LO). The funding bodies played no role in the design of the study and collection, analysis, and interpretation of data and in writing the manuscript.

Availability of data and materials

The datasets analyzed during the current study are available in the TCGA repository, https://portal.gdc.cancer.gov/projects/TCGA-KIRC. All data analyzed during this study are included in this published article. All datasets used and analyzed during the current study are available from the corresponding author on reasonable request.

Declarations

Ethics approval and consent to participate

Samples from resected tumors were obtained from the Maine Medical Center BioBank, which obtains surgical samples with the written informed consent of patients. The study was approved by the Maine Medical Center Institutional Review Board (IRB #4202X and IRB #4392). All animal studies were done in accordance with the National Research Council Guide for the Care and Use of Laboratory Animals, and all experiments were approved by the Institutional Animal Care and Use Committee of the New York Blood Center, where the Rogosin Institute research laboratory is located.

Consent for publication

Not applicable.

Competing interests

The authors declare that they have no competing interests.

Author details

[1]The Rogosin Institute, 310 East 67th Street, New York, NY 10065, USA. [2]Graduate School of Biomedical Sciences and Engineering, University of Maine, 168 College Ave, Orono 04469, ME, USA. [3]Maine Medical Center Research Institute, 81 Research Drive, Scarborough, ME 04074, USA. [4]Current affiliation: ICON Plc, 2100 Pembrook Parkway, North Wales 19446, PA, USA.

Received: 9 September 2020 Accepted: 23 February 2021
Published online: 24 March 2021

References

1. Lam EW, Brosens JJ, Gomes AR, Koo CY. Forkhead box proteins: tuning forks for transcriptional harmony. Nat Rev Cancer. 2013;13(7):482–95.
2. Bruno S, Bussolati B, Grange C, Collino F, Graziano ME, Ferrando U, et al. CD133+ renal progenitor cells contribute to tumor angiogenesis. Am J Pathol. 2006;169(6):2223–35.
3. Qian CN, Huang D, Wondergem B, Teh BT. Complexity of tumor vasculature in clear cell renal cell carcinoma. Cancer. 2009;115(10 Suppl):2282–9.

4. Hatini V, Huh SO, Herzlinger D, Soares VC, Lai E. Essential role of stromal mesenchyme in kidney morphogenesis revealed by targeted disruption of winged Helix transcription factor BF-2. Genes Dev. 1996;10(12):1467–78.
5. Zhao YF, Zhao JY, Yue H, Hu KS, Shen H, Guo ZG, et al. FOXD1 promotes breast cancer proliferation and chemotherapeutic drug resistance by targeting p27. Biochem Biophys Res Commun. 2015;456(1):232–7.
6. Nakayama S, Soejima K, Yasuda H, Yoda S, Satomi R, Ikemura S, et al. FOXD1 expression is associated with poor prognosis in non-small cell lung cancer. Anticancer Res. 2015;35(1):261–8.
7. Gao YF, Zhu T, Mao XY, Mao CX, Li L, Yin JY, et al. Silencing of Forkhead box D1 inhibits proliferation and migration in glioma cells. Oncol Rep. 2017; 37(2):1196–202.
8. Ju W, Yoo BC, Kim IJ, Kim JW, Kim SC, Lee HP. Identification of genes with differential expression in chemoresistant epithelial ovarian cancer using high-density oligonucleotide microarrays. Oncol Res. 2009;18(2–3):47–56.
9. Fetting JL, Guay JA, Karolak MJ, Iozzo RV, Adams DC, Maridas DE, et al. FOXD1 promotes nephron progenitor differentiation by repressing decorin in the embryonic kidney. Development (Cambridge, England). 2014;141;(1): 17–27.
10. Jassal B, Matthews L, Viteri G, Gong C, Lorente P, Fabregat A, et al. The reactome pathway knowledgebase. Nucleic Acids Res. 2020;48(D1):D498–d503
11. Shannon P, Markiel A, Ozier O, Baliga NS, Wang JT, Ramage D, et al. Cytoscape: a software environment for integrated models of biomolecular interaction networks. Genome Res. 2003;13(11):2498–504
12. Williams RD, Elliott AY, Stein N, Fraley EE. In vitro cultivation of human renal cell cancer. II. Characterization of cell lines. In Vitro. 1978;14(9):779–86
13. Quintero-Ronderos P, Laissue P. The multisystemic functions of FOXD1 in development and disease. J Mol Med (Berlin, Germany). 2018;96(8):725–39
14. Shanmughapriya S, Tomar D, Dong Z, Slovik KJ, Nemani N, Natarajaseenivasan K, et al. FOXD1-dependent MICU1 expression regulates mitochondrial activity and cell differentiation. Nat Commun. 2018;9(1):3449
15. Pan F, Li M, Chen W. FOXD1 predicts prognosis of colorectal cancer patients and promotes colorectal cancer progression via the ERK 1/2 pathway. Am J Transl Res. 2018;10(5):1522–30
16. Briston T, Stephen JM, Thomas LW, Esposito C, Chung YL, Syafruddin SE, et al. VHL-mediated regulation of CHCHD4 and mitochondrial function. Front Oncol. 2018;8:388.
17. Kim JW, Tchernyshyov I, Semenza GL, Dang CV. HIF-1-mediated expression of pyruvate dehydrogenase kinase: a metabolic switch required for cellular adaptation to hypoxia. Cell Metab. 2006;3(3):177–85.
18. Wang X, Zhang L, O'Neill A, Bahamon B, Alsop DC, Mier JW, et al. Cox-2 inhibition enhances the activity of sunitinib in human renal cell carcinoma xenografts. Br J Cancer. 2013;108(2):319–26.
19. Bhatt RS, Wang X, Zhang L, Collins MP, Signoretti S, Alsop DC, et al. Renal cancer resistance to antiangiogenic therapy is delayed by restoration of angiostatic signaling. Mol Cancer Ther. 2010;9(10):2793–802.
20. Wang Y, Qiu C, Lu N, Liu Z, Jin C, Sun C, et al. FOXD1 is targeted by miR-30a-5p and miR-200a-5p and suppresses the proliferation of human ovarian carcinoma cells by promoting p21 expression in a p53-independent manner. Int J Oncol. 2018;52(6):2130–42.
21. Lindqvist A, Rodríguez-Bravo V, Medema RH. The decision to enter mitosis: feedback and redundancy in the mitotic entry network. J Cell Biol. 2009; 185(2):193–202.
22. Strelkov IS, Davie JR. Ser-10 phosphorylation of histone H3 and immediate early gene expression in oncogene-transformed mouse fibroblasts. Cancer Res. 2002;62(1):75–8.
23. Oktay K, Buyuk E, Oktem O, Oktay M, Giancotti FG. The c-Jun N-terminal kinase JNK functions upstream of Aurora B to promote entry into mitosis. Cell Cycle. 2008;7(4):533–41.
24. Hendzel MJ, Wei Y, Mancini MA, Van Hooser A, Ranalli T, Brinkley BR, et al. Mitosis-specific phosphorylation of histone H3 initiates primarily within pericentromeric heterochromatin during G2 and spreads in an ordered fashion coincident with mitotic chromosome condensation. Chromosoma. 1997;106(6):348–60.
25. Wei Y, Yu L, Bowen J, Gorovsky MA, Allis CD. Phosphorylation of histone H3 is required for proper chromosome condensation and segregation. Cell. 1999;97(1):99–109.
26. Cancer_Genome_Atlas_Research_Network. Comprehensive molecular characterization of clear cell renal cell carcinoma. Nature. 2013; 499(7456):43–49.
27. Lunt SY, Vander Heiden MG. Aerobic glycolysis: meeting the metabolic requirements of cell proliferation. Annu Rev Cell Dev Biol. 2011;27:441–64.
28. Yoda K, Ando S, Morishita S, Houmura K, Hashimoto K, Takeyasu K, et al. Human centromere protein a (CENP-A) can replace histone H3 in nucleosome reconstitution in vitro. Proc Natl Acad Sci U S A. 2000;97(13): 7266–71.
29. Dimitriadis EK, Weber C, Gill RK, Diekmann S, Dalal Y. Tetrameric organization of vertebrate centromeric nucleosomes. Proc Natl Acad Sci U S A. 2010;107(47):20317–22.
30. Bui M, Dimitriadis EK, Hoischen C, An E, Quénet D, Giebe S, et al. Cell-cycle-dependent structural transitions in the human CENP-A nucleosome in vivo. Cell. 2012;150(2):317–26.
31. Frew IJ, Moch H. A clearer view of the molecular complexity of clear cell renal cell carcinoma. Annu Rev Pathol. 2015;10:263–89.
32. Kobayashi A, Mugford JW, Krautzberger AM, Naiman N, Liao J, McMahon AP. Identification of a multipotent self-renewing stromal progenitor population during mammalian kidney organogenesis. Stem Cell Rep. 2014;3(4):650–62.
33. Lindstrom NO, Guo J, Kim AD, Tran T, Guo Q, De Sena Brandine G, et al. Conserved and divergent features of Mesenchymal progenitor cell types within the cortical Nephrogenic niche of the human and mouse kidney. Journal of the American Society of Nephrology : JASN. 2018.
34. Liu J, Edgington-Giordano F, Dugas C, Abrams A, Katakam P, Satou R, et al. Regulation of nephron progenitor cell self-renewal by intermediary metabolism. J Am Soc Nephrol. 2017;28(11):3323–35.

Publisher's Note

Springer Nature remains neutral with regard to jurisdictional claims in published maps and institutional affiliations.

Ready to submit your research? Choose BMC and benefit from:

- fast, convenient online submission
- thorough peer review by experienced researchers in your field
- rapid publication on acceptance
- support for research data, including large and complex data types
- gold Open Access which fosters wider collaboration and increased citations
- maximum visibility for your research: over 100M website views per year

At BMC, research is always in progress.

Learn more biomedcentral.com/submissions

Materials Science & Engineering C 126 (2021) 112141

Contents lists available at ScienceDirect

Materials Science & Engineering C

journal homepage: www.elsevier.com/locate/msec

Development of a mechanically matched silk scaffolded 3D clear cell renal cell carcinoma model

Alycia Abbott [a], Kyle Bond [b], Takuto Chiba [c], Sunder Sims-Lucas [c], Leif Oxburgh [b], Jeannine M. Coburn [a,*]

[a] Worcester Polytechnic Institute, 60 Prescott St, Biomedical Engineering Department, Worcester, MA 01605, United States of America
[b] Rogosin Institute, 310 East 67th St, Room 2-43, New York, NY 10065, United States of America
[c] Children's Hospital of Pittsburgh of UPMC, 4401 Penn Ave, Rangos Research Bldg, Pittsburgh, PA 15224, United States of America

ARTICLE INFO

Keywords:
Scaffold
Mechanical testing
Tissue engineering
Cancer modeling

ABSTRACT

Development of a 3D, biomaterials-based model for clear cell renal cell carcinoma (ccRCC) would be advantageous for understanding disease progression *in vitro*. This study demonstrated the development of lyophilized silk scaffolds that mechanically match the experimentally determined Young's modulus for *ex vivo* ccRCC samples and normal kidney tissue. Scaffolds fabricated from silk solutions ranging from 3 to 12% (*w/v*) were evaluated through mechanical testing. Following mechanical characterization of ccRCC samples, it was demonstrated that 6% silk scaffolds mechanically matched ccRCC samples. No impact of pathological grade and stage on the calculated ccRCC modulus was observed and all tumors evaluated mechanically matched the 6% silk scaffold formulation. Stratifying tissue specimens based upon histological observations (*e.g.* evidence of high levels of collagen deposition) resulted in no significant differences between groups. To investigate the impact of a mechanically matched culturing environment on *in vitro* ccRCC disease characteristics a model ccRCC cell line, 786-O, was utilized. Scaffolded 786-O cells demonstrated increased lipid droplet accumulation, a hallmark of ccRCC, compared to standard two-dimensional (2D) culture conditions. Additionally, scaffolded 786-O cells demonstrated increased expression of genes associated with ccRCC aggressiveness (ex. *VEGFA, TNF,* and *IL-6*) or immune markers under investigation as therapeutic targets (ex. *PDL1*, *CTLA4*). Comparison with 786-O cells grown on non-mechanically matched scaffolds demonstrated that these improved ccRCC characteristics were driven by scaffold modulus. Overall, our findings support the use of silk scaffolds in replicating physiologic tumor behavior for clear cell renal cell carcinoma and provide a platform for investigating disease progression.

1. Introduction

Clear cell renal cell carcinoma (ccRCC) cases comprise 75% of all kidney tumors. In ccRCC, mutation or loss of the von Hippel Lindau (*VHL*) gene results in hypoxia-inducible transcription factors (HIFs) accumulation [1]. HIF accumulation results in dysregulated glycolysis, angiogenesis, and lipolysis, creating highly vascular tumors with rich lipid content [2]. Localized ccRCC can be addressed through curative surgery while metastatic ccRCC requires therapeutic treatment [3,4]. Unlike a number of other carcinomas, ccRCC does not typically respond to cytotoxic chemotherapeutic drugs [5]. Instead, current treatments utilize small molecule inhibitor drugs that target the vascular endothelial growth factor (VEGF) pathway or use novel immunotherapy agents [6–8]. Many immunotherapy agents utilize immune checkpoint inhibitor antibodies that target immune checkpoint-related proteins such as programmed death ligand 1 (PDL1) and cytotoxic T-lymphocyte associated protein 4 (CTLA4) to control disease progression [9]. However, ccRCC remains resistant to many therapeutic treatments and also develops resistance to efficacious therapies over time. Therefore, recent research focuses on understanding pathways involved in disease progression as the expression of tumor checkpoint molecules may impact therapeutic efficacy on ccRCC [9–11].

Current models of ccRCC include cell lines grown in 2D, 3D organoid systems, and mouse models [12–15]. Standard 2D culture techniques for ccRCC cells lines allow high throughput screening of therapeutics, but lack the 3D architecture found in ccRCC [11,16,17]. Despite this lack of

* Corresponding author at: 60 Prescott St, Rm 4035, Worcester, MA 01605, United States of America.
E-mail addresses: aaabbott@wpi.edu (A. Abbott), kyb9010@nyp.org (K. Bond), chibat@pitt.edu (T. Chiba), sunder.sims-lucas@chp.edu (S. Sims-Lucas), leo9022@nyp.org (L. Oxburgh), jmcoburn@wpi.edu (J.M. Coburn).

https://doi.org/10.1016/j.msec.2021.112141
Received 9 September 2020; Received in revised form 14 April 2021; Accepted 24 April 2021
Available online 29 April 2021
0928-4931/© 2021 Elsevier B.V. All rights reserved.

3D architecture, gene clustering analysis of ccRCC and ccRCC cell lines suggests that cell lines tend to cluster with more aggressive tumors (higher grade and stage) and can display corresponding clinical and genomic features [18]. Several ccRCC cell lines, such as 786-O cells, display lipid droplet accumulation which is considered a hallmark of ccRCC [19]. However, the mechanism behind this accumulation is poorly understood and some culture methods rely on further genetic modification, lipid loading, or stress-based situations such as over-confluency to achieve lipid accumulation [19,20]. It is possible these additional steps could be eliminated by the creation of a more physiologically relevant culture environment.

Biomaterials-based 3D culture methods present an attractive intermediate between 2D cell line culture and *in vivo* animal models due to the ability to develop and control the 3D microenvironment. Recapitulation of the tumor microenvironment has been demonstrated as an important factor in replicating *in vivo* tumor aggressiveness and progression [21,22]. Currently 3D culture methods for ccRCC cells are focused on sphere, spheroid, and aggregate formation [13,23]. Some of these methods require specialty media formulations supplemented with stem cell growth factors while growth on biomaterials could offer 3D support without the need for complex media formulations [13,14,23]. Silk fibroin (silk) has previously been used to develop 3D models for a wide variety of diseases [24–27]. Silk, an abundant and natural biomaterial, demonstrates excellent biocompatibility, exhibits long-term stability, and can be produced in a variety of formats with high reproducibility at low costs [28–30]. Silk scaffolds are currently available commercially for reconstructive surgery as well as soft tissue regeneration applications [31–33]. Lyophilized silk scaffolds allow a high degree of control over physical properties such as pore structure and Young's modulus [29]. Both the biomaterial pore structure and the underlying scaffold stiffness have previously been shown to influence cancer cell behavior [34].

In this work, we developed lyophilized silk scaffolds to mechanically match experimentally determined Young's modulus for *ex vivo* ccRCC and kidney tissue. While performing mechanical characterization of the clinical specimens, we evaluated the impact of pathological grade and stage on the Young's modulus. Additionally, we grouped tissue specimens based upon histological observations and mechanically matched those groups to silk scaffolds. Following matching, we utilized the 786-O ccRCC cell line to examine the impact of 3D growth within silk scaffolds on ccRCC disease progression indicators, including lipid droplet accumulation and modulation of ccRCC-associated transcripts.

2. Materials and methods

2.1. Silk fibroin extraction

Silk solutions were generated as described previously [28]. Silk fibroin was extracted from *Bombyx mori* silkworm cocoons kindly provided by Dr. David L. Kaplan (Tufts University, Medford, MA). In brief, 1 cm × 1 cm pieces of cocoons were boiled in 0.02 M sodium carbonate (Sigma-Aldrich, St. Louis, MO) for 30 min followed by washing with ultrapure water (Milli-Q, Millipore, Burlington, MA). The resulting silk fibers were dissolved in 9.3 M lithium bromide (Sigma-Aldrich) for 4 h at 60 °C. The silk solution was dialyzed against ultra-pure water using 3500 molecular weight cutoff tubing (Fisher Scientific, Hampton, NH) for 3 d with at least 6 water changes. Non-soluble debris were removed through centrifugation at 9000 rpm for 20 min. The aqueous silk solution was stored at 4 °C for future use.

2.2. Silk scaffold fabrication

Silk solutions of 3% and 6% (*w/v*) were generated through dilution of silk with ultrapure water (Fig. 1A). Silk solutions of 9% and 12% were generated through placing lower concentration silk solutions in dialysis tubing and allowing the water to evaporate with the use of dry heat at

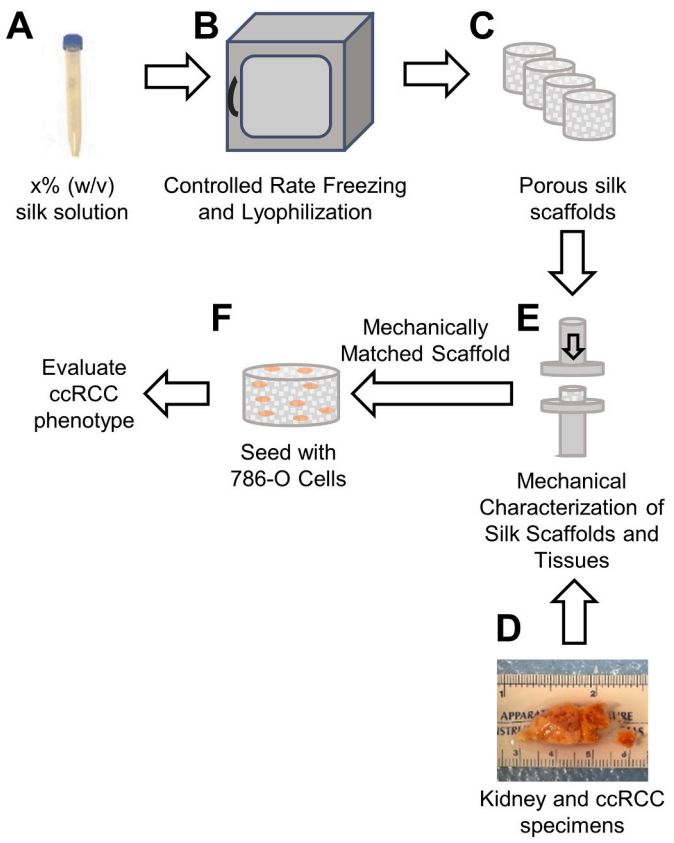

Fig. 1. Schematic of silk scaffold fabrication, mechanical testing, and *in vitro* ccRCC evaluation. (A) Different concentrations of silk solution underwent (B) controlled rate freezing and lyophilization to produce (C) porous silk scaffolds. Scaffolds, (D) ccRCCs and healthy kidney tissues were (E) mechanically characterized *via* compression testing. (F) Silk scaffolds mechanically matched to ccRCC specimens were seeded with the 786-O ccRCC cell line and evaluated for ccRCC characteristics and compared to traditional monolayer culturing.

60 °C until the desired concentration was achieved. Silk scaffolds were fabricated through rate-controlled freezing of the silk solutions using a controlled temperature shelf lyophilizer (Labconco, Fisher Scientific) through a protocol modified from previous works (Fig. 1B) [24,25]. Briefly, 1 mL of silk solution was added to 15.6 mm cylindrical molds. Samples were equilibrated at 20 °C and then cooled to −45 °C at a rate of −0.5 °C/min. The vacuum was then pulled to begin primary drying. After a 2 h hold at −45 °C, samples were heated to −25 °C at a rate of 1 °C/min and maintained at −25 °C for 6 days. Secondary drying was conducted through heating to 4 °C at a rate of 1 °C/min followed by a 2 h hold. This was followed by heating to 20 °C at a rate of 1 °C/min. The vacuum was held at 0.210 Torr for all drying. After removing the lyophilized silk scaffolds from the mold, all samples underwent a 20 min dry autoclave cycle to render the scaffolds water insoluble (Fig. 1C). Insoluble silk scaffolds were autoclaved in ultrapure water for 30 min to hydrate samples for mechanical testing or sterilize for cell seeding.

2.3. Fourier transfer inverse spectrophotometry (FTIR)

FTIR and Fourier self-deconvolution were used to analyze secondary protein structures of the silk scaffolds. Background and spectral scans were measured from 600 to 4000 cm^{-1} at a resolution of 4 cm^{-1} for 64 scans per sample. Scaffolds were analyzed after the dry autoclave step (pre wet autoclave) and after the wet autoclave step (post wet autoclave) for mechanical testing. Hydrated samples were dried in a 60 °C oven overnight prior to FTIR analysis. Deconvolution was performed using

Opus 5.0 software (Bruker, Billerica, MA) as previously reported [35,36]. Secondary structure contributions were calculated through a ratio of the area under the curve to the sum of all areas under the curve of the fitted amide I region. Secondary structures were assigned as previously reported [36].

2.4. Pore size analysis

Silk scaffolds were sectioned into 100 μm thick sections on an oscillating tissue slicer (Electron Microscopy Sciences, Hatfield, PA). Sections were then stained with AdipoRed (Lonza, Switzerland), a fluorescent stain that non-specifically binds to silk, and imaged on an Eclipse 3600 microscope (Nikon, Tokyo, Japan). ImageJ was used to quantify the Feret diameter on the silk scaffold pores. Feret diameter, or maximum caliper, was selected due to observations of non-spherical pore shape.

2.5. Kidney sample collection

Whole kidneys rejected for organ transplant were provided by the University of Pittsburgh Medical Center. Kidney tumor tissue was obtained as part of surgical nephrectomies performed at the University of Pittsburgh Medical Center (Fig. 1D). Cancer diagnosis was performed by certified pathologists. Tissue adjacent to the surgical biopsy was collected at the discretion of the surgeon. All tissue was maintained in PBS at 4 °C and tested within 24 h of collection. All tissue specimens received were de-identified using an honest broker system. Images of all kidney specimens received may be found in Appendix A (**Fig. A1-A3**). Demographical and pathological information provided for the nephrectomy specimens and whole kidneys may be found in Appendix A (**Table A1; Table A3**). All experiments were reviewed by IRB boards at Worcester Polytechnic Institute, University of Pittsburgh, and the Rogosin Institute.

2.6. Mechanical testing

Silk scaffolds, ccRCC specimens, and rejected kidney specimens were biopsy punched to 6 mm in diameter. All samples were preloaded with 0.1 N on an Electropuls 1000 fitted with a 50 N load cell (accuracy to 1/500th of load capacity, Instron, Norwood, MA) before being compressed at a rate of 2 mm/min until 50% strain was achieved (Fig. 1E**; Fig. A4**). All compression tests were video recorded. The young's modulus were calculated from the linear region of the stress-strain curves.

2.7. Histology

Compressed tissue specimens were fixed in 10% buffered formalin, serially dehydrated, and embedded in paraffin or frozen in optimal cutting temperature media. The specimens were then sectioned at either 4 μm thickness (paraffin) or 6 μm thickness (frozen), affixed to glass slides, and underwent Masson's Trichrome (paraffin), Oil Red O (frozen), or immunostaining (paraffin). Immunostaining was conducted as previously described [37]. PDGFRβ primary antibody (ab32570, Abcam, Cambridge, United Kingdom) was used at 1:250 and donkey anti-rabbit HRP (A21206, Life Technologies, Carlsbad, CA). Vectastain ABC Elite kit (PK-7100, Vector Labs, Burlingame, CA) was used to amplify signal and the colorimetric reaction was performed using DAB. PDGFRβ stained sections were imaged on a Axioskop 2 plus micrscope (Zeiss, Oberkochen, Germany) while Masson's Trichrome and Oil Red O stained sections were imaged on an Eclipse 3600 microscope (Nikon, Tokyo, Japan). In addition, TissueFAXS PLUS (TissueGnostics, Vienna, Austria) was used for image tiling to capture the entire field of an Oil Red O stained kidney section with 20× objectives. The amount of collagen (blue colour) within Masson's Trichome images, the amount of lipids (red colour) within Oil Red O images, and the Feret diameter of PDGFRβ was quantified using ImageJ (NIH). Sections with greater than 30% blue content were classified as high collagen content.

2.8. 786-O cell culturing and seeding into Silk scaffolds

786-O cells were maintained in Advanced RPMI 1640 medium (Corning, Corning, NY) supplemented with 10% Premium Select FBS (Fisher Scientific), 100 U/mL penicillin (VWR, Radnor, PA), 100 μg/mL streptomycin (VWR), and GlutaMAX (Gibco, Gathersburg, MD). Cells were passaged at 70% confluence and seeded on 3, 6, or 12% silk scaffolds (Fig. 1F). Cell seeding was modified from a previously described method [25]. Silk scaffolds of 15.6 mm diameter or 6 mm diameter were used throughout all cell experiments. Scaffolds were sectioned by vibrating microtome to 200 μm thickness and sterilized through autoclaving. One million 786-O cells were seeded on the silk scaffolds in 24-well plates or 150,000,786-O cells were seeded on the silk scaffolds in 96-well plates and centrifuged for 50 s at 500 *g*. After 24 h, cell-seeded silk scaffolds were moved to 12-well plates or 48-well plates, respectively. For DNA content analysis, metabolic activity assays, and gene expression, 786-O cells were seeded on gelatin-coated 96-well plates or 24-well plates. For confocal imaging of 2D culture, cells were seeded onto gelatin-coated glass coverslips and grown to 70% confluency at time point zero.

2.9. DNA content analysis

DNA was collected after 3, 10, and 17 d of culture for analysis with a Quant-iT-PicoGreen dsDNA Assay Kit (Fisher Scientific). Samples were lysed for 20 min at room temperature with 0.5% Triton-X-100. All samples underwent a freeze-thaw cycle (−20 °C) prior to analysis. DNA concentration was determined by measuring fluorescence (480/520 nm, Victor^3 Multilabel Plate Reader, PerkinElmer, Waltham, MA) and comparing to both a lambda DNA and a 786-O cell standard curve.

2.10. Resazurin metabolic assay

Resazurin (0.15 mg/mL, Acros Organics, Pittsburgh, PA) was added in a 1:5 ratio with the cell medium after 3, 10, and 17 d of culture . Cells were incubated with resazurin for 3 h at 37 °C. Resazurin fluorescence was then read at an excitation of 544 nm and emission at 590 nm (Victor^3). Metabolic activity was normalized to cell numbers determined through Pico Green analysis.

2.11. Lipid droplet quantification in 786-O cells

Cell-seeded silk scaffolds and 2D cells were fixed in 4% paraformaldehyde after 3, 10, and 17 d of culture and stained with 0.5 μg/mL DAPI (D1306, Invitrogen, Carlsbad, CA) or 1:1000 DRAQ7 (ab109202, Abcam) and 2 μg/ml BODIPY 493/507 (Invitrogen) for 30 min at room temperature. Fluorescent imaging was conducted on an LSM 510 Meta Confocal Microscope (Zeiss) and the number of lipid droplets (BODIPY) per area was normalized to the number of cells (DAPI or DRAQ7) using Fiji.

2.12. Gene expression in 786-O cells

Total RNA was isolated after 3 d of culture using Buffer RLT and a RNeasy Mini Kit (Qiagen, Hilden, Germany) according to manufacturer's instructions. On column DNAse treatment was performed to remove DNA. Complement DNA (cDNA) was synthesized using iScript^{tm} Reverse Transcription Supermix for RT-qPCR (Bio-Rad, Hercules, CA). Real-time polymerase chain reactions were performed on a CFX384 Touch Real-Time PCR Detection System (Bio-Rad). Primer sequences are listed in **Table A1**. Primer validation was performed through creation of a 5-point dilution series standard curve. The geometric mean of the reference genes *TUBB*, *PGK1*, and *RPS18* were used for normalization, and the level of expression was calculated using the ΔΔCt method. Data are

presented as relative to 2D controls or to 6% silk scaffolded cells.

2.13. Statistical analysis

All statistical analysis was performed in Graphpad Prism 7. Normality of FTIR and Instron data was evaluated through Shapiro-Wilks testing while normality of pore size and lipid accumulation data was evaluated through D'Agostino & Pearson testing. Outlier analysis of Instron data was performed through ROUT analysis (Q = 1%). FTIR, pore size, and lipid accumulation data was compared through Student's *t*-test or nonparametric equivalent. Statistical analysis of the mechanical testing data was conducted using an ANOVA followed by a Tukey test or Dunnett's test. Equal variance was confirmed through the Brown-Forsythe test. RT-qPCR data C_q (quantitation cycle) values were normalized to the geometric mean of the indicated reference genes. Fold change was determined using the ΔΔCt method and statistical significance was calculated using a two-tailed Students *t*-test. All data are presented as mean ± standard deviation unless otherwise indicated.

3. Results

3.1. Impact of hydration method on secondary structures in Silk scaffolds

The mechanics of silk scaffolds were determined in a hydrated state to better match the envisioned end use as a cell culture scaffold. Porous silk scaffolds were created through the lyophilization of 3%, 6%, 9%, and 12% (*w/v*) solutions and autoclaved to render insoluble through induction of the beta-sheet conformation (Fig. 1A-C). Initially, the insoluble silk scaffolds were hydrated at room temperature in ultrapure water. However, we observed that the two highest silk scaffold formulations, 9% and 12%, were insufficiently hydrated. This insufficient hydration was apparent through differences in opacity and texture throughout the cross-section of the silk scaffolds with the interior being more opaque and stiffer to the touch. Therefore, autoclaving in ultrapure water was used to thoroughly hydrate the silk scaffolds. Following this hydration step, uniform opacity and texture was observed throughout the silk scaffold cross-sections and silk scaffolds were considered fully hydrated. FTIR analysis was used to investigate if the second autoclave step impacted the secondary structure of the silk scaffolds (**Fig. A5**). This analysis demonstrated that the hydration step did not significantly alter the secondary structures within the silk as the beta-sheet content in all silk scaffolds evaluated was unchanged pre and post the wet autoclaving step (Fig. 2A). Additionally, beta-sheet content did not significantly vary across silk scaffold formulations indicating that the silk solution concentration does not impact scaffold beta-sheet content.

3.2. Young's Modulus of lyophilized Silk scaffolds increases as the concentration increases

Once an appropriate hydration method for lyophilized silk scaffolds was determined, 3%, 6%, 9%, and 12% silk scaffolds underwent compression testing to determine the Young's modulus of each silk scaffold formulation (Fig. 1E). The Young's modulus of the silk scaffolds increased as the silk concentration increased with values of 0.406 ± 0.140 kPa, 3.200 ± 0.880 kPa, 6.133 ± 1.913 kPa, and 9.298 ± 1.255 kPa measured for the 3%, 6%, 9%, and 12% silk, respectively (Fig. 2B). Additionally, the Young's modulus of each silk group was significantly different from all other silk groups.

3.3. Evaluation of Young's Modulus for human kidney tissue

To understand the range of Young's modulus found in human kidney tissues, multiple types of human kidney specimens were evaluated (Fig. 1D) including ccRCC tumor tissue (tumor), tissue adjacent to the tumor biopsy site (adjacent), and the cortex and medulla region of rejected transplant kidneys. Tumor tissue had the lowest modulus (3.082 ± 0.963 kPa) while cortex tissue had the highest modulus (5.480 ± 1.409 kPa). A significant difference in Young's modulus was seen between the tumor and cortex tissue (Fig. 3A). No significant difference in modulus was seen between the tumor and adjacent tissue (4.303 ± 1.300 kPa) or between the cortex and medulla (4.813 ± 1.113 kPa) tissue. Individual modulus values for kidney tissues tested are provided in **Tables A2–5** to demonstrate the range of measurements recorded.

3.4. Silk scaffolds mechanically match ccRCC tissue

Next, the Young's modulus of the different silk scaffolds was compared to the human kidney tissue Young's moduli to determine which scaffold(s) would be best suited to replicate the ccRCC microenvironment for *in vitro* ccRCC modeling. ANOVA, followed by Dunnet's *post hoc* testing, with the kidney tissue type (tumor, cortex, *etc.*) set as the control, was performed to make these comparisons. The Young's modulus of the 6% silk scaffolds (3.200 ± 0.880 kPa) matched the Young's modulus of the ccRCC tumor tissue (3.082 ± 0.963 kPa) while all other silk scaffold formulations were significantly different (Fig. 3B). It was also found that the 9% silk scaffolds (6.133 ± 1.913 kPa) matched the Young's modulus of the cortex tissue (5.480 ± 1.409 kPa). Additionally, the 6% and 9% silk scaffolds mechanically matched both the adjacent and medulla tissue (**Fig. A6**). Overall, the 6% silk scaffold formulations matched the ccRCC tumor tissue and was used for all subsequent experiments.

3.5. ccRCC Tumor Composition Causes No Variation in Mechanical Properties

Of the eight confirmed ccRCC tumors, each possible tumor grade (1–4) was represented by two tumors. There was no clear relationship between tumor grade and Young's modulus (**Fig. A7**). Therefore, histological examination of several ccRCC tumor samples was conducted to investigate how ccRCC tumor composition may impact the mechanical

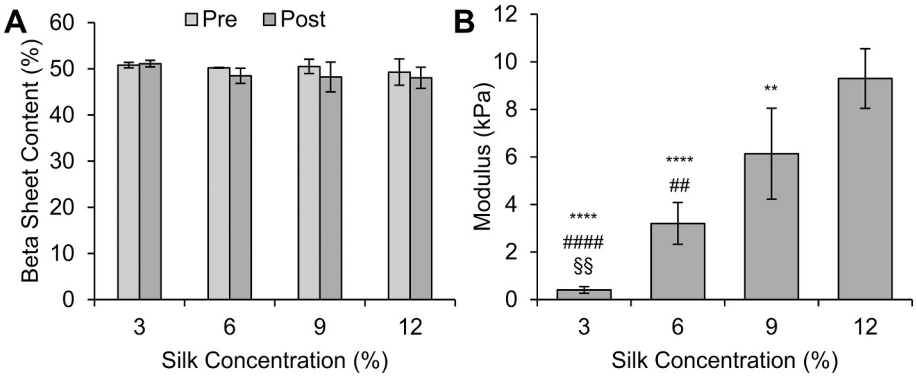

Fig. 2. Characterization of lyophilized silk scaffolds. (A) β-sheet content of the silk scaffolds pre and post the wet autoclave step. Data are presented as mean ± SD from 3 independent experiments with 3–4 samples. No significant difference in β-sheet content was seen between scaffolds in the pre and post wet autoclave groups. (B) Young's modulus of silk scaffolds presented as mean ± SD and is representative of four (9% and 12% silk) or five (3% and 6% silk) independent experiments with 3 samples. Young's modulus of each silk scaffold formulation is significantly different than Young's modulus of all other silk scaffolds (ANOVA with Tukey test: * indicates difference from 12% silk; # from 9% silk; § from 6% silk; two symbols = $p < 0.01$; three symbols = $p < 0.001$; four symbols = $p < 0.0001$).

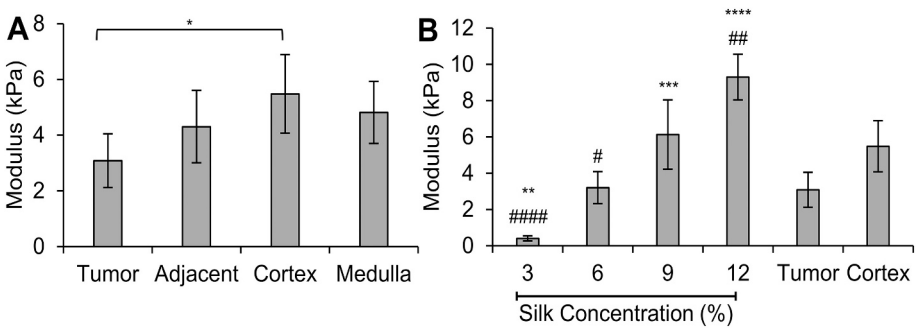

Fig. 3. Silk scaffolds match ccRCC Young's modulus. (A) Kidney data presented as mean ± SD and is representative of four (Cortex and Medulla), eight (Tumor), or seven (Adjacent) experiments with 1–5 samples. Young's modulus of Cortex and Tumor tissue are significantly different (ANOVA with Tukey test: $*p < 0.05$) (B) Young's modulus of silk scaffolds matched the kidney tissues. All data presented as mean ± SD. The asterisk (*) indicates significant difference from Tumor while the number symbol (#) indicates significant difference from Cortex (ANOVA with Dunnett's test: one symbol = $p < 0.05$; two symbols = $p < 0.01$; three symbols = $p < 0.001$; four symbols = $p < 0.0001$).

properties. Evidence of potential differences in intratumoral composition was observed when samples from the same tumor displayed large differences in Young's moduli as evidence by the large coefficient of variance, such as TP19-S080 and TP20-S063 (**Table A2**). To further investigate this, samples from three ccRCC tumors and respective adjacent tissue samples were stained with Masson's Trichrome after compression to gain an understanding of the tissue architecture and how it may impact mechanical properties. Tissue samples were divided into "high collagen" and "low collagen" groups using a 30% blue tissue area as the threshold stratifying the two groups (Fig. 4A). The impact of this stratification on mechanical properties was evaluated by comparing the Young's moduli of the stratified groups (Fig. 4B). No significant difference was seen between high collagen ccRCC (3.177 ± 1.314 kPa), low collagen (3.130 ± 1.508 kPa), high collagen adjacent (3.761 ± 1.989 kPa), or low collagen adjacent (3.834 ± 0.890 kPa) tissue suggesting collagen content is not the underlying cause of mechanical variations. Nonetheless, stratification due to collagen content demonstrated that 6% silk scaffolds match all groups of histologically stratified tissues while 9% scaffolds match all groups except for high collagen ccRCC tissue (Fig. 4C).

3.6. Silk scaffolds mechanically match multiple kidney tumor types

All tumor specimens received were mechanically characterized prior to receiving diagnostic information as there was a time delay between receipt of specimen and specimen diagnosis. Therefore, a portion of the specimens mechanically characterized were not classified as ccRCC. Including the non-ccRCC tumor and associated adjacent samples with the confirmed ccRCC tumor and their associated adjacent samples into a generalized kidney tumor and adjacent tissue pool resulted in minor, non-significant changes to the previously determined averages. The average Young's modulus of the tumor was reduced by 0.011 kPa while the average Young's modulus of the adjacent tissue increased by 0.150 kPa. Comparison of the pooled tumor and adjacent tissue samples to the cortex and medulla groups demonstrated that the tumor and cortex tissue were significantly different (**Fig. A8A**). Comparing the tissue and silk scaffold Young's modulus revealed that the 6% silk scaffolds (3.200 ± 0.880 kPa) mechanically match the pooled tumors and adjacent samples (3.071 ± 1.144 kPa) (**Fig. A8B**).

3.7. Silk scaffold Pore structure mimics ccRCC tumor clustering

Once 6% silk scaffolds were determined to be mechanically matched

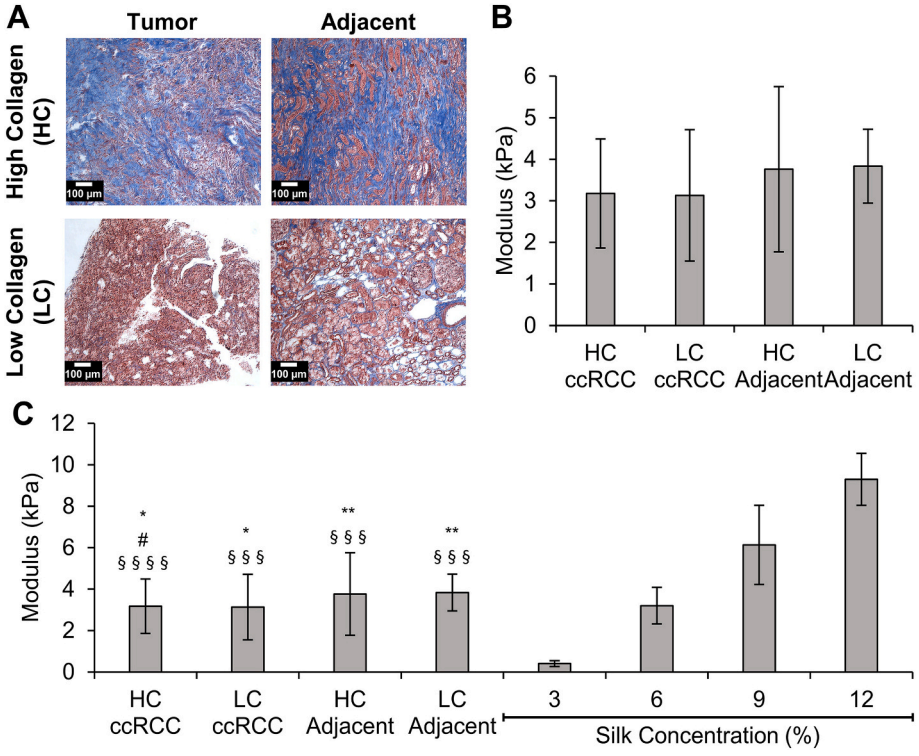

Fig. 4. Investigation of ccRCC total collage composition and modules. (A) Representative Masson's Trichrome images of "high collagen" (HC) and "low collagen" (LC) tumor and adjacent samples to show differences in collagen (blue) staining. (B) Young's modulus of histologically classified ccRCC and adjacent tissue. Data presented as mean ± SD with 3–6 samples. HC = high collagen content, LC = low collagen content. No significant difference between groups. (C) Young's modulus of histologically classified tumor and adjacent tissue compared to silk scaffolds. All data presented as mean ± SD. * indicates difference from 3% silk; # from 9% silk; § from 12% silk (ANOVA with Dunnett's test: one symbol = $p < 0.05$; two symbols = $p < 0.01$; three symbols = $p < 0.001$; four symbols = $p < 0.0001$). (For interpretation of the references to colour in this figure legend, the reader is referred to the web version of this article.)

to the ccRCC tumor tissue, further investigation into the silk scaffold pore structure was conducted to better understand the potential microenvironment. Silk scaffolds were stained to visualize the pore structure using fluorescence microscopy for imaging (Fig. 5A). To visualize ccRCC cluster size within received tumor samples, PDGFRβ staining was performed (Fig. 5B). Pore analysis conducted in ImageJ showed the average Feret diameter of the silk pores to be 49 ± 8 μm (Fig. 5C). The average Feret diameter of the ccRCC clusters was found to be 52 ± 22 μm. No significant difference between Feret diameter was seen between the silk scaffold and ccRCC clusters. Therefore, it can be concluded that the 6% silk scaffold pore size matches that of the ccRCC clusters.

3.8. Scaffolded 786-O cells exhibit increased lipid droplet development

After 6% silk scaffolds were shown to be matched to the ccRCC tumors based on Young's modulus and pore size, the 786-O cell line was used to investigate the potential of scaffolded ccRCC as a platform for investigating ccRCC progression (Fig. 1F). 786-O cells were cultured for up to 17 days in 6% silk scaffolds (3D) or on gelatin-coated glass cover slips (2D) and evaluated for lipid droplet accumulation as a hallmark of ccRCC phenotype (Fig. 6A). Scaffolded 786-O cells had significantly more lipid droplets per cell as compared to 2D culture on all days evaluated (Fig. 6C**; Fig. A9**). At 17 days, the amount of lipid droplets per cell in scaffolded 786-O cells was significantly greater when compared to all earlier time points. For comparison to the lipid droplet accumulation seen in scaffolded 786-O cells, Oil Red O staining was performed on a ccRCC specimen and adjacent tissue (Fig. 6B). Characteristic lipid accumulation was seen in ccRCC specimens while less lipid accumulation was seen in the adjacent tissue (Fig. 6D).

3.9. Scaffolded 786-O cells exhibit increased ccRCC characteristics

Since scaffolded 786-O cells demonstrated increased lipid droplet accumulation, a hallmark of ccRCC, transcriptional levels of genes associated with ccRCC were also investigated. Scaffolded 786-O cells were cultured for 3 days and then lysed for RNA. In parallel, RNA was collected from cells grown in 2D culture to 70% confluency. Markers chosen for investigation were linked to genetic alteration of VHL and were validated on cDNA pooled from human ccRCC tissue (data not shown). Gene expression data was divided into characteristics related to angiogenic recruitment [38](Fig. 7A), immune regulation [39] (Fig. 7B), fatty acid synthesis [40] (Fig. 7C) metabolic dysregulation [41] (Fig. 7D**),** and aggressiveness [42](Fig. 7E). Significant upregulation in genes related to signaling cytokines (*VEGFA, TNF,* and *IL6*) was observed in scaffolded 786-O cells (Fig. 7A**,7B**). Similarly, a significant upregulation *PDL1* and *CTLA4* (prognostic markers for immune checkpoint inhibition therapy) was observed in scaffolded 786-O cells (Fig. 7B) [39]. In contrast, significant downregulation of *CXCL8* (ccRCC stemness) [43], *ACACA* (Acetyl-CoA carboxylase), *FASN* (fatty acid synthesis) [40], and *CD10* (a VHL-dependent glycoprotein) [44] was seen in scaffolded 786-O cells compared to 2D culture (Fig. 7B**,** 7D).

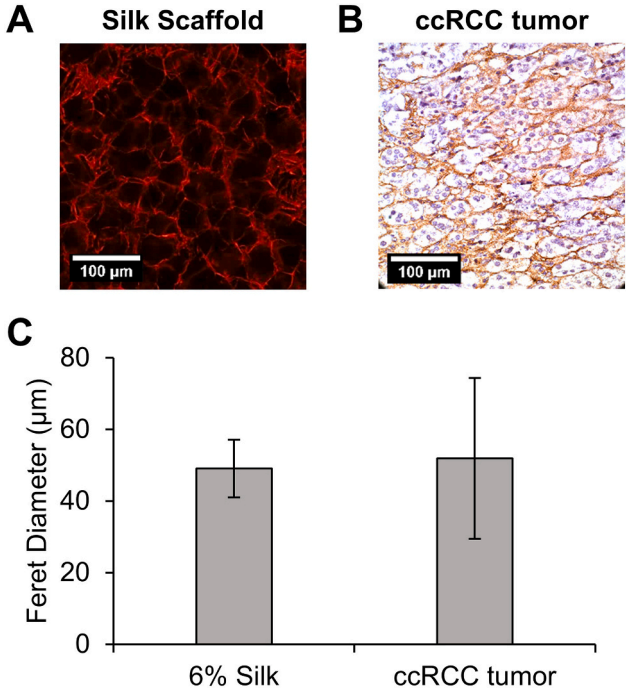

Fig. 5. Silk Scaffolds mimic ccRCC microenvironment. (A) Representative fluorescent staining of 6% silk pore structure. (B) Representative PDGFRβ stained ccRCC tumor clustering. (C) Average Feret diameter determined through ImageJ analysis. Data presented as mean ± SD and represents measurements from 8 silk images and 1 tumor image.

3.10. Impact of silk scaffold modulus on ccRCC characteristics

To further evaluate the impact of the Young's modulus of the silk scafolds on ccRCC characteristics, 786-O cells were grown on 3, 6, and 12% silk scaffolds. The impact of scaffold modulus on metabolic activity, gene expression, and lipid droplet accumulation was evaluated. The 3% and 12% scaffolds were chosen to represent the low and high end of Young's modulus of the silk scaffolds studied. There was no significant difference in metabolic activity found when normalized to cell number for any time point evaluated (Fig. 8A). A subset of metabolic and immune related genes (Section 3.9) were evaluated with 786-O cells scaffolded on 3% silk scaffolds expressing significantly less *Glut1* than 786-O cells scaffolded on 6% silk scaffolds (Fig. 8B). All 786-O cells grown on silk scaffolds demonstrated some level of lipid accumulation (Fig. 8C**; Fig. A10**). Scaffolded 786-O cells in 6% silk demonstrated increased lipid droplet accumulation compared to cells grown on 12% silk scaffolds after 17 d (Fig. 8D**).** To further investigate this, genes related to fatty acid synthesis (Fig. 8E) and pyruvate metabolism were evaluated (Fig. 8F). No significant differences in fatty acid synthesis gene expression was found; however, *PDP1* expression was significantly reduced in 786-O cells scaffolded on 12% scaffolds.

4. Discussion

Clear cell renal cell carcinoma (ccRCC) is a disease for which surgical treatment is the most common corrective measure. The five-year survival rate ranges from 91% to 32% with increasing stage and grade, and developing experimental platforms to investigate new drugs for treatment of cancers that recur following surgery is a priority [45]. Current 3D *in vitro* models to investigate disease progression are limited [46]. Here we developed a model system that incorporates 3D culturing and mechanical features, including substrate stiffness and pore size, similar to the tumor microenvironment to better develop the ccRCC phenotype *in vitro*.

It has been demonstrated that the underlying substrate stiffness impacts tumor progression [21,22]. Porous silk scaffolds with a range of Young's moduli have previously been fabricated through lyophilization [29,47]. Varying the initial silk concentration has been shown to impact the Young's modulus of the resultant silk scaffolds [48]. As expected, increasing the silk concentration from 3% to 12% increased the Young's modulus with average values obtained from 0.4 to 9.3 kPa. These results were shown to be repeatable between multiple silk batches and different lyophilization runs. The use of rate-controlled freezing for silk scaffold fabrication may have contributed to these consistent results as rate-controlled freezing produces more homogenous and consistent structures than non-rate controlled freezing [49]. The Young's moduli in this work were lower than previously reported values for similar silk

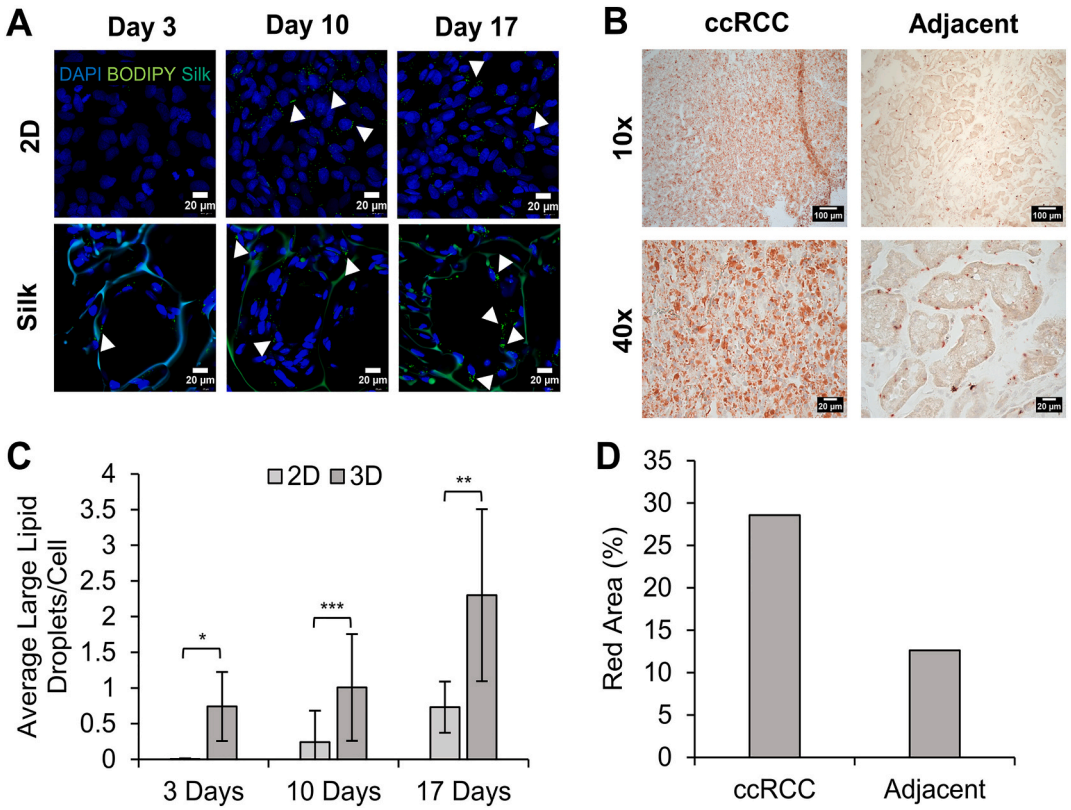

Fig. 6. Increased lipid droplet accumulation in scaffolded 786-O cells. (A) Fluorescent images (40×) of 786-O cells grown in 2D or on 6% silk scaffolds showing greater lipid droplet accumulation in scaffolded cells. Blue = nuclei. Green = lipids/silk. (B) Representative Oil Red O staining of ccRCC tumor and adjacent tissue indicating lipid droplet accumulation in tumor (red stain). (C) Area of lipid droplets per 786-O cell over culture period. Data presented as mean ± SD of 3 independent experiments. Significantly greater lipid droplet area in scaffolded 786-O cells compared to 2D on Day 3 (*t*-test, * $p < 0.05$), Day 10 (Mann-Whitney test: *** $p < 0.001$) and 17 (*t*-test: ** $p < 0.01$). (D) Percentage of lipid droplet area in ccRCC and adjacent tissue samples. (For interpretation of the references to colour in this figure legend, the reader is referred to the web version of this article.)

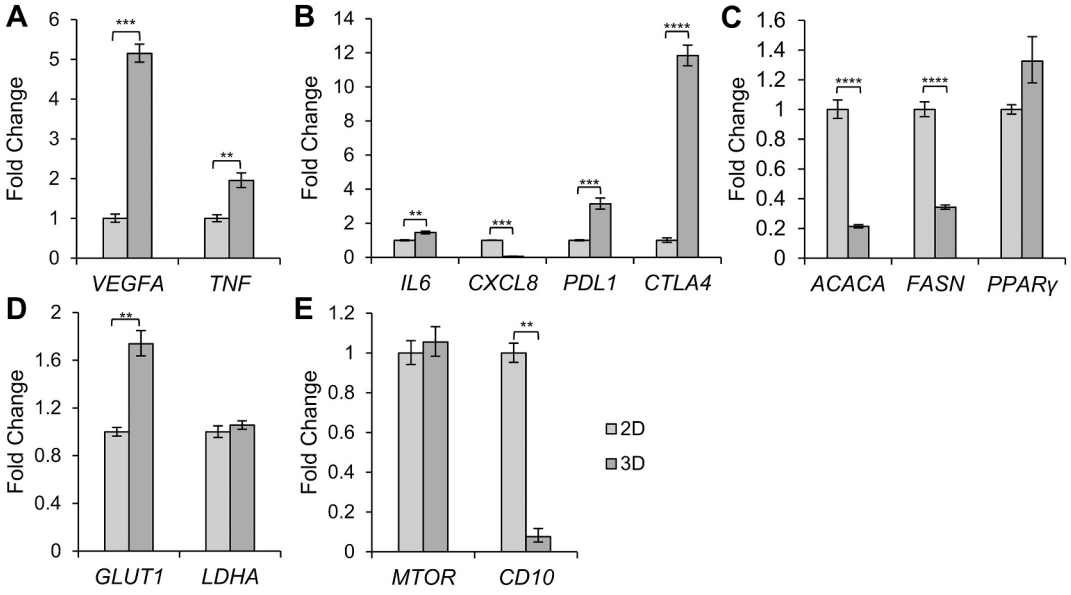

Fig. 7. Increased ccRCC characteristics in scaffolded 786-O cells. (A) Angiogenic recruiting related (B) immune regulation related (C) metabolic dysregulation related and (D) aggressiveness related gene expression of 786-O cells grown for 3 d in monolayer (2D) or silk scaffolds (3D) normalized to 2D condition. Data are presented as mean ± SD of 3 independent experiments. * indicates statistical significance between the groups (*t*-test, * $p < 0.05$).

concentrations; we observed that 3% silk scaffold modulus to be 0.406 kPa while it has previously been reported to be 3.9 kPa [50]. However, these differences are likely due to processing variations including lyophilization parameters and post-lyophilization differences. For example, the silk scaffolds used in this work underwent rate-controlled freezing while silk scaffolds in the comparative work underwent non-

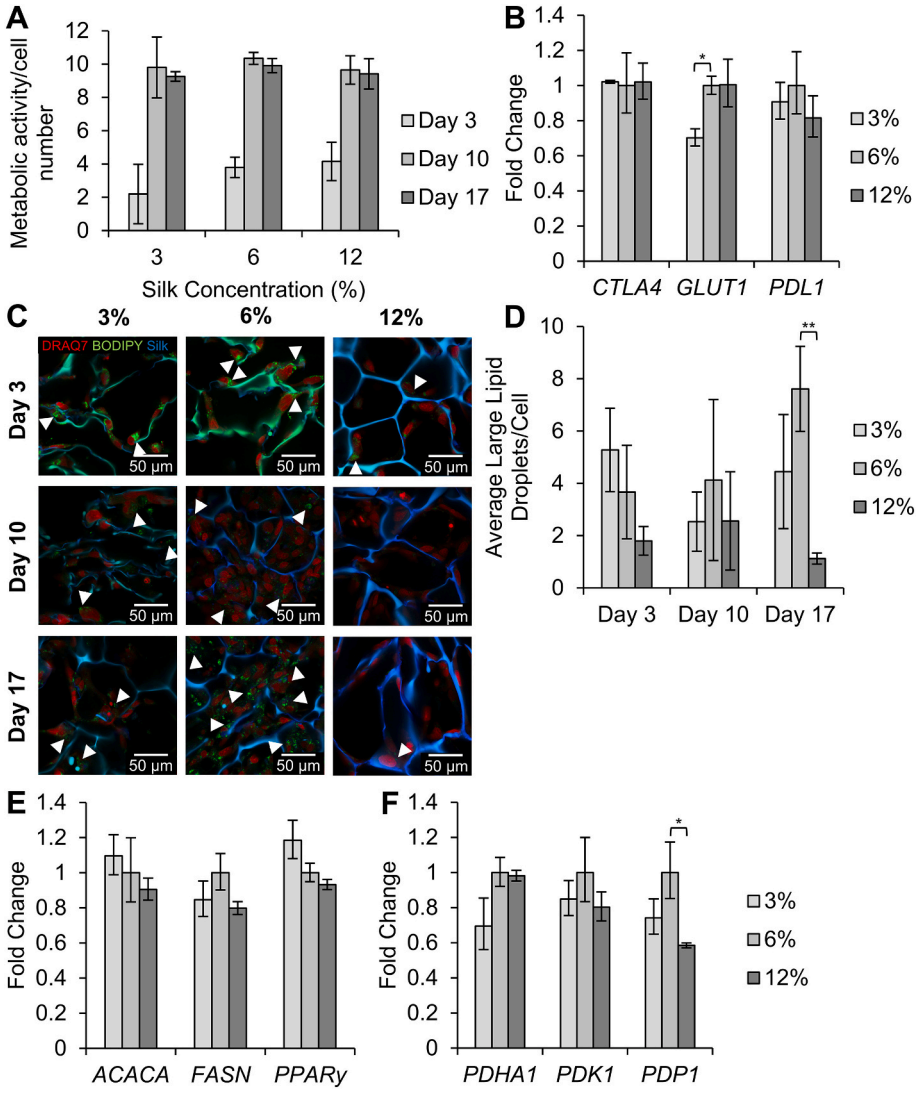

Fig. 8. Impact of modulus on ccRCC disease characteristics. (A) Average metabolic activity normalized to cell number for each silk scaffold group over the experimental timeline. No significant difference between time-matched silk scaffold groups. (B) Metabolic and immune related gene expression of 786-O cells after 3 d of culture on 3, 6, and 12% silk scaffolds normalized to the 6% silk scaffold group. Data are presented as mean ± SD of 3 independent samples. * indicates statistical significance (ANOVA, * $p < 0.05$). (C) Fluorescent images (40×) of 786-O cells grown on 3, 6, or 12% silk scaffolds showing greater lipid droplet accumulation in 6% scaffolded cells on Day 17. Red = nuclei. Green = lipids/silk. (D) Area of lipid droplets per 786-O cell over culture period. Data presented as mean ± SD of 3 independent samples. There was significantly greater lipid content in 6% silk scaffolds on Day 17 (ANOVA, ** $p < 0.01$). (E) Fatty acid synthesis and (F) pyruvate metabolism related gene expression of 786-O cells grown for 3 d in 3,6, or 12% silk scaffolds normalized to the 6% silk scaffold group. Data are presented as mean ± SD of 3 independent samples. * indicates statistical significance (ANOVA, * $p < 0.05$). (For interpretation of the references to colour in this figure legend, the reader is referred to the web version of this article.)

rate controlled freezing. This potentially influenced the pore structure and resultant mechanics of the silk scaffolds. Additionally, silk scaffolds in this work were autoclaved post-lyophilization to render them water insoluble, while the comparative work used methanol treatment to accomplish water insolubility [50]. It is likely a combination of these processing variations resulted in differences between this work and previously published work.

Comparison of ccRCC tumor tissue with rejected transplant kidney cortex tissue revealed a significant difference in Young's modulus with the modulus of ccRCC tumor tissue being more than 2 kPa less than cortex tissue. ccRCC is a cortical tumor and expected to have altered tissue architecture [51]. One explanation for the decrease in modulus of ccRCC compared to cortex could be increased accumulation of lipid droplets within tumor cells which is predicted to make them more pliable. However, the modulus of ccRCC was not found to be significantly different from adjacent non-tumor cortex tissue, suggesting that changes in modulus might affect the entire cortex in the region of the tumor. Histological examination of both tumor and adjacent samples demonstrated that adjacent tissue was structurally abnormal, not representing healthy kidney architecture, and exhibiting high levels of collagen deposition. This high collagen content is likely due to patients having comorbidities or other health concerns that could impact the stiffness of the adjacent tissue [52]. Additionally, kidney function and integrity is known to decline with age [53]. The average age of ccRCC patients was 63 years and the average age of kidney donors was 64.5 years. While the average chronological age between the two groups was similar, individuals of similar ages can display differences in age-related kidney decline which may have influenced these results [54].

The concentrations of silk solution investigated in this work were chosen with the expectation that the resultant Young's moduli would span the range of kidney stiffnesses measured. Through the use of 3–12% silk solutions, the full range of the tumor and kidney tissue stiffnesses were matched, with 6% silk mechanically matching the ccRCC tumors measured. It is common for ccRCC to be characterized through different forms of elastography which is a non-invasive means of measuring tissue stiffness [55]. Strain elastography methods have reported the mean strain index of ccRCC to be 4.04 ± 0.72 [56]. However, strain elastography measurements are difficult to directly compare to other forms of measurement since they are unitless. Sheer elastography has measured the mean elasticity of ccRCC to be 7.2 ± 2.5 kPa and the mean elasticity of healthy cortical kidney to be 4.7 ± 1.7 kPa [57]. The average Young's modulus for the ccRCC we measured was 3.082 ± 0.963 kPa while the cortical tissue modulus was 5.480 ± 1.409 kPa. Our ccRCC range is lower than the range reported through elastography while our cortical tissue range overlapped ones previously reported. Differences in the ccRCC Young's modulus values could be due to differences in measurement techniques. Sheer elastography values incorporate the intrinsic stiffness of the tissue (in the case of ccRCC, the

surrounding cortical kidney tissue) as well as the direction of the ultrasound beam which are not included in the *ex vivo* mechanical testing we conducted. Additionally, sheer elasticity values can vary depending on orientation of the ultrasound beams, tissue anisotropy, or renal perfusion [57,58]. In contrast to the elastography results, we measured the ccRCC tumor stiffness as lower than cortical tissue stiffness. Due to the increase of lipids present within ccRCC tumors compared to healthy cortical tissue, the reduction in tissue stiffness is not surprising.

Although ccRCC was the focus of this work, the modulus of several other types of kidney cancer (papillary, collecting duct) was also determined. Most RCCs are classified based on histological criteria; however, some tumors can display features of different subtypes [51]. For example, clear cells can be present in RCCs other than ccRCC. Despite different diagnoses, inclusion of all tumors evaluated into a pooled group of kidney cancer specimens varied from the ccRCC-only modulus by less than 0.1 kPa. Similar to the ccRCC-only results, the modulus of the pooled tumor specimens was significantly different from that of the cortex tissue. Furthermore, the 6% silk scaffolds still mechanically matched the tumors. This suggests that 6% silk scaffolds could have relevance to 3D models for additional types of kidney cancer beyond ccRCC. Furthermore, lyophilized silk scaffolds could have applications for many different solid tumor types. Our group has previously developed silk scaffolds for the study of neuroblastoma [24], while others have developed salt-leached silk scaffolds to model breast cancer [26,59]. The lyophilized silk scaffold presented here could be further evaluated for use in 3D breast cancer models, as well as other solid tumors including lung, prostate, and bladder.

The tumors received for this study encompassed several grade and stage combinations, but not all possible grade and stage combinations were obtained. The tumors studied had varied tissue composition; no clear relationship between grade, stage, and Young's modulus was observed. However, the number of specimens for each grade/stage was small and stiffness relationships may become more apparent with increased sample sizes.

We further investigated differences in intratumoral tissue composition by staining individual ccRCC specimens from the same mechanically tested sample. The number of ccRCC specimens tested depended on tumor size; all specimens were biopsy punched successively across the tumor sample when possible. Features such as distinct fibrotic encapsulation and typical clear cell morphology were variable between individual specimens. When stratified based upon high and low collagen content, the 6% silk scaffolds still mechanically match all groups, while the 9% silk scaffolds mechanically matched all except the high collagen ccRCC tissue. While no significant difference in the Young's moduli were seen between the samples stratified by collagen content, the intratumoral architecture differed. Previously, genetic intratumoral heterogeneity has been demostrated across ccRCC samples [11]. While VHL is generally mutated in all cells of the entire tumor, mutations in other genes associated with aggressive clinical disease progression such as *PBRM1*, *SETD2*, *BAP1*, and *KDM5C* frequently exhibit regional variability [11]. Regional variability in gene mutations controlling tumor cell proliferation and local invasiveness could explain the stiffness heterogeneity and Young's modulus differences, seen throughout the tumors in our experiments [51]. Additionally, as mentioned above other factors such as immunological state and comorbidities may play a role in the differences seen in tissue composition. Although the categorized tumors span the Young's moduli of both 6% and 9% silk scaffolds, the 6% silk scaffolds encompassed all divisions of ccRCC.

In addition to matching the overall modulus of the tumor tissue, the 6% silk scaffolds also matched the existing structure of ccRCC. The Feret diameter of the 6% silk scaffolds matched the Feret diameter of stained ccRCC clusters. In addition to overall modulus, pore size of a supporting biomaterial has been shown to impact cancer cell behavior [34]. By matching the pore size of the silk scaffolds to the native tumor structure, the *in vivo* environment will be better replicated *in vitro*.

Of the established ccRCC cell lines, the 786-O cell line is the most widely used [60]. This is due to the VHL mutation and altered VEGF pathways of the cell line which matches well to aggressive ccRCC [18,61]. 786-O cells give rise to ccRCC when injected into nude mice [62]. In our silk scaffolding approach, we demonstrated 786-O cells can be cultured in silk scaffolds and show increased accumulation of lipid droplets when compared to standard 2D culture. This was demonstrated through quantification of BODIPY staining after 3, 10, and 17 days of culture. After 3 days of culture, significantly higher lipid content was present in scaffolded 786-O cells than in 2D culture. The higher lipid content was maintained throughout the culture period. Additionally, the amount of lipids increased in scaffolded 786-O cells over time with Day 17 having significantly higher lipid content than both Day 3 and Day 10. The increase in lipid droplet accumulation follows the expected phenotype of ccRCC cells and matches the lipid accumulation seen in ccRCC specimens [63]. The significantly increased lipid accumulation shown in scaffolded 786-O cells demonstrates important progress towards replicating the ccRCC microenvironment as a platform for studying *in vitro* disease progression.

Lipid droplet accumulation by 786-O cells in 2D culture has previously been reported [64]. It is thought this accumulation may be due to loss of VHL and increased HIF signaling. However, 786-O cells are devoid of VHL. Therefore, the 3D culture conditions were suspected of contributing to this pathway. To further understand how the scaffolded culture environment could influence ccRCC disease development *in vitro*, genetic markers characteristic of ccRCC were investigated. A significant increase in *PDL1* and *CTLA4* expression was found in scaffolded 786-O cells compared to 2D culture. Both PDL1 and CTLA4 are known immune checkpoint activators and lead to T-cell exhaustion [9]. In 2015, the FDA approved nivolumab, an anti-PD-1 antibody, for ccRCC to treat patients who have stopped responding to anti-angiogenic drugs. In 2018, the FDA approved combination treatment with nivolumab and ipilimumab, an anti-CTLA4 antibody, for previously untreated intermediate and high risk ccRCC. The increased *PDL1* and *CTLA4*expression we observed with the scaffolded 786-O cells suggests that this model may be useful for the study of immune checkpoint inhibition *in vitro*. Future work could investigate co-culturing with mixed lymphocytes, or more specifically T-cells, for immune checkpoint inhibitor studies.

Increases in *VEGFA* [65], *TNF* [38], and *IL6* [66] have been associated with malignant or aggressive ccRCC. Significant increases in gene expression for *VEGFA*, *TNF*, and *IL6* by scaffolded 786-O cells were observed. This indicates that 786-O cells cultured in silk scaffolds better replicate *in vivo* characteristics than 2D culture methods. First line treatment of ccRCC includes tyrosine kinase inhibitors that target blood vessel and tumor growth. Given the increased in *VEGFA* expression, co-culturing with endothelial cells may give rise to insight into vascular ingrowth into these tumors and responsiveness to drugs such as sunitinib, sorafenib, cabozantinib, and pazopanib.

CXCL8 expression has been associated with ccRCC cancer stem cells [43]. Scaffolded 786-O cells exhibited decreased *CXCL8* expression. This data suggests that the scaffolded 786-O cells exhibit less stemness than 2D culture and could be considered more differentiated towards the ccRCC phenotype.

Scaffolded 786-O cells exhibited increased lipid droplet accumulation as compared to the 2D culture 786-O cells. However, expression of *ACACA* and *FASN* were significantly decreased in scaffolded 786-O cells. This suggests that the cause for the increased lipid droplet accumulation was not due to increased fatty acid synthesis. Other pathway changes, such as suppression of β-oxidation, have been associated with increased lipid content in ccRCC and could be explored further [40]. Similarly, *CD10* expression was also decreased in this work. *CD10* expression has been shown to be regulated by the pVHL-HIF axis, but variable expression has been seen in ccRCC cases and may be dependent on *VHL* mutation status [44,67]. Since significant differences in other HIF target genes (ex. *VEGFA, CTLA4*) were observed, it is likely *CD10* expression was also affected by HIF-related changes. Overall, the increased expression of genes associated with aggressive ccRCC supports our

observations of increased ccRCC characteristics in scaffolded 786-O cells and demonstrates an improvement in replicating the tumor microenvironment.

To further investigate the role of microenvironment modulus in the changes seen in scaffolded 786-O cells, characteristics of 786-O cells grown on 3, 6, and 12% scaffolds were evaluated. The 3% and 12% scaffolds were selected to explore significantly lower (3%; 0.406 ± 0.140 kPa) and higher (12%; 9.298 ± 1.255 kPa) Young's modulus than those experimentally determined to mechanically match the ccRCC modulus (6%; 3.200 ± 0.880 kPa). No significant difference in metabolic activity of the 786-O cells was seen between the different modulus microenvironments, which agrees with previous works on gels of differing stiffnesses [68]. However, significantly less expression of *GLUT1* by 786-O cells in 3% scaffolds as compared to in 6% scaffolds was observed, suggesting a change in glucose uptake. Increased expression of *GLUT1* has been associated with ccRCC resistance to immunotherapeutic treatment and suggests 6% scaffolds could be well suited as an *in vitro* model for this purpose [69]. Confocal imaging of scaffolded 786-O cells demonstrated greater lipid droplet accumulation when grown in 6% scaffolds. This result further suggests that the mechanically matched modulus faithfully reproduces ccRCC characteristics. Lastly, gene expression related to fatty acid synthesis and pyruvate metabolism were evaluated to understand why lipid accumulation differed between scaffold conditions. No significant differences in fatty acid gene expression were found which agrees with the 2D *vs* scaffolded comparison data suggesting that lipid droplet accumulation is not due to increased synthesis. 786-O cells grown on 12% scaffolds had significantly reduced *PDP1* expression suggesting decreased pyruvate metabolism could contribute to the lower lipid accumulation. Overall, the 6% scaffolds demonstrated superior ccRCC characteristics including lipid droplet accumulation and gene expression compared to non-mechanically matched silk scaffolds.

This work demonstrated that lyophilized 6% silk scaffolds reproduce the mechanical features of the ccRCC microenvironment. Although 786-O cells were used as a model cell line in this work, this model has the potential to be used for personalized medicine. Primary ccRCC cells isolated from patients could be grown in mechanically matched silk scaffolds, providing a useful therapeutic testing platform. Translation to clinical use would require manufacturing scale-up of silk fibroin scaffolds. Silk scaffolds and injectable silk microparticles are FDA approved materials marketed by Sofregen for soft tissue reconstruction [31,70], suggesting the viability of scale-up of lyophilized silk scaffolds for *in vitro* cancer modeling. Similar to the scaffolds presented here, both available silk products undergo lyophilization. Improvements would need to be made to the current lyophilization process for the scaffolds as they are produced in plastic molds which could hinder rapid heat transfer in an industrial setting. These plastic molds could be replaced with metal molds to ensure improved heat transfer and streamline the lyophilization process for mass production.

This work focused on developing a mechanically matched silk scaffold system to better enable 3D *in vitro* modeling of ccRCC. The use of silk enables a highly repeatable lyophilized scaffold model that can be produced at low costs and could be translated to clinical use. While the work presented here has focused on evaluating the impact of modulus on one cell type of the ccRCC microenvironment, our results show promising changes in improving and advancing ccRCC characteristics of 786-O cells. It is likely that the mechanically matched 3D scaffolded model presented here would impact how 786-O cells signal and interact with other features of the tumor microenvironment, especially lymphocytes given the increase in *PDL1* and *CTLA4* expression. Inclusion of additional cell types, such as immune cells and endothelial cells, could further improve the model and allow the testing of first line treatment options such as immune checkpoint inhibitors and tyrosine kinase inhibitors [6,7,9]. Overall, the scaffolded culture approach presented here provides an improvement in fidelity to patient tumors for *in vitro* ccRCC modeling.

5. Conclusion

Silk scaffolds of varying Young's modulus were fabricated through lyophilization of aqueous silk solutions. The Young's modulus of the silk scaffolds spanned the range of Young's moduli measured from ccRCC and tissue adjacent to tumor biopsy site as well as cortical and medullar regions from discarded donor kidneys. A match between 6% silk scaffolds and ccRCC mechanical properties was demonstrated. Scaffolded culturing of 786-O cells improved the ccRCC phenotype as opposed to 2D culture as demonstrated by significantly increased lipid droplet accumulation over a culture period of 17 days. Scaffolded 786-O cultures on mechanically matched scaffolds also increased expression of markers characteristic of ccRCC and potentially indicative of drug response. Comparison with 786-O cells grown on non-mechanically matched scaffolds demonstrated that these improved ccRCC characteristics were driven by scaffold modulus. Overall, our findings support the use of silk scaffolds in replicating tumor behavior for clear cell renal cell carcinoma and provide a platform for investigating disease progression and novel therapeutics.

Author contributions

Alycia Abbott: Investigation, Formal Analysis, Data Curation, Writing – Original Draft, Writing – Review & Editing, Visualization. **Kyle Bond:** Investigation, Formal Analysis, Data Curation, Writing – Review & Editing, Visualization. **Takuto Chiba:** Visualization, Data Curation, Writing – Review & Editing. **Sunder Sims-Lucas:** Conceptualization, Formal Analysis, Resources, Writing – Review & Editing, Supervision, Funding Acquisition. **Leif Oxburgh:** Supervision, Conceptualization, Formal Analysis, Resources, Writing – Review & Editing, Funding Acquisition. **Jeannine M. Coburn:** Conceptualization, Formal Analysis, Supervision, Resources, Writing – Review & Editing, Visualization, Funding Acquisition.

Declaration of competing interest

The authors declare that they have no known competing financial interests or personal relationships that could have appeared to influence the work reported in this paper.

Acknowledgment

This work was supported by Department of Defense grant W81XWH-18-1-0620. This project used the UPMC Hillman Cancer Center and Tissue and Research Pathology/Pitt Biospecimen Core shared resource which is supported in part by award P30CA047904. We would like to give special thanks to the Center for Biologic Imaging at the University of Pittsburgh for training and instrumentation of the image tiling. We would like to thank Dr. David Emlet of the Center for Critical Care Nephrology at the University of Pittsburgh for providing all rejected transplant kidneys used in this work. We would also like to thank the Children's Hospital of Pittsburgh histology core and Michele Mulkeen from the core for her histological skills and knowledge. Additionally, we would like to acknowledge the New York Blood Center Electron and Confocal Microscopy Core Facility for their assistance in confocal imaging.

Appendix A. Supplementary data

Supplementary data to this article can be found online at https://doi.org/10.1016/j.msec.2021.112141.

References

[1] J.R. Gnarra, K. Tory, Y. Weng, L. Schmidt, M.H. Wei, H. Li, F. Latif, S. Liu, F. Chen, F.M. Duh, I. Lubensky, D.R. Duan, C. Florence, R. Pozzatti, M.M. Walther, N.

H. Bander, H.B. Grossman, H. Brauch, S. Pomer, J.D. Brooks, W.B. Isaacs, M. I. Lerman, B. Zbar, W.M. Linehan, Mutations of the vhl tumour suppressor gene in renal carcinoma, Nat. Genet. 7 (1) (1994) 85–90.
[2] A.A. Hakimi, E. Reznik, C.-H. Lee, C.J. Creighton, A.R. Brannon, A. Luna, B. A. Aksoy, E.M. Liu, R. Shen, W. Lee, Y. Chen, S.M. Stirdivant, P. Russo, Y.-B. Chen, S.K. Tickoo, V.E. Reuter, E.H. Cheng, C. Sander, J.J. Hsieh, An integrated metabolic atlas of clear cell renal cell carcinoma, Cancer Cell 29 (1) (2016) 104–116.
[3] S.B. Stewart-Merrill, R.H. Thompson, S.A. Boorjian, S.P. Psutka, C.M. Lohse, J. C. Cheville, B.C. Leibovich, I. Frank, Oncologic surveillance following surgical resection for renal cell carcinoma: a novel risk-based approach, BJU Int. 116 (2015) 16–17.
[4] D.Y.C. Heng, W.L. Xie, M.M. Regan, M.A. Warren, A.R. Golshayan, C. Sahi, B. J. Eigl, J.D. Ruether, T. Cheng, S. North, P. Venner, J.J. Knox, K.N. Chi, C. Kollmannsberger, D.F. McDermott, W.K. Oh, M.B. Atkins, R.M. Bukowski, B. I. Rini, T.K. Choueiri, Prognostic factors for overall survival in patients with metastatic renal cell carcinoma treated with vascular endothelial growth factor-targeted agents: results from a large, multicenter study, J. Clin. Oncol. 27 (34) (2009) 5794–5799.
[5] R.R. McKay, D. Bosse, T.K. Choueiri, Evolving systemic treatment landscape for patients with advanced renal cell carcinoma, J. Clin. Oncol. https://doi.org/10.1200/jco.2018.79.0253 (2018) Jco2018790253.
[6] P.C. Barata, B.I. Rini, Treatment of renal cell carcinoma: current status and future directions, CA Cancer J. Clin. 67 (6) (2017) 507–524.
[7] C.-H. Lee, A.M. Hötker, M.H. Voss, D.R. Feldman, K.M. Woo, S. Patil, D.T. Coskey, O. Akin, J.J. Hsieh, R.J. Motzer, Bevacizumab monotherapy as salvage therapy for advanced clear cell renal cell carcinoma pretreated with targeted drugs, Clin, Genitourin. Cancer 14 (1) (2016) 56–62.
[8] R.J. Motzer, B. Escudier, D.F. McDermott, S. George, H.J. Hammers, S. Srinivas, S. S. Tykodi, J.A. Sosman, G. Procopio, E.R. Plimack, D. Castellano, T.K. Choueiri, H. Gurney, F. Donskov, P. Bono, J. Wagstaff, T.C. Gauler, T. Ueda, Y. Tomita, F. A. Schutz, C. Kollmannsberger, J. Larkin, A. Ravaud, J.S. Simon, L.A. Xu, I. M. Waxman, P. Sharma, C. Investigators, Nivolumab versus everolimus in advanced renal-cell carcinoma, New Engl. J. Med. 373 (19) (2015) 1803–1813.
[9] Q. Wang, J. Zhang, H. Tu, D. Liang, D.W. Chang, Y. Ye, X. Wu, Soluble immune checkpoint-related proteins as predictors of tumor recurrence, survival, and t cell phenotypes in clear cell renal cell carcinoma patients, J. Immunother. Cancer 7 (1) (2019) 334.
[10] V. Di Stefano, B. Torsello, C. Bianchi, I. Cifola, E. Mangano, G. Bovo, V. Cassina, S. De Marco, R. Corti, C. Meregalli, S. Bombelli, P. Vigano, C. Battaglia, G. Strada, R. A. Perego, Major action of endogenous lysyl oxidase in clear cell renal cell carcinoma progression and collagen stiffness revealed by primary cell cultures, Am. J. Pathol. 186 (9) (2016) 2473–2485.
[11] A. Sankin, A.A. Hakimi, N. Mikkilineni, I. Ostrovnaya, M.T. Silk, Y. Liang, R. Mano, M. Chevinsky, R.J. Motzer, S.B. Solomon, E.H. Cheng, J.C. Durack, J.A. Coleman, P. Russo, J.J. Hsieh, The impact of genetic heterogeneity on biomarker development in kidney cancer assessed by multiregional sampling, Cancer Med. 3 (6) (2014) 1485–1492.
[12] V.C. Crentsil, H. Liu, D.F. Sellitti, Comparison of exosomal micrornas secreted by 786-o clear cell renal carcinoma cells and hk-2 proximal tubule-derived cells in culture identifies microrna-205 as a potential biomarker of clear cell renal carcinoma, Oncol. Lett 16 (1) (2018) 1285–1290.
[13] Y. Zhong, K. Guan, S. Guo, C. Zhou, D. Wang, W. Ma, Y. Zhang, C. Li, S. Zhang, Spheres derived from the human sk-rc-42 renal cell carcinoma cell line are enriched in cancer stem cells, Cancer Lett. 299 (2) (2010) 150–160.
[14] H.A. Bolck, C. Corrò, A. Kahraman, A. von Teichman, N.C. Toussaint, J. Kuipers, F. Chiovaro, V.H. Koelzer, C. Pauli, W. Moritz, P.K. Bode, M. Rechsteiner, N. Beerenwinkel, P. Schraml, H. Moch, Tracing clonal dynamics reveals that two- and three-dimensional patient-derived cell models capture tumor heterogeneity of clear cell renal cell carcinoma, Eur. 7 (1) (2019) 152–162.
[15] E. Kleymenova, J.I. Everitt, L. Pluta, M. Portis, J.R. Gnarra, C.L. Walker, Susceptibility to vascular neoplasms but no increased susceptibility to renal carcinogenesis in vhl knockout mice, Carcinogenesis 25 (3) (2004) 309–315.
[16] N.C. Wolff, A. Pavía-Jiménez, V.T. Tcheuyap, S. Alexander, M. Vishwanath, A. Christie, X.-J. Xie, N.S. Williams, P. Kapur, B. Posner, R.M. McKay, J. Brugarolas, High-throughput simultaneous screen and counterscreen identifies homoharringtonine as synthetic lethal with von hippel-Lindau loss in renal cell carcinoma, Oncotarget 6 (19) (2015) 16951–16962.
[17] B. Hong, Y. Yang, S. Guo, S. Duoerkun, X. Deng, D. Chen, S. Yu, W. Qian, Q. Li, Q. Li, K. Gong, N. Zhang, Intra-tumour molecular heterogeneity of clear cell renal cell carcinoma reveals the diversity of the response to targeted therapies using patient-derived xenograft models, Oncotarget 8 (30) (2017) 49839–49850.
[18] R. Sinha, A.G. Winer, M. Chevinsky, C. Jakubowski, Y.B. Chen, Y. Dong, S. K. Tickoo, V.E. Reuter, P. Russo, J.A. Coleman, C. Sander, J.J. Hsieh, A.A. Hakimi, Analysis of renal cancer cell lines from two major resources enables genomics-guided cell line selection, Nat. Commun. 8 (2017) 15165.
[19] B. Qiu, D. Ackerman, D.J. Sanchez, B. Li, J.D. Ochocki, A. Grazioli, E. Bobrovnikova-Marjon, J.A. Diehl, B. Keith, M.C. Simon, Hif2alpha-dependent lipid storage promotes endoplasmic reticulum homeostasis in clear-cell renal cell carcinoma, Cancer Discov. 5 (6) (2015) 652–667.
[20] C. Du, Y. Feng, D. Qiu, Y. Xu, M. Pang, N. Cai, A.P. Xiang, Q. Zhang, Highly efficient and expedited hepatic differentiation from human pluripotent stem cells by pure small-molecule cocktails, Stem Cell Res. Ther. 9 (1) (2018) 58.
[21] V. Seewaldt, Ecm stiffness paves the way for tumor cells, Nat. Med. 20 (4) (2014) 332–333.
[22] P. Lu, V.M. Weaver, Z. Werb, The extracellular matrix: a dynamic niche in cancer progression, J. Cell Biol. 196 (4) (2012) 395–406.
[23] K. Maliszewska-Olejniczak, K.K. Brodaczewska, Z.F. Bielecka, W. Solarek, A. Kornakiewicz, C. Szczylik, C. Porta, A.M. Czarnecka, Development of extracellular matrix supported 3d culture of renal cancer cells and renal cancer stem cells, Cytotechnology 71 (1) (2019) 149–163.
[24] K.J. Ornell, K.S. Mistretta, E. Newman, C.Q. Ralston, J.M. Coburn, Three-dimensional, scaffolded tumor model to study cell-driven microenvironment effects and therapeutic responses, ACS Biomater-Sci Eng. 5 (12) (2019) 6742–6754.
[25] A.K. Gupta, J.M. Coburn, J. Davis-Knowlton, E. Kimmerling, D.L. Kaplan, L. Oxburgh, Scaffolding kidney organoids on silk, J. Tissue Eng. Regen. Med. 13 (5) (2019) 812–822.
[26] E. Dondajewska, W. Juzwa, A. Mackiewicz, H. Dams-Kozlowska, Heterotypic breast cancer model based on a silk fibroin scaffold to study the tumor microenvironment, Oncotarget 9 (4) (2018) 4935–4950.
[27] W. Zhang, J. Chen, L.J. Backman, A.D. Malm, P. Danielson, Surface topography and mechanical strain promote keratocyte phenotype and extracellular matrix formation in a biomimetic 3d corneal model, Adv. Healthc. Mater. 6 (5) (2017).
[28] D.N. Rockwood, R.C. Preda, T. Yucel, X. Wang, M.L. Lovett, D.L. Kaplan, Materials fabrication from bombyx mori silk fibroin, Nat. Protoc. 6 (10) (2011) 1612–1631.
[29] J. Rnjak-Kovacina, L.S. Wray, K.A. Burke, T. Torregrosa, J.M. Golinski, W. Huang, D.L. Kaplan, Lyophilized silk sponges: a versatile biomaterial platform for soft tissue engineering, ACS Biomater-Sci Eng. 1 (4) (2015) 260–270.
[30] C.P. Gulka, J.E. Brown, J.E.M. Giordano, J.E. Hickey, M.P. Montero, A. Hoang, T. L. Carroll, A novel silk-based vocal fold augmentation material: 6-month evaluation in a canine model, Laryngoscope 129 (8) (2019) 1856–1862.
[31] M. Kijanska, A. Marmaras, A. Hegglin, V. Kurtcuoglu, P. Giovanoli, N. Lindenblatt, In vivo characterization of the integration and vascularization of a silk-derived surgical scaffold, J. Plast. Reconstr. Aesthet. Surg. 69 (8) (2016) 1141–1150.
[32] O. Etienne, A. Schneider, J.A. Kluge, C. Bellemin-Laponnaz, C. Polidori, G.G. Leisk, D.L. Kaplan, J.A. Garlick, C. Egles, Soft tissue augmentation using silk gels: an in vitro and in vivo study, J. Periodontol. 80 (11) (2009) 1852–1858.
[33] J.E. Gross, R.L. Horan, M. Gaylord, R.E. Olsen, L.D. McGill, J.M. García-López, K. Biber, K. Barnico, I. Toponarski, G. Altman, An evaluation of seri surgical scaffold for soft-tissue support and repair in an ovine model of two-stage breast reconstruction, Plast. Reconstr. Surg. 134(5) (2014) 700e-704e.
[34] D. Huang, Y. Nakamura, A. Ogata, S. Kidoaki, Characterization of 3d matrix conditions for cancer cell migration with elasticity/porosity-independent tunable microfiber gels, Polym. J. 52 (3) (2020) 333–344.
[35] J.M. Coburn, E. Na, D.L. Kaplan, Modulation of vincristine and doxorubicin binding and release from silk films, J. Control. Release 220(Pt A (2015) 229–238.
[36] X. Hu, D. Kaplan, P. Cebe, Determining beta-sheet crystallinity in fibrous proteins by thermal analysis and infrared spectroscopy, Macromolecules 39 (18) (2006) 6161–6170.
[37] J.L. Fetting, J.A. Guay, M.J. Karolak, R.V. Iozzo, D.C. Adams, D.E. Maridas, A. C. Brown, L. Oxburgh, Foxd1 promotes nephron progenitor differentiation by repressing decorin in the embryonic kidney, Development 141 (1) (2014) 17–27.
[38] R.S. Al-Lamki, T.J. Sadler, J. Wang, M.J. Reid, A.Y. Warren, M. Movassagh, W. Lu, I.G. Mills, D.E. Neal, J. Burge, P. Vandenebeele, J.S. Pober, J.R. Bradley, Tumor necrosis factor receptor expression and signaling in renal cell carcinoma, Am. J. Pathol. 177 (2) (2010) 943–954.
[39] S.-F. Kammerer-Jacquet, A. Deleuze, J. Saout, R. Mathieu, B. Laguerre, G. Verhoest, F. Dugay, M.-A. Belaud-Rotureau, K. Bensalah, N. Rioux-Leclercq, Targeting the pd-1/pd-l1 pathway in renal cell carcinoma, Int. J. Mol. Sci. 20(7) (2019) 1692.
[40] Z. Zhao, Y. Liu, Q. Liu, F. Wu, X. Liu, H. Qu, Y. Yuan, J. Ge, Y. Xu, H. Wang, The mrna expression signature and prognostic analysis of multiple fatty acid metabolic enzymes in clear cell renal cell carcinoma, J. Cancer 10 (26) (2019) 6599–6607.
[41] C. Chen, N. Pore, A. Behrooz, F. Ismail-Beigi, A. Maity, Regulation of glut1 mrna by hypoxia-inducible factor-1. Interaction between h-ras and hypoxia, J. Biol. Chem. 276 (12) (2001) 9519–9525.
[42] J.H. Park, C. Lee, M.S. Chang, K. Kim, S. Choi, H. Lee, H.-S. Lee, K.C. Moon, Molecular characterization and putative pathogenic pathways of tuberous sclerosis complex-associated renal cell carcinoma, Transl. Oncol. 11 (4) (2018) 962–970.
[43] C. Corrò, M.E. Healy, S. Engler, B. Bodenmiller, Z. Li, P. Schraml, A. Weber, I. J. Frew, M. Rechsteiner, H. Moch, Il-8 and cxcr1 expression is associated with cancer stem cell-like properties of clear cell renal cancer, J. Pathol. 248 (3) (2019) 377–389.
[44] G. Boysen, D. Bausch-Fluck, C.R. Thoma, A.M. Nowicka, D.P. Stiehl, I. Cima, V.-D. Luu, A. von Teichman, T. Hermanns, T. Sulser, B. Ingold-Heppner, N. Fankhauser, R.H. Wenger, W. Krek, P. Schraml, B. Wollscheid, H. Moch, Identification and functional characterization of pvhl-dependent cell surface proteins in renal cell carcinoma, Neoplasia 14 (6) (2012) 535–546.
[45] S. di Martino, G. De Luca, L. Grassi, G. Federici, R. Alfonsi, M. Signore, A. Addario, L. De Salvo, F. Francescangeli, M. Sanchez, V. Tirelli, G. Muto, I. Sperduti, S. Sentinelli, M. Costantini, L. Pasquini, M. Milella, M. Haoui, G. Simone, M. Gallucci, R. De Maria, D. Bonci, Renal cancer: new models and approach for personalizing therapy, J. Exp. Clin. Cancer Res. 37 (1) (2018) 217.
[46] M.M. Wolf, W. Kimryn Rathmell, K.E. Beckermann, Modeling clear cell renal cell carcinoma and therapeutic implications, Oncogene 39 (17) (2020) 3413–3426.
[47] S. Bai, H. Han, X. Huang, W. Xu, D.L. Kaplan, H. Zhu, Q. Lu, Silk scaffolds with tunable mechanical capability for cell differentiation, Acta Biomater. 20 (2015) 22–31.
[48] L.S. Wray, J. Rnjak-Kovacina, B.B. Mandal, D.F. Schmidt, E.S. Gil, D.L. Kaplan, A silk-based scaffold platform with tunable architecture for engineering critically-sized tissue constructs, Biomaterials 33 (36) (2012) 9214–9224.

[49] F.J. O'Brien, B.A. Harley, I.V. Yannas, L. Gibson, Influence of freezing rate on pore structure in freeze-dried collagen-gag scaffolds, Biomaterials 25 (6) (2004) 1077–1086.
[50] J.E. Brown, J.E. Moreau, A.M. Berman, H.J. McSherry, J.M. Coburn, D.F. Schmidt, D.L. Kaplan, Shape memory silk protein sponges for minimally invasive tissue regeneration, Adv. Healthc. Mater. 6 (2) (2017), https://doi.org/10.1002/adhm.201600762.
[51] J.J. Hsieh, M.P. Purdue, S. Signoretti, C. Swanton, L. Albiges, M. Schmidinger, D. Y. Heng, J. Larkin, V. Ficarra, Renal cell carcinoma, Nat. Rev. Dis. Primers 3 (2017) 17009.
[52] J. Rowland, A. Akbarov, J. Eales, X. Xu, J.P. Dormer, H. Guo, M. Denniff, X. Jiang, P. Ranjzad, A. Nazgiewicz, P.R. Prestes, A. Antczak, M. Szulinska, I.A. Wise, E. Zukowska-Szczechowska, P. Bogdanski, A.S. Woolf, N.J. Samani, F.J. Charchar, M. Tomaszewski, Uncovering genetic mechanisms of kidney aging through transcriptomics, genomics, and epigenomics, Kidney Int. 95 (3) (2019) 624–635.
[53] A. Denic, R.J. Glassock, A.D. Rule, Structural and functional changes with the aging kidney, Adv. Chronic Kidney Dis. 23 (1) (2016) 19–28.
[54] J. Rowland, A. Akbarov, A. Maan, J. Eales, J. Dormer, M. Tomaszewski, Tick-tock chimes the kidney clock - from biology of renal ageing to clinical applications, Kidney Blood Press. Res. 43 (1) (2018) 55–67.
[55] C.F. Dietrich, R.G. Barr, A. Farrokh, M. Dighe, M. Hocke, C. Jenssen, Y. Dong, A. Saftoiu, R.F. Havre, Strain elastography - how to do it? Ultrasound Int. Open 3 (4) (2017) E137–E149.
[56] M.F. Inci, T.O. Kalayci, S. Tan, S. Karasu, E. Albayrak, V. Cakir, I. Ocal, F. Ozkan, Diagnostic value of strain elastography for differentiation between renal cell carcinoma and transitional cell carcinoma of kidney, Abdom. Radiol. 41 (6) (2016) 1152–1159.
[57] Y. Cai, F. Li, Z. Li, L. Du, R. Wu, Diagnostic performance of ultrasound shear wave elastography in solid small (</=4 cm) renal parenchymal masses, Ultrasound Med. Biol. 45 (9) (2019) 2328–2337.
[58] J.M. Correas, D. Anglicheau, J.L. Gennisson, M. Tanter, Renal elastography, Nephrol. Ther. 12 (Suppl. 1) (2016) S25–S34.
[59] S. Talukdar, M. Mandal, D.W. Hutmacher, P.J. Russell, C. Soekmadji, S.C. Kundu, Engineered silk fibroin protein 3d matrices for in vitro tumor model, Biomaterials 32 (8) (2011) 2149–2159.
[60] K.K. Brodaczewska, C. Szczylik, M. Fiedorowicz, C. Porta, A.M. Czarnecka, Choosing the right cell line for renal cell cancer research, Mol. Cancer Ther. 15 (1) (2016) 83.
[61] O. Iliopoulos, A. Kibel, S. Gray, W.G. Kaelin Jr., Tumour suppression by the human von hippel-lindau gene product, Nat. Med. 1 (8) (1995) 822–826.
[62] J.M. Kozlowski, I.J. Fidler, D. Campbell, Z.L. Xu, M.E. Kaighn, I.R. Hart, Metastatic behavior of human tumor cell lines grown in the nude mouse, Cancer Res. 44 (8) (1984) 3522–3529.
[63] J.C. Chappell, L.B. Payne, W.K. Rathmell, Hypoxia, angiogenesis, and metabolism in the hereditary kidney cancers, J. Clin. Invest. 129 (2) (2019) 442–451.
[64] W. Du, L. Zhang, A. Brett-Morris, B. Aguila, J. Kerner, C.L. Hoppel, M. Puchowicz, D. Serra, L. Herrero, B.I. Rini, S. Campbell, S.M. Welford, Hif drives lipid deposition and cancer in ccrcc via repression of fatty acid metabolism, Nat. Commun. 8 (1) (2017) 1769.
[65] X. Wang, J. Zhang, Y. Wang, M. Tu, Y. Wang, G. Shi, Upregulated vegfa and dll4 act as potential prognostic genes for clear cell renal cell carcinoma, Onco Targets Ther. 11 (2018) 1697–1706.
[66] Q. Fu, Y. Chang, H. An, H. Fu, Y. Zhu, L. Xu, W. Zhang, J. Xu, Prognostic value of interleukin-6 and interleukin-6 receptor in organ-confined clear-cell renal cell carcinoma: a 5-year conditional cancer-specific survival analysis, Brit. J. Cancer 113 (11) (2015) 1581–1589.
[67] A.K. Avery, J. Beckstead, A.A. Renshaw, C.L. Corless, Use of antibodies to rcc and cd10 in the differential diagnosis of renal neoplasms, Am. J. Surg. Pathol. 24 (2) (2000) 203–210.
[68] S. Majo, S. Courtois, W. Souleyreau, A. Bikfalvi, P. Auguste, Impact of extracellular matrix components to renal cell carcinoma behavior, Front. Oncol. 10 (2020) 625.
[69] K. Singer, M. Kastenberger, E. Gottfried, C.G. Hammerschmied, M. Büttner, M. Aigner, B. Seliger, B. Walter, H. Schlösser, A. Hartmann, R. Andreesen, A. Mackensen, M. Kreutz, Warburg phenotype in renal cell carcinoma: high expression of glucose-transporter 1 (glut-1) correlates with low cd8(+) t-cell infiltration in the tumor, Int. J. Cancer 128(9) (2011) 2085–95.
[70] J.E. Brown, C.P. Gulka, J.E.M. Giordano, M.P. Montero, A. Hoang, T.L. Carroll, Injectable silk protein microparticle-based fillers: a novel material for potential use in glottic insufficiency, J. Voice 33 (5) (2019) 773–780.

cancers

MDPI

Review

The Extracellular Matrix Environment of Clear Cell Renal Cell Carcinoma

Leif Oxburgh

Rogosin Institute, 310 East 67th St., Room 2-43, New York, NY 10065, USA; leo9022@nyp.org

Simple Summary: The extracellular matrix (ECM) controls fundamental properties of tumors, including growth, blood vessel investment, and invasion. The ECM defines rigidity of tumor tissue and individual ECM proteins have distinct biological effects on tumor cells. This article reviews the composition and biological functions of the ECM of clear cell renal cell carcinoma (ccRCC). The most frequent initiating genetic mutation in ccRCC inactivates the *VHL* gene, which plays a direct role in organizing the ECM. This is predicted to result in local ECM modification, which promotes the growth of tumor cells and the invasion of blood vessels. Later in tumor growth, connective tissue cells are recruited, which are predicted to produce large amounts of ECM, affecting the growth and invasive behaviors of tumor cells. Strategies to therapeutically control the ECM are under active investigation and a better understanding of the ccRCC ECM will determine the applicability of ECM-modifying drugs to this type of cancer.

Abstract: The extracellular matrix (ECM) of tumors is a complex mix of components characteristic of the tissue of origin. In the majority of clear cell renal cell carcinomas (ccRCCs), the tumor suppressor VHL is inactivated. VHL controls matrix organization and its loss promotes a loosely organized and angiogenic matrix, predicted to be an early step in tumor formation. During tumor evolution, cancer-associated fibroblasts (CAFs) accumulate, and they are predicted to produce abundant ECM. The ccRCC ECM composition qualitatively resembles that of the healthy kidney cortex in which the tumor arises, but there are important differences. One is the quantitative difference between a healthy cortex ECM and a tumor ECM; a tumor ECM contains a higher proportion of interstitial matrix components and a lower proportion of basement membrane components. Another is the breakdown of tissue compartments in the tumor with mixing of ECM components that are physically separated in healthy kidney cortex. Numerous studies reviewed in this work reveal effects of specific ECM components on the growth and invasive behaviors of ccRCCs, and extrapolation from other work suggests an important role for ECM in controlling ccRCC tumor rigidity, which is predicted to be a key determinant of invasive behavior.

Keywords: collagen; fibronectin; TGFBI; tenascin; periostin; kidney cortex; basement membrane; interstitial matrix; cancer-associated fibroblasts; CAFs

check for updates

Citation: Oxburgh, L. The Extracellular Matrix Environment of Clear Cell Renal Cell Carcinoma. *Cancers* **2022**, *14*, 4072. https://doi.org/10.3390/cancers14174072

Academic Editors: Jeffrey A. Borgia, Valeria Visconte, Nelson S. Yee and Eakaterina Semenova

Received: 19 July 2022
Accepted: 19 August 2022
Published: 23 August 2022

Publisher's Note: MDPI stays neutral with regard to jurisdictional claims in published maps and institutional affiliations.

Copyright: © 2022 by the author. Licensee MDPI, Basel, Switzerland. This article is an open access article distributed under the terms and conditions of the Creative Commons Attribution (CC BY) license (https://creativecommons.org/licenses/by/4.0/).

1. Introduction

Several different primary tumors have been identified in the kidney; renal cell carcinoma (RCC) is the most common and one of the 10 most prevalent cancers overall [1]. In clear cell renal cell carcinoma (ccRCC), which is the most common subtype of RCC, clusters of tumor cells with clear cytoplasm are found in the kidney cortex [2]. The tumor suppressor *VHL* is lost in over 90% of ccRCCs through genetic or epigenetic mechanisms [3]. *VHL* plays a central role in cellular oxygen sensing [4,5], and its inactivation causes persistent pseudo-hypoxia, resulting in a strong angiogenic profile of tumors [6]. Evidence suggests that the cells of origin for ccRCC are epithelial cells that line the proximal tubule [7,8], one of the most metabolically active cell types in the human body [9]. Transformed epithelial cells in the tumor are surrounded by a network of stroma containing vasculature, interstitial

fibroblasts and inflammatory and immune cells [10]. The cellular tumor components are embedded in the extracellular matrix (ECM).

Many fundamental properties of tumors are controlled by their ECM environment [11], including proliferation [12,13], vascularization [14,15] and invasion [16], making the ECM a key determinant of malignancy. Interplay between the ECM and tumor cells is complex and multifactorial. ECM provides the substrate for cancer cell attachment, and determines rigidity, which has a strong influence on malignancy [17]. It also controls signal transduction in cancer cells, exerting a strong influence on their behaviors [18].

The ECM is a mix of components with distinct physicochemical and signaling properties [19,20]. For the reasons outlined above, the ECM composition characteristic of a tumor type is predicted to play a central role in determining the behavior of that tumor. The ECM profile of a tumor is likely characteristic of the organ from which it arises, but also characteristic of the tumor's cellular composition, with cancer-associated fibroblasts (CAFs) playing a major role in producing the tumor ECM [21]. Difficulties in isolating and maintaining CAFs have hampered experimental studies of these cells in ccRCC. The finding that the outgrowth of CAFs may be dependent on culture conditions that provide the complex ECM environment that they, themselves, generate highlights one important obstacle in the characterization of CAF biology [22]. Indeed, in modeling ccRCC in vitro, we have demonstrated that the CAF population can be maintained by culturing it in an ECM environment that mimics the tumor of origin [23]. CAFs have features in common with activated myofibroblasts seen in fibrosis [24], and one interesting possibility is that insults that convert growth-suppressed fibroblasts in a healthy kidney to a proliferative and synthetic myofibroblast state may provide the appropriate environment for tumor formation from proximal tubule epithelial cells in which *VHL* has been mutated.

The Cancer Genome Atlas includes RNA-seq data for over 500 ccRCC tumors, along with information on patient outcomes, providing a popular resource for studies of association between gene expression and survival that may have prognostic value [25]. Using this resource, a gene signature has been identified that is comprised of 12 genes functionally associated with the ECM [26]. This dataset has also been used to derive a proxy signature for CAF investment in ccRCC, which anti-correlates with survival, suggesting that CAF infiltration in tumors is associated with poor prognosis [27]. While these correlative in silico studies cannot establish causality, they do suggest important relationships between ECM deposition, CAF abundance and tumor aggressiveness. This review discusses published work on the ECM composition of ccRCC, the cellular sources of the matrix components, and the effects of these proteins on cells within tumors.

2. VHL Regulation of the ECM

VHL plays a central role in cellular oxygen sensing by ubiquitinating the HIFα transcription factors in normoxia and targeting them for destruction. In the normoxic state, prolyl hydroxylase domain (PHD) proteins hydroxylate proline residues at the amino terminus of the HIFαs, allowing VHL to bind [28]. The function of the PHDs is strictly oxygen-dependent, and when oxygen becomes scarce, PHD hydroxylation is reduced, the VHL-dependent degradation of HIFαs ceases and they accumulate, dimerizing with HIFβs and localizing to the nucleus where they control a hypoxia-dependent gene expression program that governs cellular metabolism, angiogenic signaling and other pathways [29,30].

In addition to this essential hypoxia-sensing function involving HIFαs, VHL controls ECM organization. This has emerged as an important factor in the interaction of *VHL*-inactivated cells with their extracellular environment and is predicted to regulate angiogenesis, invasiveness and metastasis. Studies of VHL disease variants have shown that variants associated with RCC fail to bind fibronectin, in contrast to wild-type VHL [31,32]. The interaction of VHL with fibronectin is dependent on neddylation, in which NEDD8 is ligated to VHL in a process similar to ubiquitination [33]. This covalent modification acts as a molecular switch, converting a fraction of the intracellular VHL pool to a fibronectin-binding form that does not participate in the degradation of HIFαs [34]. Cultured cells

were used to demonstrate the physical interaction of VHL with fibronectin in the cytoplasm, and gain-of-function experiments with 786-O ccRCC cells that lack the expression of a functional VHL revealed that VHL is required for extracellular deposition of fibronectin matrix in its fibrillar form [35]. The fibrillogenesis of fibronectin is a force-dependent process in which extracellular fibronectin is bound to integrin receptors α5β1 [36,37] or αVβ3 [38]. Fibronectin-induced clustering of integrins at the cell surface promotes the interactions of focal adhesion kinase and its partners, which initiate actin polymerization and intracellular signaling [39,40]. The polymerization of actin and the modification of the cytoskeletal network applies traction force to the fibronectin molecules that are anchored between integrins or between integrin and another binding partner [41,42]. Stretching of fibronectin unfolds the molecule and exposes cryptic epitopes, greatly increasing the binding of additional soluble fibronectin, and inducing fibrillar matrix formation [43].

The finding that VHL is required for fibronectin matrix formation is supported by studies of *Vhl* mutant mouse embryos, which reveal an absence of fibronectin matrix deposition [35]. The physical interaction between VHL and fibronectin, coupled with the diminutive fibronectin deposition by VHL mutant tumor cells, suggest that the cellular phenotype may be explained by an intracellular build-up of unprocessed fibronectin. However, despite the fact that the transgenic expression of VHL reverses the phenotype and promotes the deposition of fibronectin fibrils, no significant difference in intracellular fibronectin content was observed between 786-O cells with or without transgenic VHL expression [44]. This observation suggests that additional molecular players may be involved in VHL-mediated fibronectin assembly and organization. The fibrillogenesis of fibronectin is an integrin-dependent process [41], and studies of 786-O cells using integrin β1-activating and -blocking antibodies revealed that fibronectin organization into fibrils could be promoted in these cells by activating integrin β1 outside-in signaling [44]. This finding suggests that VHL is required for integrin β1 function, which in turn, is required for fibronectin fibrillogenesis. While fibronectin is generally considered an interstitial matrix (IM) component, its fibrillar form is associated with the BM, and may be important for structural integrity [45]. The loss of fibronectin fibrillogenesis as an early event in the transformation of proximal tubule cells is supported by several reports; however, protein expression analysis using validated antisera does not unambiguously show fibronectin expression in the extracellular space surrounding proximal tubules in adult human kidney biopsies (www.proteinatlas.org, accessed on 12 August 2022), introducing a significant caveat to this aspect of the model for local basement membrane (BM) degeneration following the loss of VHL. Whether or not fibronectin fibrillogenesis is a major contributor to changes in the interaction between the proximal tubule epithelial cell and its BM when VHL is inactivated, changes in integrin associations with other matrix components are likely to be affected since VHL has been shown to be physically associated with integrin β1 and to control its half-life [44,46].

Collagen IVα2 is a VHL interaction partner in 786-O ccRCC cells that express wild-type VHL, but not in cells that express disease variants of VHL. Collagen IVα2 and VHL colocalize at the endoplasmic reticulum membrane, and this association is required for the assembly of the triple-helical collagen IV matrix [47]. Xenografting studies reveal that 786-O tumor cells expressing wild-type VHL form tumors with a tightly packed collagen matrix, whereas 786-O cells either without functional VHL or expressing disease variants form tumors with a loose collagen matrix and more extensive blood vessel infiltration [48]. Interestingly, the angiogenic tumor phenotype is seen in cells expressing VHL variants in which the HIFα-degrading function remains intact but the collagen IVα2-interacting function is lost [47,48]. A comparison was made between tumors derived from 786-O cells expressing VHL with inactivated HIF1α degradation and tumors derived from 786-O cells expressing VHL with intact HIF1α degradation but inactivated collagen/fibronectin interaction; it indicated that the elevation of the angiogenic growth factor VEGF by stabilized HIF1α is not sufficient to generate the highly vascular tumor phenotype. Rather, the disruption of ECM organization is required to promote the highly angiogenic tumor

phenotype [48]. Ubiquitome analysis has identified additional candidate ECM targets of VHL such as TGFBI [49], which may influence the invasiveness of ccRCC cells [50].

Based on these studies, one model for the initial events in the formation of a ccRCC tumor (Figure 1) would be that VHL plays an essential role in organizing the matrix immediately surrounding the proximal tubule epithelial cell prior to the somatic mutation of *VHL* and the loss of its matrix-organizing function. The *VHL* mutant cell would alter its turn-over of integrins and relax or perhaps even dissolve its BM locally, generating a loose matrix microenvironment conducive to vascularization while engaging its HIFα proangiogenic program. Studies of ccRCC cell lines with or without the expression of wild-type VHL indicate that VHL suppresses the expression of matrix metallopeptidase (MMP) 2 and 9, while amplifying the expression of tissue inhibitor of metalloproteinase (TIMP) 1 and 2 [51], and that the level of MMP2 expression in ccRCC cells correlates with their capacity for invasion in three-dimensional cell culture [48]. Thus, in addition to local ECM modification with the formation of an angiogenic niche, the loss of VHL would promote the expression of MMP, which would cause ECM degradation and invasive behavior of the tumor cells. This model of VHL-dependent ECM changes that initiate tumor formation is derived from cell culture and xenografting studies, and how it relates to the ECM environment in patient ccRCC tumors at the time of diagnosis is not clear. Based on genetic studies of patient material, the genetic inactivation of *VHL* often precedes the diagnosis of ccRCC by decades, and tumor formation is predicted to be an indolent process [52]. Furthermore, the mutation of *VHL* alone does not appear to be sufficient to initiate tumor formation, as patients with loss of both copies of *VHL* can show benign lesions including cysts [53,54]. Whether local ECM modification caused by the loss of *VHL* predisposes cells to genetic events that lead benign lesions to become malignant is not known, but structural changes associated with cyst formation do suggest that matrix remodeling already occurs in the benign lesion.

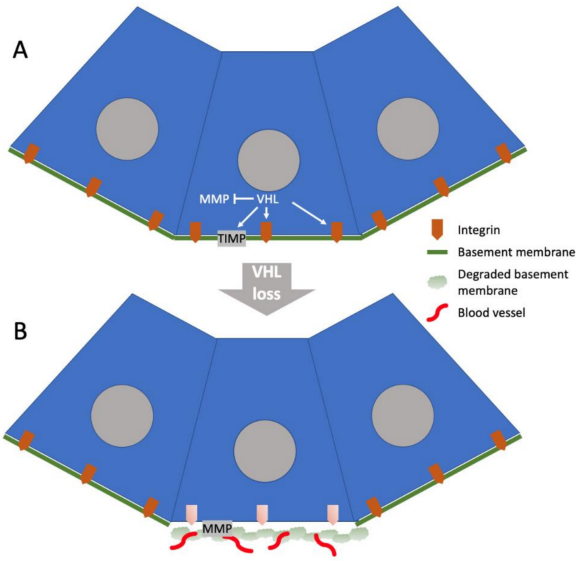

Figure 1. Hypothetical model for changes in the ECM environment of the proximal tubule following loss of VHL. (**A**) VHL controls the half-life of integrins that apply force to fibronectin molecules associated with the basement membrane, which regulates their fibrillogenesis. VHL also suppresses expression of matrix metallopeptidases (MMPs) and upregulates tissue inhibitors of metalloproteinases (TIMPs), ensuring integrity of the basement membrane. (**B**) Following inactivation of *VHL*, fibronectin fibrillogenesis is reduced and MMPs become active, degrading the basement membrane and promoting angiogenesis.

3. ECM Composition of ccRCC Tumors

Clinical material presents a complex matrix profile compared with cell line and short-term xenografting studies, since the tumor at the time of resection is perhaps decades old and composed of many different cell types. While the information that this type of material can yield regarding initiating events in the formation of the tumor is very limited, it does provide an important snapshot of the matrix environment at the time of surgery, and can potentially be correlated with invasiveness and metastasis. Additionally, recreating the matrix environment of the tumor is an important foundation for culturing primary tumor cells. We investigated the repertoire of ECM molecules in patient-derived ccRCC tumor samples with the goal of defining matrix components that could be defined as characteristic of ccRCC [23]. Seven stage pT3 tumors were collected from consenting patients undergoing partial nephrectomy along with healthy neighboring kidney cortex tissue. We designate the neighboring tissue "healthy" because it has a tissue layout and cell types characteristic of a healthy kidney cortex. Whether the cortex tissue neighboring the tumor is genuinely healthy or whether it is affected by proximity to the tumor is not known, and this is a general feature of studies that compare resected tumor tissue with healthy margins. The tumors and matched healthy cortices were analyzed via mass spectrometry using sequential window acquisition of all theoretical fragment ion spectra (SWATH) and data-dependent acquisition (DDA) modalities, which provided both a comparative analysis and a frequency table that could be used to infer protein abundance in tumor versus cortex. A defining feature of the ccRCC ECM composition characterized in this work is its qualitative similarity to the healthy kidney cortex ECM. Within the detection limits of our analysis, neoplastic transformation does not lead to the de novo expression of matrix molecules, but rather, alters the relative abundance of components. One generalization that emerges from the analysis is that the abundance of BM components is diminished in the ccRCC matrix, while the abundance of IM components increases. Tissue from the healthy kidney cortex can be divided into functional units, which are nephrons and blood vessels, and the interstitial space between them. Nephrons and blood vessels are surrounded by BM, which insulates them from the IM scaffold in which renal fibroblasts are embedded (Figure 2). Considering the breakdown of normal epithelial structure that is characteristic of ccRCC, the abundance of IM and loss of BM seen in tumors is not surprising.

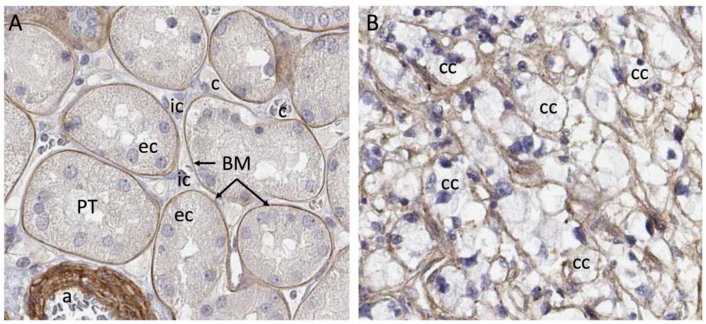

Figure 2. Breakdown of compartments in ccRCC. (**A**) Laminin a5 immunostaining shows strict basement membrane segregation of proximal tubule epithelial cells from the interstitium. (**B**) Cancer cells in ccRCC, which are thought to originate from the proximal tubule cell are embedded in matrix containing laminin a5, but there is no clear segregation of the interstitial cell space from the epithelium. Abbreviations: a—arteriole; BM—basement membrane; c—capillary; cc—clear cell; ec—epithelial cell; ic—interstitial cell. Images from Human Protein Atlas www.proteinatlas.org, licensed under the Creative Commons Attribution-ShareAlike 3.0 International License. https://www.proteinatlas.org/ENSG00000130702-LAMA5/tissue/kidney#img and https://www.proteinatlas.org/ENSG00000130702-LAMA5/pathology/renal+cancer#img were accessed on 12 August 2022.

In contrast to healthy cortex, ccRCC ECM is enriched in the IM components collagen VI, fibronectin, tenascin C, fibrin, TGFBI and periostin. Several studies indicate that

these matrix components can influence the behavior of tumor cells, suggesting that the ECM environment could be an important determinant of tumor aggressiveness. Collagen VI is abundantly expressed in tumors from several organs, including breast [55], colon, and lung [56]. It promotes the survival of tumor cells [57] and fibroblasts [58] and has been shown to stimulate tumor angiogenesis [59]. The tumor content of collagen VI also promotes the invasive behavior of breast cancer cells [60] and colorectal cancer cells [61]. Studies of xenografted ccRCC cells show that collagen VI expression increases tumor size [62].

In summary, many lines of evidence support a role for collagen VI in promoting the aggressive behavior of tumor cells. Collagen VI is also an important driver of organ fibrosis and has been shown to directly promote the differentiation of cardiac fibroblasts to the hypersecretory myofibroblast phenotype, which is central to scarring after infarction [63]. The phenotypic conversion of vascular mural cells and fibroblasts to myofibroblasts is also central to fibrosis of the kidney [64], and the abundance of collagen VI in the ccRCC tumor may promote the development of a fibrotic local environment through the conversion of interstitial cells to myofibroblasts that secrete additional ECM components, the most characteristic being fibronectin [65]. Because collagen VI is a major component of the healthy kidney IM, it is difficult to argue that its presence in the tumor is sufficient to convert the matrix environment to a pro-fibrotic and pro-tumorigenic state. Rather, the contribution that collagen VI makes in the establishment of these pathologic environments may be contextual. Collagen VI is physically associated with a wide variety of other matrix proteins such as fibronectin [66], decorin [67,68], biglycan [68], fibulin [69], and collagens I [70] and IV [71], which were also identified as abundant components of ccRCC ECM in our analysis [23]. The transition from healthy cortex to tumor tissue with its associated alterations in structure and the abundance of these proteins may generate a higher-order matrix complex combining BM and IM components that are normally sequestered in distinct tissue compartments. This matrix complex is predicted to have unique properties and may influence the behaviors of both tumor and stroma cells very differently from the healthy cortex BM and IM compartments.

Another possibility is that processing of the collagen VI peptide fragment endotrophin (ETP) increases in the tumor environment. ETP is a peptide generated by proteolytic cleavage of the carboxy-terminus of collagen VI α3 [72], normally occurring in the adipocytes of white adipose tissue. As fat mass increases, so does circulating ETP, and the finding that this "matrikine" acts as a driver of malignant tumor growth has led investigators to conclude that it may contribute to the association between obesity and cancer [73,74]. ETP is abundant in mammary tumors, which are surrounded by adipocytes [72]. Little is reported on the mechanism by which adipocytes release ETP from collagen VI α3, but one intriguing observation is that this mechanism is engaged when 3T3-L1 fibroblasts are chemically induced to accumulate lipid and form adipocytes [72]. It is possible that the ETP cleavage mechanism could also be activated in renal epithelial cells as they undergo the metabolic transformation to ccRCC tumor cells, in which fatty acid oxidation is repressed and lipids accumulate in the cytoplasm [75]. Alternately, ETP may be locally supplied by perirenal fat, the abundance of which has been correlated with cancer progression in ccRCC [76]. The increased relative risk of kidney cancer in obese individuals [77] strongly suggests a role for adiposity in ccRCC, and further investigation is required to understand whether ETP circulates to or is produced locally in ccRCC tumors.

Fibronectin can be found circulating as a soluble dimer, and in tissue as an insoluble ECM component [78]. Although fibronectin proteins are encoded by a single gene, functionally distinct isoforms are generated by alternate splicing. Circulating fibronectin produced by hepatocytes is largely devoid of the EIIIA and EIIIB domains present in the insoluble protein that is deposited in the tissue [79]. As previously described, fibronectin establishes fibrillar networks through integrin interactions, and these may be disturbed in VHL-inactivated ccRCC cells [35]. The understanding that fibronectin interacts with multiple other matrix molecules has led to a model of fibronectin as an organizer of higher-order

matrix structure [80]. Together with its interacting partner collagen VI [66], it would be predicted to function as an adhesive for the majority of the most abundant matrix proteins identified in ccRCC tumors. Binding partners of particular relevance to the ccRCC matrisome include fibrin [81], periostin [82] and tenascin C [83]. Studies of cultured ccRCC cells in which fibronectin was knocked down suggest a role for fibronectin in promoting cell growth and migration in ccRCC [84]. The correlation of fibronectin expression with patient survival in the TCGA database shows an inverse relationship, suggesting detrimental effects of fibronectin in tumors [85]. A study of tumor tissue from 270 ccRCC patients that scored fibronectin protein expression in the membrane, cytoplasm and nucleus of tumor cells found higher disease-related mortality in patients with cytoplasmic fibronectin [86]. The genetic status of VHL was not defined in this patient cohort, and the impact of the loss of VHL-dependent fibronectin fibrillogenesis was not evaluated.

Tenascin C closely resembles fibronectin, shares receptor-binding properties and is expressed in the stroma of many solid tumors [87]. Little has been reported on the role of tenascin C in ccRCC, but a study of prognostic significance based on the correlation of clinical outcomes with histopathological evaluation of tumors from 137 patients showed that patients with tenascin C-positive tumors had a significantly lower survival rate and suggested that they also had increased risk of metastasis [88]. Studies in a model of glioblastoma have shown that tenascin C promotes proliferation and reduces cell adhesion by reducing the binding of fibronectin to its receptor syndecan 4, suggesting a cell biological mechanism for clinical correlation in ccRCC [89].

TGFBI is a TGFβ-induced protein that is secreted into the extracellular space [90] where it can bind to collagen VI [91] and fibronectin [92]. It shares almost 50% similarity with periostin and has been assigned roles as both a tumor suppressor and a tumor promoter in different experimental systems [93]. Studies in cultured ccRCC cells indicate that TGFBI promotes migration and invasion [50], suggesting a tumor-promoting role. A fluorescent in situ hybridization study of genes with predicted copy number variations in ccRCC confirmed copy number gain in TGFB1 and concluded that it may have a tumor-promoting role [94].

Periostin plays an important role in the organization of collagens by physically interacting with the enzymatic complex that covalently cross-links collagens and enhancing its activity [95]. It binds to both fibronectin and tenascin C [82], which are abundantly represented in the ccRCC ECM [23]. A study of tumor material from 1007 RCC patients concluded that elevated amounts of periostin in tumor cells were correlated with sarcomatoid differentiation and more aggressive tumor cell behavior [96].

Proteoglycans such as HSPG2 (perlecan), lumican and biglycan were identified in tumor ECM, although their abundance was similar to that in healthy cortex [23]. Proteoglycans are composed of a protein core to which glycosaminoglycan chains are covalently bound. HSPG2 is represented in the stroma of several tumor types [97], where it is predicted to bind tenascin C and modify growth factor signaling, including VEGF and FGF, by increasing the binding of these ligands to their receptors [98,99]. Lumican and biglycan are small leucine-rich proteoglycans (SLRPs) that promote collagen fibrillogenesis [100,101]. No reports correlating the properties of ccRCC tumors or patient outcomes with HSPG2 or biglycan could be found for this review. A study of 128 ccRCC patients, including 14 with matched primary ccRCC tumors and pulmonary metastases, correlated lumican expression with metastasis-free and overall patient survival [102].

Many of the studies reviewed in this section suggest a connection between the abundance of specific ECM components, tumor aggressiveness and patient outcome. However, none of the ECM components reviewed in this section are unique to ccRCC tumors, and all are represented in healthy kidney cortex where there is abundant representation of healthy tubule epithelial cells. One major difference between tumor tissue and the neighboring healthy cortex is that epithelial cells in the healthy cortex are insulated from the IM (Figure 2). In the tumor, the BM structure is broken down and these cells are exposed

directly to the components of the IM. This may provide novel matrix signals that influence the process of transformation and tumor growth.

4. Cellular Sources of ECM in ccRCC Tumors

Single-cell transcriptome analysis of the healthy adult proximal tubule, the presumed cell of origin for ccRCC, reveals little or no expression of genes that encode essential BM components such as collagen IV, laminin or nidogen. Other tubule epithelial cells of the cortex such as the collecting duct, as well as fibroblasts, do express these components [103]. From this analysis, it appears likely that the role of the proximal tubule cell may primarily be to organize the BM on which it sits. Components of the IM such as collagens V and VI are expressed by the fibroblast in the healthy kidney. Whether the proximal tubule cell ever becomes a significant source of ECM from the point of its initial transformation to the time of tumor diagnosis decades later, or whether the matrix composition of the evolving tumor is defined by other cell types, are interesting questions. Histopathology shows that endothelial cells, pericytes, fibroblasts, and immune and inflammatory cells accumulate in and around the tumor, and the matrix proteins secreted by these cells may largely or entirely define ECM composition as the tumor grows. Deconvolving the sources of specific ECM components is challenging, but single-cell transcriptome analysis of ccRCC does provide an insight into the expression of matrix genes. Single-cell transcriptome analysis of human tumors has been reported [104], and reanalysis of this data, focusing on matrix components, indicates that tumor fibroblasts are a major ECM source [23]. This finding agrees with observations of tumors in other organ systems [105], where ECM from myofibroblasts is a major determinant of the tumor microenvironment. Interestingly, fibroblasts that were identified in the Young et al. single-cell dataset [104] were segregated into two clusters; the smaller subset had high smooth muscle actin (ACTA2) expression, suggesting they are myofibroblasts. This subset expressed many of the ECM components identified by mass spectrometry of tumor material: collagen VI, fibronectin, lumican, laminin and collagen XII. Based on this, we hypothesize that a minor subset of fibroblasts in an activated myofibroblast state plays a major role in generating ECM in ccRCC (Figure 3). A sparse population of ACTA2-expressing cells can be seen surrounding clusters of clear cells in ccRCC tissue via immunostaining [23]. The location of these cells indicates that they deposit the matrix within the stromal network around tumor cells that contains vessels and immune cells. These ccRCC myofibroblasts also express the gene encoding the angiotensinogen protease renin, which activates the renin–angiotensin system (RAS) to promote vasoconstriction. Renin-expressing cells have previously been reported in ccRCC stroma [106], and they have been proposed as cancer stem cells [107]. Single-cell analysis indicates that they are instead a myofibroblast subpopulation of ccRCC CAFs. Renin is expressed in a subpopulation of cells in the vessel walls of the healthy kidney [108], which maintains blood pressure by secreting renin in response to neural and chemical cues [109]. Involvement of the RAS system in ccRCC progression is suggested by the clinical observation that patients treated with angiotensin inhibitors display improved survival in metastatic ccRCC [110]. While the interpretation of this finding is complex because of the systemic effects of angiotensin inhibition, recent laboratory-based studies have shown that RAS inhibition prevents ccRCC tumor colony formation, indicating that the pathway does act directly on tumor tissue [111]. The local myofibroblast activation of RAS in ccRCC is, therefore, an intriguing possibility.

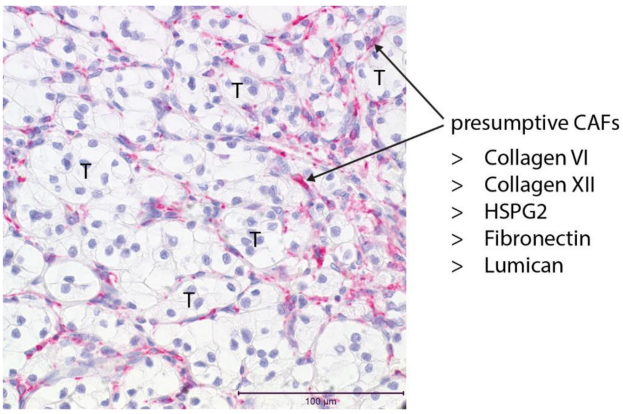

Figure 3. The putative CAF population in ccRCC. Smooth muscle actin immunostaining (red) with hematoxylin nuclear counterstain (blue) reveals a sparse population of cells in the stroma surrounding clusters of tumor cells (T). Single-cell transcriptome analysis indicates that this cell population actively expresses many of the components of the tumor ECM, including collagen VI, collagen XII, HSPG2, fibronectin and lumican.

5. ECM as Therapeutic Target

In addition to the effects of specific ECM components on tumor cells, reviewed above, ECM determines the rigidity of tumor tissue. Measurements of ccRCC tumor samples have shown that the rigidity of the tumor tissue is reduced compared with the surrounding cortex, and that the collagen content of ccRCCs does not correlate with rigidity [112]. A study with a sample size large enough to correlate tumor rigidity with tumor progression and patient outcomes in ccRCC has not yet been reported, but based on studies of other tumor types [113], one would expect increases in tumor matrix rigidity due to collagen crosslinking to promote tumor progression and the invasive behaviors of ccRCC tumor cells. As described in Section 2, VHL is thought to play a major role in controlling the fibrillogenesis of the matrix, and its loss in ccRCC would be predicted to weaken the matrix. Counteracting this, the gene encoding lysyl oxidase (*LOX*) is under the control of HIF transcription factors, which are transcriptionally active when VHL is lost. LOX crosslinks collagens, and in vitro studies of ccRCC cells have shown that LOX increases matrix rigidity [114]. Controlling matrix rigidity may be therapeutically tractable through the modification of LOX, an approach that has been clinically tested using the antibody Simtuzumab, which targets LOXL2. While this is an attractive concept, no clinical improvement was seen in randomized clinical trials of patients with colorectal adenocarcinoma treated with FOLFIRI [115] or in those with pancreatic adenocarcinoma treated with gemcitabine [116] when Simtuzumab was added to the treatment regimen. While Simtuzumab is specific to LOXL2, there are multiple LOX homologs, and it is possible that targeting these proteins more broadly may be required to see an effect in the tissue.

The CAF is a major source of tumor matrix, and numerous approaches have been developed to target this cell type. While the cellular origins of CAFs remain unclear, and presumably vary between cancer types, there is agreement on the common signaling pathways that promote their activation [24]. Inflammatory signaling, matrix composition and matrix rigidity are contributing factors, as is the expression of the fibroblast activation protein (FAP) and signaling through the TGFβ and hedgehog (Hh) pathways. Therapeutic targeting of CAFs is an attractive strategy because these cells are generally non-transformed and prospects for the evolution of escape mechanisms are presumed to be minimal in contrast to the transformed tumor cells. Strategies have been developed to specifically target fibroblast activation pathways including FAP, TGFβ and Hh. A summary of clinical trials using drugs that target each of these pathways is reviewed in [24]. The CAF has multiple functions in addition to the production of the matrix, including growth factor and cytokine production, which establish a local microenvironment, potentially with distinct subcompartments within the tumor. Because of their diverse functions, it is not clear

if CAFs promote tumor growth and aggressiveness in all contexts. For example, the depletion of CAFs in pancreatic cancer reduced survival in a mouse model [117]. Too little is known about CAFs in ccRCC to make predictions regarding the benefit of targeting them therapeutically. Further investigation of their role in cell signaling, immunomodulation and matrix production is needed to accurately define the functions of these cells in ccRCC. Recent progress in the genetic modeling of ccRCC in mice [118] and the development of 3D culture systems for studies of ccRCC tumor cell interactions with CAFs [23] now provide powerful platforms for the study of these cells.

6. Conclusions

The ECM environment controls many fundamental properties of tumors, including their proliferation, vascularization and invasion, and is therefore a key determinant of their malignancy. The tumor ECM is a complex mix of components, characteristic of the organ from which the tumor arises. Each component has distinct physicochemical and signaling properties, and in aggregate, the ECM defines the overall layout and rigidity of the tumor tissue. In ccRCC, the relationship between the ECM and VHL is of particular interest since VHL is lost in the majority of these tumors. In addition to its role in controlling the availability of HIF transcription factors, which is foundational for cellular oxygen sensing, VHL regulates integrins, controls the organization of matrix proteins and suppresses the expression of matrix-degrading enzymes. The loss of VHL promotes a loosely organized and angiogenic matrix environment that may represent one of the first steps in tumor formation. Later in the evolution of the tumor, multiple cell types accumulate, including CAFs, which express matrix proteins and are predicted to be a major determinant of ECM composition in ccRCC at the time of diagnosis. While this tumor ECM composition qualitatively resembles that of the healthy neighboring kidney cortex in which the tumor arises, there are important differences. One is the quantitative difference between the healthy cortex ECM and the tumor ECM; tumor ECM contains a higher proportion of interstitial matrix components and a lower proportion of basement membrane components. Another important difference is the breakdown of tissue compartments in the tumor with mixing of ECM components that are physically separated in the healthy kidney cortex. Numerous studies reviewed in this work suggest effects of specific ECM components on growth and invasive behaviors of ccRCCs. Studies using novel animal and in vitro models will refine our understanding of the roles of individual ECM components in promoting or inhibiting tumor growth and aggressiveness, and will also answer questions regarding how tissue rigidity is determined in ccRCC.

Funding: This work was supported by The Assistant Secretary of Defense for Health Affairs, endorsed by the Department of Defense, through the Kidney Cancer Research Program under Award No. W81XWH-18-1-0620 (KC170016) (LO). The opinions, interpretations, conclusions and recommendations are those of the author and are not necessarily endorsed by the Department of Defense.

Acknowledgments: Many thanks to Kyle Bond for many interesting discussions about ccRCC.

Conflicts of Interest: The author declares no conflict of interest.

Abbreviations

BM—basement membrane; CAF—cancer-associated fibroblast; ccRCC—clear cell renal cell carcinoma; DDA—data-dependent acquisition; ECM—extracellular matrix; ETP—endotrophin; IM—interstitial matrix; MMP—matrix metallopeptidase; PHD—prolyl hydroxylase domain; RAS—renin-angiotensin system; SWATH—sequential window acquisition of all theoretical fragment ion spectra; TIMP—tissue inhibitor of matrix metalloproteinase; VHL—Von Hippel Lindau.

References

1. Siegel, L.R.; Miller, K.D.; Jemal, A. Cancer statistics, 2020. *CA Cancer J. Clin.* **2020**, *70*, 7–30. [CrossRef]
2. Haake, M.S.; Rathmell, W.K. Renal cancer subtypes: Should we be lumping or splitting for therapeutic decision making? *Cancer* **2017**, *123*, 200–209. [CrossRef] [PubMed]
3. Nickerson, M.L.; Jaeger, E.; Shi, Y.; Durocher, J.A.; Mahurkar, S.; Zaridze, D.; Matveev, V.; Janout, V.; Kollarova, H.; Bencko, V.; et al. Improved identification of von Hippel-Lindau gene alterations in clear cell renal tumors. *Clin. Cancer Res.* **2008**, *14*, 4726–4734. [CrossRef] [PubMed]
4. Iliopoulos, O.; Levy, A.P.; Jiang, C.; Kaelin, W.G., Jr.; Goldberg, M.A. Negative regulation of hypoxia-inducible genes by the von Hippel-Lindau protein. *Proc. Natl. Acad. Sci. USA* **1996**, *93*, 10595–10599. [CrossRef] [PubMed]
5. Maxwell, P.H.; Wiesener, M.S.; Chang, G.W.; Clifford, S.C.; Vaux, E.C.; Cockman, M.E.; Wykoff, C.C.; Pugh, C.W.; Maher, E.R.; Ratcliffe, P.J. The tumour suppressor protein VHL targets hypoxia-inducible factors for oxygen-dependent proteolysis. *Nature* **1999**, *399*, 271–275. [CrossRef] [PubMed]
6. Choueiri, T.K.; Kaelin, W.G., Jr. Targeting the HIF2-VEGF axis in renal cell carcinoma. *Nat. Med.* **2020**, *26*, 1519–1530. [CrossRef]
7. Lindgren, D.; Sjölund, J.; Axelson, H. Tracing Renal Cell Carcinomas back to the Nephron. *Trends Cancer* **2018**, *4*, 472–484. [CrossRef] [PubMed]
8. Lindgren, D.; Eriksson, P.; Krawczyk, K.; Nilsson, H.; Hansson, J.; Veerla, S.; Sjolund, J.; Hoglund, M.; Johansson, M.E.; Axelson, H. Cell-Type-Specific Gene Programs of the Normal Human Nephron Define Kidney Cancer Subtypes. *Cell Rep.* **2017**, *20*, 1476–1489. [CrossRef]
9. Bhargava, P.; Schnellmann, R.G. Mitochondrial energetics in the kidney. *Nat. Rev. Nephrol.* **2017**, *13*, 629–646. [CrossRef]
10. Delahunt, B.; Srigley, J.R. The evolving classification of renal cell neoplasia. *Semin. Diagn. Pathol.* **2015**, *32*, 90–102. [CrossRef]
11. Cox, T.R. The matrix in cancer. *Nat. Rev. Cancer* **2021**, *21*, 217–238. [CrossRef]
12. Weaver, V.M.; Petersen, O.W.; Wang, F.; Larabell, C.A.; Briand, P.; Damsky, C.; Bissell, M.J. Reversion of the malignant phenotype of human breast cells in three-dimensional culture and in vivo by integrin blocking antibodies. *J. Cell Biol.* **1997**, *137*, 231–245. [CrossRef]
13. Mettouchi, A.; Klein, S.; Guo, W.; Lopez-Lago, M.; Lemichez, E.; Westwick, J.K.; Giancotti, F.G. Integrin-specific activation of Rac controls progression through the G(1) phase of the cell cycle. *Mol. Cell* **2001**, *8*, 115–127. [CrossRef]
14. Brooks, P.C.; Clark, R.A.; Cheresh, D.A. Requirement of vascular integrin alpha v beta 3 for angiogenesis. *Science* **1994**, *264*, 569–571. [CrossRef]
15. Brooks, P.C.; Montgomery, A.M.; Rosenfeld, M.; Reisfeld, R.A.; Hu, T.; Klier, G.; Cheresh, D.A. Integrin alpha v beta 3 antagonists promote tumor regression by inducing apoptosis of angiogenic blood vessels. *Cell* **1994**, *79*, 1157–1164. [CrossRef]
16. Wang, Y.; McNiven, M.A. Invasive matrix degradation at focal adhesions occurs via protease recruitment by a FAK-p130Cas complex. *J. Cell Biol.* **2012**, *196*, 375–385. [CrossRef]
17. Paszek, M.J.; Zahir, N.; Johnson, K.R.; Lakins, J.N.; Rozenberg, G.I.; Gefen, A.; Reinhart-King, C.A.; Margulies, S.S.; Dembo, M.; Boettiger, D.; et al. Tensional homeostasis and the malignant phenotype. *Cancer Cell* **2005**, *8*, 241–254. [CrossRef]
18. Guo, W.; Pylayeva, Y.; Pepe, A.; Yoshioka, T.; Muller, W.J.; Inghirami, G.; Giancotti, F.G. Beta 4 integrin amplifies ErbB2 signaling to promote mammary tumorigenesis. *Cell* **2006**, *126*, 489–502. [CrossRef]
19. Naba, A.; Clauser, K.R.; Ding, H.; Whittaker, C.A.; Carr, S.A.; Hynes, R.O. The extracellular matrix: Tools and insights for the "omics" era. *Matrix Biol.* **2016**, *49*, 10–24. [CrossRef]
20. Theocharis, A.D.; Skandalis, S.S.; Gialeli, C.; Karamanos, N.K. Extracellular matrix structure. *Adv. Drug Deliv. Rev.* **2016**, *97*, 4–27. [CrossRef]
21. Tian, C.; Clauser, K.R.; Öhlund, D.; Rickelt, S.; Huang, Y.; Gupta, M.; Mani, D.R.; Carr, S.A.; Tuveson, D.A.; Hynes, R.O. Proteomic analyses of ECM during pancreatic ductal adenocarcinoma progression reveal different contributions by tumor and stromal cells. *Proc. Natl. Acad. Sci. USA* **2019**, *116*, 19609–19618. [CrossRef] [PubMed]
22. Avery, D.; Govindaraju, P.; Jacob, M.; Todd, L.; Monslow, J.; Puré, E. Extracellular matrix directs phenotypic heterogeneity of activated fibroblasts. *Matrix Biol.* **2018**, *67*, 90–106. [CrossRef] [PubMed]
23. Bond, K.H.; Chiba, T.; Wynne, K.P.H.; Vary, C.P.H.; Sims-Lucas, S.; Coburn, J.M.; Oxburgh, L. The Extracellular Matrix Environment of Clear Cell Renal Cell Carcinoma Determines Cancer Associated Fibroblast Growth. *Cancers* **2021**, *13*, 5873. [CrossRef] [PubMed]
24. Sahai, E.; Astsaturov, I.; Cukierman, E.; DeNardo, D.G.; Egeblad, M.; Evans, R.M.; Fearon, D.; Greten, F.R.; Hingorani, S.R.; Hunter, T.; et al. A framework for advancing our understanding of cancer-associated fibroblasts. *Nat. Rev. Cancer* **2020**, *20*, 174–186. [CrossRef]
25. The Cancer Genome Atlas Research Network. Comprehensive molecular characterization of clear cell renal cell carcinoma. *Nature* **2013**, *499*, 43–49. [CrossRef]
26. Ahluwalia, P.; Ahluwalia, M.; Mondal, A.K.; Sahajpal, N.; Kota, V.; Rojiani, M.V.; Rojiani, A.M.; Kolhe, R. Prognostic and therapeutic implications of extracellular matrix associated gene signature in renal clear cell carcinoma. *Sci. Rep.* **2021**, *11*, 7561. [CrossRef]
27. Liu, B.; Chen, X.; Zhan, Y.; Wu, B.; Pan, S. Identification of a Gene Signature for Renal Cell Carcinoma-Associated Fibroblasts Mediating Cancer Progression and Affecting Prognosis. *Front. Cell Dev. Biol.* **2020**, *8*, 604627. [CrossRef]

28. Kaelin, W.G., Jr.; Ratcliffe, P.J. Oxygen sensing by metazoans: The central role of the HIF hydroxylase pathway. *Mol. Cell* **2008**, *30*, 393–402. [CrossRef]
29. Meléndez-Rodríguez, F.; Roche, O.; Sanchez-Prieto, R.; Aragones, J. Hypoxia-Inducible Factor 2-Dependent Pathways Driving Von Hippel-Lindau-Deficient Renal Cancer. *Front. Oncol.* **2018**, *8*, 214. [CrossRef]
30. Bacigalupa, Z.A.; Rathmell, W.K. Beyond glycolysis: Hypoxia signaling as a master regulator of alternative metabolic pathways and the implications in clear cell renal cell carcinoma. *Cancer Lett.* **2020**, *489*, 19–28. [CrossRef]
31. Hoffman, M.A.; Ohh, M.; Yang, H.; Klco, J.M.; Ivan, M.; Kaelin, W.G., Jr. von Hippel-Lindau protein mutants linked to type 2C VHL disease preserve the ability to downregulate HIF. *Hum. Mol. Genet.* **2001**, *10*, 1019–1027. [CrossRef]
32. Clifford, S.C.; Cockman, M.E.; Smallwood, A.C.; Mole, D.R.; Woodward, E.R.; Maxwell, P.H.; Ratcliffe, P.J.; Maher, E.R. Contrasting effects on HIF-1alpha regulation by disease-causing pVHL mutations correlate with patterns of tumourigenesis in von Hippel-Lindau disease. *Hum. Mol. Genet.* **2001**, *10*, 1029–1038. [CrossRef]
33. Stickle, N.H.; Chung, J.; Klco, J.M.; Hill, R.P.; Kaelin, W.G., Jr.; Ohh, M. pVHL modification by NEDD8 is required for fibronectin matrix assembly and suppression of tumor development. *Mol. Cell Biol.* **2004**, *24*, 3251–3261. [CrossRef]
34. Russell, R.C.; Ohh, M. NEDD8 acts as a 'molecular switch' defining the functional selectivity of VHL. *EMBO Rep.* **2008**, *9*, 486–491. [CrossRef]
35. Ohh, M.; Yauch, R.L.; Lonergan, K.M.; Whaley, J.M.; Stemmer-Rachamimov, A.O.; Louis, D.N.; Gavin, B.J.; Kley, N.; Kaelin, W.G., Jr.; Iliopoulos, O. The von Hippel-Lindau tumor suppressor protein is required for proper assembly of an extracellular fibronectin matrix. *Mol. Cell* **1998**, *1*, 959–968. [CrossRef]
36. Ichihara-Tanaka, K.; Maeda, T.; Titani, K.; Sekiguchi, K. Matrix assembly of recombinant fibronectin polypeptide consisting of amino-terminal 70 kDa and carboxyl-terminal 37 kDa regions. *FEBS Lett.* **1992**, *299*, 155–158. [CrossRef]
37. Sechler, J.L.; Takada, Y.; Schwarzbauer, J.E. Altered rate of fibronectin matrix assembly by deletion of the first type III repeats. *J. Cell Biol.* **1996**, *134*, 573–583. [CrossRef]
38. Yang, J.T.; Hynes, R.O. Fibronectin receptor functions in embryonic cells deficient in alpha 5 beta 1 integrin can be replaced by alpha V integrins. *Mol. Biol. Cell* **1996**, *7*, 1737–1748. [CrossRef]
39. Geiger, B.; Bershadsky, A.; Pankov, R.; Yamada, K.M. Transmembrane crosstalk between the extracellular matrix-cytoskeleton crosstalk. *Nat. Rev. Mol. Cell Biol.* **2001**, *2*, 793–805. [CrossRef]
40. Singh, P.; Carraher, C.; Schwarzbauer, J.E. Assembly of fibronectin extracellular matrix. *Annu. Rev. Cell Dev. Biol.* **2010**, *26*, 397–419. [CrossRef]
41. Pankov, R.; Cukierman, E.; Katz, B.Z.; Matsumoto, K.; Lin, D.C.; Lin, S.; Hahn, C.; Yamada, K.M. Integrin dynamics and matrix assembly: Tensin-dependent translocation of alpha(5)beta(1) integrins promotes early fibronectin fibrillogenesis. *J. Cell Biol.* **2000**, *148*, 1075–1090. [CrossRef]
42. Wu, C.; Keivens, V.M.; O'Toole, T.E.; McDonald, J.A.; Ginsberg, M.H. Integrin activation and cytoskeletal interaction are essential for the assembly of a fibronectin matrix. *Cell* **1995**, *83*, 715–724. [CrossRef]
43. Zhong, C.; Chrzanowska-Wodnicka, M.; Brown, J.; Shaub, A.; Belkin, A.M.; Burridge, K. Rho-mediated contractility exposes a cryptic site in fibronectin and induces fibronectin matrix assembly. *J. Cell Biol.* **1998**, *141*, 539–551. [CrossRef]
44. Esteban-Barragán, M.A.; Avila, P.; Alvarez-Tejado, M.; Gutiérrez, M.D.; García-Pardo, A.; Sánchez-Madrid, F.; Landázuri, M.O. Role of the von Hippel-Lindau tumor suppressor gene in the formation of beta1-integrin fibrillar adhesions. *Cancer Res.* **2002**, *62*, 2929–2936.
45. Lu, J.; Doyle, A.D.; Shinsato, Y.; Wang, S.; Bodendorfer, M.A.; Zheng, M.; Yamada, K.M. Basement Membrane Regulates Fibronectin Organization Using Sliding Focal Adhesions Driven by a Contractile Winch. *Dev. Cell* **2020**, *52*, 631–646. [CrossRef]
46. Ji, Q.; Burk, R.D. Downregulation of integrins by von Hippel-Lindau (VHL) tumor suppressor protein is independent of VHL-directed hypoxia-inducible factor alpha degradation. *Biochem. Cell Biol.* **2008**, *86*, 227–234. [CrossRef]
47. Kurban, G.; Duplan, E.; Ramlal, N.; Hudon, V.; Sado, Y.; Ninomiya, Y.; Pause, A. Collagen matrix assembly is driven by the interaction of von Hippel-Lindau tumor suppressor protein with hydroxylated collagen IV alpha 2. *Oncogene* **2008**, *27*, 1004–1012. [CrossRef]
48. Kurban, G.; Hudon, V.; Duplan, E.; Ohh, M.; Pause, A. Characterization of a von Hippel Lindau pathway involved in extracellular matrix remodeling, cell invasion, and angiogenesis. *Cancer Res.* **2006**, *66*, 1313–1319. [CrossRef]
49. Wang, X.; Hu, J.; Fang, Y.; Fu, Y.; Liu, B.; Zhang, C.; Feng, S.; Lu, X. Multi-Omics Profiling to Assess Signaling Changes upon VHL Restoration and Identify Putative VHL Substrates in Clear Cell Renal Cell Carcinoma Cell Lines. *Cells* **2022**, *11*, 472. [CrossRef]
50. Shang, D.; Liu, Y.; Yang, P.; Chen, Y.; Tian, Y. TGFBI-promoted adhesion, migration and invasion of human renal cell carcinoma depends on inactivation of von Hippel-Lindau tumor suppressor. *Urology* **2012**, *79*, e1–e7. [CrossRef]
51. Koochekpour, S.; Jeffers, M.; Wang, P.H.; Gong, C.; Taylor, G.A.; Roessler, L.M.; Stearman, R.; Vasselli, J.R.; Stetler-Stevenson, W.G.; Kaelin, W.G., Jr.; et al. The von Hippel-Lindau tumor suppressor gene inhibits hepatocyte growth factor/scatter factor-induced invasion and branching morphogenesis in renal carcinoma cells. *Mol. Cell Biol.* **1999**, *19*, 5902–5912. [CrossRef] [PubMed]
52. Mitchell, T.J.; Turajlic, S.; Rowan, A.; Nicol, D.; Farmery, J.H.R.; O'Brien, T.; Martincorena, I.; Tarpey, P.; Angelopoulos, N.; Yates, L.R.; et al. Timing the Landmark Events in the Evolution of Clear Cell Renal Cell Cancer: TRACERx Renal. *Cell* **2018**, *173*, 611–623. [CrossRef] [PubMed]
53. Lubensky, I.A.; Gnarra, J.R.; Bertheau, P.; Walther, M.M.; Linehan, W.M.; Zhuang, Z. Allelic deletions of the VHL gene detected in multiple microscopic clear cell renal lesions in von Hippel-Lindau disease patients. *Am. J. Pathol.* **1996**, *149*, 2089–2094. [PubMed]

54. Paraf, F.; Chauveau, D.; Chrétien, Y.; Richard, S.; Grünfeld, J.P.; Droz, D. Renal lesions in von Hippel-Lindau disease: Immunohistochemical expression of nephron differentiation molecules, adhesion molecules and apoptosis proteins. *Histopathology* **2000**, *36*, 457–465. [CrossRef]
55. Motrescu, E.R.; Blaise, S.; Etique, N.; Messaddeq, N.; Chenard, M.P.; Stoll, I.; Tomasetto, C.; Rio, M.C. Matrix metalloproteinase-11/stromelysin-3 exhibits collagenolytic function against collagen VI under normal and malignant conditions. *Oncogene* **2008**, *27*, 6347–6355. [CrossRef]
56. Nanda, A.; Carson-Walter, E.B.; Seaman, S.; Barber, T.D.; Stampfl, J.; Singh, S.; Vogelstein, B.; Kinzler, K.W.; St Croix, B. TEM8 interacts with the cleaved C5 domain of collagen alpha 3(VI). *Cancer Res.* **2004**, *64*, 817–820. [CrossRef]
57. Iyengar, P.; Espina, V.; Williams, T.W.; Lin, Y.; Berry, D.; Jelicks, L.A.; Lee, H.; Temple, K.; Graves, R.; Pollard, J.; et al. Adipocyte-derived collagen VI affects early mammary tumor progression in vivo, demonstrating a critical interaction in the tumor/stroma microenvironment. *J. Clin. Investig.* **2005**, *115*, 1163–1176. [CrossRef]
58. Rühl, M.; Sahin, E.; Johannsen, M.; Somasundaram, R.; Manski, D.; Riecken, E.O.; Schuppan, D. Soluble collagen VI drives serum-starved fibroblasts through S phase and prevents apoptosis via down-regulation of Bax. *J. Biol. Chem.* **1999**, *274*, 34361–34368. [CrossRef]
59. You, W.K.; Bonaldo, P.; Stallcup, W.B. Collagen VI ablation retards brain tumor progression due to deficits in assembly of the vascular basal lamina. *Am. J. Pathol.* **2012**, *180*, 1145–1158. [CrossRef]
60. Wishart, A.L.; Conner, S.J.; Guarin, J.R.; Fatherree, J.P.; Peng, Y.; McGinn, R.A.; Crews, R.; Naber, S.P.; Hunter, M.; Greenberg, A.S.; et al. Decellularized extracellular matrix scaffolds identify full-length collagen VI as a driver of breast cancer cell invasion in obesity and metastasis. *Sci. Adv.* **2020**, *6*, eabc3175. [CrossRef]
61. Liu, W.; Li, L.; Ye, H.; Tao, H.; He, H. Role of COL6A3 in colorectal cancer. *Oncol. Rep.* **2018**, *39*, 2527–2536. [CrossRef]
62. Wan, F.; Wang, H.; Shen, Y.; Zhang, H.; Shi, G.; Zhu, Y.; Dai, B.; Ye, D. Upregulation of COL6A1 is predictive of poor prognosis in clear cell renal cell carcinoma patients. *Oncotarget* **2015**, *6*, 27378–27387. [CrossRef]
63. Naugle, J.E.; Olson, E.R.; Zhang, X.; Mase, S.E.; Pilati, C.F.; Maron, M.B.; Folkesson, H.G.; Horne, W.I.; Doane, K.J.; Meszaros, J.G. Type VI collagen induces cardiac myofibroblast differentiation: Implications for postinfarction remodeling. *Am. J. Physiol. Heart Circ. Physiol.* **2006**, *290*, H323–H330. [CrossRef]
64. Kuppe, C.; Ibrahim, M.M.; Kranz, J.; Zhang, X.; Ziegler, S.; Perales-Patón, J.; Jansen, J.; Reimer, K.C.; Smith, J.R.; Dobie, R.; et al. Decoding myofibroblast origins in human kidney fibrosis. *Nature* **2021**, *589*, 281–286. [CrossRef]
65. Schiessl, I.M. The Role of Tubule-Interstitial Crosstalk in Renal Injury and Recovery. *Semin. Nephrol.* **2020**, *40*, 216–231. [CrossRef]
66. Tillet, E.; Wiedemann, H.; Golbik, R.; Pan, T.C.; Zhang, R.Z.; Mann, K.; Chu, M.L.; Timpl, R. Recombinant expression and structural and binding properties of alpha 1(VI) and alpha 2(VI) chains of human collagen type VI. *Eur. J. Biochem.* **1994**, *221*, 177–185. [CrossRef]
67. Bidanset, D.J.; Guidry, C.; Rosenberg, L.C.; Choi, H.U.; Timpl, R.; Hook, M. Binding of the proteoglycan decorin to collagen type VI. *J. Biol. Chem.* **1992**, *267*, 5250–5256. [CrossRef]
68. Wiberg, C.; Hedbom, E.; Khairullina, A.; Lamandé, S.R.; Oldberg, A.; Timpl, R.; Mörgelin, M.; Heinegård, D. Biglycan and decorin bind close to the n-terminal region of the collagen VI triple helix. *J. Biol. Chem.* **2001**, *276*, 18947–18952. [CrossRef]
69. Sasaki, T.; Göhring, W.; Pan, T.C.; Chu, M.L.; Timpl, R. Binding of mouse and human fibulin-2 to extracellular matrix ligands. *J. Mol. Biol.* **1995**, *254*, 892–899. [CrossRef]
70. Specks, U.; Nerlich, A.; Colby, T.V.; Wiest, I.; Timpl, R. Increased expression of type VI collagen in lung fibrosis. *Am. J. Respir. Crit. Care Med.* **1995**, *151*, 1956–1964. [CrossRef]
71. Kuo, H.J.; Maslen, C.L.; Keene, D.R.; Glanville, R.W. Type VI collagen anchors endothelial basement membranes by interacting with type IV collagen. *J. Biol. Chem.* **1997**, *272*, 26522–26529. [CrossRef]
72. Park, J.; Scherer, P.E. Adipocyte-derived endotrophin promotes malignant tumor progression. *J. Clin. Investig.* **2012**, *122*, 4243–4256. [CrossRef]
73. Bu, D.; Crewe, C.; Kusminski, C.M.; Gordillo, R.; Ghaben, A.L.; Kim, M.; Park, J.; Deng, H.; Xiong, W.; Liu, X.Z.; et al. Human endotrophin as a driver of malignant tumor growth. *JCI Insight* **2019**, *5*, e125094. [CrossRef]
74. Park, J.; Scherer, P.E. Endotrophin—A novel factor linking obesity with aggressive tumor growth. *Oncotarget* **2012**, *3*, 1487–1488. [CrossRef]
75. Du, W.; Zhang, L.; Brett-Morris, A.; Aguila, B.; Kerner, J.; Hoppel, C.L.; Puchowicz, M.; Serra, D.; Herrero, L.; Rini, B.I.; et al. HIF drives lipid deposition and cancer in ccRCC via repression of fatty acid metabolism. *Nat. Commun.* **2017**, *8*, 1769. [CrossRef]
76. Huang, H.; Chen, S.; Li, W.; Wu, X.; Xing, J. High perirenal fat thickness predicts a poor progression-free survival in patients with localized clear cell renal cell carcinoma. *Urol. Oncol.* **2018**, *36*, 157.e1–157.e6. [CrossRef]
77. Chow, W.H.; Dong, L.M.; Devesa, S.S. Epidemiology and risk factors for kidney cancer. *Nat. Rev. Urol.* **2010**, *7*, 245–257. [CrossRef]
78. Yamada, K.M.; Kennedy, D.W. Fibroblast cellular and plasma fibronectins are similar but not identical. *J. Cell Biol.* **1979**, *80*, 492–498. [CrossRef]
79. To, W.S.; Midwood, K.S. Plasma and cellular fibronectin: Distinct and independent functions during tissue repair. *Fibrogenesis Tissue Repair* **2011**, *4*, 21. [CrossRef]
80. Zollinger, A.J.; Smith, M.L. Fibronectin, the extracellular glue. *Matrix Biol.* **2017**, *60*, 27–37. [CrossRef]
81. Weisel, J.W.; Litvinov, R.I. Fibrin Formation, Structure and Properties. *Subcell. Biochem.* **2017**, *82*, 405–456. [PubMed]

82. Kii, I.; Nishiyama, T.; Li, M.; Matsumoto, K.; Saito, M.; Amizuka, N.; Kudo, A. Incorporation of tenascin-C into the extracellular matrix by periostin underlies an extracellular meshwork architecture. *J. Biol. Chem.* **2010**, *285*, 2028–2039. [CrossRef] [PubMed]
83. Tremble, P.; Chiquet-Ehrismann, R.; Werb, Z. The extracellular matrix ligands fibronectin and tenascin collaborate in regulating collagenase gene expression in fibroblasts. *Mol. Biol. Cell* **1994**, *5*, 439–453. [CrossRef] [PubMed]
84. Ou, Y.C.; Li, J.R.; Wang, J.D.; Chang, C.Y.; Wu, C.C.; Chen, W.Y.; Kuan, Y.H.; Liao, S.L.; Lu, H.C.; Chen, C.J. Fibronectin Promotes Cell Growth and Migration in Human Renal Cell Carcinoma Cells. *Int. J. Mol. Sci.* **2019**, *20*, 2792. [CrossRef] [PubMed]
85. Majo, S.; Courtois, S.; Souleyreau, W.; Bikfalvi, A.; Auguste, P. Impact of Extracellular Matrix Components to Renal Cell Carcinoma Behavior. *Front. Oncol.* **2020**, *10*, 625. [CrossRef] [PubMed]
86. Steffens, S.; Schrader, A.J.; Vetter, G.; Eggers, H.; Blasig, H.; Becker, J.; Kuczyk, M.A.; Serth, J. Fibronectin 1 protein expression in clear cell renal cell carcinoma. *Oncol. Lett.* **2012**, *3*, 787–790. [PubMed]
87. Midwood, K.S.; Orend, G. The role of tenascin-C in tissue injury and tumorigenesis. *J. Cell Commun. Signal.* **2009**, *3*, 287–310. [CrossRef]
88. Ohno, Y.; Izumi, M.; Yoshioka, K.; Ohori, M.; Yonou, H.; Tachibana, M. Prognostic significance of tenascin-C expression in clear cell renal cell carcinoma. *Oncol. Rep.* **2008**, *20*, 511–516. [CrossRef]
89. Huang, W.; Chiquet-Ehrismann, R.; Moyano, J.V.; Garcia-Pardo, A.; Orend, G. Interference of tenascin-C with syndecan-4 binding to fibronectin blocks cell adhesion and stimulates tumor cell proliferation. *Cancer Res.* **2001**, *61*, 8586–8594.
90. Skonier, J.; Neubauer, M.; Madisen, L.; Bennett, K.; Plowman, G.D.; Purchio, A.F. cDNA cloning and sequence analysis of beta ig-h3, a novel gene induced in a human adenocarcinoma cell line after treatment with transforming growth factor-beta. *DNA Cell Biol.* **1992**, *11*, 511–522. [CrossRef]
91. Hanssen, E.; Reinboth, B.; Gibson, M.A. Covalent and non-covalent interactions of betaig-h3 with collagen VI. Beta ig-h3 is covalently attached to the amino-terminal region of collagen VI in tissue microfibrils. *J. Biol. Chem.* **2003**, *278*, 24334–24341. [CrossRef]
92. Billings, P.C.; Whitbeck, J.C.; Adams, C.S.; Abrams, W.R.; Cohen, A.J.; Engelsberg, B.N.; Howard, P.S.; Rosenbloom, J. The transforming growth factor-beta-inducible matrix protein (beta)ig-h3 interacts with fibronectin. *J. Biol. Chem.* **2002**, *277*, 28003–28009. [CrossRef]
93. Corona, A.; Blobe, G.C. The role of the extracellular matrix protein TGFBI in cancer. *Cell Signal.* **2021**, *84*, 110028. [CrossRef]
94. Matsuda, D.; Khoo, S.K.; Massie, A.; Iwamura, M.; Chen, J.; Petillo, D.; Wondergem, B.; Avallone, M.; Kloostra, S.J.; Tan, M.H.; et al. Identification of copy number alterations and its association with pathological features in clear cell and papillary RCC. *Cancer Lett.* **2008**, *272*, 260–267. [CrossRef]
95. Maruhashi, T.; Kii, I.; Saito, M.; Kudo, A. Interaction between periostin and BMP-1 promotes proteolytic activation of lysyl oxidase. *J. Biol. Chem.* **2010**, *285*, 13294–13303. [CrossRef]
96. Morra, L.; Rechsteiner, M.; Casagrande, S.; Duc Luu, V.; Santimaria, R.; Diener, P.A.; Sulser, T.; Kristiansen, G.; Schraml, P.; Moch, H.; et al. Relevance of periostin splice variants in renal cell carcinoma. *Am. J. Pathol.* **2011**, *179*, 1513–1521. [CrossRef]
97. Cruz, L.A.; Tellman, T.V.; Farach-Carson, M.C. Flipping the Molecular Switch: Influence of Perlecan and Its Modifiers in the Tumor Microenvironment. *Adv. Exp. Med. Biol.* **2020**, *1245*, 133–146.
98. Ishijima, M.; Suzuki, N.; Hozumi, K.; Matsunobu, T.; Kosaki, K.; Kaneko, H.; Hassell, J.R.; Arikawa-Hirasawa, E.; Yamada, Y. Perlecan modulates VEGF signaling and is essential for vascularization in endochondral bone formation. *Matrix Biol.* **2012**, *31*, 234–245. [CrossRef]
99. Zhou, Z.; Wang, J.; Cao, R.; Morita, H.; Soininen, R.; Chan, K.M.; Liu, B.; Cao, Y.; Tryggvason, K. Impaired angiogenesis, delayed wound healing and retarded tumor growth in perlecan heparan sulfate-deficient mice. *Cancer Res.* **2004**, *64*, 4699–4702. [CrossRef]
100. Robinson, K.A.; Sun, M.; Barnum, C.E.; Weiss, S.N.; Huegel, J.; Shetye, S.S.; Lin, L.; Saez, D.; Adams, S.M.; Iozzo, R.V.; et al. Decorin and biglycan are necessary for maintaining collagen fibril structure, fiber realignment, and mechanical properties of mature tendons. *Matrix Biol.* **2017**, *64*, 81–93. [CrossRef]
101. Chen, S.; Young, M.F.; Chakravarti, S.; Birk, D.E. Interclass small leucine-rich repeat proteoglycan interactions regulate collagen fibrillogenesis and corneal stromal assembly. *Matrix Biol.* **2014**, *35*, 103–111. [CrossRef]
102. Ho, T.H.; Serie, D.J.; Parasramka, M.; Cheville, J.C.; Bot, B.M.; Tan, W.; Wang, L.; Joseph, R.W.; Hilton, T.; Leibovich, B.C.; et al. Differential gene expression profiling of matched primary renal cell carcinoma and metastases reveals upregulation of extracellular matrix genes. *Ann. Oncol.* **2017**, *28*, 604–610. [CrossRef]
103. Hansen, J.; Sealfon, R.; Menon, R.; Eadon, M.T.; Lake, B.B.; Steck, B.; Anjani, K.; Parikh, S.; Sigdel, T.K.; Zhang, G.; et al. A reference tissue atlas for the human kidney. *Sci. Adv.* **2022**, *8*, eabn4965. [CrossRef]
104. Young, M.D.; Mitchell, T.J.; Vieira Braga, F.A.; Tran, M.G.B.; Stewart, B.J.; Ferdinand, J.R.; Collord, G.; Botting, R.A.; Popescu, D.M.; Loudon, K.W.; et al. Single-cell transcriptomes from human kidneys reveal the cellular identity of renal tumors. *Science* **2018**, *361*, 594–599. [CrossRef]
105. De Wever, O.; Demetter, P.; Mareel, M.; Bracke, M. Stromal myofibroblasts are drivers of invasive cancer growth. *Int. J. Cancer* **2008**, *123*, 2229–2238. [CrossRef]
106. Lindop, G.B.; Fleming, S. Renin in renal cell carcinoma—An immunocytochemical study using an antibody to pure human renin. *J. Clin. Pathol.* **1984**, *37*, 27–31. [CrossRef]

107. Siljee, S.; Milne, B.; Brasch, H.D.; Bockett, N.; Patel, J.; Davis, P.F.; Kennedy-Smith, A.; Itinteang, T.; Tan, S.T. Expression of Components of the Renin-Angiotensin System by Cancer Stem Cells in Renal Clear Cell Carcinoma. *Biomolecules* **2021**, *11*, 537. [CrossRef]
108. Everett, A.D.; Carey, R.M.; Chevalier, R.L.; Peach, M.J.; Gomez, R.A. Renin release and gene expression in intact rat kidney microvessels and single cells. *J. Clin. Investig.* **1990**, *86*, 169–175. [CrossRef]
109. Sequeira López, M.L.; Pentz, E.S.; Nomasa, T.; Smithies, O.; Gomez, R.A. Renin cells are precursors for multiple cell types that switch to the renin phenotype when homeostasis is threatened. *Dev. Cell* **2004**, *6*, 719–728. [CrossRef]
110. McKay, R.R.; Rodriguez, G.E.; Lin, X.; Kaymakcalan, M.D.; Hamnvik, O.P.; Sabbisetti, V.S.; Bhatt, R.S.; Simantov, R.; Choueiri, T.K. Angiotensin system inhibitors and survival outcomes in patients with metastatic renal cell carcinoma. *Clin. Cancer Res.* **2015**, *21*, 2471–2479. [CrossRef]
111. Khanna, P.; Soh, H.J.; Chen, C.H.; Saxena, R.; Amin, S.; Naughton, M.; Joslin, P.N.; Moore, A.; Bakouny, Z.; O'Callaghan, C.; et al. ACE2 abrogates tumor resistance to VEGFR inhibitors suggesting angiotensin-(1-7) as a therapy for clear cell renal cell carcinoma. *Sci. Transl. Med.* **2021**, *13*, eabc0170. [CrossRef] [PubMed]
112. Abbott, A.; Bond, K.; Chiba, T.; Sims-Lucas, S.; Oxburgh, L.; Coburn, J.M. Development of a mechanically matched silk scaffolded 3D clear cell renal cell carcinoma model. *Mater. Sci. Eng. C* **2021**, *126*, 112141. [CrossRef] [PubMed]
113. Levental, K.R.; Yu, H.; Kass, L.; Lakins, J.N.; Egeblad, M.; Erler, J.T.; Fong, S.F.; Csiszar, K.; Giaccia, A.; Weninger, W.; et al. Matrix crosslinking forces tumor progression by enhancing integrin signaling. *Cell* **2009**, *139*, 891–906. [CrossRef] [PubMed]
114. Di Stefano, V.; Torsello, B.; Bianchi, C.; Cifola, I.; Mangano, E.; Bovo, G.; Cassina, V.; De Marco, S.; Corti, R.; Meregalli, C.; et al. Major Action of Endogenous Lysyl Oxidase in Clear Cell Renal Cell Carcinoma Progression and Collagen Stiffness Revealed by Primary Cell Cultures. *Am. J. Pathol.* **2016**, *186*, 2473–2485. [CrossRef]
115. Hecht, J.R.; Benson, A.B., 3rd; Vyushkov, D.; Yang, Y.; Bendell, J.; Verma, U. A Phase II, Randomized, Double-Blind, Placebo-Controlled Study of Simtuzumab in Combination with FOLFIRI for the Second-Line Treatment of Metastatic KRAS Mutant Colorectal Adenocarcinoma. *Oncologist* **2017**, *22*, 243.e23. [CrossRef]
116. Benson, A.B., III; Wainberg, Z.A.; Hecht, J.R.; Vyushkov, D.; Dong, H.; Bendell, J.; Kudrik, F. A Phase II Randomized, Double-Blind, Placebo-Controlled Study of Simtuzumab or Placebo in Combination with Gemcitabine for the First-Line Treatment of Pancreatic Adenocarcinoma. *Oncologist* **2017**, *22*, 241.e15. [CrossRef]
117. Ozdemir, B.C.; Pentcheva-Hoang, T.; Carstens, J.L.; Zheng, X.; Wu, C.C.; Simpson, T.R.; Laklai, H.; Sugimoto, H.; Kahlert, C.; Novitskiy, S.V.; et al. Depletion of carcinoma-associated fibroblasts and fibrosis induces immunosuppression and accelerates pancreas cancer with reduced survival. *Cancer Cell* **2014**, *25*, 719–734. [CrossRef]
118. Wolf, M.M.; Rathmell, W.K.; Beckermann, K.E. Modeling clear cell renal cell carcinoma and therapeutic implications. *Oncogene* **2020**, *39*, 3413–3426. [CrossRef]